Understanding of degradation mechanisms and quantification of performance losses in a Proton Exchange Membrane Fuel Cell during shut-down/start-up phases

Timothée Drugeot

To cite this version:

Timothée Drugeot. Understanding of degradation mechanisms and quantification of performance losses in a Proton Exchange Membrane Fuel Cell during shut-down/start-up phases. Chemical and Process Engineering. Université Grenoble Alpes [2020-..], 2023. English. NNT : 2023GRALI016 . tel-04109893

HAL Id: tel-04109893
https://theses.hal.science/tel-04109893v1

Submitted on 30 May 2023

THÈSE

Pour obtenir le grade de

DOCTEUR DE L'UNIVERSITÉ GRENOBLE ALPES

École doctorale : I-MEP2 - Ingénierie - Matériaux, Mécanique, Environnement, Energétique, Procédés, Production
Spécialité : MEP : Mécanique des fluides Energétique, Procédés
Unité de recherche : CEA Grenoble / LITEN

Compréhension des mécanismes de dégradations et quantification des pertes de performances dans une Pile à Combustible à Membrane Echangeuse de Protons lors des phases d'arrêt/démarrage

Understanding of degradation mechanisms and quantification of performance losses in a Proton Exchange Membrane Fuel Cell during shut-down/start-up phases

Présentée par :

Timothée DRUGEOT

Direction de thèse :

Yann BULTEL PROFESSEUR DES UNIVERSITES, Université Grenoble Alpes	Directeur de thèse
Eric PINTON INGENIEUR - CHERCHEUR, CEA	Co-encadrant de thèse
Fabrice MICOUD INGENIEUR - CHERCHEUR, CEA	Co-encadrant de thèse

Rapporteurs :

Gaël MARANZANA
PROFESSEUR DES UNIVERSITES, Université de Lorraine
Nadia YOUSFI STEINER
PROFESSEUR DES UNIVERSITES, Université Bourgogne Franche-Comté

Thèse soutenue publiquement le **3 mars 2023**, devant le jury composé de :

Yann BULTEL PROFESSEUR DES UNIVERSITES, Université Grenoble Alpes	Directeur de thèse
Gaël MARANZANA PROFESSEUR DES UNIVERSITES, Université de Lorraine	Rapporteur
Nadia YOUSFI STEINER PROFESSEUR DES UNIVERSITES, Université Bourgogne Franche-Comté	Rapporteure
Bruno AUVITY PROFESSEUR DES UNIVERSITES, Université de Nantes	Examinateur
Marian CHATENET PROFESSEUR DES UNIVERSITES, Université Grenoble Alpes	Président

Invités :

Eric PINTON
INGENIEUR DE RECHERCHE, CEA
Fabrice MICOUD
INGENIEUR DE RECHERCHE, CEA

« Si tu veux courir, cours un kilomètre. Si tu veux changer ta vie, cours un marathon. »

« If you want to run, run a mile. If you want to change your life, run a marathon »

Emil Zatopek, multiple champion olympique

« … ou fais une thèse »

« …or do a thesis »

Timothée Drugeot

ACKNOWLEDGEMENTS / REMERCIEMENTS

La thèse, c'est comme un marathon : une épreuve ambitieuse qui nécessite une longue préparation, avec des moments éprouvants puis d'autres plus encourageants. Les mois et les kilomètres se défilent, en serrant les dents et en repoussant sans cesse ses limites. C'est avec cette volonté hors-norme qu'on arrive à franchir la ligne d'arrivée, qu'on éprouve enfin la joie du devoir accompli et de la fierté. Mais c'est surtout grâce aux personnes qui m'ont encadré, aidé et soutenu pendant cette longue préparation que la médaille de « finisher », le diplôme de doctorat est à porter de main. Je souhaite exprimer ma gratitude envers toutes ces personnes.

Je remercie tout d'abord les membres du jury d'avoir accepté de participer à ma soutenance de thèse, en particulier, Gaël Maranzana et Nadia Yousfi Steiner de rapporter mon mémoire de thèse.

Je remercie globalement le CEA LITEN, le Département de l'Electricité et de l'Hydrogène pour les Transports et le Service Technologies Pile à combustibles pour avoir financé ma thèse. Merci de m'avoir accueilli au Laboratoire Système Pile à combustible, au bâtiment Y9 dans une équipe inoubliable.

Je remercie d'abord Eric Pinton, mon co-encadrant « expert système » qui a su m'accompagner, malgré sa fonction de chef de laboratoire, et me guider durant ma thèse. On a partagé beaucoup de réflexions sur ton tableau où on se perdait « un peu » après le n-ième coup de feutre. On a également appris les fondamentaux de l'électrochimie ensemble, j'espère que tu t'en souviendras. Moi en tout cas, je me souviendrais de ta rigueur scientifique et de ton exigence en termes de clarté et de concision. J'ai énormément appris grâce à toi, tout « en serrant les dents » comme tu me le disais. Parler le « Pinton » à l'écrit et à l'oral est ma plus grande fierté et encore j'ai encore beaucoup à apprendre.

Puis est arrivé en cours de route Fabrice Micoud, mon co-encadrant « expert électrochimie ». Je te remercie de m'avoir accompagné sur le développement, les analyses, et les interprétations expérimentales. Je suis parti de rien et j'ai tout appris grâce à toi. J'ai également beaucoup appris de ton intransigeance en termes de communication. Parler le « Pinton » et le « Micoud » à la fois m'a demandé un engagement supplémentaire (rigole). Finalement je m'en suis sorti. Ne t'inquiète pas, après tous ces mois, tu les auras tes financiers et macarons. PS : je cours toujours plus vite que toi malgré mon accident.

Puis je souhaite remercier Yann Bultel, mon directeur de thèse qui a su canaliser mes deux encadrants (humour). Merci pour ton implication dans ma thèse, de l'avoir orchestré régulièrement, d'avoir partagé ton point de vue plus critique avec plus de recul, d'avoir été aussi actif sur la rédaction de la publication et de mon manuscrit de thèse.

Je remercie par la suite Jean-Philippe Poirot et Sébastien Rosini pour leur expertise apportée à chacune de mes réunions d'avancement et pour avoir su répondre à mes questions.

Je remercie Lucas Poupin, tu m'as accompagné 1 an et demi de très près sur mes expériences et sur ma rédaction d'article. Tu as été un mentor avec qui je pouvais parler ouvertement quand ça n'allait pas.

Je remercie l'équipe pile à combustible du Laboratoire Analyse Post-mortem de m'avoir permis d'utiliser les bancs d'essais. Je remercie Laurent Jacqmin qui m'a formé sur leur utilisation, ainsi que Terrence Asencio-Lopez pour m'avoir accompagné sur les modifications/améliorations des bancs nécessaires à la réalisation de mes essais. Merci également à Nicolas Mariage pour m'avoir aidé sur les caractérisations électrochimiques.

Je remercie Mathis Lelievre pour avoir programmé mon cycle expérimental sur le banc d'essai. Tu vois qu'après tout ce travail et ces difficultés, je les ai finalement réalisées ces essais stack.

Je remercie Laure Guetaz pour avoir réalisé les observations MEB sur mes échantillons *post-mortem* et apporté son expertise microstructurale.

Merci également à Arnaud Morin pour les échanges pointilleux sur mes analyses *post-mortem* (électrochimiques et sorption d'eau), ainsi que d'avoir été membres de CSI auprès d'Oliver Lottin, que je remercie également.

Je tiens aussi à remercier tout particulièrement Raky Wane que j'ai eu le privilège d'encadrer durant son stage. Ton soutien sur la réalisation et le traitement des analyses *post-mortem* a été un véritable soulagement. Désolé si j'ai été pointilleux parfois, mes encadrants ont déteint sur moi. Sans doute pour ça que tu as rejoint le camp des batteries (snif).

En globalité, je remercie toute l'équipe du Y9 pour cette ambiance, cette convivialité, ce panel de compétences. J'ai beaucoup appris de chacun de vous avec beaucoup de fous rires. Je ne trouverais certainement nulle part ailleurs une telle ambiance.

Pour finir, je souhaite remercier toutes les personnes qui m'ont de près et de loin. Mes collègues de l'athlétisme et mon coach. Courir avec vous me permettait de me défouler et me libérait l'esprit. A mes amis thésards, avec qui je pouvais discuter avec une totale compréhension, merci !

Merci pour tout Marie. Je n'aurais pas surmonté la dernière épreuve de la rédaction de la sorte sans toi.

RESUME

La pile à combustible à membrane échangeuse de protons est une technologie « bas carbone » prometteuse pour alimenter les véhicules électriques. Cependant, les phases d'arrêt et de démarrage ont été identifiées comme critiques car l'existence d'un front H_2|Air transitoire du côté anodique provoque la circulation de courants internes causant de fortes réactions de dégradation au sein de la couche catalytique cathodique. Les performances et *in fine* la durée de vie de la pile sont ainsi fortement altérées. Bien que ces mécanismes de dégradation aient été étudiés à petite échelle, la mise en œuvre de stratégies d'atténuation à l'échelle pile/système demeure insuffisante pour répondre aux exigences de durée de vie. Cette thèse s'intéresse donc à comprendre les mécanismes de dégradations et à quantifier les pertes de performances à l'échelle représentative d'un design de cellule, à l'état de l'art, en fonction des conditions d'arrêt et de démarrage. Ceci passe donc par :

- Le développement de tests de vieillissement accéléré émulant un profil réaliste du potentiel cathodique lors de la phase de démarrage en mono-cellule de 100 cm² avec un design fluidique et un cœur de pile, à l'état de l'art. Une étude de sensibilité a été réalisée pour évaluer l'impact respectif du potentiel maximal atteint, de la durée du front, de l'humidité du gaz et de la température sur les pertes de performances. Des analyses *post-mortem* ont également été menées pour caractériser finement l'évolution des propriétés physico-chimiques et électrochimiques de la couche active en lien avec les mécanismes de dégradation.
- La transposition des stratégies d'atténuation par dérivation de courant à l'échelle de l'empilement de puissance. Pour cela, une série de tests a été développée afin de reproduire la phase de démarrage pour comparer deux architectures électriques : la connexion de résistance de fuite pour l'ensemble de la pile ou pour chaque cellule individuellement. Des mesures locales de densité de courant ont été effectuées simultanément pour accéder au fonctionnement interne local des cellules et ainsi comprendre les différences en termes de protection de ces architectures par rapport au cas de référence sans dérivation.

ABSTRACT

The Proton Exchange Membrane Fuel Cell is a promising "low carbon" technology to power electric vehicles. However, the shut-down and start-up phases have been identified as critical events because the existence of a transient H_2|Air front on the anode side causes the circulation of internal currents leading to huge degradation reactions within the cathode catalytic layer. The performance and ultimately the lifetime of the cell are thus strongly altered. Although these degradation mechanisms have been studied at small scale, the implementation of mitigation strategies at stack/system scale remains insufficient to meet the lifetime requirements. This thesis is therefore interested in understanding the degradation mechanisms and quantifying the performance losses at the representative scale of a state-of-the-art cell design as a function of shut-down and start-up conditions. This is achieved through:

- The development of accelerated ageing tests emulating a realistic profile of the cathode potential during the start-up phase in a 100 cm² single cell with a state-of-the-art fluidic design and cell core. A sensitivity study has been performed to evaluate the respective impact of the maximum potential reached, the duration of the front, the gas humidity, and the temperature on the performance losses. *Post-mortem* analyses have also been conducted to characterize the evolution of the physicochemical and electrochemical properties of the active layer in relation to the degradation mechanisms.
- The transposition of the current by-pass mitigation strategies up to the short-stack scale. For this purpose, a series of tests has been developed to reproduce the start-up phase and to compare two electrical architectures: the shunt resistance connection for the entire stack or for each cell individually. Local current density measurements have also been performed simultaneously to access the local and internal operation of the cells and thus to understand the differences in terms of protection of these architectures compared to the reference case without by-pass.

TABLES OF CONTENTS

LIST OF ACRONYMS

ACL	Anode Catalyst Layer
AFC	Alkaline Fuel Cell
AST	Accelerated Stress Test
BEV	Battery Electric Vehicle
BoT	Beginning of Test
BP	Bipolar Plate
CCL	Cathode Catalyst Layer
CCM	Catalyst-Coated Membrane
CDDM	Current Density Distribution Mapping
CL	Catalyst Layer
CSC	Carbon Support Corrosion
CV	Cyclic Voltammetry
CVM	Cell Voltage Monitoring
DEA	Dead-End Anode
DoE	U.S. Department of Energy
DVS	Dynamic Vapor Sorption
EC	Electrolysis Cell
ECSA	Electro-Chemical Surface Area
EIS	Electrochemical Impedance Spectroscopy
EoT	End of Test
FC	Fuel Cell
FCEV	Fuel Cell Electric Vehicle
GDL	Gas Diffusion Layer
GHG	Green House Gas
HER	Hydrogen Evolution Reaction
HOR	Hydrogen Oxidation Reaction
HSAC	High Surface Area Carbon
ICE	Internal Combustion Engine
LHV	Low Heating Value
MB	Membrane
MEA	Membrane Electrode Assembly
MCFC	Molten Carbonate Fuel Cell

MPL	Micro Porous Layer
OC	Open Circuit
OCV	Open Circuit Voltage
OER	Oxygen Evolution Reaction
ORR	Oxygen Reduction Reaction
PAFC	Phosphoric Acid Fuel Cell
PEIS	Potentiostatic Electrochemical Impedance Spectroscopy
PEM	Proton Exchange Membrane
PEMFC	Proton Exchange Membrane Fuel Cell
PFSA	PerFluoroSulfonic Acid
PTFE	PolyTetraFluoroEthylene
Pt/C	Platinum / Carbon
RCD	Reverse Current Decay
R&D	Research & Development
$RH_{a/c}$	Anode / Cathode Relative Humidity
RHE	Reversible Hydrogen Electrode
SEM	Scanning Electron Microscopy
SOFC	Solid Oxide Fuel Cell
SU/SD	Start-Up / Shut-Down
SU-AST	Start-Up Accelerated Stress Test
SU/SD-AST	Start-Up / Shut-Down Accelerated Stress Test

NOMENCLATURE

a	Chemical activity for the reactant species	$[-]$
$E^{0}_{ox/red}$	Reversible Potential in standard conditions	$[V\ vs\ RHE]$
$E_{ox/red}$	Reversible Potential in given conditions	$[V\ vs\ RHE]$
E_{front}	Front potential	$[V\ vs\ RHE]$
F_{H2}	Fuel molar flow rate	$[mole.s^{-1}]$
F	Faraday constant	$[C.mole^{-1}]$
H_{LHV}	Enthalpy of combustion linked to Low Heating Value	$[kJ.mole^{-1}]$
i	Current density	$[A.cm^{-2}]$
I	Overall Current	$[A]$
L_a	Mean crystallite size (based on Raman measurements)	$[nm]$
n	Number of electrons exchanged	$[-]$
P_{H2}	Fuel partial pressure	$[bar]$
P_{O2}	Oxidant partial pressure	$[bar]$
$Q_{PtH-des}$	Charge of proton desorption	$[C]$
$Q_{PtOx-red}$	Charge of oxide reduction	$[C]$
R	Ideal Gas Constant	$[J.K^{-1}mole^{-1}]$
R_{cell}	Individual Cell Resistance	$[\Omega]$
R_{ct}	Charge transfer resistance	$[\Omega]$
$R_{H^+,MB}$	Protonic resistance in the membrane	$[\Omega]$
$R_{H^+,CCL}$	Protonic resistance in the cathode catalyst layer	$[\Omega]$
R_{ohm}	Ohmic resistance	$[\Omega]$
R_{ion}	Ionic resistance	$[\Omega]$
R_{elec}	Electronic resistance	$[\Omega]$
R_{stack}	Stack Resistance	$[\Omega]$
RH	Relative Humidity	$[\%]$
T_{cell}	Cell temperature	$[°C]$
t_{front}	Front duration	$[s]$
U_{rev}	Cell reversible voltage	$[V]$
U_{OCV}	Cell voltage in open-circuit	$[V]$

$U\,(i)$	Cell voltage in operation	$[V]$
η_{act}	Activation overpotential	$[V]$
η_{mass}	Mass-transport overpotential	$[V]$
η_{mixed}	Mixed overpotential	$[V]$
η_{ohm}	Ohmic overpotential	$[V]$

GENERAL INTRODUCTION

Long-term strategies submitted to the European Commission encourage the reduction of the greenhouse gas emissions in order to limit the global warming to less than 2 °C and to ultimately reach the carbon neutrality for 2050. Laboratories and industries are engaged in the energy transition for the transportation applications. Concrete solutions are being developed to market "zero carbon" electric powered by battery or fuel cell. Indeed, one promising technology to power the hydrogen vehicle is the Proton Exchange Membrane Fuel Cell (PEMFC) based on electrochemical reactions: the oxidation of the hydrogen in the anode and the reduction of the oxygen in the cathode.

However, the number of Fuel Cell electrical vehicles in traffic remains negligible compared to the battery electric vehicles. In fact, the PEMFC technology still requires further research and development efforts to reach the mass market. For that, key technical challenges need to be overcome: the high cost and the insufficient durability of PEMFC stack. Roadmaps have been published during the last decades to give guidelines and support the improvement of the components of the PEMFC, especially for the catalyst layers in terms of resistance under severe operating degradations. Moreover, the optimization of the PEMFC system control in the vehicle operation is also required to avoid degrading conditions within the stack. In transportation applications, the unprotected Start-Up and Shut-down (SU/SD) phases have been identified to be very damaging to the cathode catalyst layer. Thus, frequent SU/SD cycle in the hydrogen-powered vehicle can lead to important performance decay and reduced durability.

During the last two decades, numerous studies have been conducted to understand the specific degradation mechanisms in SU/SD. The well-known Reverse Current Decay (RCD) has been highlighted as the most degrading mechanism when the anode side is subject to an H_2|Air front. Local cathode potential can be then significantly elevated and promote oxidation reactions: mainly the water electrolysis, plus, the irreversible corrosion of the carbon support and the Platinum nanoparticles. To diminish the impact of these internal currents, several mitigation strategies have been reported in the literature mainly at small scale such as:

- Lowering of the cell temperature;
- Decreasing of the partial pressure and relative humidity of the reactant gas;
- Accelerating of the H_2|Air front propagation;
- Lowering of the cathode potential by shunting the PEMFC stack with dummy load.

However, it is difficult to compare and identify the most impactful mitigation way due to the various PEMFC technologies and experimental protocols used in these studies. In addition, the development and the implementation of mitigation strategies and architecture at stack/system scale remains insufficient to meet the lifetime requirements. This thesis is therefore interested in understanding the degradation mechanisms and quantifying the performance losses at the representative scale of a state-of-the-art cell design as a function of shut-down and start-up conditions.

In this thesis manuscript, Chapter I is dedicated to the general description of PEMFC operation and components. A review on the main degradation mechanisms is also presented.

Then, Chapter II is focused on the specific degradations linked to the protocols and operating conditions during the transient start-up and shut-down phases. The detailed SU and SD processes from literature and patents are both explored to finally report and discuss the existing mitigation strategies.

Chapter III presents the fuel cell design, the materials, the experimental protocols and the coupled *in-situ* and *post-mortem* characterizations used in this work. The description of the two specific accelerated stress tests at single cell level and at short-stack level are described to emulate the start-up and shut-down phases.

Chapter IV is then dedicated to present the main experimental results obtained at single cell level at the state of the art. The work is here focused on identifying the most impactful parameter on performance loss during realistic cathode potential profile in the start-up phases. *Post-mortem* characterizations make it possible to discuss and to understand deeper the physico-chemical and electro-chemical property modifications of the cathode catalyst layer along the ageing. These results will then support the rise of stack-level protection architectures.

Finally, Chapter V shows the results obtained using an ageing test on short-stacks developed in this thesis. Repeated H_2|Air front propagations are carried out using three different current by-pass architectures to compare their effectiveness. Moreover, a Current Density Distribution Mapping device (S++®) inserted in the center of the stack provides local and internal measurements of the stack operation. The temporal evolution of local current density distribution during the start-up and shut-down phases are analyzed and discussed to understand in detail the respective effects of shunting the whole stack or shunting each cell individually.

Chapter I.REVIEW ON PROTON EXCHANGE MEMBRANE FUEL CELL

TECHNOLOGY AND DURABILITY CHALLENGES

I.1. FUEL CELL

I.1.1. Presentation of the different technologies

The fuel cell is an electrochemical converter based on the oxidation of a fuel (usually dihydrogen and simply denoted hereafter “hydrogen”) and the reduction of an oxidant (classically dioxygen simply denoted “oxygen” hereafter, pure or coming from ambient Air), respectively in the anode and cathode electrodes. The half-reactions depend on the FC technologies as summarized in the Table I-1 [1]. They are differentiated by the nature of the electrolyte used to separate the two electrodes and therefore the ionic species exchanged (H^+ cations in an acidic environment and OH^-, O^{2-}, CO_3^{2-} anions in a basic environment). Their operating temperature and thus their field of applications also differentiate them:

- Low-temperature technologies (PEMFC, AFC) for transportation and both small portable and stationary applications;
- Medium-temperature technology (PAFC) for stationary generators;
- High-temperature technologies (MCFC, SOFC) for mass electricity production and industrial cogeneration.

In Europe, the maturity of these technologies depends on the scope of their applications. To date, most types are at the laboratory, prototype, and demonstrator stages. PEMFC and SOFC technologies are the most advanced in their developments towards mass market. In particular, the PEM Fuel Cell in the transportation application is already being used in vehicles on the road.

Table I-1: Summary of the different fuel cell technologies assuming H_2 used as fuel

Technology	**Electrolyte / Ionic species**	**Electrochemical half-reactions** *(anode / cathode)*	**Operating temperature**	**Application**
PEMFC	Polymer (solid) H^+	$H_2 \rightarrow 2H^+ + 2e^-$ $\frac{1}{2}O_2 + 2H^+ + 2e^- \rightarrow H_2O$	25 – 90 °C	Portable, Transports
AFC	Potassium hydroxide (liquid) OH^-	$H_2 + 2OH^- \rightarrow 2H_2O + 2e^-$ $\frac{1}{2}O_2 + H_2O + 2e^- \rightarrow 2OH^-$	25 – 80 °C	Portable, Transports
PAFC	Phosphoric acid (liquid) H^+	$H_2 \rightarrow 2H^+ + 2e^-$ $\frac{1}{2}O_2 + 2H^+ + 2e^- \rightarrow H_2O$	150-200 °C	Stationary
MCFC	Molten carbonate (liquid) CO_3^{2-}	$H_2 + CO_3^{2-} \rightarrow H_2O + CO_2 + 2e^-$ $\frac{1}{2}O_2 + CO_2 + 2e^- \rightarrow CO_3^{2-}$	650 °C	Stationary
SOFC	Ceramic (solid) O^{2-}	$H_2 + O^{2-} \rightarrow H_2O + 2e^-$ $\frac{1}{2}O_2 + 2e^- \rightarrow O^{2-}$	600-1000 °C	Stationary

I.1.2. PEM fuel cell in mobility applications

The European Commission published in 2019 the European Green Deal that dictates climate neutrality. The goal is to reduce Greenhouse Gas emissions by 2030 (-55% compared to 1990), among which 23% is due to transport in 2019 [2]. To this end, Europe is imposing "zero carbon" for 2035 by the commercialization of electric and hydrogen vehicles only.

The decarbonation and electrification of our modes of transport has already been started with the emergence of the Lithium-ion battery. Since 2020, the sales of Battery Electric Vehicles (BEV) and hybrid vehicles have taken off with 1.3 million in Western Europe (144% more than the year 2019) [3]. Hydrogen vehicle powered by fuel cell, as known as Fuel Cell Electrical Vehicle (FCEV), also seems to be a promising candidate for the energy transition. Its main advantages for the transportation applications are:

- Low-temperature operation (80 - 100 °C) with fast start-up/shut-down;
- Satisfactory autonomy comparable to thermal vehicles (600 km);
- Fast hydrogen recharge (3 - 5 minutes);
- Correct cold start behavior (- 30 °C).

Despite these assets close to the internal combustion vehicle, the place of the FCEV in the automotive market is restrained. Currently, only few light-duty FCEV models are on the road (Toyota Mirai I & II, Hyundai Nexo, Honda Clarity) against roughly 50 Battery Electrical Vehicle (BEV) models. PEMFC technology has a hard time convincing light-vehicle manufacturers because of its high cost (60 - 80 k€), its higher fuel cost (13.6 € / 100 km) and the lack of refueling infrastructure. There were 12,000 FCEV registered worldwide, compared to 2.2 million BEV in 2019. However, its autonomy and storage capacity are of key-interest for manufacturers for heavy-duty vehicles (buses, trucks), rail vehicles (trains, streetcars) and naval / aviation vehicles (Airplanes, boats), where batteries are more difficult to implement and do not fulfill autonomy specifications. Heavy-duty mobility is currently the most viable option for hydrogen vehicle short-term deployment. Indeed, the architecture and operating conditions are often less restrictive in heavy-duty vehicles, making it easier to integrate a fuel cell system. Industrials and equipment manufacturers are investing and innovating, bringing fuel cells to the forefront and allowing a first approach in the transportation application very soon.

The Volvo and Daimler Group have invested 1.2 billion euro on the mass production of fuel cells for trucks by 2025. The French automotive supplier Faurecia has invested in the development of storage systems. It will supply 10,000 tanks to Hyundai to equip 1,600 trucks [4]. France is also supporting this deployment, aiming at up to 5,000 trucks by 2028. Some cities have already opted for hydrogen-powered public transport (8 buses in the city of Pau and 5 in Auxerre). PEMFC technology is also being deployed in river and maritime mobility. In 2017, the first hydrogen-powered "laboratory" boat, Energy Observer, was developed in collaboration with CEA-Liten (Grenoble, FRANCE) and launched with the aim of sailing around the world in complete energetic autonomy. In 2022, Energy Observer is partnering with Air Liquide, EO Dev and CMA-CGM, a leader in maritime transport and logistics, in the development of a marketable "zero emission" boat: Energy Observer 2. This cargo ship powered by liquid hydrogen will be dedicated to goods transportation with a range of 4,000 nautical miles (7,500 km). On the aviation side, Airbus has signed an agreement with Elringklinger, a German automotive manufacturer of components, to develop the first commercial hydrogen Aircraft by 2035. The Airbus ZEROe concept will be powered by six electric motors driven by high-power fuel cells with reliability adapted to aeronautical criteria. Finally, rail transport has already successfully demonstrated the growth of hydrogen with the Coradia iLint train developed by Alstom. This alternative to diesel on non-electrified lines was tested from 2018 to 2020 in Germany, in 2020 in the Netherlands and Austria, and in 2021 in Sweden. France has ordered 12 trainsets for initial testing in 2023-2024 and for commissioning in late 2025.

Many stakeholders in the transport sector have embarked on the "zero carbon" path. While the rail and heavy-road applications show an encouraging trend, the case of aviation and light vehicles is further away. In all cases, the use of fuel cells is qualified as a low carbon technology, provided that the hydrogen is produced by a decarbonized process. At present, most of the so-called "grey" hydrogen is produced by "steam reforming" of natural gas, which emits a lot of CO_2 (10 kg of CO_2 for 1 kg of hydrogen). The alternative solution is "green" hydrogen produced by electrolysis of water by using electricity from intermittent renewable energy sources (such as wind turbines and solar panels). However, green hydrogen remains too expensive and has not been developed enough yet to consider a massive deployment at the moment. Technological developments are in progress to produce and distribute the hydrogen at large scale and to give visibility to economic and territorial entities.

The PEMFC seems to be the best candidate for decarbonizing heavy-duty mobility. However, before massive commercialization, some technological barriers remain to be overcome: its cost, performance and durability. The work presented here will focus on the stresses associated to the transport applications, particularly the start-up and shut-down phases, and their impact on the lifetime of the fuel cell. Subsequently, new strategies and system architectures will be studied to improve PEMFC systems durability. Before that, it is necessary to review in this first chapter the electrochemical principles and the components of the PEMFC.

I.2. PEMFC TECHNOLOGY

I.2.1. Electrochemical principle

I.2.1.1. Redox couples and reversible potential

An electrochemical cell for PEMFC technology uses the redox couples H^+/H_2 and O_2/H_2O. Each redox couple is brought into play within an electrode on each side of the Proton Exchange Membrane (PEM). In PEMFC operation, the two half-reactions taking place are the Hydrogen Oxidation Reaction (HOR) (I-1) and the Oxygen Reduction Reaction (ORR) (I-2) with liquid water production.

$$H_{2\,(gas)} \leftrightarrow 2H^+ + 2e^- \qquad E^0_{H^+/H_2} = 0\ V\ vs\ RHE\text{[1]} \qquad \text{(I-1)}$$

$$\frac{1}{2}O_{2\,(gas)} + 2H^+ + 2e^- \leftrightarrow 2H^+ + H_2O_{(liq)} \qquad E^0_{O_2/H_2O_{(liq)}} = 1.23\ V\ vs\ RHE \qquad \text{(I-2)}$$

We talk about generator mode because the difference between the potential of the two electrodes forces spontaneously HOR and ORR reactions and thus the passage of electrons through an external electrical circuit. The membrane acts as an electronic insulator but ionic conductor between both electrodes. The electrochemical system thus converts chemical energy into electrical and thermal energies, as illustrated in Figure I-1. The global reaction (I-3) of the fuel cell is written as follows:

$$H_{2\,(gas)} + \frac{1}{2}O_{2\,(gas)} \rightarrow H_2O_{(liq)} + heat + electricity \qquad \text{(I-3)}$$

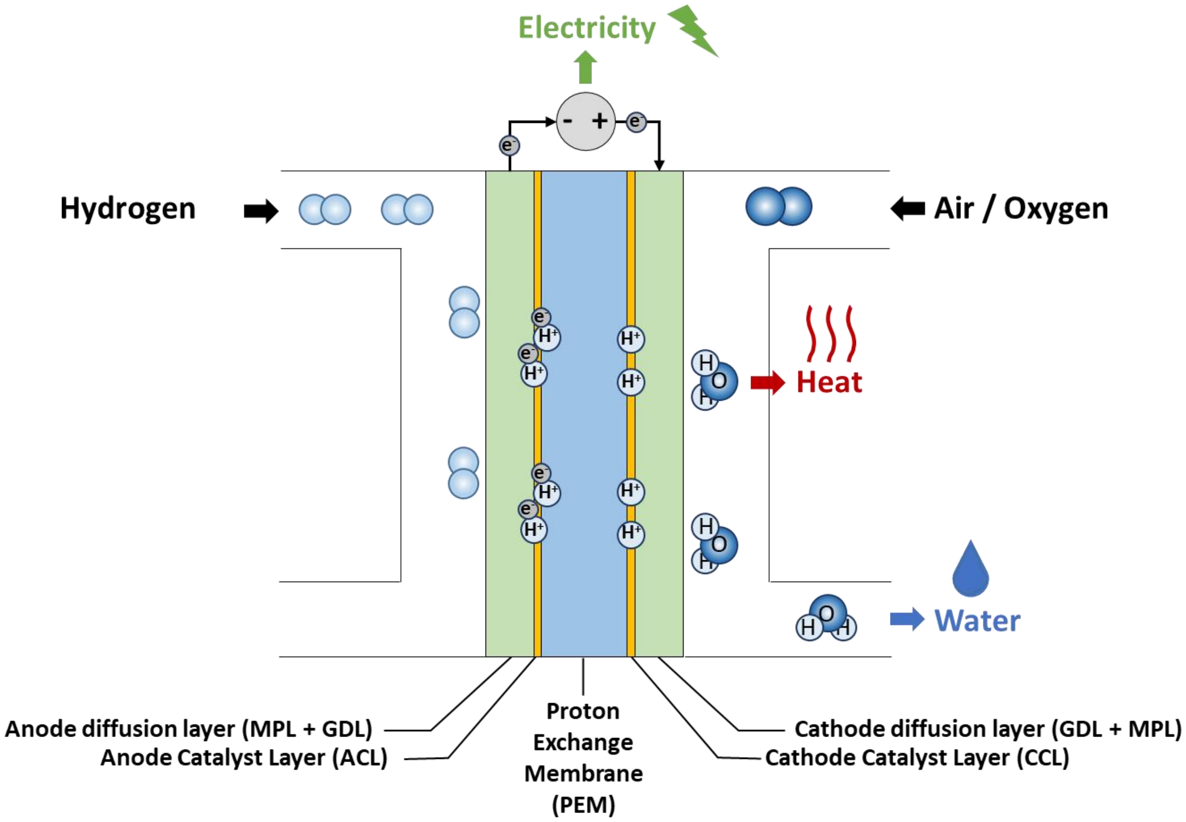

Figure I-1 : Electrochemical description of PEMFC operation

---

[1] *In electrochemistry, the physical quantity allowing to evaluate the chemical reactivity of chemical species between them is the electrochemical potential. However, since the absolute value for potential does not exist, a reference must be used. The Reference Hydrogen Electrode (RHE), taking the redox couple H^+/H_2 as reference, is the most commonly used.*

I.2.1.2. Reversible potential

An electrochemical system is said to be in Open Circuit Voltage (OCV) when it is electrically isolated with no current flowing through it. The so-called reversible potentials $E_{eq\ \mathrm{ox/red}}$ can be expressed according to the Nernst equation (I-4) at equilibrium for each electrode:

$$E_{eq\ \mathrm{ox/red}} = E^0_{\mathrm{ox/red}} + \frac{RT}{nF} ln \frac{a_{ox}}{a_{red}} \tag{I-4}$$

With

- E_{eq}, the reversible potential in given conditions;
- E^0, the reversible potential in standard conditions (298.15 K, 1 $\mathrm{bar_{abs}}$, $a_{ox/red} = 1$);
- R, the ideal gas constant (8.314 $\mathrm{J.K^{-1}.mol^{-1}}$);
- n, the number of electrons transferred in the half-reaction;
- F, the Faraday constant (96 485 $\mathrm{C.mol^{-1}}$);
- a, the chemical activity for the relevant species.

The reversible potential in standard conditions of the redox couple H^+/H_2 at the anode is 0 V *vs.* RHE while the reversible potential in standard conditions of the redox couple O_2/H_2O at the cathode is 1.18 and 1.23 V *vs.* RHE (in case of vapor and liquid formation, respectively). We deduce a theoretical/reversible maximum voltage of the cell U^0_{rev} in standard conditions with liquid water generation from its following formulation:

$$U^0_{rev} = E_{O_2/H_2O} - E_{H^+/H_2} = 1.23\ V \tag{I-5}$$

I.2.1.3. Open- circuit voltage

In practice, the equilibrium state and thus the corresponding reversible voltage is not reached in PEMFC. Indeed, other reactions take place mainly within the cathodic electrode at open circuit: the oxidation of hydrogen (HOR) after its permeation through the membrane and the partial oxidation of the platinum nanoparticles. Therefore, a mixed potential is also present at the anode (negligible) electrode and at the cathode (non-negligible) electrode. The drop of the voltage is called mixed overvoltage (η_{mixed}) and defines the Open Circuit Voltage U_{OCV} as:

$$U_{OCV} = U_{rev} - \eta_{mixed} = E_{O_2/H_2O} - E_{H^+/H_2} - \eta_{mixed} \tag{I-6}$$

Commonly, the cell voltage measured at the OCV is about 0.95 – 1.0 V under H_2/Air conditions.

I.2.1.4. Cell voltage under load

When a current is delivered, the electrochemical cell is out of equilibrium and has a voltage lower than the OCV. The potentials at the anodic and cathodic electrodes deviate from their open circuit values due to irreversible phenomena that induce a cell voltage drop. This voltage loss can be broken down into three contributions (charge transfer, ohmic drop and mass-transport) which are explained hereafter.

I.2.1.4.1.Activation overpotential $\boldsymbol{\eta_{act}}$

The main contribution at low current densities is the activation overpotential which is related to the energy necessary to initiate the two redox half-reactions within the active layers at the anode and cathode electrodes. We note thus the Equation (I-7):

$$\eta_{act} = \eta_{mixed} + \eta_{act}^{anode} + \left|\eta_{act}^{cathode}\right| \tag{I-7}$$

The η_{mixed} term is similar to that mentioned earlier in section I.2.1.3. Both the anodic η_{act}^{anode} (positive) and cathodic $\eta_{act}^{cathode}$ (negative) activation overpotentials are governed by the electrochemical kinetics. Figure I-2 is a qualitative representation of the intensity-potential curves for the redox couples H^+/H_2 and O_2/H_2O using platinum-based catalyst. Ohmic and mass-transport limitations are not considered here (explained in following sections). The curves show that the H^+/H_2 reaction kinetics are "fast" whereas the O_2/H_2O reaction kinetics are "slow". It is admitted that the anodic activation can usually be neglected compared to the cathodic activation: $\left|\eta_{act}^{cathode}\right| \gg \eta_{act}^{anode}$. In other words, ORR kinetics is the limiting reaction and responsible for the voltage loss at low current density. To accelerate ORR kinetics, the Pt catalyst loading is generally much higher at the cathode than at the anode.

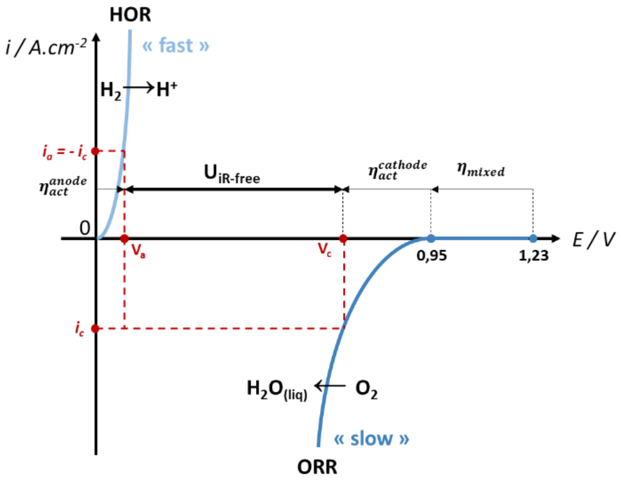

Figure I-2 : Schematic current-potential curves at both anode (H^+/H_2 couple) and cathode ($O_2/H_2O_{(liq)}$ couple) in PEMFC operation without considering ohmic and mass-transport limitations

I.2.1.4.1.Ohmic overpotential $\boldsymbol{\eta_{ohm}}$

A second irreversible phenomenon contributes to the decrease of the cell voltage over the whole current density range. This overpotential is related the ohmic resistance R_{ohm} caused by the ionic transport (ionic resistance R_{ion}) through the membrane and the ionomer phase in the electrodes and secondly by the electronic transport (electronic resistance R_{elec}) through the bipolar plates, the GDL and the electrodes. It can be expressed according to the equation (I-8):

$$\eta_{ohm} = i * S * R_{ohm} = i * S * (R_{ion} + R_{elec}) \tag{I-8}$$

I.2.1.4.2.Mass-transport overpotential $\boldsymbol{\eta_{mass}}$

Finally, at high current density, the mass-transport overpotential, also called concentration overpotential becomes more and more predominant and is linked to the mobility of the species mobility that is to say, the supply of reactant gas (H_2 and O_2) and the exhaust of water. This irreversible phenomenon is mainly observed at the cathode especially if Air is used and where water is produced. Concentration gradient of reactant gas is formed through the thickness of electrodes. A large cell voltage drop is observed when the load tends towards the mass-transport limited current density i_{lim} due to insufficient gas supply near the active sites, as shown in Figure I-3.

I.2.1.5. Polarization curve

It is possible to express the operating cell voltage $U(i)$ (I-9) considering all the overpotential terms according to the current density:

$$U(i) = U_{rev} - \eta_{act}(i) - \eta_{mass}(i) - \eta_{ohm}(i) \tag{I-9}$$

With:

- U_{rev}, Reversible cell voltage;
- $\eta_{act}(i)$, activation overpotential according to the current density;
- $\eta_{mass}(i)$, mass overpotential according to the current density;
- $\eta_{ohm}(i)$, ohmic overpotential according to the current density;
- i, current density delivered by the cell.

The voltage response of the cell U as a function of the current is called the polarization curve and its typical shape is illustrated in the Figure I-3. The contribution of the different overpotentials according to the current is also qualitatively represented.

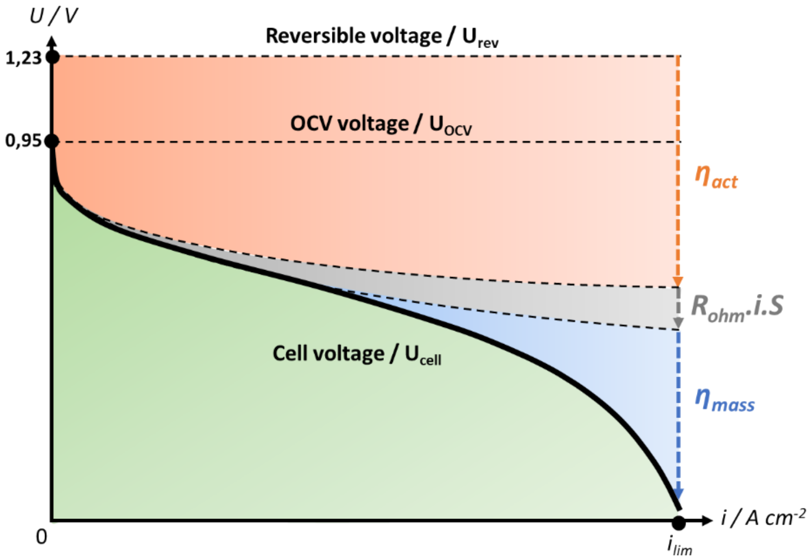

Figure I-3 : Typical polarization curve of a PEM electrochemical cell in FC operation with qualitative representation of each type overpotential

I.2.1.6. Electric efficiency of the PEM fuel cell

We can then express the electric efficiency of the cell by comparing the electrical power supplied to the load with the theoretical chemical power according to the low heating value of hydrogen. The fuel cell efficiency, ρ, is expressed as follows:

$$\rho = \frac{U * i * S}{F_{H_2} * \Delta H_{LHV}} \qquad \text{(I-10)}$$

With

- U (V), cell voltage in given operating conditions from Eq. (I-9);
- i (A.cm^{-2}), current density;
- F_{H_2} (mole.s^{-1}), the hydrogen molar flow rate;
- ΔH_{LHV} (J.mole^{-1}), the low heating value of hydrogen (-241 kJ.mol^{-1});
- S (cm^2), active surface area.

In practice, stack efficiency is about 40 to 60% compared to the LHV enthalpy value. In order to optimize the FC performance and efficiency, the impact of overpotentials on the cell voltage must be therefore minimized. The key-points reside on the formulation of components in the core of the cell and the system management. The desired composition and physical properties of the cell components are described hereafter, followed by the system architecture necessary for the proper functioning of the stack.

I.2.2. Fuel Cell components

The Membrane-Electrode Assembly (MEA) is the core of the cell where the electrochemical reactions take place. As illustrated in the Figure I-4a, it consists of a Proton Exchange Membrane (PEM) as solid electrolyte and porous electrodes on both sides (anode and cathode). These electrodes are themselves composed of a catalytic layer (CL) and both diffusion layers: Micro-Porous Layer (MPL) and Gas Diffusion Layer (GDL). We talk about Catalyst-Coated Membrane (CCM) a triple layer composed by the membrane with both anodic and cathodic catalyst layers. MEA is then inserted between two bipolar plates as illustrated in Figure I-4b to obtain an elementary cell. Detailed description of materials and functions of each component is given in this section.

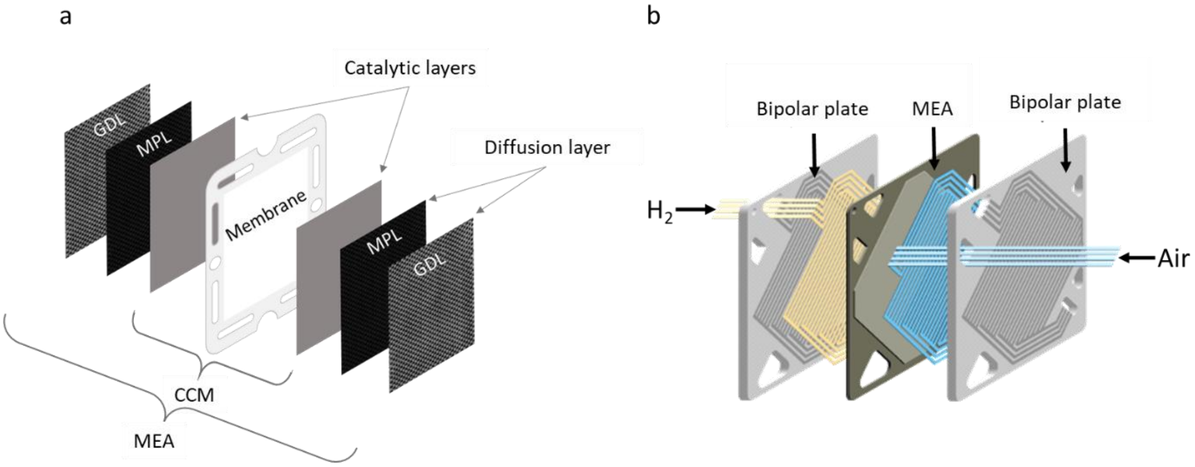

Figure I-4: Presentation of (a) 7-layer MEA and (b) cell components [5]

I.2.2.1. Membrane

The particularity of the PEM technology relies mainly in the nature of its solid electrolyte that consists in a PerFluoro-Sulfonic Acid-based membrane (PFSA). The most known PEM product is the Nafion® membrane developed by DuPont de Nemours. Under the operating conditions of the FC, this membrane ensures the migration of protons released at the anode and recombined with oxygen at the cathode. Its ionic conductivity must be as high as possible to limit the ohmic loss. Its electronic insulation (but ionic conductivity) thus forces the transport of electrons through an external circuit and the generation of electrical energy. High impermeability to gases (H_2, N_2 and O_2) is also necessary to limit the permeation of hydrogen to the cathode and oxygen to the anode resulting in direct combustion of reactants to produce water without the passage of electrons into the external circuit, thus without electricity generation. In practice, the permeation of hydrogen is twice as high as the one of oxygen. The sulfonated groups allow the transport of protons, and the effective ionic conductivity strongly depends on the temperature and water content. A good hydration is therefore necessary to obtain good ionic conductivity. It is also advised to remain below an operating temperature of 85 °C to limit the drying and degradation of the membrane. Similarly, hydrated gases (about 50% RH at cell inlet) should be supplied to hydrate correctly the MEA and to optimize performance. Then, the membrane must have good mechanical properties to reduce its thickness, thus reducing the resistance associated with proton transport. Good mechanical properties also limit the risk of membrane pinholes. Depending on the manufacturer, the thickness of the membrane is usually between 10 – 20 µm using a PTFE mesh reinforcement.

I.2.2.2. Catalyst layer

Localized on both sides of the membrane, catalyst layers are the zones where electrochemical reactions take place at the active sites. Materials and properties of CLs must be optimized to promote:

- Electroactive catalyst to accelerate reaction kinetics (named thereafter active sites);
- Carbon porous support to transport both electrons and reactant gas to active sites;
- Ionomer phase to ensure proton conductivity to the active sites.

The amount of catalyst active sites must be maximized to optimize catalytic utilization and cell performance. The loss of one function implies inactive or inaccessible active platinum sites, reducing cell performance and durability. Figure I-5 illustrates the Cathode Catalyst Layer (CCL) structure and the ORR mechanism.

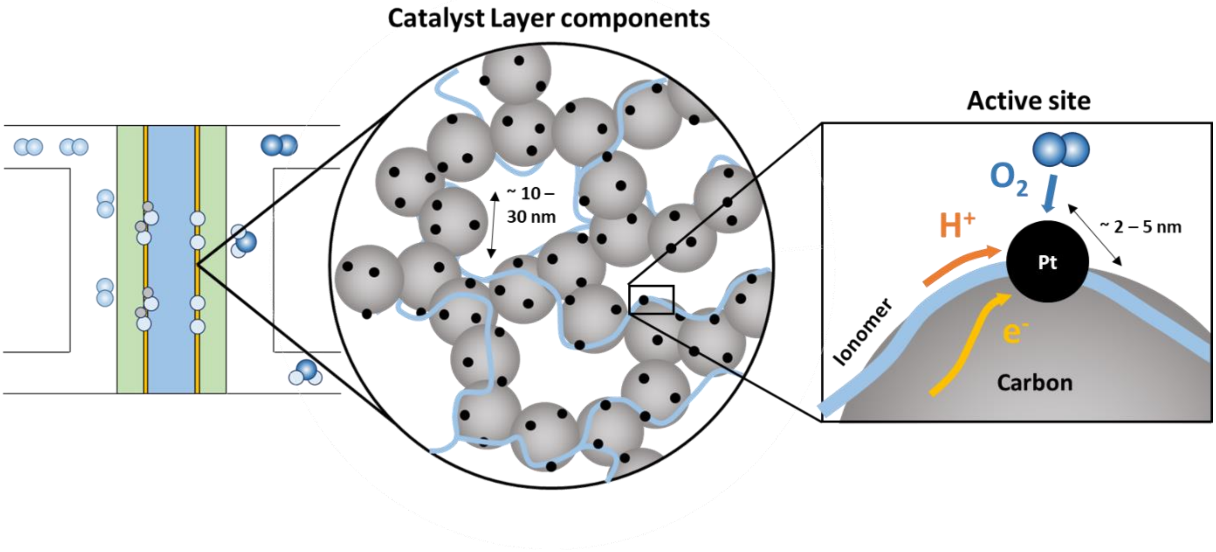

Figure I-5: Schemes of cathode catalyst layer structure and local operation in PEM fuel cell

I.2.2.2.1.Carbon support

Reactant gas and electron accessibility up to active sites are ensured by a porous support generally a carbon compound. It is also the mechanical support of the Pt nanoparticles and the ionomer phase. It must be also resistant to corrosion in acidic environment and under PEMFC operating conditions. The most common materials marketed for PEMFC application are carbon blacks (such as Vulcan XC-72 from Cabot). It consists in general of spherical carbon particles of 10 - 30 nm in diameter grouped in aggregates and agglomerates of about 250 nm in diameter.

I.2.2.2.2.Catalyst

Catalyst is used to accelerate kinetics of electrochemical reactions. In PEM application, Platinum is the most common material due to its high electro-catalytic activity for both HOR and ORR, its selectivity and its stability [6]. It is deposited onto carbon support in the form of nanoparticles (diameter about 2 – 5 nm) to maximize the electrochemical active surface area and to reduce the amount of Pt. Its loading is higher at the cathode than at the anode because of the sluggish ORR kinetics. Conventional Pt loading is about 0.1 – 0.4 mg/cm² at the anode and cathode respectively. Huge efforts are made to diminish the amount of Pt used since Pt represents about 50% of the cost of the stack (at mass production scale). That is why, developments on alternative solutions such as Pt-based alloys (with Cr, Co, Ru or Cu metals) are in progress to improve mass activity but required further investigation on their durability [7]. Non-Pt-based catalysts such as cobalt-based (or nitrogen-based) modified-carbon catalysts and others metal oxides could be a solution to replace Pt-based catalyst, but these materials are not mature enough for their integration into stacks.

I.2.2.2.3.Ionomer phase

Some ionomer phase (possibly the same type as in the membrane) is also included in CL to ensure proton transport from the PEM|CL interface to Pt active sites. Similarly, to bulk membrane, proton conductivity within the CL depends strongly on the water content.

I.2.2.3. Diffusion Layers

Diffusion layers play an important role in the gas supply and water evacuation between the catalyst layers and the channels of the bipolar plate. Generally, they are composed of a Micro-Porous Layer (MPL) with carbon powder and both hydrophilic/hydrophobic agents, plus, a Gas Diffusion Layer (GDL) composed of carbon paper or carbon cloth and hydrophobic agents [8], [9]. GDL in contact with bipolar plates favors reactant gas distribution from gas channel and the drainage of water. MPL in contact with CLs ensures water removal from CL to the GDL and refines gas diffusion thanks to its micro-porous structure. Their high electronic conductivity also ensures the electron transport between the CLs and BPs.

I.2.2.4. Bipolar plates

MEA and diffusion layer are finally inserted between two bipolar plates to obtain an elementary cell. The plate design shall allow on the whole surface of electrodes:

- The passage of fluids (reactant gas), including the cooling fluid;
- The tightness between the three fluidic circuits;
- The collection of electrons;
- The removal of heat produced.

These plates can be made of coated-stainless steel or carbon-based composite, making it more electronically conductive. Flow-field channels used for gas distribution and water evacuation are designed on these plates and are more commonly based on serpentine or linear shapes. The design of the gas supply channels is a compromise between the optimization of reactant distribution which shall be as homogenous as possible within each cell and within the whole stack, the evacuation of water, the electronic contact between rib and GDL and the pressure drop.

I.2.2.5. Stack assembly

The individual cell voltage in FC operation is about 0.6 to 0.9 V. It is therefore necessary to connect electrically in series and fluidly in parallel several cells in order to attain the desired electric power to form a stack configuration in which the output voltage is the addition of individual cell voltages (Figure I-6). The stack assembly consists in applying a clamping effort to minimize the internal electrical resistance of the fuel cell without altering the integrity of the components, while ensuring the tightness of the various Air, H_2 and coolant circuits by crushing a gasket integrated into the bipolar plate. Conventional effort is about 1.2 MPa (12 kN for a 100 cm² cell).

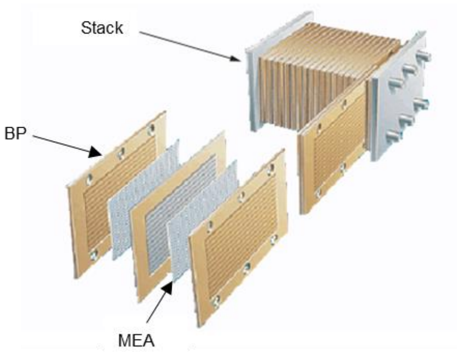

Figure I-6: PEMFC stack assembly [5]

I.2.3. PEMFC system

Stack performance depends on the operating conditions such as the current density, the stack temperature, pressure, humidity and flow rates of the reactant gases. PEMFC system and its auxiliary shall ensure nominal working conditions via proper control and management of operating parameters including the transient phases such as start-up/shut-down or idle/peak power periods. It includes 3 fluidic circuits (H_2, Air and coolant) and an electrical circuit. This section focuses on common and conventional PEMFC architecture for transportation applications. Battery, H_2 storage and power electronics are not treated hereafter.

I.2.3.1. Air circuit

Air circuit function is to manage the Air flow rate at the stack inlet and its pressure and humidity. Pressured Air is generally supplied thanks to a compressor. Most of the architectures are therefore distinguished by the method of gas humidification. The most common is the passive humidification thanks to a membrane separator which collects water vapor at the cathode outlet and transfers it back to the cathode inlet (see Figure I-7). This passive humidifier implies that the inlet relative humidity is driven by cathode outlet conditions, and it makes it difficult to control actively this parameter without changing the operating conditions of the fuel cell. Even if, this type of humidification is not necessarily optimal for application with frequent dynamic operations, it is usually used for sake of its simplicity of integration.

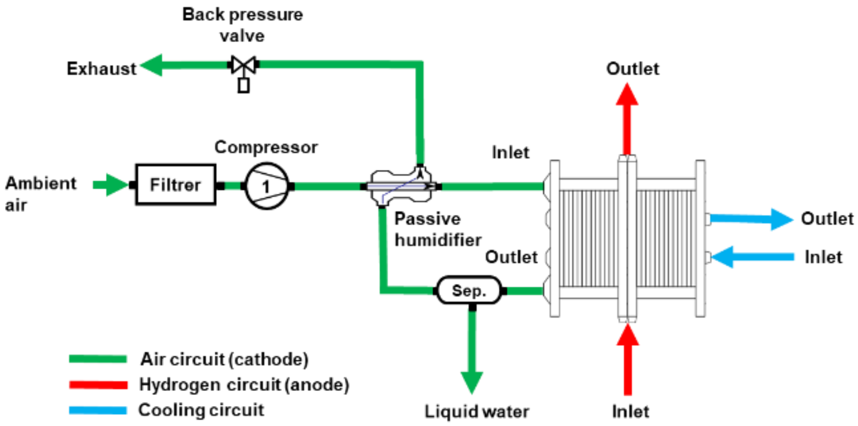

Figure I-7: PEMFC system architecture with passive humidification architecture of Air circuit [10]

I.2.3.2. H_2 circuit

Hydrogen circuit function is to manage the flow rate and gas pressure supplied at the anode inlet. Generally, humidification is rarely controlled. Hydrogen gas is mainly provided from a pressurized tank (about 350 – 700 bar_{abs}) and is then depressurized until nominal pressure (about 1 – 2 bar_{abs}) before the fuel cell inlet.

As noted in equation (I-10), fuel utilization must be optimized as much as possible by minimizing purges. Gas management is usually ensured thanks to valves on both anode inlet and outlet. The simplest strategy is the Dead-End Anode (DEA) and consists in maintaining the anode outlet closed to reduce hydrogen loss (cf. Figure I-8). Intermittent opening evacuates undesired species such as N_2 and water accumulated at the anode to avoid local gas starvation and degradations. However, DEA requires significant and frequent purge frequencies to operate the stack properly and reliably. Moreover, non-humidified fuel supply may dry the anode inlet. Heterogeneous conditions along anode side impact therefore cell performance. Nowadays, most of the systems are equipped with passive (via ejector) or active (with a pump) recirculation loop to minimize H_2 losses and promote a homogeneous and sufficient circulation of H_2 in the stack.

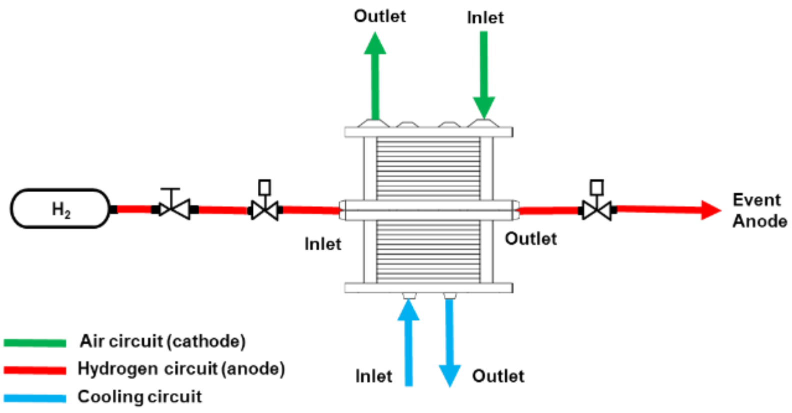

Figure I-8: DEA architecture in H_2 circuit [10]

I.2.3.3. Cooling circuit

Heat power generated in the stack is approximatively equal to the electric power in nominal operating conditions. High temperature elevation in cells must be limited to avoid degradation of cell components. A coolant fluid flows inside the bipolar plates and evacuates heat to ambient Air by the means of a heat exchanger and a circulator. This fluid must be non-conductor to avoid internal corrosion and short circuit between cells. It shall operate from cold start-events (< 0 °C) to high temperature (95 °C). Glycolated water is commonly used as coolant in PEMFC applications. Typical range for operating temperature of fuel cell is about 60 – 95 °C and requires a significant heat exchanger size due to the low differential temperature with Air ambient.

I.3. DURABILITY CHALLENGE FOR PEMFC AND AGEING MECHANISMS

I.3.1. Fuel Cell Road Map

In order to promote PEMFC technology, public institutions have published roadmaps over the past decades [11]–[14]. Guidelines for evaluating cell/system components and defining key-challenges for automotive applications have targeted 8,000-hours durability and low-cost mass production (35 $/kW_e$). The lifetime target for heavy-duty system is even higher up to 30,000 hours.

I.3.1.1. Cost

Cost reduction in PEMFC system is required to be competitive with Internal Combustion Engines (ICE), from 45 (status) to 35 $/kW_e$ (2025). As illustrated in Figure I-9, attention must be paid to both stack and system scales (representing 45% and 55% of total cost, respectively). The principal contributions of stack cost in decreasing order are the catalyst (41%), the bipolar plate (28%), the balance of stack (10%) and the membrane (8%). The improvement of stack components makes it possible to improve power density and to reduce either the active surface area or the number of cells, thus the size/cost of cell components. Another way to reduce stack cost is to improve the mass activity by developing Pt-M alloy and Pt-free catalyst [15]. At system scale, the simplification and/or downsizing of auxiliary units can also contribute to reduce the final cost. However, system optimization strongly depends on the stack operating conditions. One way is to eliminate the humidifier, but it would also imply to be able to operate efficiently under dry gas. Increasing stack operating temperature would permit to reduce heat exchanger capacity in the coolant circuit but would also favor higher degradation rates of stack/system components. Finally, the optimization about Air management is also challenging because optimized compressor technologies for FCEV are commercially scarce.

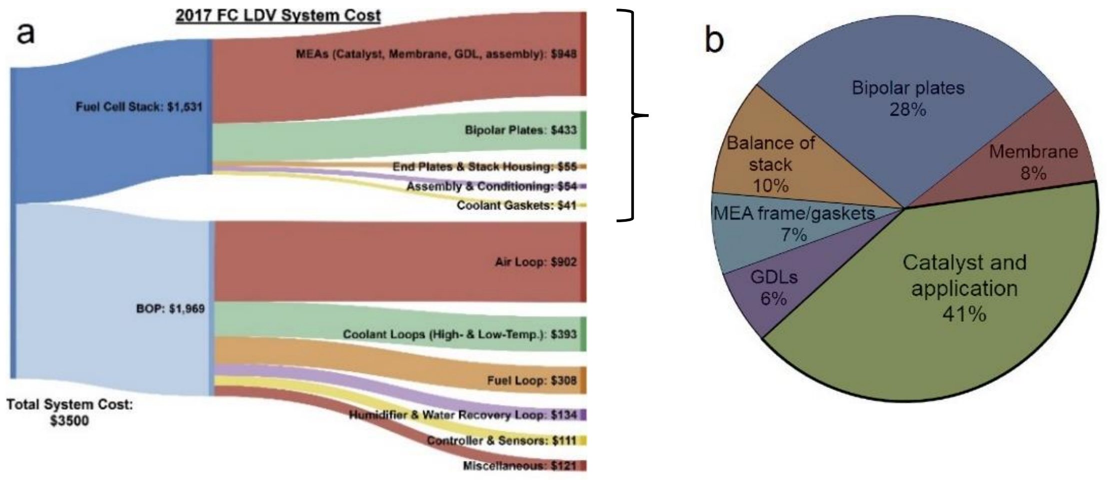

Figure I-9: Component cost breakdown in 2017: a) for the 2017 system and b) for the stack (for a production volume of 500,000 units/year) [16]

I.3.1.2. Durability

The stack durability for automotive application is targeted to 8,000 h by 2025 corresponding to 150,000 miles, similarly to conventional thermal vehicles, with a total performance decay less than 10% under nominal operation as preconized by Department of Energy (DoE) teams [17]. To improve PEMFC stack lifetime, it is essential to identify the ageing mechanisms of materials. In fact, automotive applications are challenging due to severe and transient conditions such as dynamic load (contributing to 56% of the performance degradation), high power (5.8%), idling/OCV (4.7%) and start-up/shut-down (33%) as predicted by Pei *et al.* [18], [19] from arithmetic equations based on buses equipped with PEMFC and laboratory test data (see Figure I-10). For sake of clarity, the impacts of impurities in the reactant gases and cold-start events (below 0 °C) are not treated in this manuscript. Vehicular operations lead to MEA ageing and the physico-chemical and electro-chemical modifications of components cause loss of performance and durability. The next section presents the interactions between the operating conditions and their impacts on MEA ageing.

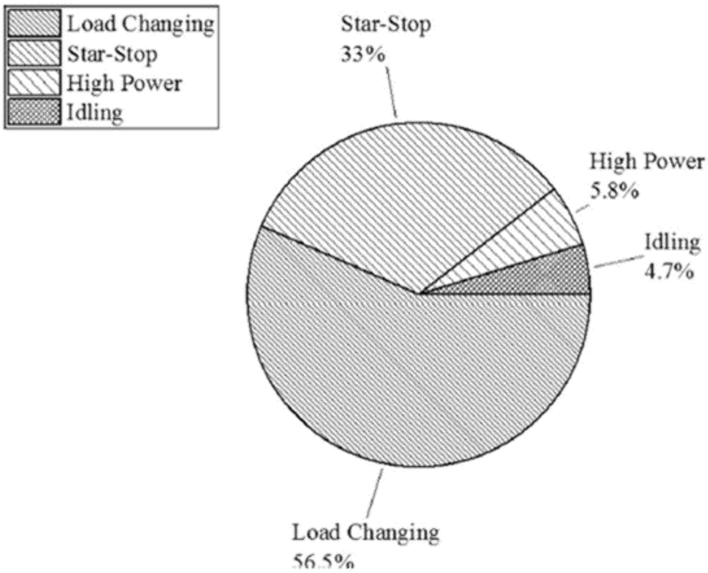

Figure I-10: Contribution of vehicle operations on the loss of durability of PEMFC [18]

I.3.2. Degradation mechanisms according to operating modes

Particular attention has been paid to the degradation mechanisms within the Cathode Catalyst Layer (CCL), which have major impacts on performances due to the sluggish ORR kinetics. In this work, it is proposed to review degradation mechanisms in several operating modes according to the cathodic potential during the use of PEMFC: (i) nominal FC operation (0.6 – 0.85 V_{RHE}); (ii) Idling/OCV (0.85 – 1.0 V_{RHE}); (iii) Unprotected Star-Up/Shut-Down phases (> 1.0 V_{RHE}).

Let us mention that specific stack failure modes such as gas starvation and flooding are not treated thereafter.

I.3.2.1. Nominal fuel Cell operation ($E_{cathode}$ ~0.6 - 0.85 V_{RHE})

In nominal mode, typical operating conditions such as dynamic load and high-power phases impose a cell voltage response, and thus a cathodic potential variation in the 0.6 – 0.85 V_{RHE} range (corresponding to ~1.5– 0.2 A/cm² range, respectively for the PEMFC technology used in this work). CCL suffers from these dynamic and oxidative conditions which lead to Pt catalyst and carbon support degradations [19].

I.3.2.1.1.Pt oxidation

Platinum nanoparticles are in fact unstable in the acidic PEMFC environment at 0.6 – 0.85 V range [20]. Electrochemical reactions occur onto Pt active sites, which are subjected to surface oxidation, noted hereafter -OH_{ad} /-O_{ad} which are also intermediate reactive species in the ORR mechanism. -OH_{ad} species are formed via reaction (I-11) from ~0.6 V_{RHE} and -O_{ad} species via reaction (I-12) from ~0.8 V_{RHE} on Pt active sites.

$$Pt + H_2O \leftrightarrow Pt - OH_{ad} + H^+ + e^- \qquad \text{(I-11)}$$

$$Pt - OH_{ad} \leftrightarrow Pt - O_{ad} + H^+ + e^- \qquad \text{(I-12)}$$

Under operation, some oxide species may passivate the active sites and therefore induce a reversible loss of performance. Performance recovery can be achieved by lowering cathode potential until the de-passivation/reduction of surface oxides [21], [22]. Jahnke *et al.* [22] investigated the Pt oxide formation/reduction by cyclic voltammetry technique depending on different potential excursions and time holdings, as illustrated in Figure I-11. The higher and/or longer the cathode potential is imposed, the higher passivation. For instance, a potential holding at 0.7 and 0.8 V_{RHE} during 6 s induces a mixed-oxide (-OH_{ad} and –O_{ad}) coverage at about 0.05 and 0.3, respectively. Furthermore, a potential holding at 0.8 V_{RHE} during 1 s and 60 s passivates the Pt with a coverage estimated about 0.23 and 0.35. To go further, a first peak during the negative potential sweep (about 0.72 V_{RHE}) suggests a reduction of $Pt - O_{ad}$ species while a second peak (about 0.6 V) may be linked to the reduction of $Pt - OH_{ad}$ species, as described by reactions (I-12) and (I-11), respectively. Further investigations would be necessary on regeneration strategies to optimize cell performance during nominal FC operation [23].

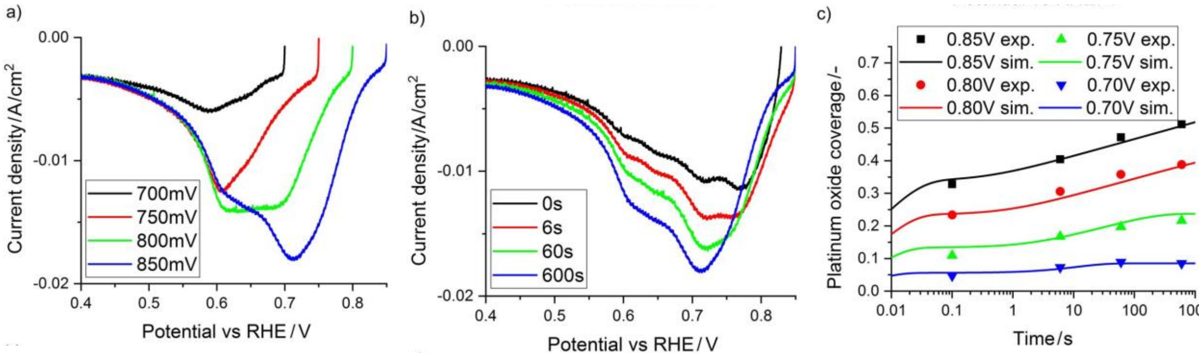

Figure I-11 : Reduction peaks of the Pt-O$_x$ during the negative potential sweep after (a) a holding time of 600 s with different potential values and (b) a holding at 0.85 V for different durations. (c) Induced oxide coverage onto Pt according to both durations and upper potential values [22].

I.3.2.1.2. Carbon Support Corrosion

Carbon support is also thermodynamically unstable at the cathode nominal potential range. Common way to investigate the Carbon Support Corrosion (CSC) pathways is to analyze the CO_2 gas emitted at the cathode outlet, according to the potential excursion [24]–[28]. The Figure I-12 illustrates the typical CO_2 profile along cyclic voltammetry from 0.1 and 1.2 V_{RHE} under inert and Air atmosphere at the cathode in PEMFC. No significant difference between both atmospheres suggests that the oxygen participation in the CSC reactions is low. In both cases, several CO_2 peaks are detected and identified according to the potential regions as detailed thereafter:

- Peak I (<0.4 V_{RHE}): hydrogen peroxide is formed under Air atmosphere by the incomplete ORR mechanism (the “2-electron pathway”) and attacks carbon support through the chemical pathway (I-13), emitting CO_2 gas. This mechanism is not treated thereafter (outside the potential range of interest for nominal PEMFC operation);

- Peak II (0.4 – 0.6 V_{RHE}): carbon surface is oxidized to form an intermediate oxidized species (noted as CO_{surf}) via reaction (I-14) in presence of H_2O which can subsequently be adsorbed onto free Pt nanoparticles resulting into carbonyl species (-CO_{ad}) via reaction (I-15). These species may be further oxidized into CO_2 according to reactions (I-16) and (I-17). This mechanism is defined as catalyzed CSC by Pt active sites;

- Peak III (0.6 – 1.0 V_{RHE} during the negative sweep): the presence of adsorbed hydroxyl species (- OH_{ad}) onto Pt participates also to the oxidation of both oxides species (CO_{surf}) and carbonyl species (-CO_{ad}) via reactions (I-16) and (I-17), respectively [29]. These reactions are also part of catalyzed CSC;

- Peak IV & V (1.0 – 1.2 V_{RHE}), the CO_2 emission follows the direct (non-catalyzed) CSC reaction (I-18) in presence of H_2O without the participation of Pt active sites. Indeed, at such high overpotential (> $E° = 0.207\ V_{RHE}$), CO_2 production from becomes quantitative above 1.0 V.

$$C + 2H_2O_2 \rightarrow CO_2 + 2H_2O \tag{I-13}$$

$$C + H_2O \rightarrow CO_{surf} + 2H^+ + 2e^- \tag{I-14}$$

$$Pt + CO_{surf} \rightarrow Pt - CO_{ad} \tag{I-15}$$

$$Pt - OH_{ad} + CO_{surf} \rightarrow Pt + CO_2 + H^+ + e^- \tag{I-16}$$

$$Pt - OH_{ad} + Pt - CO_{ad} \rightarrow 2Pt + CO_2 + H^+ + e^- \tag{I-17}$$

$$C + 2H_2O \leftrightarrow CO_2 + 4H^+ + 4e^- \qquad E° = 0.207\ V_{RHE}\ [25] \tag{I-18}$$

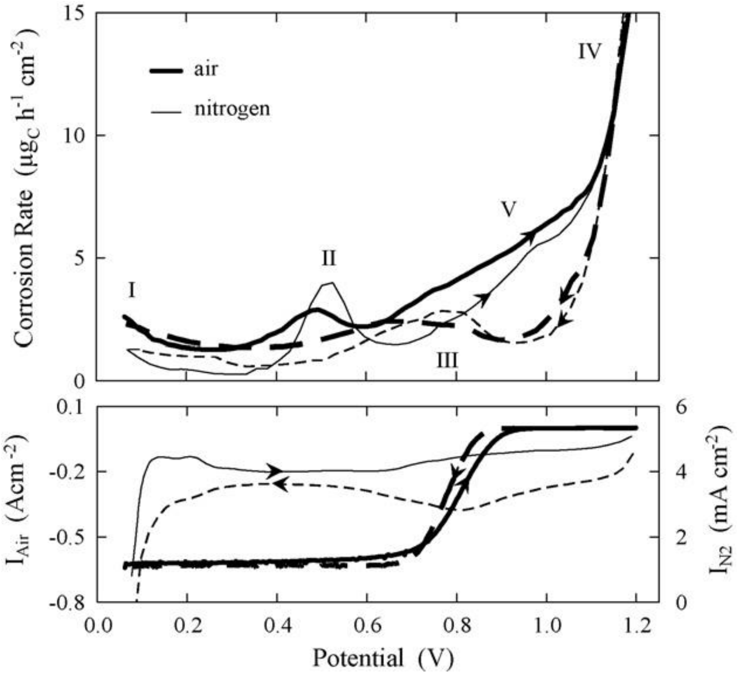

Figure I-12: Simultaneous CO_2 gas emission (upper figure) and corresponding cyclic voltammetry measurements (lower figure) on Pt/C electrode in Air (solid line) and nitrogen (dotted line) atmosphere in 45-cm² single cell [25]

To quantify and to compare these CSC pathways, Linse *et al.* [27] estimated global CO_2 emission rates during CV technique with different lower and upper potential limits. They demonstrated that the CSC during the potential sweeping between 0.6 and 1.0 V is less severe than in 1.0 – 1.4 V range, with a CO_2 emission estimated at about 1.5 and 30 μg_{CO2}/cycle respectively. That confirms the direct CSC, corresponding to the peak IV (> 1.0 V_{RHE}), is the most damaging reaction. Thus, we can suppose the CSC kinetic is slow during nominal FC operation (0.6 – 0.85 V_{RHE} range).

From recent studies, CSC kinetics strongly depends on the structure of carbon and occurs below 1.0 V_{RHE}. Castanheira *et al* [30] demonstrated by Raman spectroscopy that the amorphous/disordered domains of High Surface Area Carbon (HSAC) domains are degraded preferentially in the 0.4 – 1.0 V_{RHE} range while the graphitic/ordered domains are mainly affected above 1.0 V_{RHE} by direct CSC from Eq. (I-18) (see Figure I-13), typically in SU/SD events as discussed in section I.3.2.3.

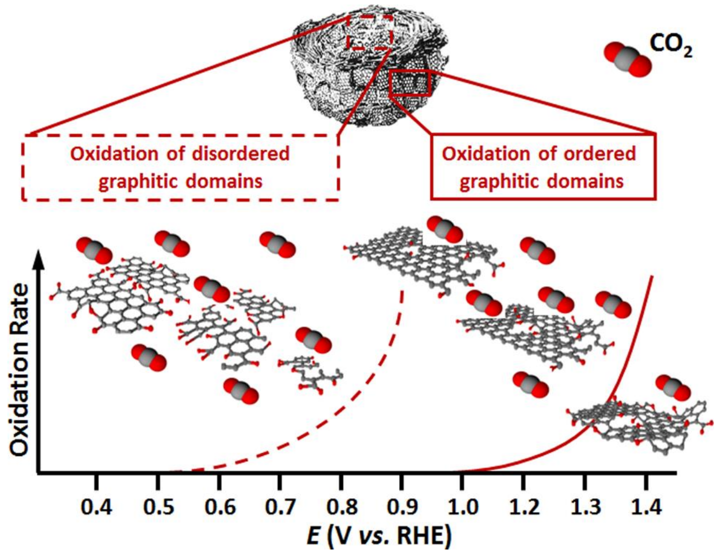

Figure I-13: Schematic description of CSC mechanism of disordered and ordered graphitic domains of HSAC support according to the potential [30]

I.3.2.2. OCV/ Idling ($E_{cathode}$ ~0.85 – 1.0 V_{RHE})

Open Circuit and idling modes occur when PEMFC stack operates at low current density (< 0.2 $A.cm^{-2}$). These modes cause irreversible performance decay about 0.3 $mV.h^{-1}$ [31]–[33]. To compare with FC operation, load cycling from 0.0 to 0.2 Acm^{-2} (corresponding to ~1.0 – 0.85 V_{RHE} as cathode potential) exhibits more irreversible degradation compared to the load cycling between 0.2 and 1.0 $A.cm^{-2}$ (corresponding to ~ 0.85 – 0.65 V_{RHE}), estimated at about 300 and 100 $mV.h^{-1}$ (@1.0 $A.cm^{-2}$) respectively [31]. Under these operating conditions, high cathode potential and high oxygen concentration damage both severely the CCL components (Pt oxidation/dissolution + CSC) and the membrane (chemical attacks) as detailed thereafter.

I.3.2.2.1.Pt oxidation and CSC

At this potential range, Pt and carbon are similarly oxidized as in nominal FC operation mentioned in section I.3.2.1. Pt surface is supposed fully covered by hydroxyl species ($-OH_{ad}$) and/or oxide species ($-O_{ad}$). The carbon support corrosion of amorphous and disordered graphitic domains is also identified as predominant in 0.85 – 1.0 V range, in accordance with Castanheira's suggestions [30]. In fact, Zhao *et al.* [34] have studied the ageing of inks composed of Pt/XC72 and Nafion® ionomer under Air atmosphere for 1.5 year and indicate a similar behavior for CSC based on Raman, X-ray spectroscopy and Fourier Transform infrared spectroscopy characterizations. Nevertheless, the ordered domains are also oxidized but at a minor rate yielding mostly to CO_{surf} formation from eq. (I-14). This may further lead to the catalyzed CSC pathways as described in the previous section (I.3.2.1.2). A thinning of the CCL (-25%) governed by the CSC has been observed by Scanning Electron Microscopy (SEM) after 140-hours load cycling between 0.0 and 0.2 Acm^{-2} (corresponding to ~1.0 – 0.85 V_{RHE} at the cathode side), whereas no significant thinning for the load cycling between 0.2 and 1.0 $A.cm^{-2}$ (corresponding to ~ 0.85 – 0.65 V_{RHE}) [31].

I.3.2.2.2. Pt dissolution / redeposition

The presence of metallic Pt particles in membrane is also observed after long-term operation at idling/OCV and depicts additional and irreversible degradations [31], [35], [36]. This degradation mechanism is governed by the Pt dissolution at the cathode, followed by the chemical reduction with H_2 in the ionomer phase.

Once oxidized, the Pt active sites are susceptible to be dissolved into cations (Pt^{2+}) via either chemical dissolution of Pt oxide species (I-19) or direct electrochemical dissolution of metallic Pt (I-20) [37]. For Pt nanoparticles, the reversible potential of the electrochemical Pt dissolution (I-20) is much lower than for bulk Platinum (1.118 V_{RHE}) and depends strongly on the particle sizes (larger sizes meaning higher reversible potential). Thus, this latter reaction evolves with the ageing and Pt nanoparticles growth: reversible potential increases from ~0.8 V_{RHE} (~3 nm) to ~1.0 V_{RHE} (> 6 nm) according to Plieth [38].

Then, dissolved Pt^{2+} cations are either redeposited onto larger Pt nanoparticles following the reaction (I-20), or precipitated into the membrane via reaction (I-21) resulting in the formation of a Pt band [36].

$$Pt - O_{ad} + 2H^{+} \leftrightarrow Pt^{2+} + H_2O \tag{I-19}$$

$$Pt \leftrightarrow Pt^{2+} + 2e^{-} \qquad E^0_{bulk} \approx 1.118\, V_{RHE} \tag{I-20}$$

$$Pt^{2+} + H_2 \rightarrow Pt + 2H^{+} \tag{I-21}$$

These Pt dissolution reactions strongly depend on potential excursion of the cathode and its exposure time. In steady state, concentrations of dissolved Pt is higher at OCV (~ 0.95 V_{RHE}) leading to a more important loss of Pt surface area than under FC operation (~ 0.75 V_{RHE}) [39]. Cherevko *et al.* [40] detected a Pt dissolution rate three times higher at 0.95 V_{RHE} than at 0.85 V_{RHE}. To go further, Myers *et al.* [41] have compared the impact of potentiostatic and potential cycling on Pt dissolution. Below

1.0 V_{RHE}, both modes lead to identical dissolution rates as illustrated in Figure I-14. However, for upper potential above this threshold potential, Pt dissolution rate under dynamic cycles is greatly accelerated while it remains low under constant high potential due to Pt passivation. The detailed mechanism during dynamic potential cycling with upper potential above 1.0 V_{RHE} is discussed in section I.3.2.3.

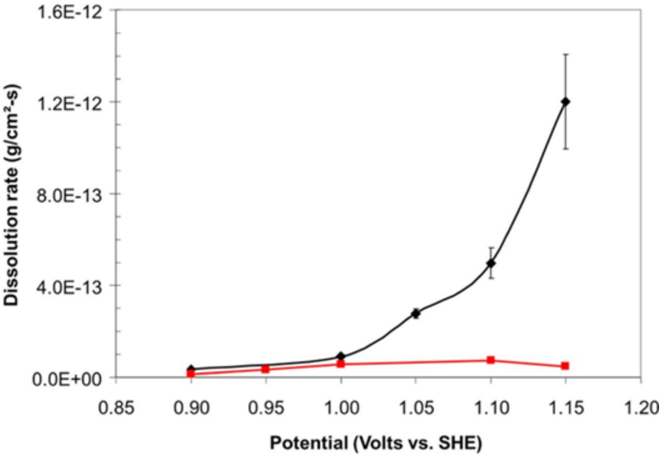

Figure I-14: Dissolution rate of Pt nanoparticles in steady state (red square) and dynamic cycle (black diamonds) between 0.4 and shown potentials (10 mV.s^{-1})[41]

I.3.2.2.3.Ionomer degradations

The literature shows that OCV is well-known for its impact on the membrane. Indeed, low oxidant consumption at the cathode and thus high oxidant concentration accentuate O_2 permeation through the membrane to the anode side. H_2 and O_2 coexistence participates in peroxide formation by incomplete 2-electron ORR reaction (I-22) due to the low anode potential and consequently yields to radicals (•OH / •OOH) [42]. These species can also be formed via Fenton's reactions in the membrane in presence of metallic cations (coming either from the metallic bipolar plate corrosion and/or from the corrosion of the co-element in PtCo/PtNi cathode catalysts for instance). Subsequently, radical species usually attack PFSA phase of membrane from the anode side and cause mechanical degradations (thinning, cracks, and pinholes). It can be supposed that similar degradation occurs with the ionomer phase of the anode catalyst layer. That affects protonic conductivity and gas permeation through the membrane by weakening the main and side chains of PFSA molecular structure yielding to Hydrofluoric acid (HF) formation, usually monitored to investigate and prospect membrane degradation [43]–[45].

$$O_2 + 2H^+ + 2e^- \leftrightarrow H_2O_2 \qquad E^0 = 0.695\, V_{RHE} \text{ [42]} \qquad \textit{(I-22)}$$

I.3.2.3. Unprotected Start-Up / Shut-Down ($E_{cathode}$ > 1.0 V_{RHE})

Unprotected Start-Up/Shut-Down (SU/SD) phases are well-known to constraint the cathode CCL at abnormal potential above 1.0 V_{RHE}. Such high potential can occur as H_2 flow flushes the Air initially present in the anode compartment during the start-up phase or inversely as Air flow replaces H_2 at the anode side during the shut-down phase as illustrated in Figure I-15. In fact, the formation and propagation of the H_2|Air front along anodic channel disturbs the distribution of electrode potentials in the cell which leads to the Reverse Current Decay mechanism [46].

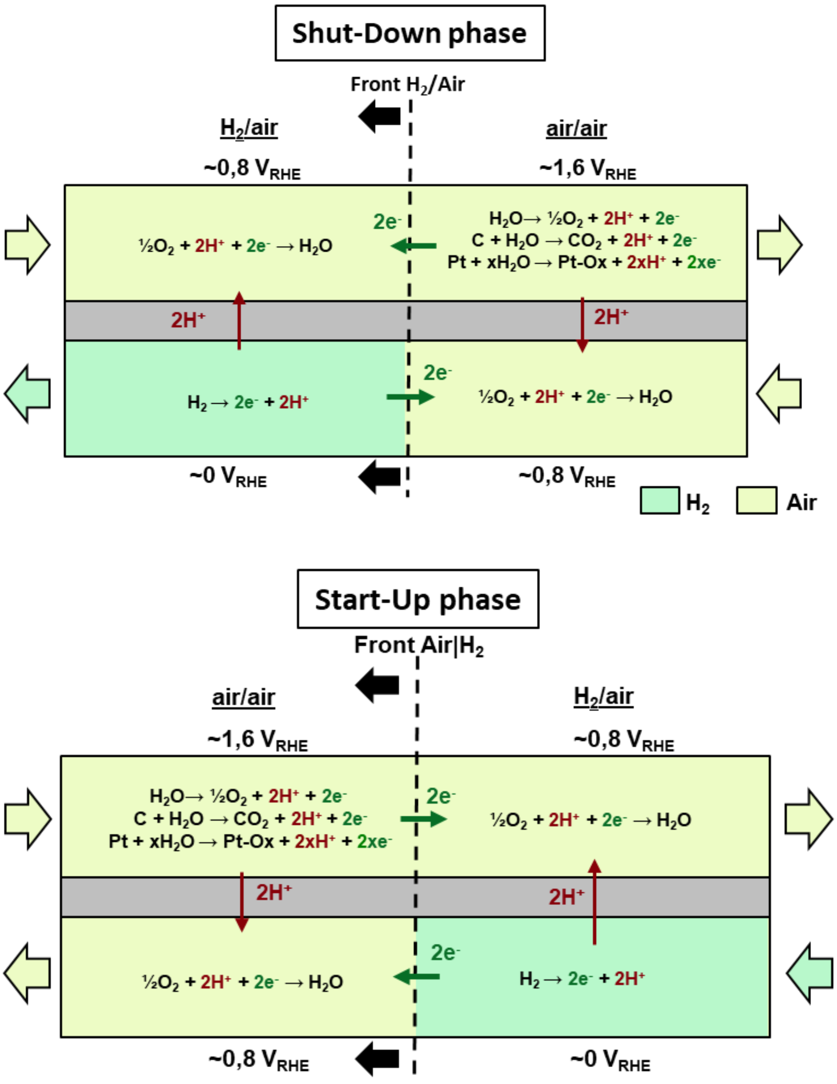

Figure I-15: Fluidic and electrochemical mechanisms during unprotected shut-down phase (Air flushing at the anode) and start-up phase (H_2 flushing at the anode)

The electrochemical cell can be therefore considered and separated in two-sub cells by the H_2|Air front:

- The sub-cell in H_2/Air configuration which operates as nominal Fuel Cell (FC) and is a current generator. No specific degradation is intended in this first sub-cell;
- The sub-cell in Air/Air configuration which acts like a current receptor and operates as an Electrolysis Cell (EC).

For the sub-cell in Air/Air configuration, reduction reaction occurs at the "FC anode side" (ORR) while oxidation reactions, mainly Oxygen Evolution Reaction (OER) via reaction (I-2) inversely to the ORR process, occurs at the "FC cathode side". Several models have predicted that local potential distribution at the cathode side can reach up to 1.4 – 1.6 V_{RHE} [47]–[49] in this sub-cell region. Such high potential is responsible for harsh oxidation/corrosion of both Pt nanoparticles and cathode carbon support from reactions (I-11) to (I-21). The detailed description of the reverse current mechanism during the SU/SD phases will be discussed and reviewed in the Chapter II.

I.3.2.3.1. Place-exchange oxide mechanism and enhanced Pt dissolution

As introduced previously (section I.3.2.2.2), potential beyond 1.0 V_{RHE} are known to accelerate the Pt dissolution rate [41] in dynamic conditions due to the Place-exchange mechanism. In fact, at such potential, surface Pt-oxides (Pt-O_{ad}) can form an oxide sub-layer named O_{bulk}-Pt, following reaction (I-23).

$$Pt - O_{ad} \leftrightarrow O_{bulk} - Pt \tag{I-23}$$

Maranzana *et al.* [50] built an electrode model including the Pt-oxide redox reactions and double layer capacitance. Their simulation gives access to the respective Pt oxide species formations and their coverage rates. Significant surface oxidation and Place-exchange take place at the cathode side with a more pronounced coverage rate and bulk oxidation in the Air/Air region above 1.4 V_{RHE}. Furthermore, the coverage of O_{bulk} can reach almost 1.5 meaning that a second sub-layer of Pt is oxidized. The Place-exchange is known to accelerate to the cathodic dissolution, as detailed thereafter.

In fact, several studies have investigated the Pt dissolution mechanism during transient states and depicts higher degradation rate than in steady state as described during Idling/OCV (section I.3.2.2.2). Commonly, CV technique with different lower and upper potential limits has been performed in order to evaluate the Pt dissolution during these transient states [51]–[54]. Topalov *et al.* [51], [54] have scanned the potential between (i) fixed lower potential value 0.05 V_{RHE} up to variable upper potential limit (from 1.0 V up to 1.8 V_{RHE}) and between (ii) variable lower potential limit (from 0.05 up to 1.0 V_{RHE}) fixed upper potential value 1.55 V_{RHE}, as illustrated in Figure I-16 (left and right, respectively).

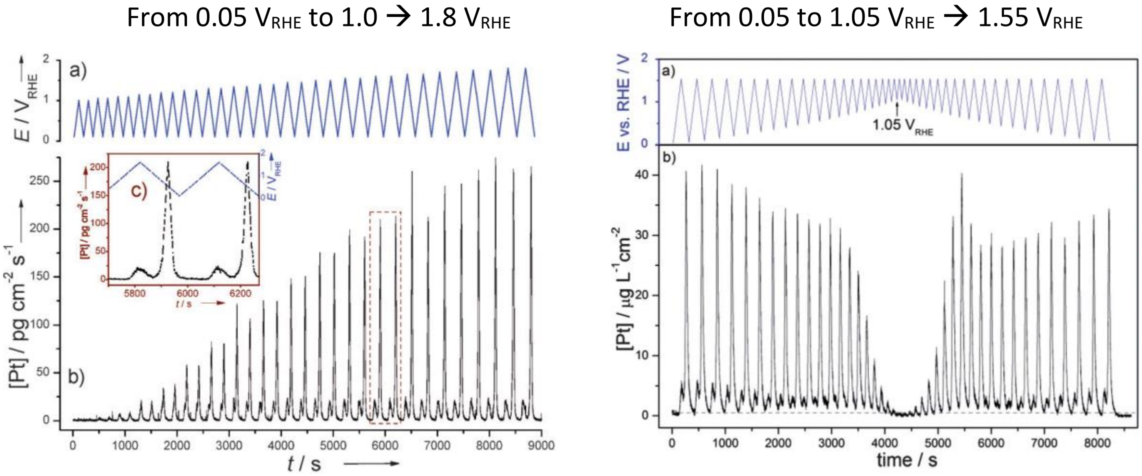

From 0.05 V_{RHE} to 1.0 → 1.8 V_{RHE}

From 0.05 to 1.05 V_{RHE} → 1.55 V_{RHE}

Figure I-16: Pt dissolution profiles during CV (at 0.01 $V.s^{-1}$) in 0.1 M $HClO_4$ between fixed lower potential limit (0.05 V_{RHE}) and variable upper potential limit (from 1.0 up to 1.8 V_{RHE}) on the left and between fixed upper potential limit (1.55 V_{RHE}) and variable lower potential limit (from 0.05 to 1.05 V_{RHE}) on the right [51], [54]

During the CV, two Pt dissolution peaks are observed during the positive (anodic) and the negative (cathodic) sweep with different rates according to the potential range. Thus, authors agreed to define both anodic and cathodic dissolution.

The global Pt dissolution in transient state increases significantly when the potential sweep goes dynamically over and below a threshold value about 1.1 V_{RHE}. On the one hand, the anodic dissolution rate becomes minor when upper potential value exceeds 1.1 V_{RHE} since the Pt^{2+} formation rate gets then strongly hindered by the formation of oxide species (-O_{ad}). On the other hand, the cathodic dissolution rate becomes much higher. Indeed, the formation of O_{bulk}-Pt species promotes the Pt dissolution during the following reduction cycle as illustrated in Figure I-17 [51].

Moreover, ECSA loss during high potential excursion has been investigated in several works. Park *et al.* [55] estimated 50% loss of ECSA after 50 h at 1.3 V_{RHE}. Likewise, Sharma *et al.* [56] suggests that 50% of ECSA loss after 7500 cycles (triangular sweep 1.0 – 1.6 V during 25 hours). Even if the dynamic protocol is shorter, it is as degrading as the fixed potential ageing at 1.3 V_{RHE} during 50 h. The transient phase accelerates the Pt dissolution/redeposition or precipitation as explained previously.

Thus, to mitigate the Pt catalyst ageing, cathodic potential must not exceed 1.1 V_{RHE}. However, during unprotected SU/SD events, this severe degradation is very likely since the cathodic potential can rise locally up to 1.6 V_{RHE} during the propagation of the front and then return to ~ 0.95 – 1.0 V_{RHE} once the anode is totally filled with H_2.

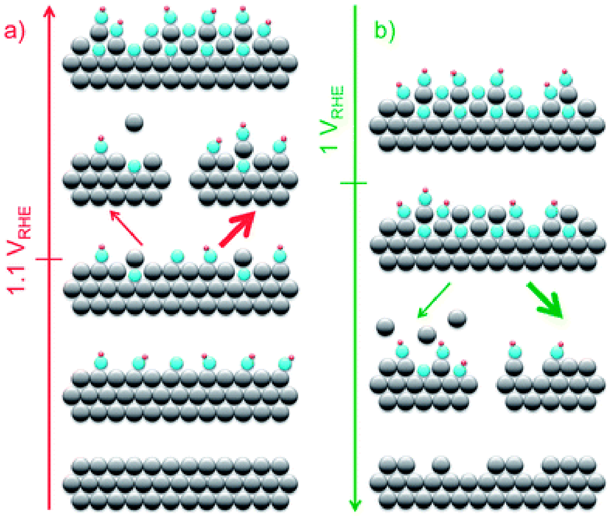

Figure I-17: Mechanistic representation of oxidation of platinum during anodic scan above 1.1 V_{RHE} and the dissolution/redeposition during sequent cathodic scan [51]

I.3.2.3.2.Impact of direct corrosion of carbon support

As explained in the previous section (I.3.2.1.2), the potential excursion above 1.0 V_{RHE} strongly accelerates the direct CSC of both amorphous/disordered domains and ordered graphitic domains. Thus, CCL properties modifications are observed after direct corrosion of support carbon above 1.0 V_{RHE}. Among the numerous consequences, some of them are of key-importance such as the exacerbated loss of the ECSA, the decrease of the porosity and the loss of hydrophobicity, until ultimately the collapse of the CCL [55].

In addition to the Pt nanoparticles growth related to the Pt dissolution/redeposition mechanism and Place-exchange explained previously, Pt nanoparticle detachment due to the quantitative carbon support corrosion above 1.0 V_{RHE} also accounts for the global ECSA loss. Indeed, the CSC weakens the Pt/C bond and induces the growth of the Pt nanoparticles. Thus, Pt nanoparticles are detached from carbon support favoring their agglomeration [57].

Hu *et al.* [58], [59] conducted a deep study on the impact of CCL collapse on the loss of performance. Potential maintained at 1.4 V during 1 h and repeated 3 times (equivalent to 700 SU/SD cycles according to the author) is experimented on 291-cm^2 single cell. They propose a three-stage degradation mechanism of the CCL as illustrated in Figure I-18 according to the corrosion level:

- Firstly, an activation phase of Pt/C components with a slight modification of CCL structure;
- Secondly, a progressive corrosion of Pt/C components with a progressive loss of performance governed by Pt oxidation/dissolution + detachment and CSC;
- Thirdly, a drastic loss of performance concomitantly with the collapse of porous structure weakened by the lack of carbon.

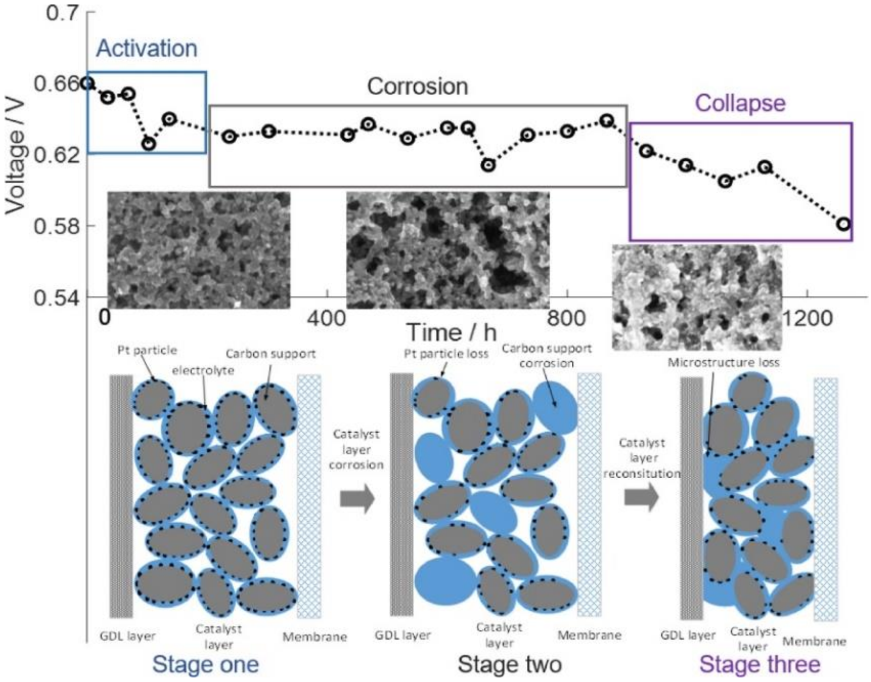

Figure I-18: CCL degradation process by CSC mechanism according to Hu et al. [58]

This collapse phenomena induces the decrease of the overall porosity from 40% (pristine) down to 5% (after 1000 unprotected SU/SD cycles) which has been quantified and visualized by FIB/SEM and electron tomography [60]. Consequently, the mass-transport of oxygen towards active sites becomes strongly hindered. Decreased water evacuation from the CCL may also aggravate this limitation. Indeed, the remaining pores are therefore easily filled with water and the carbon surface facilitates their adsorption due to the formation of functional groups onto carbon support [30], [61].

The impact of CSC on cell performance has been investigated by electrochemical impedance analysis after potentiostatic ageing test at 1.3, 1.4 and 1.5 V during 30 min under H_2/N_2 gas supply with different RH (50 and 100%) [62]. From polarization curve, the loss of performance at 0.7 V is estimated at 3.6%, 25%, and 30% (under RH 50%) and 4.0%, 46%, and 90% (under RH 100%), at 1.3, 1.4 and 1.5 V respectively. The higher potential value exposition, the higher kinetics for CSC and thus, a higher cell performance decay.

Moreover, high H_2O content in gas supply exacerbates the degradations. As detailed in section I.3.2.1.2, water is needed for the oxidation/corrosion reactions. Regarding EIS analysis at 0.8 V, transmission line model is used to quantify the charge transfer resistance, the electronic resistance and the protonic resistance of the aged CCL [62]. The increase of each resistance with potential and RH values is in agreement with polarization curve measurements. Authors concluded that CCL collapse is responsible for these trends.

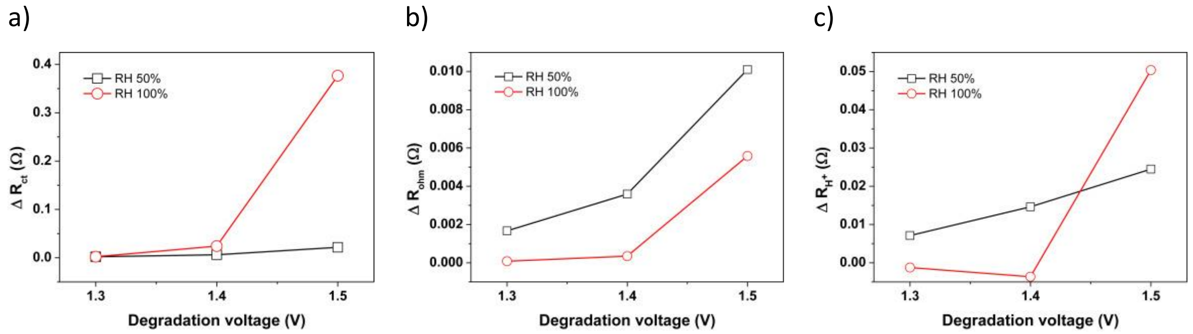

Figure I-19: Evolutions of a) Charge transfer resistance, b) Ohmic resistance and c) Ionic resistance in the CCL under FC operation at 0.8 V after specific ageing tests (30 min at 1.3, 1.4 and 1.5 V under RH 50 or 100%)[62]

Despite all these works, advanced studies of the CSC mechanism and their impact on CCL properties under realistic potential profile for SU/SD events using representative and state-of-art objects (MEA and cell designs) are scarce in literature. Indeed, such studies are required to quantify accurately the degradation and would be helpful to understand and then to mitigate the performance decay.

I.4. CONCLUSIONS

PEMFC-powered electrical vehicles are clearly identified as promising alternatives to thermal engines in the objective to reduce GHG emissions. However, their commercialization remains limited since key challenges still need to be solved. Durability is one of these technical barriers on which R&D effort must be carried out. The lifetime of a fuel cell stack remains unsatisfactory in transportation compared to stationary applications due to more severe operating conditions. Indeed, dynamic load, idling/OCV, high power and SU/SD phases all favor component degradations within the fuel cell stack. High cathode potential damages preferentially the cathode catalyst layer. Individual mechanisms are well-identified and have been presented in this introduction chapter and they are well-identified such as the Pt oxidation/ dissolution – redeposition/precipitation and the corrosion of the carbon support, leading to Pt detachment/agglomeration. Generally, a loss of ECSA due to the growth of Pt nanoparticles (Pt dissolution → redeposition & CSC → Pt detachment) accompanied with a loss of hydrophobicity and porosity within CCL results in an irreversible loss of performance. All of degradations reactions taking place in the CCL are summarized in the Figure IV-33 according to the cathodic potential excursion during operational modes.

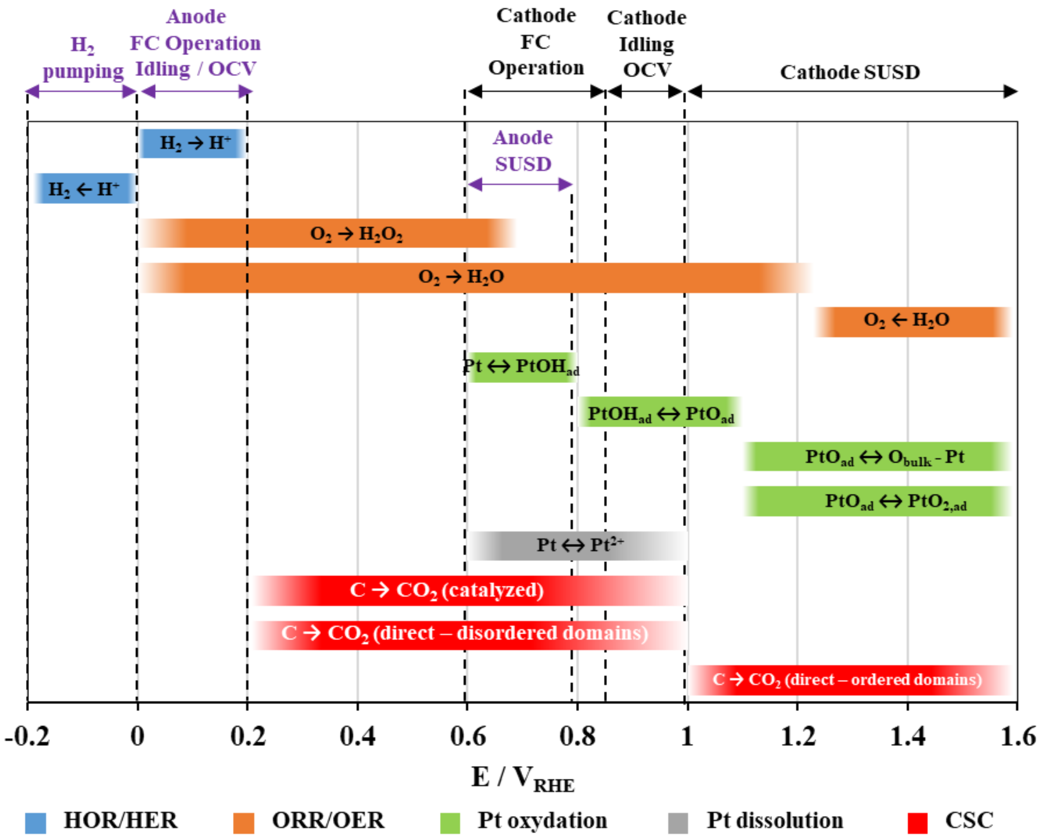

Figure I-20: Summary of FC electrochemical reactions and CCL degradation reactions according to the potential range during fuel cell operation

Let us stress that these degradation mechanisms are extremely severe when cathode electrode goes beyond 1.0 V_{RHE} during SU/SD events inducing the well-identified Reverse Current Decay mechanism. The propagation of an H_2|Air front at the anode side yield locally to potential elevation as high as 1.6 V_{RHE} at the cathode side. Initially filled with Air, the injection of H_2 during start-up propagates the H_2|Air front in the anode compartment from inlet to outlet, damaging heterogeneously the whole surface of the cell. That is why, mitigation strategies are mandatory and must be implemented during these phases in order to reduce their impact on cell performance and durability. This PhD work will be focused on quantifying the degradation mechanisms and the loss of performances on real stack designs to select the best protective architecture for the future PEMFC systems.

In the next chapter, a detailed review of mitigation and alternative strategies during start-up and shut-down events is proposed to identify the most impactful parameters and processes based on literature and patent data to guide and support our experimental approach.

Chapter II. STATE-OF-ART OF STRATEGIES IN START-UP AND SHUT-DOWN

II.1. INTRODUCTION

PEM fuel cell in transportation applications includes numerous start-up and shut-down phases. One of the key challenges to improve durability is to reduce their impact on cell performance. Indeed, unprotected SU/SD phases contribute to 33% of degradations [18]. The status of durability according to the number of SU/SD cycles for automotive application is proposed by DoE and aims to reach 8000 cycles by 2025 with a voltage loss of 10% with our nominal current density (@ 1.2 A/cm²) [13]. That implies an average loss of voltage less than 5 µV per cycle, approximatively.

During the two past decades, R&D teams develop promising SU/SD processes to mitigate their impact on cell performance and durability [63], [64]. Literature reveals two main solutions. The first mitigation strategy consists in improving CCL materials stability, especially during the well-known Reverse Current Decay (RCD) occurrence with the anodic H_2|Air front formation. More corrosion resistant material for catalyst support such as graphitized [65] or fluorinated [66] carbon have been studied and have demonstrated better durability under SU/SD conditions. Otherwise, incorporated alternative catalysts such as IrRu [67] or Sb-doped SnO_2 [68] at the cathode, and TiN [69] or Ta-TiO_2 [70] at the anode, have been studied to limit CSC reactions. Durability of cell is improved during the SU/SD phase but the alternative catalysts at the anode and cathode side reduce respectively their HOR or ORR activity and thus cell performance in operating conditions. The second mitigating solution consists in optimizing system control and operating conditions during SU/SD phases. This chapter reviews “system” strategies reported in literature and patents.

II.2. START-UP & SHUT-DOWN OVERVIEW

A definition and an overview of several SU/SD processes is reported in this section to better understand the framework of this chapter, as illustrated in Figure II-1.

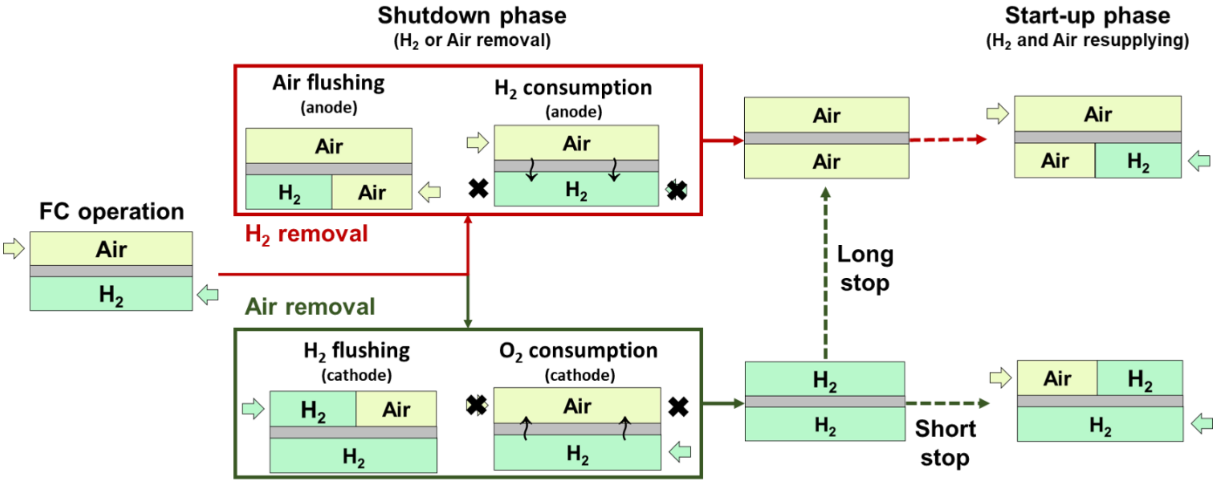

Figure II-1: Overview of different scenarios during shut-down and start-up phases

II.2.1. Shut-down process

Initially, FC operates under H_2 and Air reactant gas supply in anode and cathode electrodes, respectively. Subsequently, shut-down phase proceeds by the removal of one of the reactant gases (H_2 from anode or O_2 from cathode). The two most common removal methods implemented in PEMFC system are:

- The gas flushing process[2]. It consists in either evacuate H_2 by flushing with Air in anode or Air by flushing with H_2 in cathode, called "Air flushing" and "H_2 flushing" in Figure II-1, respectively. Both processes generate an H_2|Air front in anode or cathode side;
- The gas consumption process. The gas supply of H_2 or Air is shut off and the FC electrochemical reactions are pursued by means of dummy load until the complete depletion of residual gas. We talk about "H_2 consumption" or "O_2 consumption" process (see Figure II-1), respectively.

Both methods lead ultimately to an Air/Air or a H_2/H_2 fluidic configuration (anode/cathode) in the fuel cell according to the removal methods.

---

[2] Inert gas such as nitrogen is not implemented in PEMFC system due to the complexity of integration and the cost/weight of additional N_2 storage

II.2.2. Prolonged stop

After the SD phase, a subsequent stop period takes place. Details of transient fluidic and electrochemical mechanisms, as well as the impact on performance decay during these periods have never been treated in literature. A simplified description is given thereafter. Stop period depends on initial fluidic configuration within the stack right after shut-down phase (Air/Air or H_2/H_2). On the one hand, from Air/Air case, internal gas composition hardly changes until the restart. On the other hand, from H_2/H_2 case, the gas composition evolves according to the stop duration. Both "short stop" and "long stop" are defined for several hours and several days/weeks, respectively. During "short stop", it can be supposed that the H_2/H_2 fluidic configuration is maintained until the restart whereas during the "long stop", ambient Air infiltrates fuel cell and consumes progressively residual H_2. A progressive H_2 leak to the outside is also presumed. The prediction of the diffusion and infiltration kinetics are difficult and depend strongly on the stack tightness and the system fluidic architecture.

Depending on the scenario in the stop period ("short" or "long" stop), the stack fluidic configuration results either in "$x_aN_2 + x_aH_2/ x_cN_2 + x_cH_2$" or "$x_aN_2 + x_aO_2/ x_cN_2 + x_cO_2$" fluidic configuration and this can impact the next start-up phase.

II.2.3. Start-up process

The restart consists in supplying both electrodes with gas reactants. In initial Air/Air fluidic configuration, H_2|Air front is formed at the anode side and leads to harsh degradation mechanisms due to the Reverse Current Decay mechanism (cf. section I.3.2.3). From H_2/H_2 initial fluidic configuration, the H_2|Air front formed at the cathode is supposed to be harmless due to the reductant atmosphere in both anode and cathode sides in the anode outlet region. This remains to be demonstrated and that there could be degradations with proton pump operation at low potential.

II.2.4. Preliminary conclusions

The next sections in this chapter report in details most of SU/SD strategies studied or patented in literature. A mechanistic description of degradations and an evaluation/comparison of their efficiency to mitigate performance decay is discussed.

The section II.3 describes the unprotected SU/SD process that corresponding to the anode "Air flushing" process during the SD phase followed by an anodic H_2 supply in Air/Air initial state. Both phases lead to the H_2|Air front formation in the anode. Various protective strategies during RCD occurrence are also reviewed.

Then, the section II.4 presents the alternative SD protocols, particularly, the "H_2 consumption" and the "Air consumption". Finally, all SD process are discussed especially in order to identify the most promising strategies for durability improvement.

II.3. RCD DESCRIPTION AND MITIGATION STRATEGIES

II.3.1. RCD description

As introduced in section II.3.1, RCD mechanism occurs when the cell is separated in two regions with the H_2|Air front in anode side and with the presence of Air at the cathode side and it can take place during so-called "unprotected" SU or SD. The cathode electrode in the Air/Air region is affected by harsh oxidative reactions (OER + Pt oxidation/dissolution + CSC) as reported in section I.3.2. The detailed description of RDC mechanism is given thereafter.

II.3.1.1. Potential profile and current density

It is impossible to have access to local distribution of current density and anodic/cathodic potential at the macroscopic scale. For that, models and segmented cells have been developed to probe local conditions in PEMFC along the cathode channel.

II.3.1.1.1. Cathodic potential profile

It is established that the cathode electrode undergoes high potential elevation above 1.4 V_{RHE} in the Air/Air region. The Table II-1 proposes a list of studies focusing on local conditions during SU/SD, with an estimation of the maximal potential reached at the cathode side.

Table II-1: Estimated maximal potential reached at the cathode side during RCD occurrence

Authors	**Methods**	**Higher local cathodic potential**	**Ref.**
Reiser *et al.*	Model	~ 1.44 V	[46]
Meyers *et al.*	Model	~ 1.69 V	[47]
Randrianarizafy *et al.*	Model	~ 1.6 V	[71]
Maranzana *et al.*	Model	~ 1.5 V	[50]
Shen *et al.*	Exp. (PEMFC with RHE)	~ 1.6 V	[48]
Lamibrac *et al.*	Exp. (segmented cell)	1.4 – 1.6 V	[72]

Authors agree that the maximal potential excursion takes place near the cathode inlet (facing the anode outlet) during the SU phase, and near the cathode outlet (facing the anode inlet) during the SD phase, in counter-flow configuration, as illustrated in the Figure II-2 [71]. Moreover, both inlet and outlet of the cathode are submitted for long exposure time at high potential while the H_2|Air front propagates along anode channel. In nominal SU phase, the model developed by Randrianarizafy *et al.* [71] predicts a high potential elevation up to 1.6 V_{RHE} and a residence time of the H_2|Air front during 1.5 s, approximately.

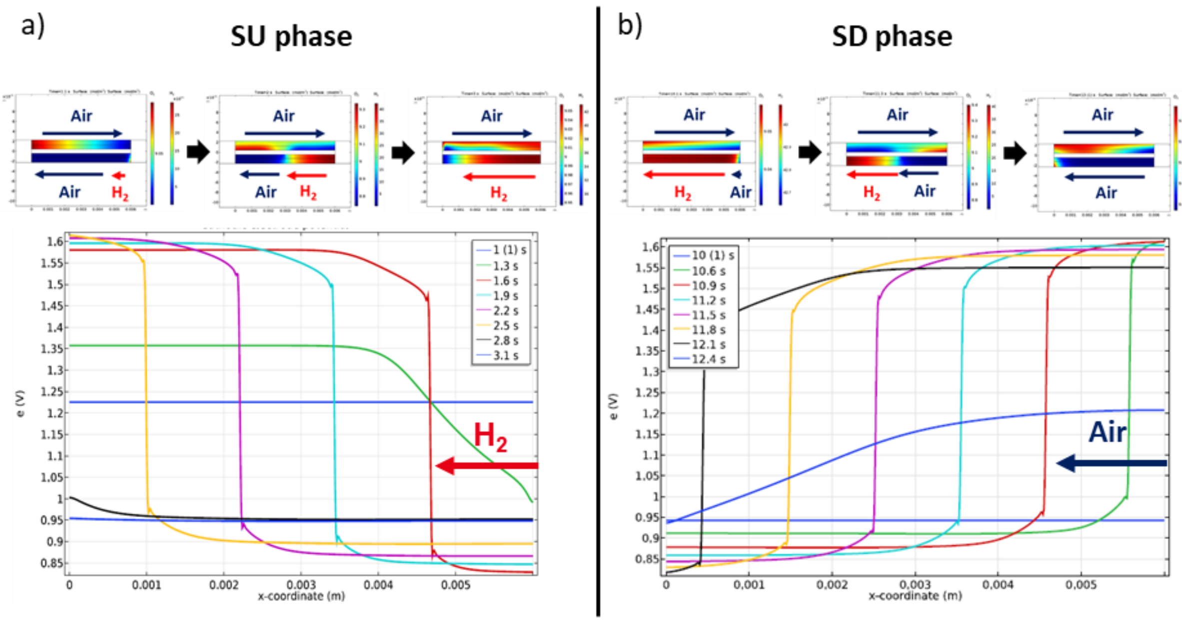

Figure II-2: Predicted local cathodic potential profile caused by RCD along the cathode channel during a) the start-up and b) the shut-down phase [73]

To better understand the reaction occurring locally under 1.6 V_{RHE}, the contribution of faradic current (OER + CSC reaction + Pt oxidation reaction) and capacitive current exchanged between both Air/Air region and H_2/Air region is evaluated.

II.3.1.1.2. Faradic / capacitive current density

By an experimental approach, Dillet *et al.* [74]–[77] have designed a segmented cell (1 x 30 cm) to inspect local current densities along the cathodic channel coupled with CO_2 measurements. The Figure II-3 illustrates the local current density during a) the SU phase (H_2 injection at the anode with Air/Air initial configuration) and b) the SD phase (Air injection at the anode with H_2/Air initial configuration). Positive and negative current densities correspond to the FC and EC region (H_2/Air and Air/Air region) respectively. Thus, the last segments supplied by H_2 (facing the cathode inlet) in SU phase and by Air (facing the cathode outlet) in SD phase are prone to higher negative current density, in agreement with the higher cathodic potential.

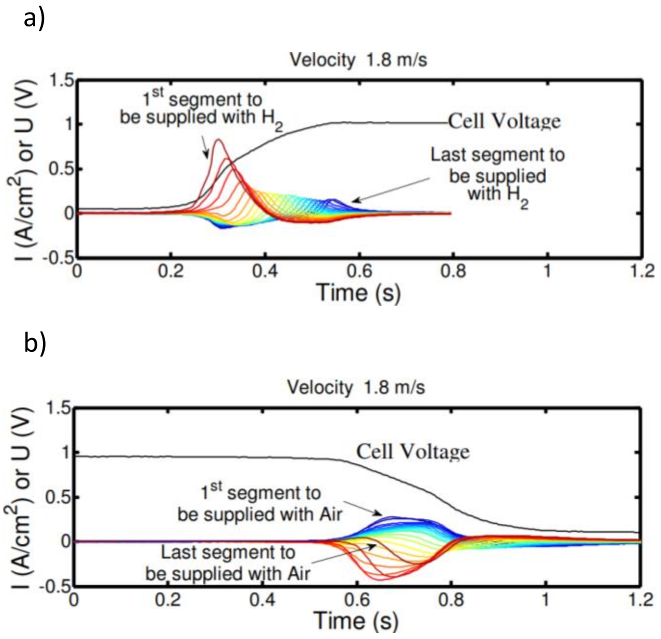

Figure II-3: Local current density and global fuel cell voltage during a) the start-up phase (H_2 injection at the anode with Air/Air initial configuration) and b) the shut-down phase (Air injection at the anode with H_2/Air initial configuration) measured with segmented single cell (20 segments) [75]

To compare impact of both SU and SD phases, it is more appropriate to look at the electrical charge. From segmented cell, the total charge exchanged between H_2/Air region and the Air/Air region is measured, as well as the capacitive contribution. The measurements of the CO_2 at the cathode outlet give access to the charge from CSC reactions. For instance, 11% of the total exchanged charge is relative to CSC reactions and 12% due to capacitive contribution with a H_2 velocity of 0.1 m/s during the SU phase [75]. The remaining electrical charge is linked to faradic currents from OER and Pt oxidation reactions. No detailed estimation has been provided in SD phase. Ultimately, the total charge measured by segments along the cathode channel during SU and SD phases, under similar operating conditions, reveals a non-uniform distribution with a higher coulometry at the inlet/outlet of the cathode, during the SD and SU respectively, as illustrated on Figure II-4. The consequences of this inhomogeneous current density distribution are detailed thereafter.

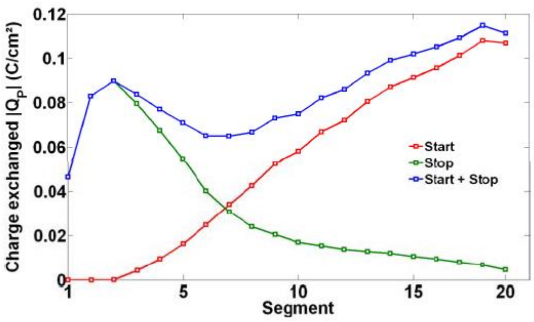

Figure II-4: Local charge exchanged by segments along the cathode channel during the SU and SD phase [75]

II.3.1.2. *Spatial distribution*

Degradation rate at the cathode side is known to be spatially non-uniform (i) along the anodic channel and (ii) under the rib and under the channel at the anode. The first one is consistent with the propagation of the H_2|Air front from the anode inlet (facing the cathode outlet) to the anode outlet (facing to cathode inlet) in a counter-flow configuration. For the second one (rib/channel), the diffusivity of flushed gas through the porous-structure of the GDL and ACL must be here taken into consideration. Actually, this is caused by the longer gas flushing under the rib (Figure II-7 and Figure II-8) than under the channel resulting to an additional H_2|Air front perpendicularly to channels.

Several models predict the distribution of the CSC rate along the channel [73], [78], [79]. In counter-flow configuration with similar operating conditions, the CSC takes place preferentially at the inlet and outlet of the cathode due to both SU & SD, and gives an asymmetrical distribution as illustrated in Figure II-5, according to the current density distribution plotted in Figure II-4.

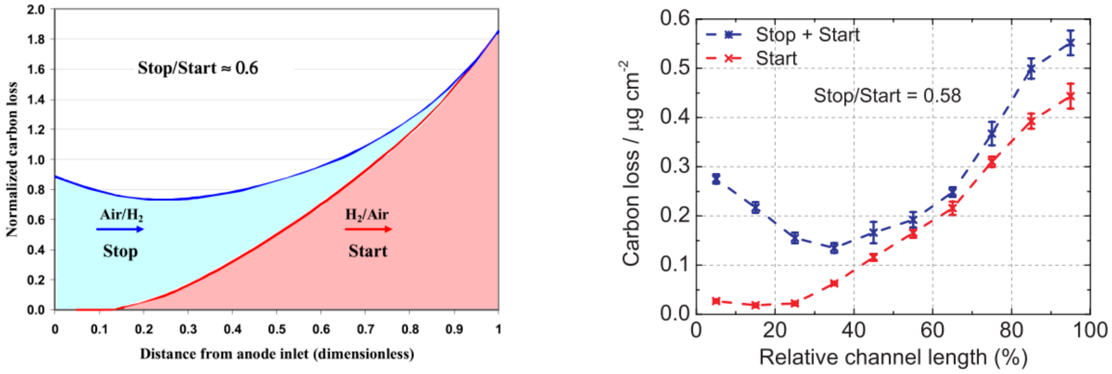

Figure II-5: Distribution along the cathode channel during both SU and SD phase of the charge related to CO_2 emission [78], [79]

The CSC distribution has been validated by SEM technique with a lower thickness of CCL at the inlet/outlet locations [79]. It is estimated that the SU phases are more degrading than the SD phase with an estimated ratio at about 0.6. The main reasons for the difference between the degradation rates are:

- The more severe SU process is related to a longer air evacuation during H_2 injection compared to the faster H_2 evacuation during the SD phase, as indicated by Babu *et al.* [76]. Ishigami *et al.* [80] used visualization technique to map the P_{O2} distribution during H_2|Air propagation along anodic channel. Oppositely, they obtained a residence time twice and five times longer in the SU and SD phase, respectively, in comparison to the raw residence time calculated only for channel filling only, making the SD process more serious. According to these studies, there is no consensus on the performance impact related to the H_2 *vs.* Air evacuation during the SU and SD phases, respectively.

- The Pseudo-capacitive effect due to the parallel oxidation or reduction reaction of the platinum active sites at the anode side, which influences the CSC reactions at the cathode side. Regarding the Figure II-6, Pt is oxidized during the SD phase when H_2 is substituted by Air (anodic potential elevation from 0.0 to 0.8 V_{RHE}) and is reduced during the SU phase when Air is purged with H_2 (anodic potential drop from 0.8 to 0.0 V_{RHE}). The faradic distribution between the anodic and cathodic reactions in the Air/Air region is impacted during both SU and SD phases.

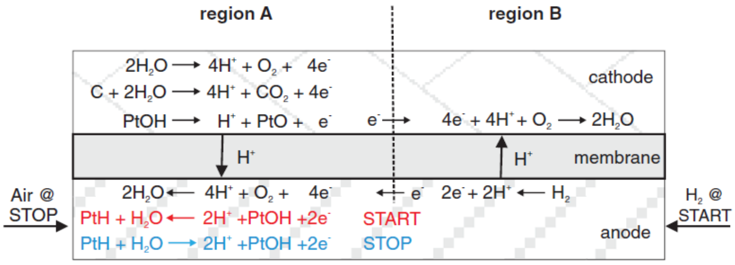

Figure II-6: Description of pseudo-capacitive effects with detailed anodic Pt oxidation/reduction according to the SU and SD phases [79]

Non-uniform degradations is also observed between rib and channel areas [71], [81]–[83]. The Figure II-7 schematizes the RCD mechanism in the rib/channel plane during the SU phase. The H_2 flushing in Air-filled anode fills firstly the channel, and subsequently, the porous media by diffusion. Thus, an H_2|Air front occurs perpendicularly to the channel. The cathode areas facing the anodic channel operates in FC (H_2/Air region) while those facing the anodic rib operates in EC (Air/Air region), and thus, are submitted to oxidative reactions (OER, CSC reactions and Pt oxidation). On the contrary, the areas facing the anodic channel are degraded in SD phase when Air flushes the H_2-filled anode.

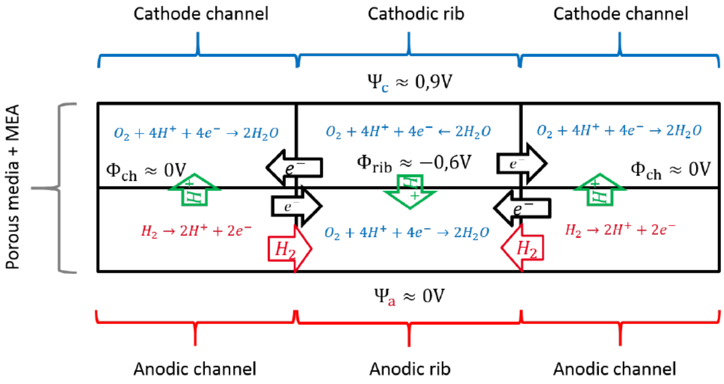

Figure II-7: Schematic description of RCD mechanism during the SU phase at the rib/channel scale [71]

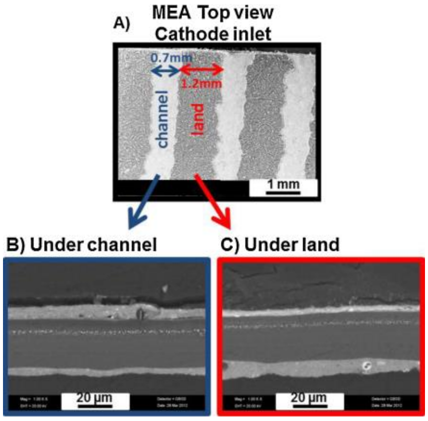

Figure II-8: SEM images of aged MEA by SU/SD under the anodic channel and rib [82]

Schneider *et al.* [83] modelled the SU/SD phase in the rib/channel plane and demonstrated that a high flow rate of flushed gas could not avoid the H_2|Air formation perpendicularly to the channel due to the mass-transport limitations under the rib. Durst *et al.* [82] validated this heterogeneity by cycling 136 SU/SD cycles on segmented cell. They observed by SEM a higher thinning and densification of the CCL facing the anodic rib than facing the anodic channel, as illustrated in Figure II-8. From Radrianarizafy's model [71], the CSC is 10% higher under the anodic rib than under the anodic channel in SU phase.

II.3.2. RCD Mitigating strategies at system scale

This section focuses on mitigation strategy provided by a system approach. Key mitigating parameters are the operating conditions managed by the 3 fluidic circuits (H_2, Air and coolant) and the electrical circuit. They are ranked below in order of significance according to the literature.

II.3.2.1. Lowering the partial pressure of reactant gas (P_{O2} and P_{H2})

Lowering partial pressure of both H_2 and O_2 reactant gas before H_2|Air front occurrence has shown a reduction of degradation mechanisms. Linse *et al.* [84] analyzed the CO_2 emission relative to CSC mechanism in function of both anodic H_2 and O_2 concentration used to flush or initially present before the anode flushing in SU and SD phase (21% O_2 in cathode) as illustrated in Figure II-9.

They depicted a strong effect of H_2 partial pressure by lowering the initial P_{H2} in the anode from 100% to 5% before the SD (by a 21% O_2 flushing), yielding a reduction factor of 20 on CSC. No variation was detected during the SU phase when diluted-H_2 with nitrogen is injected in the Air-filled anode (at 21% O_2). This trend is explained by the easier Air flushing (21% O_2) in an anode poorly filled with H_2, and thus, the rapid diffusion across GDL and CL accelerating the H_2|Air front propagation.

Similarly, lowering the O_2 partial pressure (P_{O2}) initially in the anode from 21% to 5% before the SU phase (by a 100% H_2 flushing) yielded a reduction factor of three on CSC. No variation in SD by flushing diluted O_2 with N_2 in a 100% H_2-filled anode is detected because the time residence of the H_2|Air front propagation is independent to P_{O2} amount. The high diffusivity of H_2 and its effect on electrode potential makes Air flushing process more dependent to H_2 concentration than O_2 concentration regarding CSC mechanism.

Eom *et al.* [85] proposed a durability test by cycling SU (H_2 flushing in anode) and alternative SD phase (O_2 consumption), followed by Air purge in anode/cathode sides emulating long stop, with different O_2 concentrations in both anodic/cathodic circuits. After 1200 cycles, cell performance degradation is 300 µV.cycle^{-1} (@ 0.4 A.cm^{-2}) at 21% of partial pressure of oxygen (P_{O2}), and is reduced at 210 µV.cycle^{-1}, 33 µV.cycle^{-1} and 17 µV.cycle^{-1} by lowering P_{O2} at 10%, 1% and 0%, respectively.

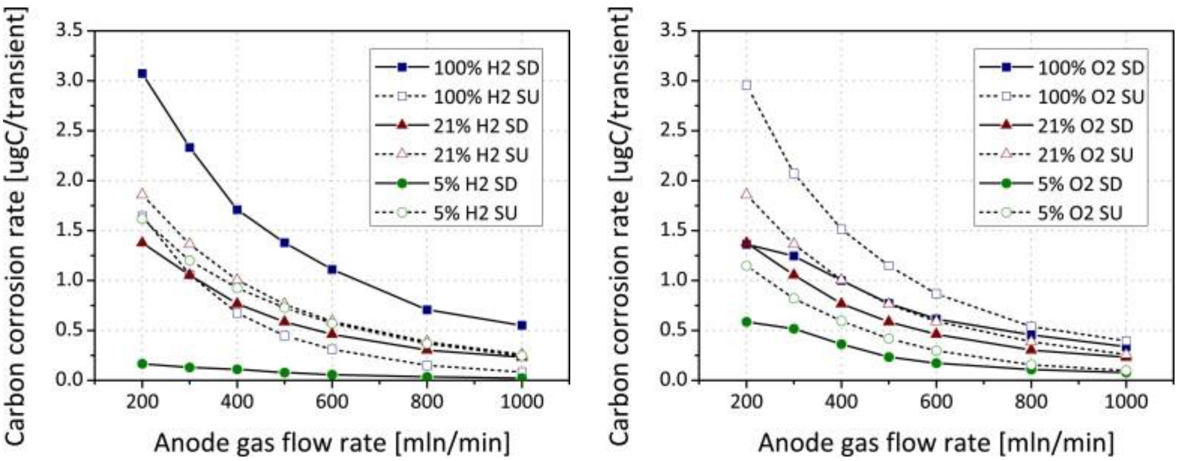

Figure II-9: Carbon corrosion rate for different hydrogen and oxygen concentration in anode (21% O_2 in cathode) during SU and SD phases in 16-cm² single cell [84]

II.3.2.2. Lowering the temperature

Lowering the temperature of both cell and reactant gases is expected to mitigate CSC reactions. As illustrated in Figure II-10, temperature effect on CSC follows Arrhenius law from 40 up to 70 °C, while the deviation above this temperature can be ascribed to a higher molar volume and thus a lower reactant gas pressure, during H_2|Air front occurrence [84]. Mittermeier *et al.* [86] predicted a 8-fold lower CSC reactions at 5 °C compared to 80 °C on conventional carbon support.

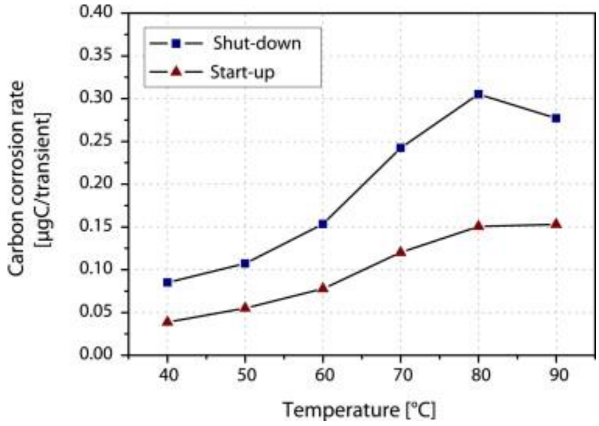

Figure II-10: CSC rate according to the cell temperature during SU/SD phases in 16-cm² single cell [84]

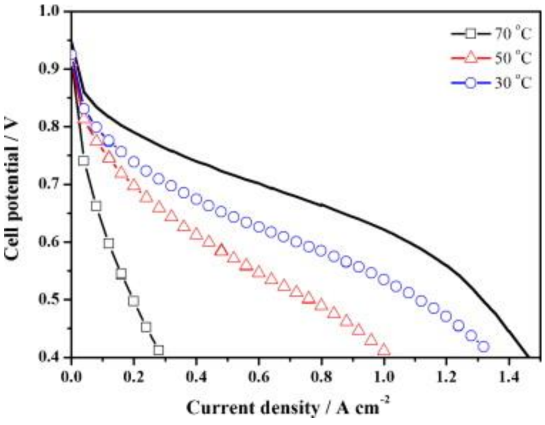

Figure II-11: Polarization curve performed on fresh (black line) and aged MEA after SU/SD ageing tests at different cell temperature in 25-cm² single cell [49]

The beneficial effect on cell voltage loss is confirmed when cell temperature is lowered [49], [87]. Kim *et al.* [49] cycled SU/SD phases (Air and H_2 flushing in anode) and depicted a harsh reduction of cell voltage decay regarding the polarization curve evolution between fresh and aged MEA at 70, 50 and 30 °C (see Figure I-11). At 1.0 A.cm^{-2}, the performance loss is estimated at about 23 and 9 mV.cycle^{-1} at 50 and 30 °C. The charge transfer resistance increases in parallel by 57% at 70 °C and 20% at 30 °C.

Total CO_2 emission during ageing test is reduced by 55% from 70 to 30 °C. Y. Y. Jo *et al.* [87] performed similar study by cycling SU phase (H_2 flushing in Air-filled anode) and alternative SD phase (cathodic O_2 consumption) followed by Air flushing in anode/cathode side emulating long stop. The cell voltage decay at 0.4 $A.cm^{-2}$ is about 0.13, 0.24 and 0.31 $mV.cycle^{-1}$ at 40, 65 and 80 °C, respectively. Regarding CV measurements, ECSA loss is about 0.061, 0.073 and 0.080%.$cycle^{-1}$ at 40, 65 and 80 °C, respectively.

II.3.2.3. Lowering the relative humidity of reactant gases

Relative Humidity (RH) of reactant defines the water content in CCL. A linear dependence between RH of gas supply in anode and cathode sides, has been observed with CO_2 emission (see Figure II-12) [84]. The variation at RH 100% is not clear and may be caused by the accumulation of liquid water in the anode electrode. Brightman et Hinds [88] suggest that H_2|Air front propagation is accelerated for elevated RH due to a higher volumetric flow rates. Indeed, their local measurements of cathode potential show a shorter duration at about 1.4 V at higher RH amount, but the CSC rate is doubled between RH 33% and 60% and then constant between RH 60% and 100%. Mittermeier *et al.* [89] modelled SU/SD phase and predicted a 3-fold lower degradation rate between 100 and 25% of relative humidity.

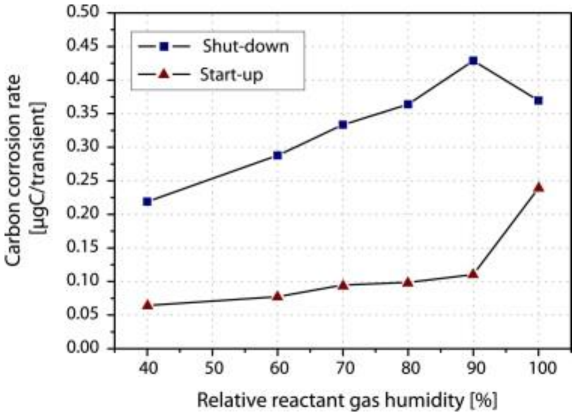

Figure II-12: CSC rate according to the RH of both anodic/cathodic reactant gases during SU/SD in 16-cm² [84]

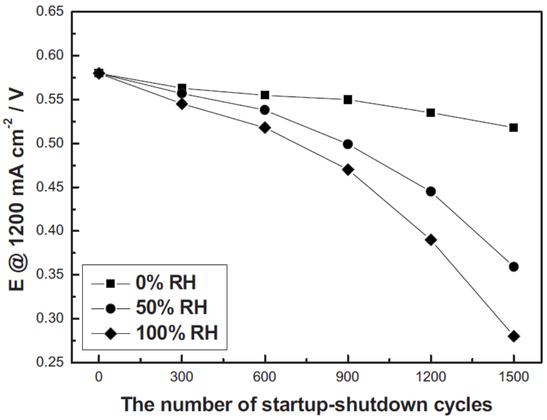

Figure II-13: Single cell performance evolution during ageing test at 1.2 $A.cm^{-2}$ with different RH (0 – 50 – 100%) in 25-cm² single cell [90]

Ultimately, the cathodic RH effect on cell performance has been investigated by Kim *et al.* [90], [91]. They measured a degradation rate about 1.9, 1.5 and 0.04 mV $cycle^{-1}$ (@ 1.2 A cm^{-2}) by lowering RH from 100% to 50% and 0%, respectively. From EIS analysis, mass-transport overpotential increases from 1 to 151 and 202 mV and the activation overpotential from 38 to 44 and 51 mV, after ageing tests at RH 0%, 50% and 100%.

II.3.2.4. Accelerating the H_2|Air front propagation

The time exposure of H_2|Air front depends strongly on the anode gas flow rates, *i.e.*, H_2 and Air in SU and SD phase respectively. However, as discussed previously, the partial pressure, the relative humidity and the temperature of this reactant gas also play a role on the flushing velocity. For a sake of clarity, this section focuses on the flow rate impact.

Regarding Figure II-9, the CSC rate follows a logarithmic dependence with the anode gas flow rate. The higher the injection rate, the lower the cathode degradations. This trend is consolidated by a model developed by Maranzana *et al.* [50] which predicted carbon loss as function of H_2 flow rates. A good correlation between simulation and experimental results is observed (see Figure II-15).

Yu *et al.* [92] measured a linear dependence of cell voltage losses with the residence time of H_2|Air (see Figure II-14). After 200 SU/SD cycles (H_2 and Air flushing in anode), decreasing the residence time from 2.6 to 1.3 and 0.26 s reduces the cell voltage decay: 1.2, 0.56 and 0.14 mV.cycle^{-1} (@ 0.2 A.cm^{-2}), respectively. Reiser *et al.* [93] preconized to flush the anode in less than 1.0 s.

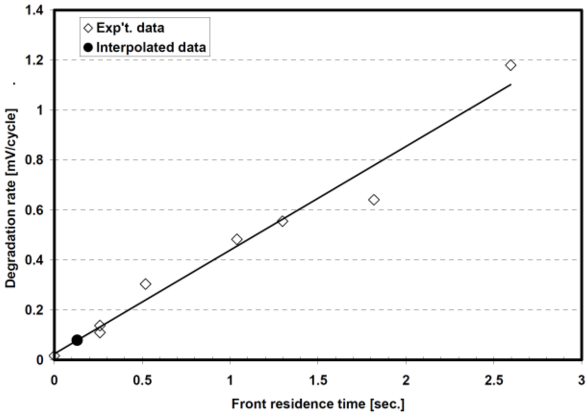

Figure II-14: Performance decay in single cell (@ 0.2 A.cm-^{2}) after ageing test according to the H_2|Air front residence time in 50-cm² single cell [92]

II.3.2.5. Lowering the cathodic potential by dummy load application

Finally, one of the most promising mitigation strategy consists in applying a dummy load in order to derivate a portion of electrical current generated by FC sub-part during H_2|Air front occurrence, as suggested by Reiser in both SU phases [94] and SD phases [95]. Randrianarizafy *et al.* [71] predicted a decrease of local cathodic potential from 1.6 to 1.5 V_{RHE} during SU with a resistor of 2 x 10^{-4} Ω.m^{-2}. As expected, the simulated CO_2 emission according to CSC reactions diminishes by 63% with this external resistor. Brightman *et al.* [88] measured a drop of maximal cathode potential from 1.45 (SU/SD) to 1.35 V (SU) and 1.10 V (SD) by using a resistor of 8.8 Ω.m^{-2}. Maranzana *et al.* [50] simulated a sensitive study of CSC rate according to the resistor value (open circuit/∞, 10 and 1 Ω.m^{-2}). During SU phase, a low resistor value increases the by-passed electrical current and mitigates the degradation mechanism, such CSC reactions as illustrated in Figure II-15. Kim *et al.* [96], [97] evaluated durability by cycling 1200 SU/SD phases with resistor (value not available) and show significant effect on cell performance (+73% saved on cell voltage with *vs.* without resistor at 0.4 A.cm^{-2}).

a)

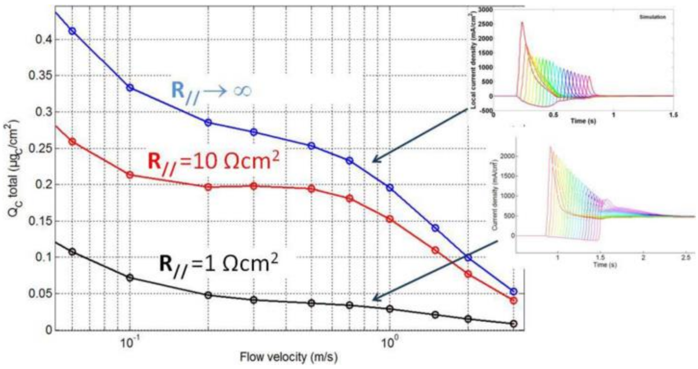

Figure II-15: Prediction of the total CO_2 amount in SU phase according to the H_2 flow rate and the resistor value [50]

b)

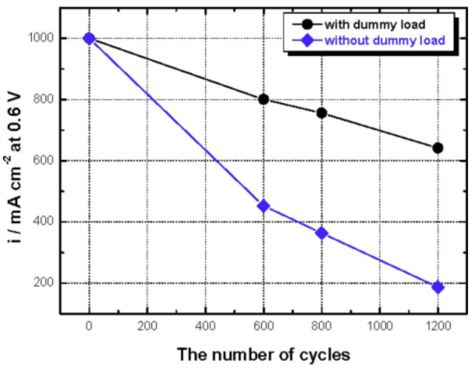

Figure II-16: Single cell performance decay during SU/SD ageing tests without and with dummy load at 0.6 V in 25-cm² single cell [97]

II.3.3. Discussion on the impact of operating conditions

Reverse Current Decay is the most damaging mechanism in the reference SU/SD phases by “Air flushing” in H_2-filled anode side oy by the “H_2 flushing” in Air-filled anode. Several methods have been employed to probe local conditions and to describe the temporal and spatial evolution during the H_2|Air front propagation. These works revealed that degradation is non-uniform along the channel, occurring preferentially at the cathode inlet/anode outlet and the cathode outlet/anode inlet during the SU/SD phase, respectively, in counter-flow configuration. Heterogeneous ageing has also been observed in the rib/channel plane governed by the mass-transport limitation, leading a 10% higher degradation rate under the anodic rib than under the anodic channel. Consequently, mitigation strategies have been investigated to reduce the degradation mechanisms and ultimately the performance decay. Main mitigating parameters reviewed are the partial pressure of reactant gas, the temperature of cell/reactant gas, the relative humidity of reactant gases, the reactant flow rate and the maximum cathode potential. Each parameter impacts the cell performance decay. However, as summarized in Table II-2, the durability tests have been performed with different protocols, operating conditions, and cell technology.

Table II-2: Durability tests using different mitigation strategies during H_2|Air events and their impact on performance decay according to operating conditions

Authors	**SU/SD Strategy**	**Parameters**	**Degradation rate**	**Ref.**
N. Linse *et al.*	SU/SD: H_2 and Air flushing in anode with (3.2 Ω cm^2) in 16-cm^2 single cell	T = 40 / 80 / 95 °C (100% RH) RH = 0 / 40 / 100% (80 °C) Open-circuit @ 80°C – 100% RH	9.8 / 18.2 / 40.2 µV cycle^{-1} @0.94A cm^{-2} 4.0 / 10.8 / 18.2 µV cycle^{-1} 1000 (OCV) µV cycle^{-1}	[98]
J. Kim *et al.*	SU/SD: H_2 and Air flushing in anode (open-circuit) in 25-cm^2 single cell	T = 70 / 50 / 30 °C (100% RH)	NA / ~ 23 / 9 mV cycle^{-1} @1.0 A cm^{-2}	[49]
Y. Y. Jo *et al.*	SU: H_2 flushing in anode (open-circuit) SD: Air consumption (NA dummy load) in 25-cm^2 single cell	T = 80 / 65 / 40 °C	310 / 240 / 130 µV cycle^{-1} @0.4A cm^{-2}	[87]
Mittermeier *et al.*	SU/SD (model): Air and H_2 flushing in anode (open-circuit)	T = 80 / 60 / 40 / 25 / 15 / 5 °C	132 / 71 / 60 / 55 / 36 / 31 µV cycle^{-1} @0.2 A.cm^{-2}	[86]
J.H. Kim *et al.*	SU: H_2 flushing in anode (open-circuit) SD: Air consumption (NA dummy load) in 25-cm^2 single cell	RH = 100 / 50 / 0 %	~ 1.9 / 1.5 / 0.04 mV cycle^{-1} @ 1.0 A.cm^{-2}	[90]
Mittermeier *et al.*	SU/SD (model): Air and H_2 flushing in anode (open-circuit)	RH = 100 / 80 / 66 / 40 / 25 %	~ 2.5 / 2.3 / 1.8 / 0.9 / 0.5 mV cycle^{-1} @ 1.0 A.cm^{-2}	[89]
Yu *et al.*	SU/SD: H_2 and Air flushing in anode (open-circuit) in 50-cm^2 single cell	t_{res} = 2.6 / 1.3 / 0.26 s	~ 1.2 / 0.56 / 0.14 mV cycle^{-1} @ 0.2 A.cm^{-2}	[92]
K. Eom *et al.*	SU: H_2 flushing in anode (open-circuit) SD: Air consumption (NA dummy load) in 25-cm^2 single cell	P_{O2} = 21 / 10 / 1 / 0%	300 / 210 / 33 / 17 µV cycle^{-1} @0.4 A.cm^{-2}	[85]
J.H. Kim *et al.*	SU: H_2 flushing in anode (OCV or dummy load) SD: Air consumption (NA dummy load) in 25-cm^2 single cell	OCV / dummy load	280 / 75 µV cycle^{-1} @0.4 A.cm^{-2}	[97]

Consequently, the quantification and the comparison of their efficiency is very difficult. Furthermore, investigations are still necessary to reach the degradation rate preconized by DoE which is defined at 5 µV.cycle^{-1}. The first way to achieve this objective could consist in coupling every mitigation strategy. However, this solution would be complex to implement into a real system.

The second way would involve other processes in which the PEMFC stack is preserved from the H_2|Air front formation at the anode, especially in SD phases. For that, alternatives SD processes have been designed and investigated by reactant gas consumption, as introduced in section II.2.1. A review of these alternative SD processes to avoid H_2|Air front formation at the anode is proposed thereafter.

II.4. ALTERNATIVE SHUT-DOWN PROCESS

Due to the difficulty to mitigate the degradations in RCD occurrence, alternative SD processes have been designed in order to prevent the formation of the H_2|Air front during SD, as reviewed thereafter. The first section II.4.1 presents the works on the "H_2 consumption" shut-down processes, as well as their impact on cell performance. The same analysis is provided in the section II.4.2 concerning the "O_2 consumption" shut-down process. Finally, a comparison is proposed in order to identify the most promising SD process and the possible improvements.

II.4.1. Anodic H_2 consumption process

The first way to avoid the H_2|Air front formation at the anode side is to consume the residual H_2 gas by pursuing the electrochemical reactions without any fuel supply. Commonly, a dummy load is applied to discharge the stack until the complete dispelling of H_2 which accelerates the SD process and avoids the OCV mode as well as corresponding degradation mechanisms described in section (I.3.2.2). A simplified representation of this SD process is schematized in Figure II-17. The dummy load is connected to the terminal plates of the stack forcing the passage of an electrical current and consuming the residual H_2. Simultaneously, a pressure and concentration gradient between the anode and the cathode leads to the diffusion of Air across the membrane. Moreover, Air may infiltrate anode by the open-ended exhaust pipe. At macroscale, cell voltage decreases progressively from 0.6 – 0.8 V down to 0.0 V in final Air/Air fluidic configuration. The transient state duration depends mainly on the dummy load value and the volume of fuel gas to be consumed. There are variants in which the Air supply can be maintained or shut off, and the fuel exhaust can be opened or close-ended. This section attempts to review and compare the research work on this process and these different variants.

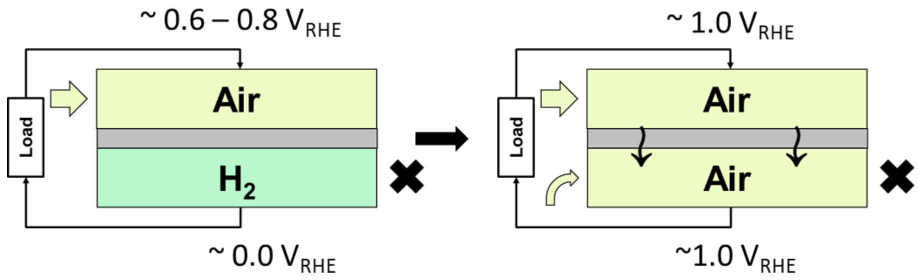

Figure II-17: Schematic representation of an example of H_2 consumption process configuration (with dummy load, Air supply and fuel exhaust open-ended)

Yang *et al.* [98] evaluated the durability of a 5-cell stack of 50 cm² by repeating SD process without (open-circuit) and with dummy load (set at 2.5 A). Consequently, a low flow of Air is injected at the cathode inlet and the anode outlet to simulate a long shut-down and Air infiltration. The individual cell voltages drop to 0.0 V according to the consumption of residual H_2 in the anode side, as plotted in Figure II-18. This descent is 6-fold faster (from 60 to 10 s) and more uniform with dummy load than in open-circuit. After ageing test, stack performance decay is 1.822 and 0.119 mV.cycle^{-1} (@ 0.4 A.cm^{-2}) in unprotected (open-circuit) and protected (2.5 A) SD phase, respectively. Segmented cell technology was used during transient SD phase and highlighted negative current density at the outlet region of anode (in co-flow configuration). They concluded that H_2|Air front occurs (probably due to the Air injection by anode outlet) also in the SD process but its exposure time is reduced by applying the dummy load, and ultimately, slowing down the degradation rate. The non-uniformity of the cell voltage drops in open circuit is not explained.

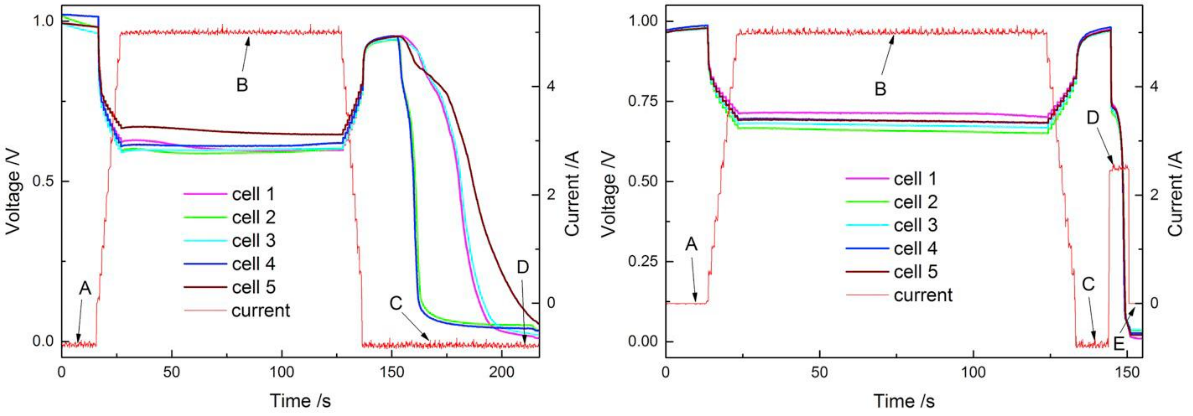

Figure II-18: Evolution of individual cell voltages in a 5-cell stack (50 cm²) during SD phase by H_2 consumption (left) in open circuit and (right) with external dummy load in 5-cell stack of 50 cm² [98]

To avoid the RCD occurrence in this previous SD process, Lin *et al.* [99] investigated and compared on 5-cell stack (50 cm²) with segmented cell technology the following optimized strategies:

- The unprotected SD process (open-circuit) identical to previous one designed by Yang *et al.* [98] (Figure II-18);
- The protected SD phase with an innovative 2-phase dummy load (explained hereafter) to consume residual H_2 with low Air injection by anode outlet;
- A combination of both (2-phase dummy load + high Air injection in anode to mimic long stop).

The 2-phase dummy load consists in imposing an electrical current set at 5 A followed by a progressive decrease to 0 A. Low Air is injected at both anode and cathode sides, mimicking long stop. For unprotected SD, significant performance decay was measured (1.697 $mV.cycle^{-1}$ @ 0.8 $A.cm^{-2}$) similarly to previous results [98]. The first protected SD with 2-phase dummy load reduced the performance decay to 0.764 $mV.cycle^{-1}$ but a local high current density is measured. Authors talk about the vacuum effect which causes degradation preferentially near the anode and cathode inlet (in co-flow configuration). In fact, H_2 in channels is rapidly consumed and induced a high drop of local pressure. Residual H_2 from inlet pipe is pumped into the channel and further generate $H_2|Air$ front. The Air in anode originates either from the Air injection rate at the outlet anode or from the diffusion across the membrane. To get more insights, Air purge is added in SD phase combined with 2-phase dummy load. The performance decay decreases to 0.108 $mV.cycle^{-1}$. They conclude that the Air purge in anode promotes a quicker consumption of residual fuel and prevents the vacuum effect.

Another way to prevent vacuum effect consists of consuming H_2 keeping anode gas recirculation and venting procedure to avoid high-pressure difference between the anode and cathode sides. Bona *et al.* [100] experimented it with a dummy load (0.1 $\Omega.m^{-2}$) connected to the terminal plates of a 24-cell PEMFC stack. H_2 and Air supplies are cut off with open-ended exhaust gas. The average performance decay is estimated at 45 $\mu V.cycle^{-1}$ (@ 0.9 $A.cm^{-2}$). In comparison, they proceeded also unprotected SU/SD cycling with identical methods without dummy load. The stop period lasts 6 minutes during which ambient Air infiltrates the H_2-filled anode by diffusion and leads to the $H_2|Air$ formation. The average performance decay is estimated to 72 $\mu V.cycle^{-1}$ (@ 0.9 $A.cm^{-2}$). In both cases, significant degradation was observed on one specific cell of the stack with a considerable drop of the performance decay at 205 and 130 $\mu V.cycle^{-1}$ (@ 0.9 $A.cm^{-2}$), during the unprotected and protected SD phases respectively. Authors suggest that partial flooding on the anode side could promote the $H_2|Air$ formation.

In summary, H_2 consumption process is originally designed to attenuate the occurrence of RCD when Air is flushed in H_2-filled anode. However, several SD configurations have been tested and authors agree that H_2 consumption process can also lead to the local H_2|Air coexistence in the anode due to Air infiltration. Mitigation ways are proposed, such as applying an adaptive dummy load in order to accompany the H_2 consumption. The most promising strategy seems to use either a variable dummy load profile with the H_2 consumption as designed by Lin *et al.* [99], or more simply, a resistive load as Bona *et al.* [100]. In fact, the current induced by the resistor is linked to the cell voltage. When the H_2 concentration tends to zero, the cell voltage decreases to 0.0 V and no more current flows through the stack. Another mitigation way is to close the exhaust valve at the anode limiting the Air penetration. However, H_2|Air coexistence is still possible due to Air diffusion across the membrane, but with a minor rate. The anodic recirculation tested by Bona *et al.* [100] seems also efficient to eliminate the formation of H_2|Air front. The last mitigation method is related to the operating conditions, similarly as the mitigation strategy in "Air flushing" process, by lowering the cell temperature and the RH of reactant gases before the SD process. Ultimately, degradation rates in literature is estimated between 45 and 341 $\mu V.cycle^{-1}$ according to the SD protocol. Developments on mitigation strategies during the SD process by H_2 consumption are still necessary. Alternatively, SD protocols have been also designed by consuming residual O_2 to prevent the H_2|Air front in the anode.

II.4.2. Cathodic Air consumption process

The consumption of the residual O_2 gas proceeds by pursuing the electrochemical reactions without any oxidant supply. A dummy load is also applied to reduce the SD duration and to avoid the OCV mode. A simplified representation of this SD process is schematized in Figure II-19 where Air inlet/outlet are closed while maintaining H_2 feeding. The cathodic potential drops from 0.7 – 0.8 V_{RHE} (with dummy load) to 0.0 V_{RHE} once O_2 is consumed and replaced by H_2. In fact, H_2 is forced to diffuse through the membrane (from anode to cathode) and, inversely, the residual N_2 diffuses from cathode to anode due to concentration gradients. This protocol results into a mixture gas (H_2 + N_2) in both compartments. The SD duration depends strongly on the dummy load and the cathode volume. Variants exist in which H_2 supply is shut off. This section attempts to review and compare the research work on this process and different variants.

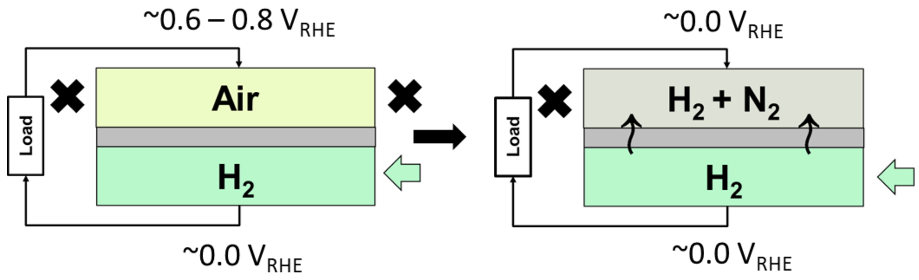

Figure II-19: Schematic representation of an example of O_2 consumption process configuration (with dummy load, H_2 supply and fuel exhaust open-ended)

Yu *et al.* [101] studied the current density distribution during the SD phase by O_2 consumption with different dummy loads (adapted to get a constant voltage at 0.83, 0.80, 0.76 and 0.73 V along the SD) on a single cell (184 cm²). Both anode and cathode exhausts are close-ended. Consequently, residual H_2 and O_2 are simultaneously consumed until the dispelling of O_2 is complete. In fact, the amount of fuel stored in the anode is greater than the quantity needed to consume all the oxygen stored in the cathode. In this case, the mixture H_2 + N_2 is reached in both anode and cathode sides. The Figure II-20 shows the load response in terms of current density. It is slightly higher near the cathode outlet than near the cathode inlet, but it is rather uniform along the cell length (not presented). The decline of current density is accelerated with higher dummy load (about 90 s and 10 s at 0.83 V and 0.73 V, respectively). However, the lower the holding voltage, more significant the fluctuation for the current distribution.

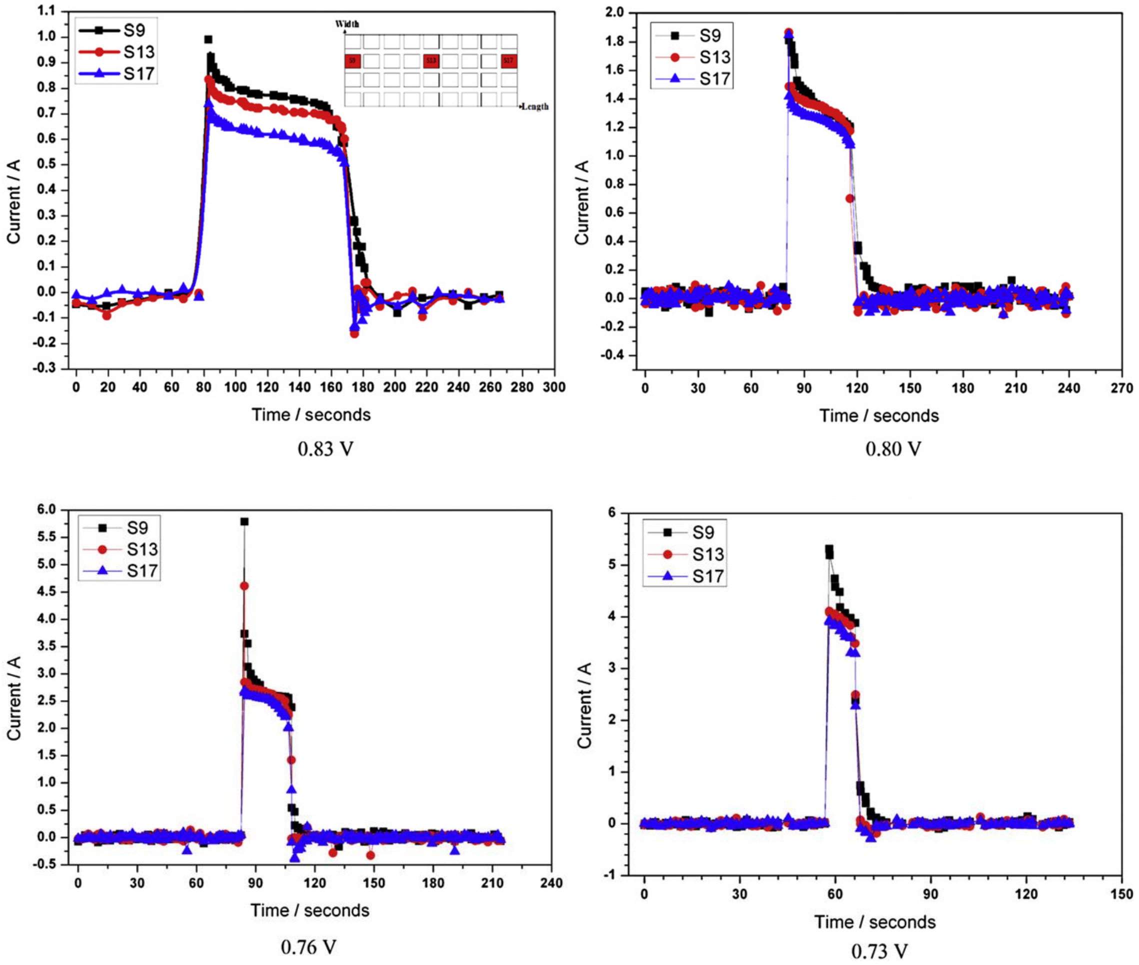

0.83 V

0.80 V

0.76 V

0.73 V

Figure II-20: Response of local current density at the inlet/middle/outlet of the cathode during SD phase by O_2 consumption process with different dummy loads corresponding to (a) 0.83 V, (b) 0.80 V, (c) 0.76 V and (d) 0.73 V in 155-cm² segmented cell [101]

Zhang *et al.* [102] attributes this heterogeneity to the Air starvation. In their durability test, O_2 consumption in SD phase with a constant (20 A) and a 2-phase dummy load have been performed on a 250-cm² single cell. The Air exhaust is close-ended while H_2 supply is maintained. The 2-phase dummy load is set to 45 A followed by a gradual decreasing to 2.5 A with a sweep rate at 3 $A.s^{-1}$. The current density distribution along both SD processes is displayed in Figure II-21. In constant dummy load case, heterogeneity is measured with a high current density near the Air outlet, related to the local Air starvation. It is attributed to a non-uniform O_2 concentration before the SD phase. That is why the two-phase dummy load has been designed in order to accompany the O_2 depletion. After this ageing test (1800 cycles), the performance decay with two-phase dummy load is measured at 3.33 $\mu V.cycle^{-1}$. Additionally, authors experimented a similar SD process with open-ended Air exhaust and showed sudden overshoot of the cell voltage. They attributed it to the pumping of the Air in the exhaust pipe, making heterogeneous the current distribution.

Constant dummy load Two-phase dummy load

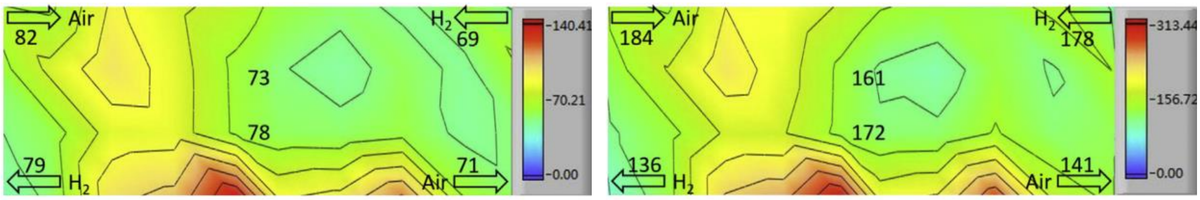

(a) 1s of SD (20A) (a) 1s of SD (45A)

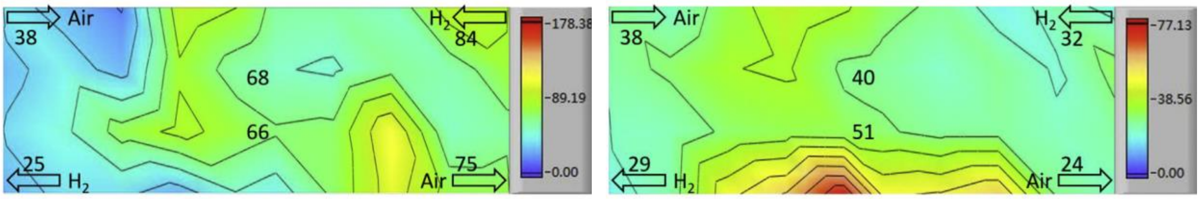

(b) 4s of SD (20A) (b) 12s of SD (9A)

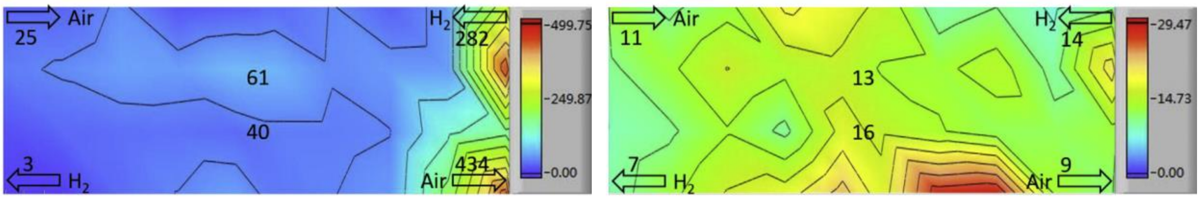

(c) 8s of SD (20A) (c) 14s of SD (3A)

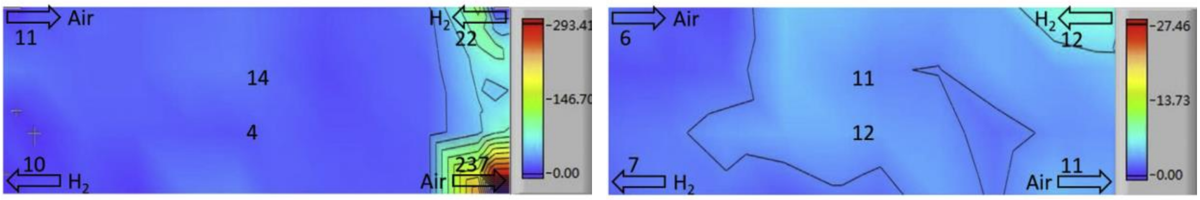

(d) 10s of SD (20A) (d) 18s of SD (2.5A)

Figure II-21: Current density distribution during the SD process with constant and 2-phase dummy load in 250-cm² segmented cell [102]

To prevent the Air starvation, Lin *et al.* [103] investigated the impact of the constant load (5 A) and the step load (5 A followed by 2.5 A) on durability. Both gas supplies are shut off during the SD process consuming simultaneously H_2 and O_2. The duration of SD process is longer in the 2-step load strategy than in the constant case (10 s *vs.* 6 s, respectively). Regarding the current density distribution, negative current density appears near the cathode outlet (-147 mA.cm^{-2}). The shut-off of both reactant gases implies a consumption of H_2 and Air, simultaneously. As discussed in previous section II.4.1, H_2 consumption can causes local starvation event and forces the diffusion of O_2 towards the anode (due to concentration gradient), resulting to a H_2|Air front. Furthermore, the open-ended exhaust allows the Air from the outlet pipe to infiltrate the cathode, maintaining the cathode pressure and increase the pressure difference between the anode and cathode. Thus, the H_2|Air formation is exacerbated. They concluded that RCD mechanism occurs when the load is too high. To solve it, the step load is designed and tested. Current density is more uniform when the current density decreases from 5.0 to 2.5 A. However, negative current density and RCD mechanism persists near the cathode outlet (-46 mA.cm^{-2}). Ultimately, the performance decay is mitigated with the 2-step load compared to the constant load (-0.027 and -0.136 mA.cm^{-2} @ 0.6 V) after 900 SU/SD cycles.

II.4.3. Discussion about alternative SD protocols

In summary and in order to prevent RCD mechanism during SU, O_2 consumption is a more promising process than H_2 consumption. However, precautions must be taken into account. The Air exhaust must be close-ended to block the Air pumping to avoid the local Air supply with high local current density near to the cathode outlet and the H_2|Air coexistence in the anode after the O_2 diffusion through the membrane. Yu *et al.* [104] compared open and close-ended cathode during O_2 consumption, maintaining the H_2 supply: the single cell (25 cm²) suffers much less during the 1500 SU/SD cycles in close-ended than in open-ended case (93 *vs.* 24 µV.cycle^{-1}, respectively). However, even with close-ended exhaust, local Air starvation can occur if the dummy load does not accompany the O_2 depletion. Consequently, variable load has been designed and tested.

A second method consists of using resistive load, as proposed in H_2 consumption. The current is correlated with the cathode potential related to the O_2 concentration. On the whole, the range of the performance decay with O_2 consumption is between 3.3 and 100 µV.cycle^{-1}, according to the literature. These values are much lower than in the H_2 consumption case (between 45 and 341 µV.cycle^{-1}). However, the principal reason accounting for this significant reduction of performance decay is linked to the following soft SU phase when H_2 and Air are resupplied in the fuel cell in H_2/H_2 configuration. In presence of hydrogen in both sides, the reductant atmosphere prevents high potential elevations and oxidative reactions. No degradation is supposed to occur in this phase. No paper in the literature deals with the detailed impact of the H_2|Air front in the cathode side when Air is supplied in H_2-filled cathode.

Oyarce *et al.* [105] experimented, in 7-cm² single cell, several SD process, followed systematically by an Air/Air purge in both sides to mimic long stop before a start-up phase by H_2/Air supply in FC in Air/Air fluidic configuration. The applied SD processes are:

- The "no purge" SD in open-circuit (without dummy load). Both H_2 and Air supplies are shut off and the exhausts are open-ended. Air infiltrates into the anode side by diffusion from exhaust pipe or across the membrane during about 820 s. After 230 SU/SD cycles, the performance decay is measured at 1,739 µV.cycle^{-1} (@ 0.86 A.cm^{-2}).

- The “Air flushing” SD in open-circuit. Anode is rapidly flushed by Air within a few seconds while Air supply in cathode is maintained. After 1100 cycles, the cell voltage decreases by 183 $\mu V.cycle^{-1}$ (@ 0.86 $A.cm^{-2}$).
- The “H_2 consumption” SD. A H_2 recirculation is operated with step load (20, 15, 10, 5 and 1 $mA.cm^{-2}$) while the cathode is continuously supply with Air. The duration of this SD process is 35 s. After 1100 cycles, the degradation rate is measured at 229 $\mu V.cycle^{-1}$ (@ 0.86 $A.cm^{-2}$). Authors supposed that sufficient O_2 crossover through the membrane may cause local H_2|Air front, and thus, degrade CCL with similar rate than the “Air flushing” process.
- The “O_2 consumption” SD with dummy load. The Air supply is shut off and exhaust gas is close-ended while H_2 supply is maintained until the cell voltage drops to 0 V. A constant load at 50 mA (7 $mA.cm^{-2}$) is applied inducing a duration about 100 s. In their protocol, the performance decay is strongly mitigated (23 $\mu V.cycle^{-1}$ @ 0.86 $A.cm^{-2}$). Coupling the Air exhaust close-ended and the low dummy load allows to prevent both Air infiltration in anode side and Air starvation.
- The “H_2 flushing” in cathode side in open circuit. After the Air supply is shut off, H_2 is injected rapidly in the cathode to evacuate residual O_2 within a few second while the anode H_2 supply is maintained. Then, both H_2 supplies are shut off in both anode and cathode sides. Finally, this strategy shows the lowest cell voltage drop about 21 $\mu V.cycle^{-1}$ (@ 0.86 $A.cm^{-2}$). The H_2|Air front is cathode side is supposed quite harmless.

Shut-down process resulting in Air/Air configuration either by “Air flushing” or “H_2 consumption” are subjected to strongly degrade the CCL because of the coexistence H_2 and Air in the anode and the RCD occurrence. On the contrary, “H_2 flushing” in cathode and “O_2 consumption” are less severe despite the coexistence of H_2 and Air in cathode due to the reductant atmosphere in anode side. The high potential elevation is therefore impossible and prevent undesired oxidation reactions. Numerous patents have been deposited concerning the O_2 consumption, as well as the method to maintain the H_2/H_2 fluidic configuration during long stops, as referred in Table II-4.

Table II-3: Durability tests using different SD protocols and their impact on performance decay

Authors	**Strategy**	**Number of cycles**	**Degradation rate**	**Ref.**
Bona *et al.*	1) SD: Air diffusion + SU: H_2 / Air reinjection (open-circuit) 2) SD: H_2 consumption + SU: H_2 / Air reinjection (w/ dummy load) in 24-cell stack of 200 cm^2	350	1) 72 µV cycle^{-1} @ 0.9 A cm^{-2} 2) 45 µV cycle^{-1} @ 0.9 A cm^{-2}	[100]
Lin *et al.*	SD: H_2 consumption (w/ dummy load) in 50-cm^2 segmented cell	900	1) 0.136 mA cm^{-2} cycle^{-1} @ 0.6 V 2) 0.027 mA cm^{-2} cycle^{-1} @ 0.6 V	[103]
Yang *et al.*	SD: H_2 consumption (open circuit vs dummy load) in 5-cell stack of 50 cm^2	1) 250 2) 1,000	1) 1.822 mV cycle^{-1} @ 0.4 A cm^{-2} 2) 0.119 mV cycle^{-1} @ 0.4 A cm^{-2}	[98]
Lin *et al.*	1) SD: low Air flushing 2) SD: H_2 consumption (w/ dummy load) 3) SD: H_2 consumption (w/ dummy load) in anode in 5-cell stack of 50 cm^2	1) 300 2) 900 3) 1,500	1) 1.697 mV cycle^{-1} @ 0.8 A cm^{-2} 2) 0.764 mV cycle^{-1} @ 0.8 A cm^{-2} 3) 0.106 mV cycle^{-1} @ 0.8 A cm^{-2}	[99]
H-J Kim *et al.*	1) SD: H_2 consumption (without and with dummy load) 2) SD: O_2 consumption (without and with dummy load) In 25-cm^2 single cell	200	1) 2.1 / 0.25 mV cycle^{-1} @ 0.4 A cm^{-2} 2) < 0.1 / 0.1 mV cycle^{-1} @ 0.4 A cm^{-2}	[106]
Y. Yu *et al.*	1) SD: O_2 consumption (w/ dummy load) 2) SD: H_2 consumption (w/ dummy load) In 25-cm^2 single cell	1,500	1) 45 µV cycle^{-2} @ 1.0 A cm^{-2} 2) 24 µV cycle^{-2} @ 1.0 A cm^{-2}	[107]
Zhang *et al.*	SD: O_2 consumption (w/ dummy load) in 250-cm^2 segmented cell	900	1) N/A 2) 3.33 µV cycle^{-1} @ 0.8A cm^{-2}	[102]
Y. Yu *et al.*	SD: O_2 consumption (w/ dummy load) in 25-cm^2 single cell	1,500	1) 93 µV cycle^{-1} @ 0.9 A cm^{-2} 2) 24 µV cycle^{-1} @ 0.9 A cm^{-2}	[104]
J.H. Kim *et al.*	SD: Air consumption + Air/Air purging (w/ dummy load) SU: H_2/Air resupplying 1) open-circuit and 2) dummy load In 25-cm^2 single cell	1,200	280 / 75 µV cycle^{-1} @ 0.4 A cm^{-2}	[97]
Jo *et al.*	SD: Air consumption + Air/Air purging (dummy load) SU: sequential H_2 and Air flushing (open-circuit) In 25-cm^2 single cell	1,200	1) 0.68 mA cm^{-2} cycle $^{-1}$ @ 0.6 V 2) 0.47 mA cm^{-2} cycle $^{-1}$ @ 0.6 V	[108]
Oyarce *et al.*	1) SD: Turn off H_2 / Air supplying (open anode exhaust) 2) SD: Air flushing in anode 3) SD: H_2 consumption (w/ dummy load) 4) SD: O_2 consumption (w/ dummy load) 5) SD: H_2 flushing in cathode in 7-cm^2 single cell	230 (1) 1,100	1) 1739 µV cycle^{-1} @ 0.86 A cm^{-2} 2) 183 µV cycle^{-1} @ 0.86 A cm^{-2} 3) 229 µV cycle^{-1} @ 0.86 A cm^{-2} 4) 49 µV cycle^{-1} @ 0.86 A cm^{-2} 5) 21 µV cycle^{-1} @ 0.86 A cm^{-2}	[105]

Table II-4: Overview of patented methods in start-up and shut-down phases

Inventors	Pub. Date	Strategy	Main claims / Patented procedure	Ref.
Reiser *et al.*	2002	SU: H_2 reintroduction in anode	Rapid hydrogen purge displacing Air in less than 1.0 second	[93]
Reiser *et al.*	2003	SD: Air flushing in anode with dummy load	Connection the dummy load device across the cell during Air purge in anode to reduce cathode potential	[94]
Reiser *et al.*	2005	SU: H_2 reintroduction in anode with dummy load	Connection of auxiliary load across the cell then hydrogen reintroduction in anode. Auxiliary load disconnection after filling the anode with H_2 then Air supply in cathode	[95]
Goebel *et al.*	2005	SD: Oxygen consumption with anode inerting	Oxygen residual consumption in cathode with recirculation loop then redirection of nitrogen gas in anode	[109]
Yu et Wagner	2006	SD: H_2 flushing in cathode	Hydrogen introduction in cathode side then Air introduction in both anode / cathode sides	[110]
Paik *et al.*	2009	SD: Inerting of anode and cathode with N_2 gas	Using a separator at the cathode outlet removing oxygen and re-injecting nitrogen-rich gas in both anode / cathode sides	[111]
Goebel *et al.* (GM)	2013	Prolonged SD: Prevent Air from entering the stack	Periodic hydrogen injection in anode side for a predetermined time of prolonged stop	[112]
Hochgraf *et al.*	2010	SU: H_2 reintroduction in anode with dummy load	Connection of a shorting line across the stack in close position during H_2 /Air supply	[113]
Usborne *et al.*	2008	SU-SD: H_2 and Air flushing in anode respectively with dummy load	Control a load on the fuel cell to regulate voltage	[114]
Yang *et al.*	2018	SD: H_2 consumption with a first dummy load SU: H_2 reinjection with a second dummy load	Shunt connection on the fuel cell with a first load in shut-down procedure and a second load in start-up procedure	[115]
Bekkedahl *et al.*	2005	SU-SD: H_2 and Air flushing in anode respectively with "short circuit" device	Discrete shunt with spring braking device across each individual cell of stack	[116]

Shimoi *et al.*	2006	SU-SD: H_2 and Air flushing in anode respectively with dummy load	Discharging resistor connection across each individual cell of the stack	[117]
Miller *et al.*	2008	SU-SD: H_2 and Air flushing in anode respectively with "short circuit" device	Connection of an electrical conductive body between anode / cathode plates of each individual cell of the stack	[118]
Paganelli *et al.*	2009	SD: O_2 consumption with dummy load and H_2 buffer tank	Consumption of residual oxygen by load application with periodic Air injection to increase nitrogen concentration. H_2 buffer tank using to maintain sufficient H_2 concentration in stack	[119]
Balliet *et al.*	2004	SD: O_2 consumption with dummy load and H_2 injection during stop phase	Oxygen residual consumption with load application then connection of a power supply to balance H_2 concentration in both anode and cathode side. H_2 injection during stop period to maintain the desired gas composition.	[120]
McElroy *et al.*	2007	SD: O_2 consumption with dummy load SU: Electrochemical pump operation then H_2 / Air resupplying	Configuration of fuel cell in electrochemical pump at the beginning of start-up phase to transfer protons from cathode to anode before reactant supply	[121]
Yu *et al.*	2008	SD: O_2 consumption with dummy load	O_2 consumption maintaining positive H_2 over pressure in anode. Close inlet and outlet valves of both anode and cathode sides.	[122]
Ojima *et al.*	2016	SD: O_2 consumption with dummy load and monitoring of the voltage, the current and the power to detect malfunction	Controlling the fuel cell to stop O_2 consumption process in case of malfunction	[123]
Condit *et al.*	2002	SD: O_2 consumption with dummy load then H_2 injection during stop phase	Equilibrium of H_2 concentration between 0.0001% and 10% within fuel cell after shut-down phases with injection H_2 or Air during prolonged stop	[124]
Arthur *et al.*	2009	Prolonged stop: H_2/H_2 holding by H_2 injection in stop phase	Periodic H_2 injection up to a predetermined duration of stop phase. Beyond, the process is disabled.	[125]
Margiott *et al.*	2007	Prolonged stop: H_2/H_2 holding thanks to a H_2 tank	Hydrogen stored within tank is released within fuel cell during stop phase	[126]

II.5. CONCLUSION

In this chapter, the quantification and comparison of several start-up and shut-down processes are reviewed in order to highlight the most promising strategies and opportunities for technical improvement, to be integrated into PEMFC system. The performance decay of principal SD strategies reported in the literature is illustrated in the Figure II-22.

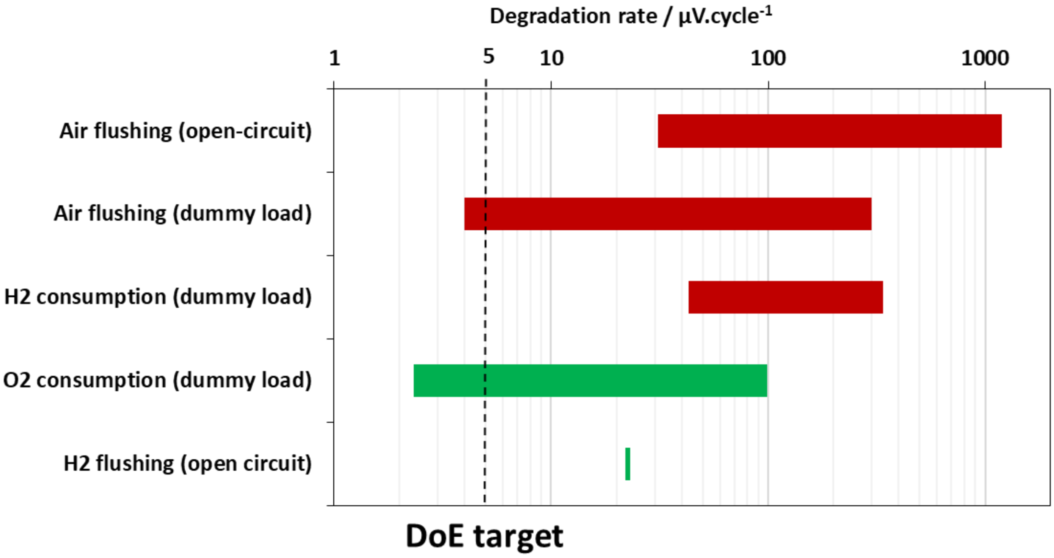

Figure II-22: Range of performance degradation according to the different shut-down phases reported in the literature

First of all, the unprotected SU/SD phase, used as reference in this work, is subjected to the H_2|Air front propagation along the anode channel during both SU and SD phase, leading to RCD degradations. Numerous studies have been conducted to better understand the RCD degradation mechanisms and their impact on cell performance. Models and segmented-cell technologies have been designed to locally probe the conditions and have highlighted a high potential elevation up to 1.4 – 1.6 V. Thus, frequent unprotected SU/SD phases may induce a drop of cell voltage between 100 and 1,000 $\mu V.cycle^{-1}$. To reduce the impact of RCD mechanism on cell performance, mitigation strategies have been investigated. The main mitigating parameters at system-scale are the partial pressure of reactant gases, the cell temperature, the relative humidity of reactant gases, the exposure time of the H_2|Air front and the cathode potential. The comparative effectiveness of such mitigations are still unclear and advanced developments are still necessary. However, coupling between every mitigating parameter would be too complex to be implemented into a real system. The best methodology would be to prevent H_2|Air front, which is responsible for the severe degradations of the cathode catalyst.

The “H_2 consumption” during SD process has been designed and tested in several configurations as reported in section II.4.1. However, these studies revealed that fuel cell could also suffer from local H_2|Air front due to partial fuel starvation. A significant concentration gradient forces the Air diffusion to the anode, across the membrane or pumped from the exhaust pipe. The main precaution to mitigate the degradations are the closure of the fuel exhaust pipe, the optimization of the dummy load accompanying the H_2 depletion and the anode gas recirculation. Despite these developments, the performance decay with this shut-down strategy is still too high: between 50 and 300 µV.cycle^{-1}. Similar shut-down strategies have been investigated by consuming the residual O_2 in the cathode side as reported in section II.4.2.

The “O_2 consumption” is much less degrading than “H_2 consumption”. H_2 diffuses across the membrane due to the high concentration gradient when the O_2 depleted. In this case, the local H_2|Air front in the cathode does not damage the fuel cell because the reductant atmosphere in both sides avoids the high potential elevation and undesired oxidation reactions. At least, this is true only if the Air exhaust is close-ended, limiting the Air infiltration and its diffusion across the membrane. Moreover, optimized dummy load is also required in order to avoid severe Air starvation and heterogeneity of current density distribution during the consumption phase. The performance decay is measured between 3.33 and 100 µV.cycle^{-1}. Finally, “H_2 flushing” in the cathode is also prone to H_2|Air front in the cathode with H_2 in the anode site. This strategy has been tested once by Oyarce *et al.* [105] and it has suitable performance decay estimated at 22 µV.cycle^{-1}. However, in their work, an Air/Air purge mimicking the long stop is performed, followed by the start-up phase in Air/Air initial fluidic configuration (causing H_2|Air front at the anode).

Regarding the literature, to shut-down properly the fuel cell stack, it would be recommended to proceed by “O_2 consumption” or “H_2 flushing” in the cathode side. Subsequently, a restart after a short stop with a FC in H_2/H_2 fluidic conditions should not affect the fuel cell thanks to the reductant gas in both sides in spite of the Air|H_2 front in the cathode side. However, after a certain duration the residual H_2 is totally consumed with the O_2 from ambient Air. A long stop resulting in Air/Air conditions for the next SU will cause severe degradation during the start-up related to the RCD mechanism. No research work has been conducted during this stop phase, and it is difficult to estimate the necessary duration to reach the equilibrium with ambient Air.

Consequently, the start-up phase under initial Air/Air fluidic configuration is unavoidable in the life of a fuel cell. However, the quantification of SU and SD strategies and the impacts of operating conditions (partial pressure of reactant gas, cell temperature, relative humidly of reactant gas, exposure time of the H_2|Air front have demonstrated) are still unclear. This is mainly due to the fact that the outcomes from literature are specific to each experiment, where experimental set-up, protocols, cell technology are too heterogeneous and too dispersed. A deeper understanding on the degradation mechanisms and the cell performance impact with mitigation strategies is the topic of this thesis work. In the chapter IV, an accelerated stress test emulating the RCD mechanism during the SU phase has been designed and tested on single cell (98 cm²) to deepen the degradation mechanisms and their impact on cell performance, coupling various *in-situ* and *post-mortem* characterization techniques. Moreover, a sensitive study has been performed on key mitigating parameters. These experimental methods are presented in the Chapter III.

Chapter III. EXPERIMENTAL PROTOCOLS FOR PEMFC TESTING AND *POST-MORTEM* ANALYSIS

III.1. INTRODUCTION

In this third chapter, the experimental methods performed during this thesis work are presented in detail. First of all, the description of the fuel cell technology, the components and their assembly process are given.

Then, the characterization techniques used for the performance monitoring and for the ageing tests on lab test bench are specified according to both single cell and short-stack configurations. Local current density mapping measurements via a CDDM device ($S^{++®}$) is presented as well as the corresponding data processing. The specific ageing tests protocols, also called Accelerated Stress Test (AST), designed, and tested in this thesis work are also described.

Finally, the methodology used on aged MEA samples for *post-mortem* study is presented. It is based on the local analysis of electro-chemical and physico-chemical properties to unravel and quantify local degradations after the different AST performed in this work.

III.2. PEMFC ASSEMBLY AND CHARACTERIZATION TECHNIQUES

III.2.1. Fuel Cell Technology

All the experiments mentioned in this PhD work were achieved with a real PEMFC technology using end plates and bipolar plates designed by CEA, also named “X-design”. Its active surface area is about 98 cm^2 with parallel and wavy rib/channel flow-field. The details of the flow-field dimensions are given in the Table III-1. This technology is suitable up to 5 kW stack for transportation and/or stationary applications (*ca*. 70 cells for full-size stack).

Table III-1: Dimension of the anodic end cathodic flow-field

	Number of channels	Channel width / mm	Rib width / mm	Channel volume / mm^3
Anode	26	0.31	1.57	23.5
Cathode	52	0.37	0.22	25.9

Commercial 7-layer MEA is used [127]. Pt loadings are 0.1 and 0.4 mg_{Pt} cm^{-2}, at the anode and cathode sides, respectively. Standard SIGRACET® 28BC is used as GDL [128]. No additional specifications have been provided due to confidentiality purposes. In this study, we are using this X-design in either a single cell or short-stack configurations (6 cells). The Figure III-1 illustrates the bipolar plates with commercial MEA. They are then inserted between two endplates which connects the fuel cell with the test bench for electrical and fluidic (H_2, Air and water) circuits (Figure III-2).

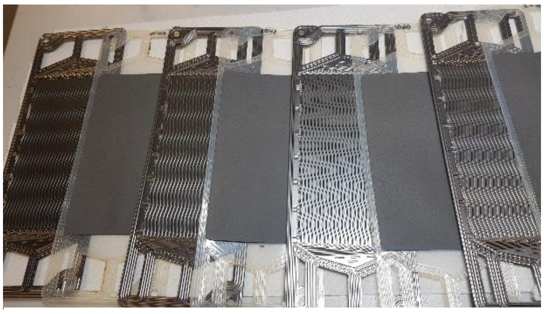

Figure III-1: Bipolar plates and commercial MEA (X-design)

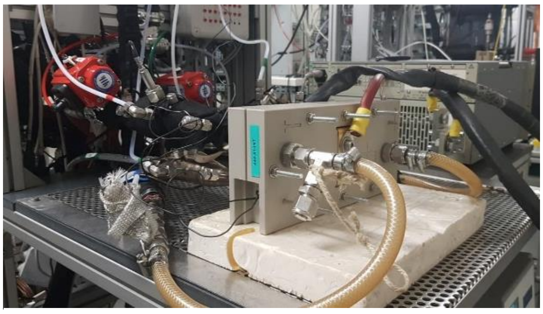

Figure III-2: Assembled fuel cell on lab test bench

The single cell/short-stack assembly process starts with the deposition of an adhesive gasket on the MEA outer reinforcement and on the end-plates in order to ensure the tightness of the 3 fluidic circuits (hydrogen, Air and coolant). Then, each fuel cell component (MEA + mono/bipolar plates + 2 end plates) are mounted to form a single cell or a short-stack compressed at 1.2 MPa (*i.e.,* 12 kN). Internal and external leakage tests are systematically performed under nitrogen for each compartment by monitoring the pressure drop over time. After this tightness validation, the fuel cell can be installed and tested on the lab test bench (see Figure III-2). Note that the cell position in stack (from cell 1 “#1” to cell 6 “#6”) is determined from the anodic endplate, the one with both reactant gas inlet/outlet pipe.

III.2.2. Description of lab test bench

A CEA-homemade test bench has been used to study PEMFC with an electrical power less than or equal to 500 W. The operating parameters of the fuel cell are supervised by a programmable controller (Rockwell, USA) connected to RSview software. Among these parameters, cell temperature is governed by a chiller system (Julabo FPW 55, Germany). Reactant gas are pre-heated (above cell temperature) along fuel cell inlet pipes to avoid any condensation of steam. Moreover, bubbler systems set the reactant gas dew point provide humidity in gases. All temperatures are measured by thermocouples. Then, gas pressures are regulated. Finally, an electronic load (H&H, Germany) is used for the electrical power and dissipation. The operational range of the test bench is summarized in Table III-2.

Table III-2: Operating range of the test bench

Anodic circuit

Pressure	1 – 4 bar$_{abs}$
H_2 Flow rate	9 – 850 nL.h^{-1}
N_2 Flow rate	20 – 2,500 nL.h^{-1}
Humidity	Bubbler system

Cooling circuit

Pressure	1 – 4 bar$_{abs}$
H_2O Flow rate	0 – 1500 nL.h^{-1}
Power	5,200 W at 20 °C
Temperature	-10 °C to 90 °C

Cathodic circuit

Pressure	1 – 4 abar$_{abs}$
O_2 Flow rate	7 – 650 nL.h^{-1}
N_2 Flow rate	31 – 3,100 nL.h^{-1}
Air Flow rate	31 – 3,100 nL.h^{-1}
Humidity	Bubbler system

Electric circuit

Power	0 – 2,000 W
Voltage	0 – 50 V
Current	0 – 400 A

III.2.3. Fuel cell operation and characterizations

III.2.3.1. Break-in phase

Once installed on the test bench, the fuel cell is systematically subjected to a leakage test before any operation. Then, a generic and protective start-up procedure under N_2/N_2 is performed until the operating parameters corresponding to break-in phase also called "activation phase" are reached (see Table III-3). The short-stack is more susceptible than single cell to flooding event, that is why the stack operating conditions are defined with lower RH condition to prevent it. When the operating parameters are reached, N_2/N_2 gas supply is switched to H_2/Air and current density is progressively increased up to 1.2 A.cm^{-2} (keeping $U_{\text{cell}} > 0.5$ V). A break-in phase is performed under these operating conditions until a steady cell voltage is measured about 0.65 V (single cell) or 0.68 V (short-stack) at 1.2 A.cm^{-2}. Afterwards, a polarization curve measurement is carried out to check the initial performance of the fuel cell.

Table III-3: Operating conditions during break-in step

Break-in phase	Single cell	Short-stack
Cell temperature	80 °C	80 °C
Anode / Cathode Stoichiometry	1.5 / 2	2 / 2
Anode / Cathode absolute pressure	1.5 / 1.5	1.8 / 1.8
Anode / Cathode relative humidity	80 / 80% (74.6 °C dew point)	50 / 50% (63.8 °C dew point)
Current density	1.2 A.cm^{-2}	1.2 A.cm^{-2}
Initial cell voltage (after break-in)	0.65 V @ 1.2 A.cm^{-2}	0.68 V @ 1.2 A.cm^{-2}
Nominal power	76 W	480 W

III.2.3.2. Polarization curve protocol

The polarization curve represents the i-V response of the fuel cell and therefore its performances under given operating conditions. The nominal operating conditions for the X-stack technology are presented in Table III-4. The higher anode stoichiometry (to avoid anode flooding) and the higher anode / cathode pressure (due to higher pressure drop) are adapted for the short-stack to ensure proper operation. Prior to the measurement, the fuel cell is maintained in operation for 30 minutes at 1.2 A/cm² under the desired operating conditions, until reaching a stationary state and hydration. The current density is then increased from 1.2 up to 1.8 A.cm^{-2} (corresponding to about 0.5 V in nominal conditions) by steps of 0.1 A.cm^{-2} every minute. Then, the measurement of the polarization curve is recorded during the decreasing scan by successive steps of 0.1 A.cm^{-2}, from 1.8 A.cm^{-2} to a minimal current density (i_{min}) equal to 0.2 or 0.5 A.cm^{-2} in single cell or short-stack configurations, respectively. In short-stack configuration, the higher i_{min} is chosen to prevent flooding at low current density. Below this minimal current density, the set point continues to decrease to 0.0 A.cm^{-2} (0.05 A.cm^{-2} steps) every 3 minutes with a fixed flow rate of reactant gas, corresponding to i_{min}. The average cell voltage is measured during the last 30 seconds of each current step.

The profile of the current density as well as the initial polarization curve in single and short-stack are given in Figure III-3. This protocol is in agreement with the suggestions of the European project STACK-TEST dealing with recommended PEMFC stack procedures [129]. In the beginning-of-Test (BoT), the performance of the single cell and short-stack at key-current densities are summarized in the

Table III-5. At nominal operation (1.2 A.cm^{-2}), the power density is estimated at 0.78 W.cm$^{-2}_{geo}$ for the single cell (± 3% at BoT) and about 0.81 W.cm$^{-2}_{geo}$ for the short-stack (± 3% at BoT).

Table III-4: Nominal operating conditions for the X-design PEMFC technology

Nominal operation	Single cell	Short-stack
Cell temperature	80 °C	80 °C
Anode / Cathode Stoichiometry	1.5 / 2	2 / 2
Anode / Cathode absolute pressure	1.5 / 1.5 bar_{abs} (in)	1.8 / 1.8 bar_{abs} (in)
Anode / Cathode relative humidity	50 / 50% (63.8 °C dew point)	50 / 50% (63.8 °C dew point)
Current density	1.2 $A.cm^{-2}$	1.2 $A.cm^{-2}$

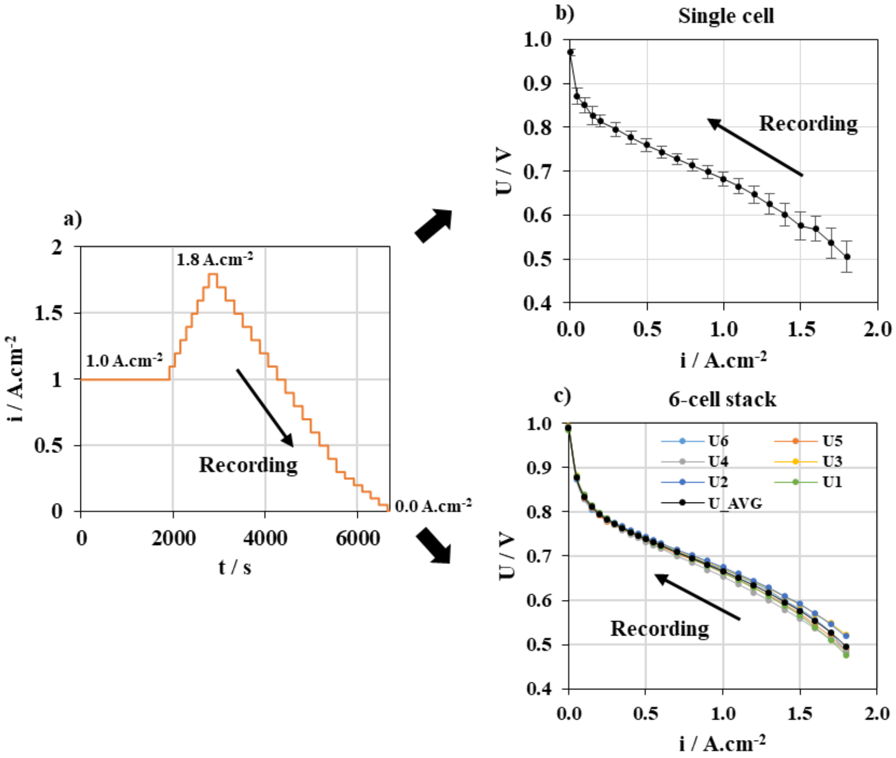

Figure III-3: (a) Typical profile of the current density set points during the polarization curve measurements and (b – c) polarization curves (i-U) in single cell (with standard deviation) and short-stack configuration, respectively, under their respective nominal operating conditions (see Table III-4)

Table III-5: Mean voltage at different key current densities measured during initial polarization curve

Initial	0.1 $A.cm^{-2}$	0.5 $A.cm^{-2}$	1.2 $A.cm^{-2}$	1.8 $A.cm^{-2}$
Single cell	0.85 V	0.76 V	0.65 V	0.51 V
Short-stack	0.87 V	0.75 V	0.68 V	0. 50 V

III.2.4. Complementary electrochemical characterizations

The aim of these additional measurements is to get access to the electro-catalytic properties of the cathode active layer. Here, the fuel cell is supplied under hydrogen and nitrogen at the “anode” (used as reference and counter electrodes) and at the “cathode” electrode (as working electrode), respectively under the operating conditions mentioned in Table III-6.

Table III-6: Operating conditions during CV characterizations

Cyclic voltammetry	Single cell	Short-stack
Cell temperature	60 °C	60 °C
Anode / Cathode flow rate	300 (H_2) / 800 (N_2) $nL.h^{-1}$	400 (H_2) / 1200 (N_2) $nL.h^{-1}$
Anode / Cathode absolute pressure	1.0 / 1.0 bar_{abs} (out)	1.0 / 1.0 bar_{abs} (out)
Anode / Cathode relative humidity	80 / 80% (55.2 °C dew point)	80 / 80% (55.2 °C dew point)

Cyclic voltammetry is classically used to scan the “cathode” potential from 0.065 to 0.700 V or 1.00 V (in single or short-stack configuration, respectively) at 50 $mV.s^{-1}$ at the cathode electrode for 3 cycles to remove any contaminants and get a proper electrochemical response of the cathode layer. The typical voltammograms obtained on the 3rd scan (after break-in) are illustrated Figure III-4 for single cell and short-stacks.

Between 0.1 and 0.4 V, we can observe the typical signature ascribed to the so-called “hydrogen region” on platinum surfaces, used to measure the Electro-Chemical Surface Area (ECSA) of the electrode. In more details, the potential range between 0.065 and 0.40 V is associated to the adsorption/desorption of H^+ onto Pt active sites from reaction (III-1). During the negative potential sweep from 0.4 V to 0.065 V, a monolayer of Pt-H_{ads} is formed on the surface of the catalytic sites. This monolayer is then electro-oxidized during the positive potential sweep up to 0.4 V. It is commonly accepted in the literature that the adsorption of a complete monolayer of H_{ads} on polycrystalline bulk Pt electrochemically results in a coulometry of 210 $\mu C.cm^{-2}_{Pt}$ [130]. An integration of current during the positive potential sweep in this region (gray area on Figure III-4) corrected from the capacitive current I_{dc} and the H_2 permeation currents I_{H2} (both commonly estimated at approximately 0.40-0.45 V) gives access to the charge $Q_{Pt-Hdes}$ and thus the ECSA from equation (III-2). Averaged initial ECSA is measured at about 203 (single cell) and 209 $cm^2_{Pt}.cm^{-2}_{geo}$ (stack average). These close values are coherent since the same MEA components are used in both cases.

$$Pt + H^+ + e^- \leftrightarrow Pt - H_{ads} \qquad 0.065 - 0.40\ V \qquad (III\text{-}1)$$

$$ECSA = \frac{Q_{Pt-Hdes}}{210 * 10^{-6} * S}\ (cm^2_{Pt}.cm^{-2}_{geo}) \qquad (III\text{-}2)$$

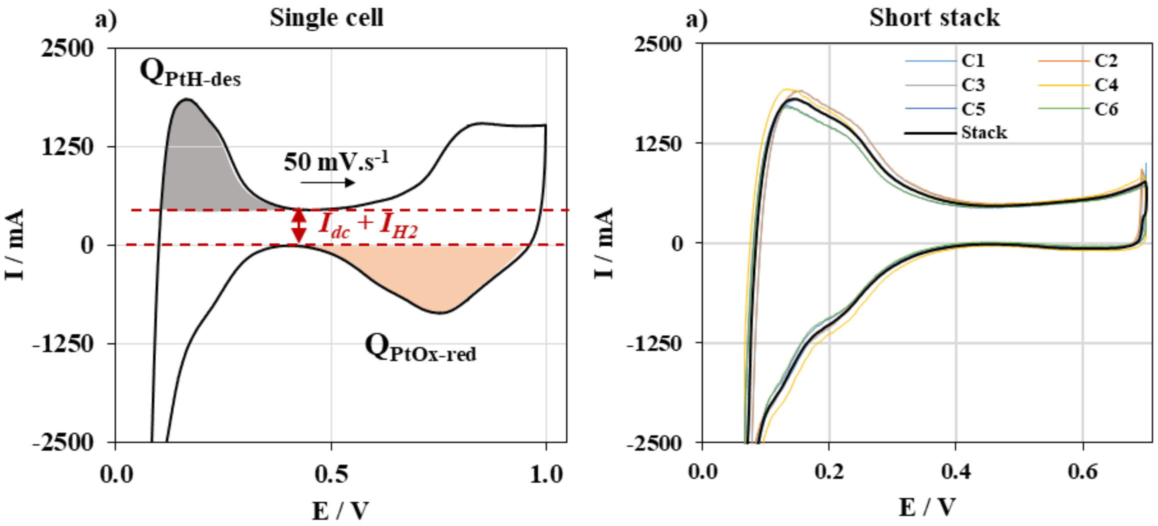

Figure III-4: Typical voltammograms at 50 mV.s^{-1} (third scan) after break-in under H_2/N_2 supply in a) single cell and b) short- stack configurations (see Table III-6 for experimental details)

Moreover, CV is also composed of peaks in the potential region between 0.6 and 1.0 V associated to the formation and the reduction of oxide species onto Pt surface, during the positive and then the negative sweep respectively, according to the reactions (I-11) and (I-12). In this work, particular attention is paid on the charge of the oxide species reduction $Q_{PtOx\text{-}red}$, by integrating the current during the negative potential sweep in the orange area on Figure III-4. It allows to evaluate the oxidation state of Pt induced by high potential increase over 1 V in SU-phase. However, it is impossible to determine the oxide coverage rate (commonly named θ) onto Platinum because the respective coverage ratio for each species such as $–OH_{ads}$ and $–O_{ads}$ or O_{bulk} cannot be clearly distinguished experimentally. In this work, we will generally use the term Pt-O_x regrouping all oxide species. It is proposed to use the ratio between both charge $Q_{PtOx\text{-}red}$ and $Q_{Pt\text{-}Hdes}$ to evaluate qualitatively the global level of oxidation of Pt.

III.2.5. Current Density Distribution Mapping (CDDM)

For the 6-cell short-stack, a segmented S$^{++®}$ card (Current Scan Shunt model) is inserted a the center of the stack (between the cell #3 and #4) to monitor the evolution of the local current densities and the local temperatures, and therefore their heterogeneities [131]. This device consists in 169 segments (13 x 13, *ca.* 0.58 cm² per segment) and 49 segments (7 x 7, *ca.* 2 cm² per segment) for the current and the temperature measurements, respectively. Currents are measured from separate resistors and voltage measurements. This information is key-data to measure and characterize *in situ* local conditions and local evolution of the MEA during our tests. The CDDM device is thus also able to probe local currents evolution during the start-up and shut-down phases and during cyclic voltammetry by fast screening measurements (see Chapter V).

The mapping of the current distribution at key-current densities during the nominal polarization curve after break-in is illustrated in the Figure III-6. By using a data treatment developed at CEA (“iPAC” based on Matlab software), it is possible to discretize the distribution of the current densities into several zones. The Figure III-7 presents the local and the global polarization curves and voltammograms (according to protocols detailed previously in short-stack configuration section III.2.4) for each zone along the cathode channel (1 x 6 zones), from the inlet to the cathode outlet.

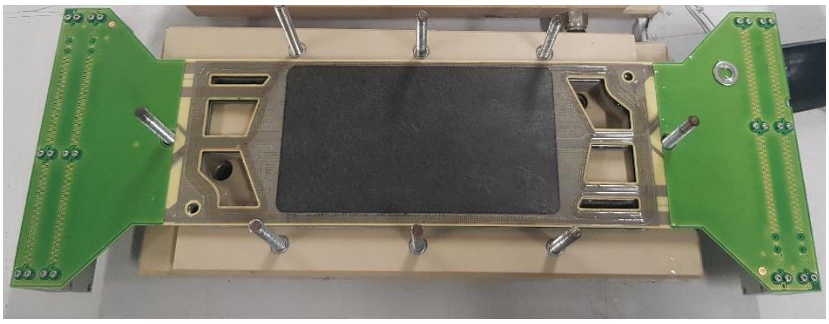

Figure III-5: CDDM device (S++®) inserted in the short-stack X-design) during the assembly process

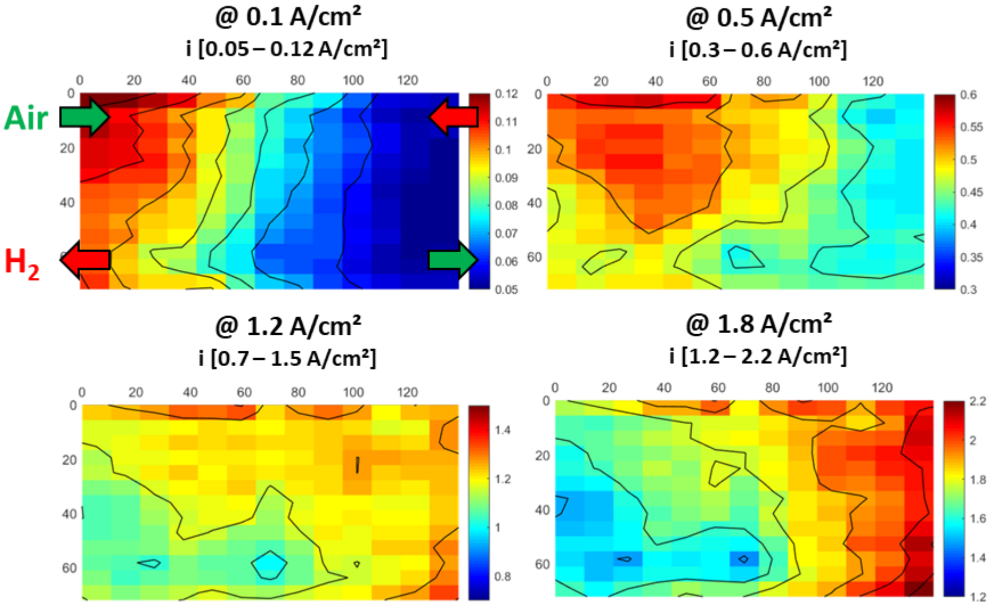

Figure III-6: CDDM during polarization curve after break-in in short-stack under nominal conditions (see Table III-4)

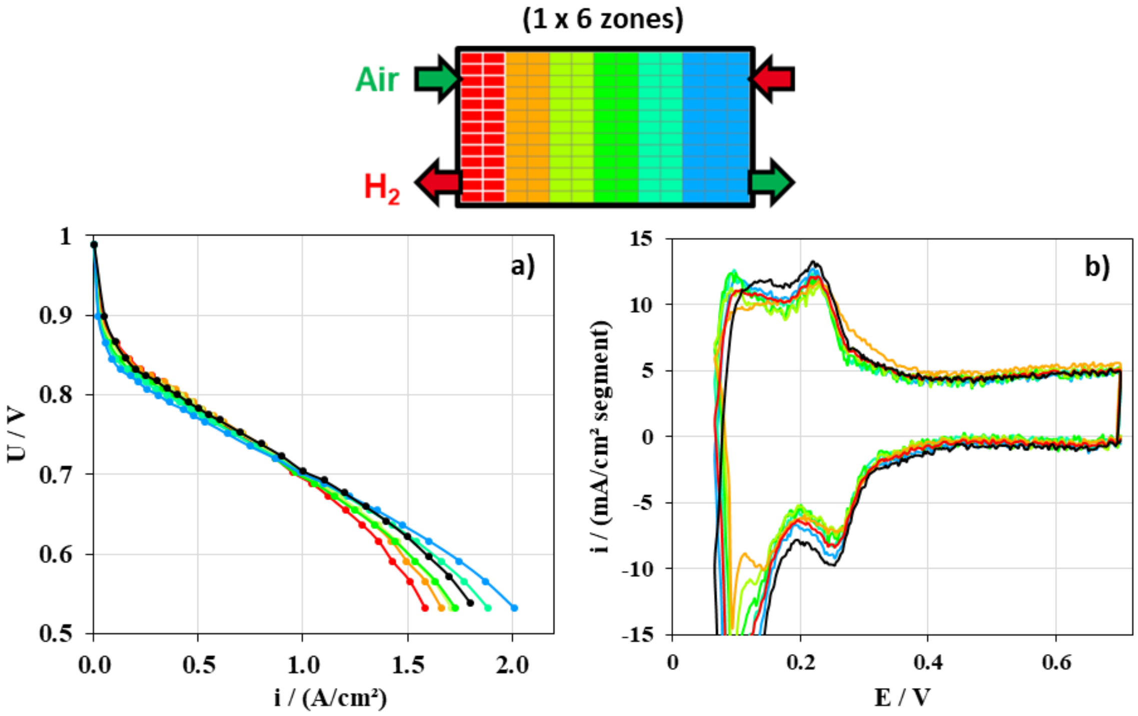

Figure III-7: Local (colored lines) and global measurements on cell #4 (black line) during a) polarization curves and b) CV measurements along the cathode channel after break-in

III.2.6. Gas analysis of CO / CO_2 at the cathode

To monitor the carbon support corrosion of the cathode electrode, a gas analyzer (Proceas AP2E, France) is plugged at the cathode outlet and detects continuously the gas emission rate of CO and CO_2. This infrared laser spectrometer detects low concentration of CO and CO_2 emission up to 55 ppm for both gases and thus requires a high and adequate flow rate of gas vector (pure N_2 or synthetic Air made of pure nitrogen and oxygen blends) to avoid the sensor saturation. This device has been especially used in ageing tests in single cell configuration.

III.3. DESCRIPTION OF THE ACCELERATED STRESS TESTS

From Chapter II, the RCD mechanism during the SU phase has been identified as critical for the PEMFC stack. Experimental study is provided in this PhD work to better understand the degradation mechanism within the CCL, their impact on the cell performance, and ultimately, to implement the mitigation strategies / architectures during the SU/SD phases.

Since real Start-up and Shut-Down phases can be time consuming, specially to ensure the presence of Air in the whole fuel cell to study the degradation caused by reversal current, two Accelerated Stress Test (AST) have been specifically designed and tested in this work:

- Start-Up AST (SU-AST) mimicking the high cathode elevation potential during the propagation of the H_2|Air front along the anode channel;
- Stack Start-Up and Shut-Down AST (Stack SU/SD AST) repeating SU phase with real H_2|Air front and SD phase by H_2 consumption with recommendations determined in the Chapter II.

SU-AST have been performed in single cell configuration and Stack SU/SD-AST in short-stack configuration (equipped with CDDM/S++® card).

III.3.1. Emulation of the Start-Up phase (SU-AST)

III.3.1.1. SU-AST profile in large single cell

The SU-AST protocol is based on the results predicted by a model previously developed at CEA, and from the literature as well, model in which local conditions are simulated during the H_2|Air front propagation coupled with carbon corrosion mechanism [71]. Of course, SU-AST cycles are preceded by a break-in phase and followed by an initial polarization curve (see section III.2.3).

The Figure III-8 illustrates the potential profile at the cathode inlet (facing the anode outlet) during unprotected SU-phase, in counter-flow configuration, between H_2 and Air. The cathode potential is initially stable at 1.2 V_{RHE} in Air/Air fluidic conditions. As soon as the H_2 is injected in the anode (at 1.0 s), the cathode potential suddenly grows at about 1.6 V for 1.5 s while the H_2|Air front propagates from the anode inlet to the outlet. Then, the potential drops to 0.95 V corresponding to the OCV in H_2/Air fluidic configuration. This more realistic profile differs from DoE carbon support testing by including a high potential plateau relative to the duration of the H_2|Air front propagation [132].

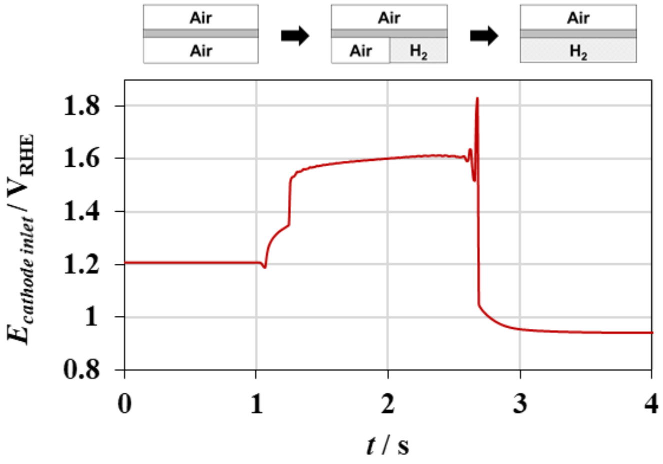

Figure III-8: Simulated potential profile at the cathode inlet during the start-up obtained from [71]

Our SU-AST protocol integrates this profile as illustrated in Figure III-9 with a N_2-fed working electrode (on “cathode” side) and with an H_2-fed counter electrode (on “anode” side). Three phases can be distinguished. From OCV under H_2/N_2 (cell voltage around 0.1 V), a first phase (red line) mimics cathodic potential elevation (Figure III-8) during realistic SU-phase as detailed below. A static potential step at 1.0 V is applied during 10 s, representative of the potential of the cathode under Air. Then, cell potential is increased at 1.0 V.s^{-1} up to a first parametric value named E_{front}. Therefore, this potential is maintained at E_{front} value during a second parametric duration named t_{front}. Afterwards, potential drops at 1.0 V s^{-1} down to 1.0 V to mimic fuel cell OCV and maintained 10 s.

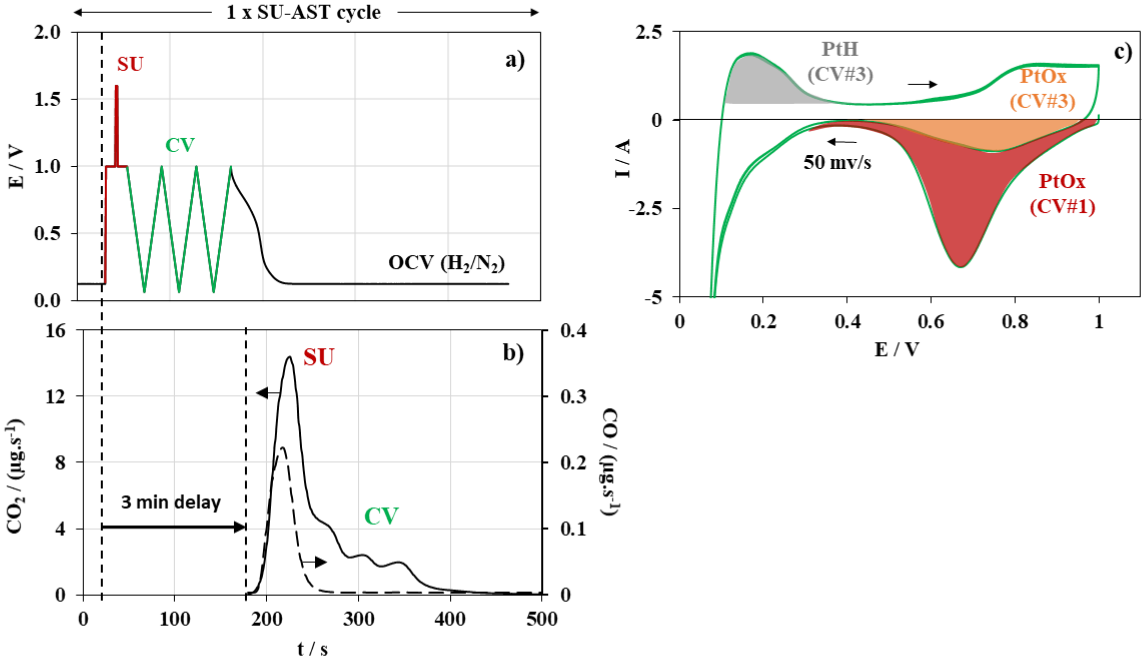

Figure III-9: a) Emulated potential profile, b) the induced CO_2 emission profile measured at the cathode outlet and c) the CV profile plotted during the 1st reference SU-AST cycle

It is important to note that potential profile is imposed on the entire working electrode surface. That should induce a homogeneous degradation rate on the whole active area in our ageing test, thereby harsher than heterogeneous degradation rate along flow-field channel in real Reverse Current Decay mechanism [133]. In fact, the chapter II reveals a more significant degradation rate near the cathode inlet (facing the anode outlet) during the SU phase. Indeed, this area stays almost all the time in Air/Air (anode/cathode) configuration during the anodic H_2/Air front passage. The grey line in Figure III-10 presents this heterogeneity. In our AST protocol, the entire surface is degraded at the same rate as illustrated by the red line. The last is supposed to be 3-fold more degrading. Consequently, our AST protocol do not reproduce the local degradation distribution during real SU phase.

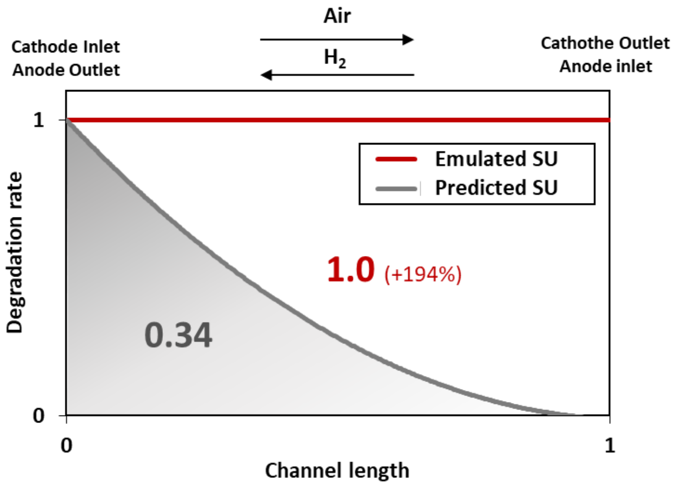

Figure III-10: Distribution of the degradation rate along the dimensionless anode channel from model (grey line) and in our SU-AST (red line)

During a second step, three Cyclic Voltammetry (CV) between 0.065 and 1.0 V (50 mV s^{-1}) are used to monitor continuously the electrochemical properties of the cathode along the ageing test (green lines in Figure III-9a). An example of such voltammograms is shown in Figure III-9c. Two reversed peaks associated to the reduction of Pt-O_x in region 0.5 – 1.0 V are measured: one large on the first cycle and the second one less pronounced on the second/third cycles, respectively. The first one, starting from 1.0 V, CV#1 (in red), is induced by the previous high potential exposure during the emulation of the SU-phase up to E_{front}, while the second one is only induced from the fast scan up to 1.0 V. It is expected that oxidation degree during the first scan is higher than the third one. To compare both Pt-O_x reduction coulometry related to proton desorption coulometry, a ratio is calculated in this work between $Q_{Pt-Ox}^{CV\#1\ or\ 3}$ (red area in Figure III-9c) and Q_{Pt-H} (grey area in Figure III-9c).

Finally, during the last phase (black line in Figure III-9c), the working electrode voltage goes back to about 0.1 V (typical OCV under H_2/N_2 gas supply). A duration of 5 minutes is applied under OCV to evacuate residual CO and CO_2 products in the cell and the bench gas lines before the next cycle. Indeed, the SU-AST is coupled with gas analyzer to monitor continuously the CO / CO_2 gas emissions.

The Figure III-9b resents the CO_2 and CO gas emissions along the 1st SU-AST cycle calculated thanks to the nitrogen flow rate and the CO and CO_2 concentrations measured by the sensors. Two CSC mechanisms in accordance with the SU and CV phases are proposed. Firstly, SU-phase induces the direct CSC mechanism Eq. (I-18) over the whole surface of the carbon support, emitting the major CO_2 peak. Secondly, the potential sweeps between 0.065 and 1.0 V during CV phase enhance the Pt-catalyzed corrosion mechanism (cf. I.3.2.1.2), leading to three CO_2 minor peaks according to the reactions from (I-13) to (I-17). A 3-min delay is observed between the potential profile and the CO_2 detection because the analyzer is plugged at the exhaust of the test bench away from the fuel cell. Indeed, the analyzer must be supplied with dry gas (at least non-condensing) at ambient pressure so downstream the water condensers and expansion valves of the bench.

The complete SU-AST protocol is performed under continuous H_2/N_2 feeding and the cycle is repeated 100 times. This corresponds to a performance drop of about 10% in our reference “unprotected” case, as suggested by DoE regarding the durability target, at our nominal current density (1.2 A cm^2)[17]. In addition, periodic characterizations by polarization curves are carried out every 20 cycles to regularly quantify the performance losses.

III.3.1.2. Sensitive study of mitigating parameters

The description of the SU-AST protocol given in previous section (III.3.1.1) stands for the reference case and it mimics standard start-up phase without any mitigation strategy for a high potential E_{front} equal to 1.6 V and standard exposure time equal to 1.5 s. Conventional cell temperature (60 °C) with high relative humidity (80%) of reactant gas is chosen to accelerate and exacerbate degradations and to better discriminate the different configurations tested. High nitrogen flow rate is set in order to dilute and detect CO_2 gas at the cathode outlet in 0 – 55 ppm_{CO2} range (limit of detection of gas analyzer), while the H_2 flow rate is adjusted to avoid high differential pressure between the anode and cathode sides. Operating conditions are described in Table III-7.

Table III-7: Operating conditions during ageing test

Reference SU-AST operating conditions	
Cell temperature	60 °C
Anode / Cathode flow rate	300 (H_2) / 800 (N_2) nL.h^{-1}
Anode / Cathode absolute pressure	1.0 / 1.0 bar$_{abs}$ (out)
Anode / Cathode relative humidity	80 / 80% (55.2 °C dew point)

The impact of the SU parameters has been evaluated through a sensitivity study about mitigating degradations during the SU phase with the RCD occurrence identified in the Chapter II:

- E_{front}, the maximal potential profile, emulating the lowering of the cathode potential by applying dummy load in the Air/Air fluidic configuration after a long stop (cf. II.2.2);
- t_{front}, the exposure time at E_{front}, relative to the velocity of the H_2 injected in Air-filled anode in SU phase;
- $RH_{a/c}$, the relative humidity of both anode and cathode gas supplies;
- T_{cell}, the cell temperature.

III.3.2. Start-Up and Shut-Down Cycling (stack SU/SD-AST) on short-stacks

III.3.2.1. Introduction of the three dummy load configurations

Literature reveals that the most promising mitigation strategy in Air/Air fluidic configuration is to reduce the cathode potential. One of the methods is to divert the internal electric current during the start-up phase by the implementation of external resistive dummy load. In this work, three configurations are compared:

- Without any resistance as a reference case (in open-circuit mode);
- With a global stack resistance (connected to the stack end plates);
- With individual cell resistances (one resistance is connected between each bipolar plate via the Cell Voltage Monitoring device), as schematized in Figure I-20.

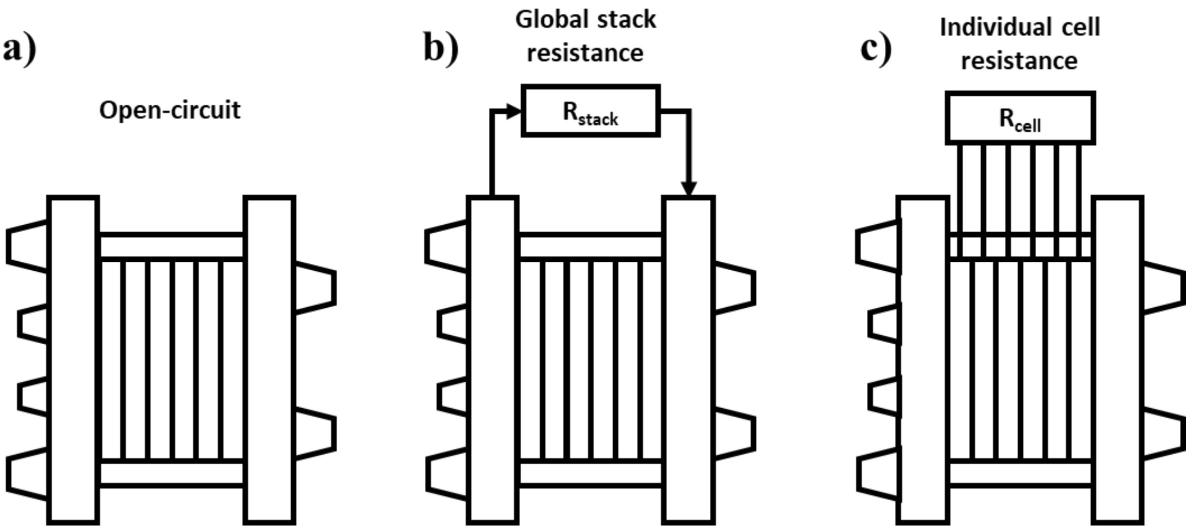

Figure III-11: Three electrical configurations used in the SU phases according to the Stack SU/SD AST protocol: a) without dummy load, b) with global stack resistance and c) with individual resistance per cell.

The stack resistance configuration is performed by using a variable resistor able to derivate between 10 and 30 A in our operating conditions (0.1 and 0.3 $A.cm^{-2}$, approximately). The stack resistor connected to the stack endplates is shown in Figure III-13. A sensitivity is carried out on this stack resistor value circulating a current through the stack of about 10 A (540 mΩ → 5.29×10^{-3} $\Omega.cm^2$) and 30 A (164 mΩ → 1.60×10^{-3} $\Omega.cm^2$) in nominal FC operation during the SU/SD AST protocol (phase 1 from Table III-9). These resistance values are based on the performances measured at the beginning of the ageing campaign. In this case, the manual switch between dummy load and the load of the bench test at each cycle is impossible. This configuration prevents from performing "fast" polarization[3] curve after each SU phase. Only standard polarization curves (protocol detailed previously in section III.2.3.2) are considered in this case.

For the case with individual resistance per cell, a SMART® Cell Voltage Monitor (CVM) equipped with discharge/by-pass system per cell is used [134]. Figure III-12a shows the electrical diagram of the discharging/by-passing system. Each by-passing circuit can be switched by the control of a contactor. This individual circuit is connected to a pin at each flow-field plate. A technological limit imposes to derivate a low electrical current (< 5 A) to prevent the overload of electrical wires, pins, and contactor. Thus, local resistance is sized in order to pass a maximal current of 5 A when the cell voltage is about 1.0 V (the maximal voltage attains in FC).

---

[3] Measurements @ 0.1 / 0.5 / 1.2 $A.cm^{-2}$ (1 min per step) at each cycle in the stack SU/SD-AST condition (see Table III-8) as illustrated in Figure III-14

The resistance of the circuit (wires + contact) is estimated to 119 mΩ and the resistance of the shunt contactor is 2.5 mΩ, by-passing a maximal current to 4 A (see Figure III-12b).

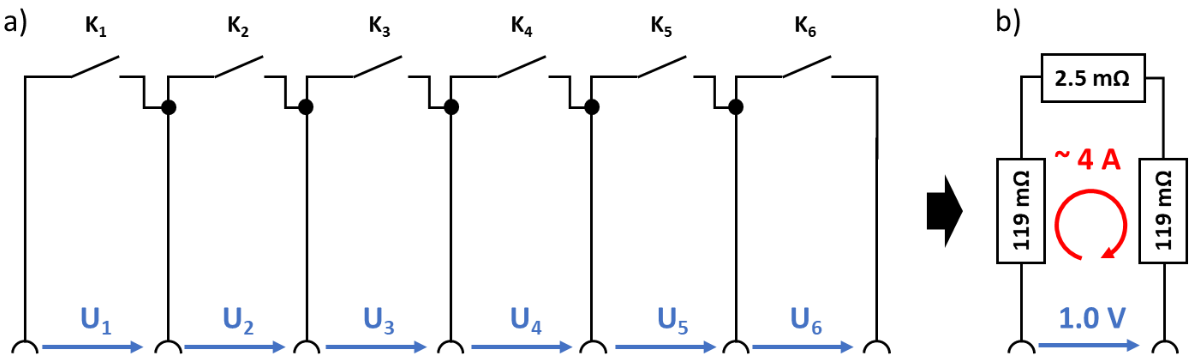

Figure III-12: a) Electrical diagram of the discharging/by-passing circuits and b) the equivalent resistive circuit with estimation of the by-passing current

III.3.2.2. Stack-SU/SD AST protocol

The Stack-SU/SD AST protocols have been designed to investigate several mitigation strategies and their impact on cell performance during the SU phase when H_2|Air front occurs at the anode side. To result in Air/Air fluidic configuration, the "H_2 consumption" shut-down process is chosen by applying the recommendations cited in the Chapter II (section 3.1): closed inlet and outlet anode valves and a resistive dummy load to consume H_2 within the stack while keeping Air flow on operation. In this work, solenoid valves are installed as close as possible to the anode inlet and outlet of the stack. The three electrical configurations have been investigated to derivate electrical current by the resistive dummy load (explained in the previous section III.3.2.1).

The SU/SD protocol is performed on the 6-cell short-stack with the segmented card inserted between the cell #3 and #4 (see Figure III-13). The operating conditions have been chosen carefully to accelerate degradations kinetics (60 °C – 80/80% RH) and high flow rates to avoid test bench and regulation failures (see Table III-8).

Table III-8: Operating conditions during ageing test in FC operation phase (see Table III-9)

Stack SU/SD-AST operating conditions	
Cell temperature	60 °C
Anode / Cathode fixed flow rate	586 / 1400 nL.h^{-1} (St 2/2 @ 1.2 A.cm^{-2})
Anode / Cathode absolute pressure	1.0 / 1.0 bar$_{abs}$ (out)
Anode / Cathode relative humidity	80 / 80% (55.2 °C dew point)

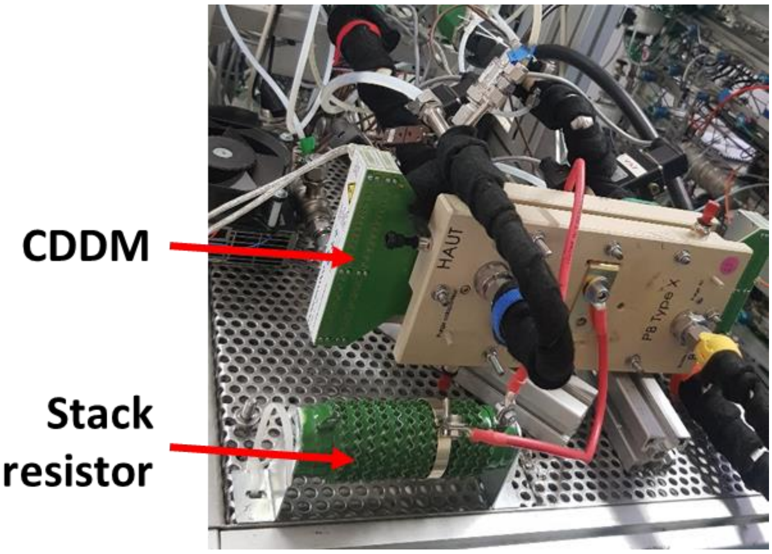

Figure III-13: Short-stack on the bench test with S++® device and stack resistor configuration as dummy load

The complete stack SU/SD-AST protocol is detailed in Table III-9 and is represented in Figure III-14 for the “open-circuit” case. The first step is to operate in FC mode with “fast” polarization curves at 0.1, 0.5 and 1.2 A.cm^{-2} (step 1) along the stack SU/SD-AST under the operating conditions mentioned in Table III-7. Such measurements are carried only for the “open-circuit” and the individual “cell resistance” configurations (Figure III-11).

Subsequently, the shut-down (step 2) is proceeded by connecting the corresponding dummy load (according to the electrical configuration R_{cell} or R_{stack}). At the same time, the H_2 supply is shut off and the anode solenoid vales are closed (at stack inlet and outlet) while the Air supply is maintained. The residual H_2 is consumed while the cell voltage drops to 0.0 V and the anode pressure decreases down to 0.2 – 0.3 bar$_{\text{abs}}$ inside the stack. A one-hour waiting period (step 3) is applied in order to fill the anode by oxygen and nitrogen (from cathode side by crossover). After 20 min, the anode is at atmospheric pressure but an extra waiting time of 40 min is added to ensure the Air filling.

Finally, H_2 is injected in the anode at a low flow rate (24 nL.h^{-1}) in phase 4 corresponding to a propagation duration of H_2|Air front at 1.0 s in the active area (based on stack internal volumes). In parallel, dummy load is also simultaneously connected according to the electrical configuration. After 10 s, H_2 is then supplied at nominal flow rate (586 nL.h^{-1}) to operate in proper FC operation (phase 1 from the protocol detailed in Table III-9).

Overall, the Stack-SU/SD-AST tests are carried out for 300 cycles which correspond to 10% of voltage drop at 1.2 A.cm^{-2} in the reference case. Then, a final polarization curve and ECSA evaluation, following protocols described in sections III.2.3.2 and III.2.4, are performed in order to get the state of health of the individual cells. CDDM measurements are also recorded during these initial and final characterizations. The experimental results will be presented in Chapter V.

Table III-9: Detailed experimental protocols of the three Stack-SU/SD AST applied on short-stack

	Open-circuit	**Cell resistance**	**Stack resistance**
1) FC operation	• Polarization @0.1 / 0.5 / 1.2 A.cm^{-2}	• Polarization @0.1 / 0.5 / 1.2 A.cm^{-2}	• Stationary operation with R_{stack}
2) SD phase	• R_{cell} connected • Anode solenoid valves closed at stack inlet/outlet • Air supply maintained	• R_{cell} connected • Anode solenoid valves closed at stack inlet/outlet • Air supply maintained	• R_{stack} connected • Anode solenoid valves closed at stack inlet/outlet • Air supply maintained
3) Long stop	• Air supply maintained • Wait for 1 h • R_{cell} connected	• Air supply maintained • Wait for 1 h • R_{cell} connected	• Air supply maintained • Wait for 1 h • R_{stack} connected
4) SU phase	• R_{cell} disconnected (open-circuit) • H_2 injected at 24 nL.h^{-1} during 10 s • H_2 injected at 586 nL.h^{-1} until next step	• R_{cell} connected • H_2 injected at 24 nL.h^{-1} during 10 s • H_2 injected at 586 nL.h^{-1} until next step (and R_{cell} disconnected)	• R_{stack} connected • H_2 injected at 24 nL.h^{-1} during 10 s • H_2 injected at 586 nL.h^{-1} until next step

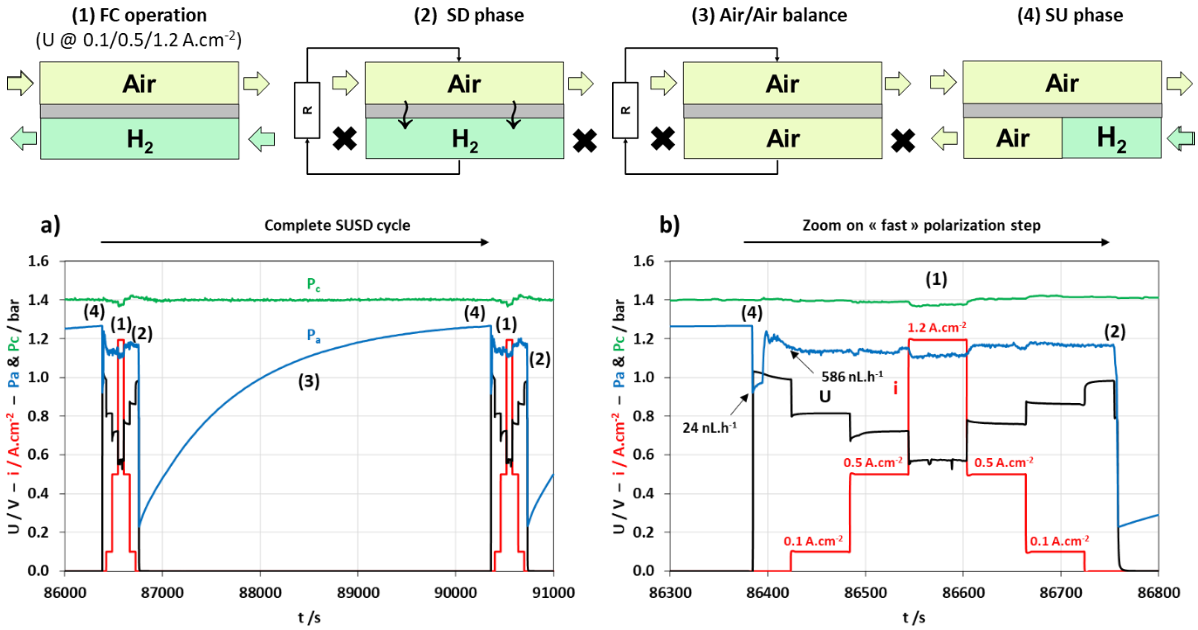

Figure III-14: Schematic protocol of the Stack-SU/SD AST process in the open-circuit configuration and the evolution of the average cell voltage (black line), the current density (red line) and the anode/cathode inlet pressure (blue and green line) during a) the complete cycle and b) zoom during the "fast" polarization step

III.4. *POST-MORTEM* ON AGED MEA

Additional analyses have been provided on aged MEA after the ageing test on single cell to better understand the degradation mechanisms and the local electrochemical performance losses. This *post-mortem* study was conducted to define the local evolution of the electro-chemical and physico-chemical properties of the Cathodic Catalytic Layer. MEA samples are manually cut in areas of interests at the inlet – middle – outlet of the cathode as illustrated in the Figure III-15. The active area for electrochemical analysis of these local MEA is 1.8 cm² (with GDL in the center; orange area in Figure III-15) and the GDL at the outer perimeter is carefully removed to delimit the border of the MEA and to ensure the gas tightness in the dedicated single cell.

In the same locations along the flow-field, smaller MEA samples are taken for physico-chemical analysis (blue samples on Figure III-15).

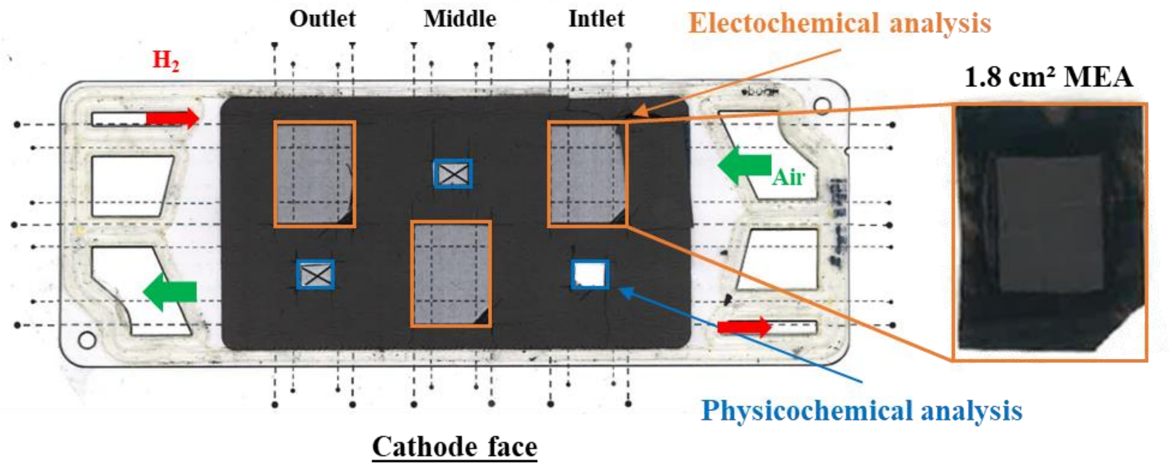

Figure III-15: Cutting pattern of aged MEA for electrochemical and SEM post-mortem analysis

III.4.1. Local Electrochemical investigation

For the electrochemical analysis, the MEA samples of 1.8 cm² are tested in differential single-cell on a bench test providing significant fixed flow-rates of the reactant gases that allow to get rid of the transport limitation along the channels (respecting anode / cathode stoichiometry of 50 / 50 @ 1.0 A.cm^{-2}). Several operating conditions are considered in this study and given in Table III-10. Three relative humidity levels are defined in order to assess the water management evolution of the samples before and after ageing test. The cell temperature and gas pressure are kept constant (80 °C and 1.5 bar$_{abs}$, respectively). Here, fresh MEA samples (taken from pristine MEA) were characterized as reference to evaluate the local degradations and evolution of the aged MEA according to the durability protocol and the location within the cell.

Table III-10: Operating conditions of the local Electro-chemical analysis differential single cell configuration

Differential characterization	Nominal	Wet	Saturated
Cell temperature		80 °C	
Anode / Cathode flow rate		38 (H_2) / 90 (Air or N_2) nL.h^{-1}	
Anode / Cathode absolute pressure		1.5 / 1.5 bar$_{abs}$ (in)	
Anode / Cathode relative humidity	50 / 50%	80/80%	> 100 / 100%
Bubbler temperature	63 °C	74 °C	85 °C

III.4.1.1. *Experimental Protocol*

Electrochemical analyses proceed by polarization curve and Electrochemical Impedance Spectra (EIS) measurements under H_2/Air atmosphere, followed by cyclic voltammetry and EIS under H_2/N_2 atmosphere with operating conditions mentioned in Table III-10. Global protocol and operating conditions are plotted in Figure III-16. Details for each technique are given in the next sections.

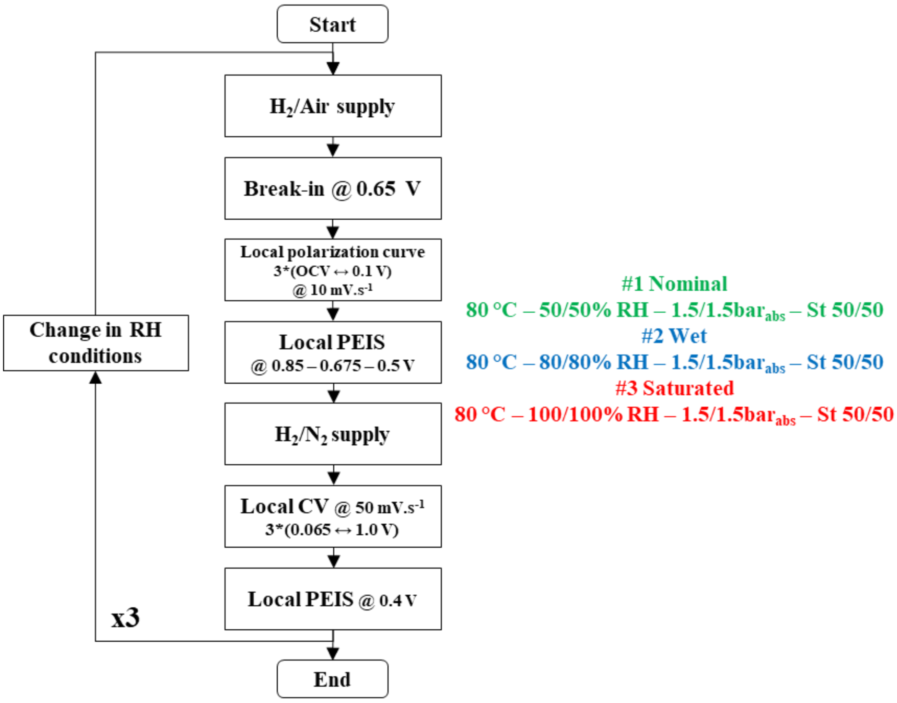

Figure III-16: Experimental protocol on local electrochemical investigation in 1.8 cm² differential cell with different relative humidity conditions

III.4.1.2. *Polarization curve (H_2/Air) in differential cell*

The "local" polarization curve in differential cell is carried out under well-controlled conditions (Table III-10) by scanning cathode potential between OCV (about 0.95 V) and 0.1 V at 10 mV.s^{-1}. The initial performance of fresh MEA (non-aged) sample at 50, 80 and 100% RH is plotted on Figure III-17. The reproducibility of the results is validated for 50 and 80% RH case. However, the 100% RH case (ensured by oversaturation and liquid water injection) shows a slight deviation at high current density (> 1.5 A.cm^{-2}) probably due to the water management difficulty of the fresh MEA sample. In practice, cell performance decreases by increasing the RH values. Indeed, the current density at 0.5 V of the single cell differential is reduced from 3.10 A.cm^{-2} to 2.35 and 2.07 A.cm^{-2} by increasing the RH from 50/50% to 80/80 and 100/100%, respectively. This commercial MEA seems to be optimized for low humidity conditions.

In the beginning-of-life, the polarization curve in 1.8 cm² single-cell attains higher current density compared to polarization curve carried out on large area MEA in single cell configuration (cf. Figure III-3a). At 0.5 V, the current density is about 1.80 A.cm^{-2} in large MEA (98 m²) and 3.10 A.cm^{-2} in small MEA (1.8 cm²) with similar operating condition (RH 50/50%). This difference is expected since the stoichiometries in the differential cell are fixed to 50 /50 (@1.0 A.cm^{-2}) making the operation homogeneous along the channel.

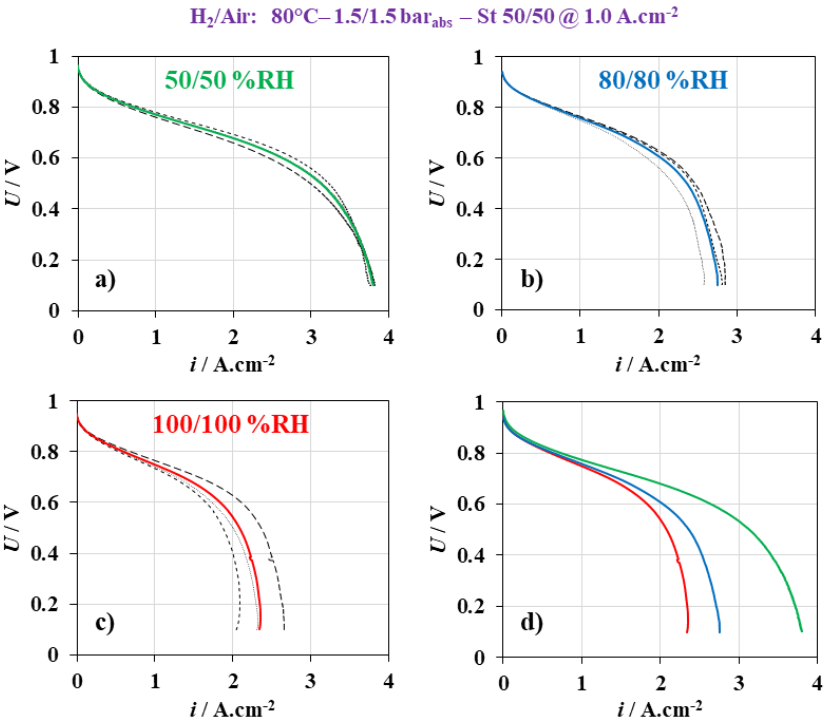

Figure III-17: Reproducibility of initial and local cell performance at 50, 80 and 100% RH (a, b and c respectively) and averaged polarization curve (d) for the three conditions.

III.4.1.3. Electrochemical Impedance Spectroscopy (H_2/Air) in differential cell

Potentiostatic Electrochemical Impedance Spectroscopy (PEIS) is an electrochemical characterization evaluating the current response to a small sinusoidal alternating potential perturbation. The impedance measurement is usually displayed in Nyquist format and is exploited to determine the respective contributions (Figure I-11d) as based on the equivalent electrical circuit for the cell operation (Figure I-11e). This approach evaluates the ORR charge transfer (R_{ct}) and protonic resistance through membrane ($R_{H+,MB}$) and CCL components ($R_{H+,CCL}$). By using this model, we suppose a homogeneous operation along the CCL thickness and that the HOR contribution at the anode side is negligible.

The technique is applied at 0.85, 0.675 and 0.5 V *ie*. at low, medium, and high current density. Figure III-18 (a, b and c) plots impedance spectra at 0.85 V with 50, 80 and 100% RH conditions. Typical resistances are fitted from impedance spectra are summarized in Table III-11. Reproducibility measurements on fresh MEA samples are evaluated 3 times for the 50%, 80% and 100% RH condition. Maximal deviation estimated at 10% (for the 50 and 80% RH) and ~50% for the water-saturated case (100% RH), in accordance with the observations by polarization curves on fresh MEA in previous section III.4.1.2.

Table III-11: Equivalent resistance (mΩ) for fresh 1.8 cm^2 MEA sample measured by PEIS (H_2/Air) at 0.85, 0.675 and 0.5 V

	@ 0.85 V			**@ 0.675 V**			**@ 0.50 V**		
RH	50%	80%	100%	50%	80%	100%	50%	80%	100%
$\boldsymbol{R_{ct}}$	124	116	132	8.0	11.5	12.7	184	338	362
$\boldsymbol{R_{H+,MB}}$	17.5	10.3	10.1	13.7	10.0	9.9	13.2	9.5	9.9
$\boldsymbol{R_{H+,CCL}}$	116 ± 14.7	29 ± 0.4	27 ± 12.9	79.9 ± 9.6	28.8 ± 0.7	30.6 ± 0.6	60.4 ± 0.1	20.2 ± 0.3	32.7 ± 4.8

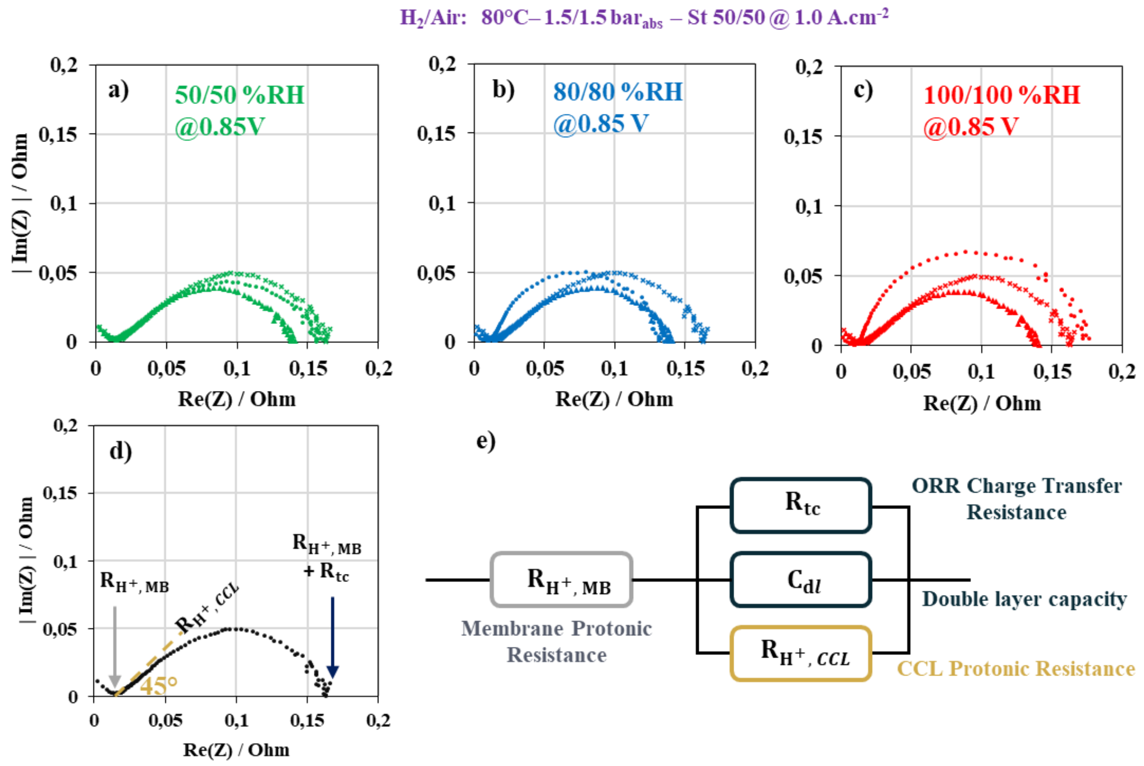

Figure III-18: Reproducibility of initial impedance spectra at 0.85 V in differential cell under H_2/Air for three fresh MEA samples at 50, 80 and 100% RH (a, b and c respectively) with (d) qualitative representation of resistances according to (e) equivalent electrical circuit for FC operation

III.4.1.4. Cyclic voltammetry (H_2/N_2) in differential cell

Cyclic voltammetry is also performed on 1.8 cm² MEA samples to get access to the local ECSA values (as explained in the section III.2.4) in the same operating conditions as the previous polarization curves and PEIS measurements (specified in the Table III-10 except that Air is replaced here by N_2). The reproducibility of the measurements was also validated on three fresh samples at 50, 80 and 100% RH as illustrated in Figure III-19. The initial ECSA does not greatly differ under the three different relative humidity conditions. It is estimated approximately at 280 cm^2_{Pt}/cm^2_{geo}. This value is higher than the one measured in large single cell (200-210 cm^2_{Pt}/cm^2_{geo}). This gap could be ascribed to the differences between characterizations conditions and possibly due to the different break-in condition. For a sake of an Air comparison, the initial value obtained in 1.8 cm² will be used with aged 1.8 cm² samples.

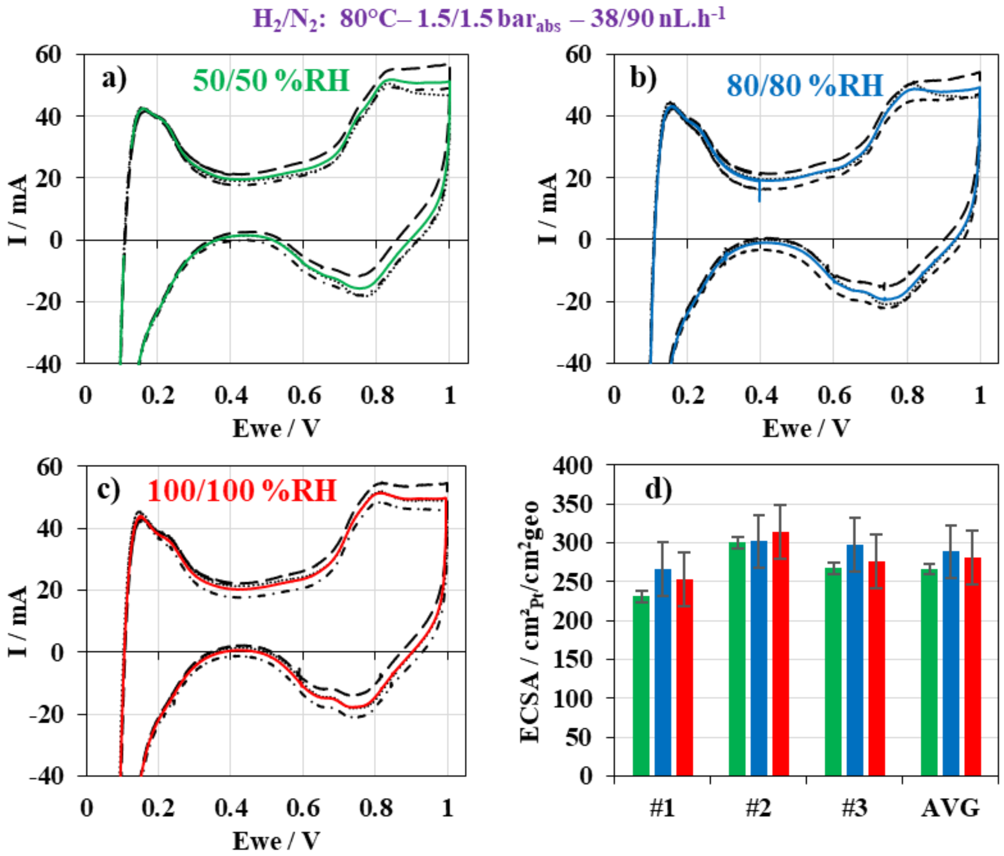

Figure III-19: Reproducibility of initial CCL characterizations by CV in differential cell at 50, 80 and 100% RH (a, b and c respectively) for three fresh MEA samples (average measurement in colored lines) and corresponding ECSA estimation (d) under the three RH conditions.

III.4.1.5. Electrochemical Impedance Spectroscopy under H_2/N_2 in differential cell

PEIS under nitrogen atmosphere is performed similarly as under Air atmosphere (cf. section III.4.1.3) but only at 0.4 V in the so-called "double layer region" to further characterize MEA properties. The details of the equivalent electrical circuit under H_2/N_2 are presented in Figure III-20 (d and e). The R_{tc} / C_{dl} part stands for the oxidation of hydrogen (HOR) permeated across the membrane. The $R_{H+,CCL}$ is related to the proton transports in the cathode layer. By using this model, we suppose a homogeneous catalyst layer in the thickness [135]. Reproducibility measurements on fresh samples have been evaluated at 50, 80 and 100% RH at 0.4 V with a small deviation for the 50% RH condition and more dispersed measurements for the 80% and 100% RH (cf. Figure III-20 a, b and c). Resistances deduced from impedance spectra are given in Table III-12.

Table III-12: Equivalent resistance (mΩ) of fresh sample MEA measured by PEIS (H_2/N_2) at 0.4 V

@ 0.4 V	Nominal	Wet	Saturated
$\boldsymbol{R_{H+,MB}}$	18.5	9.9	9.6
$\boldsymbol{R_{H+,CCL}}$	152	32	21

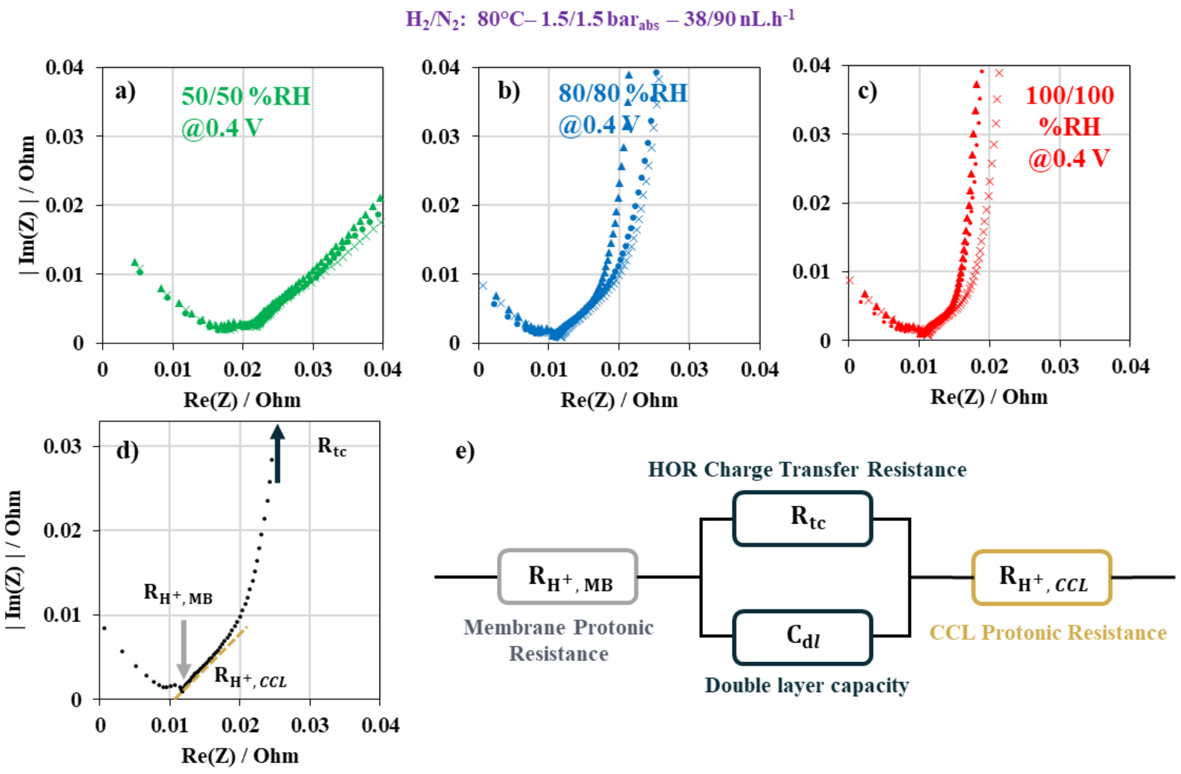

Figure III-20: Reproducibility of initial impedance spectra at 0.4 V in differential cell for three fresh MEA samples under H_2/N_2 at 50, 80 and 100% RH (a, b and c respectively) with (d) qualitative representation of resistances according to (e) equivalent electrical circuit under H_2/N_2 condition

III.4.2. Local physico-chemical investigation

For physico-chemical analyses, MEA samples are either cut from large-area MEAs (Figure III-15) for SEM and Raman, removing gently GDL components. Some CCL powder is scraped from the surface of the CCL for water sorption.

III.4.2.1. Scanning Electron Microscopy (SEM)

The microstructure evolution between fresh and aged of MEA was analyzed by Scanning Electron Microscopy (SEM) in cross-section. Small samples (10 x 7 mm²) from MEA were collected in selected regions (see Figure III-15) and embedded in epoxy resin. All samples were mechanically polished to obtain a proper surface for observation by SEM. A layer of carbon is then deposited on the surface to make the sample conductive. The observations were made on a Merlin type ZEISS SEM-FEG (field emission gun) operating at 5 keV. The images were recorded on the backscattered electron detector. Figure III-21 shows SEM images of a fresh MEA with several magnifications. Let us stress that this MEA has not been mounted in a stack and thus it has not been submitted to compression/deformation and break-in phase. The thickness of the different layers is irregular and averaged at 5, 20 and 15 µm for the Anode Catalyst Layer, the membrane, and the Cathode Catalyst Layer, respectively. Regarding the CCL, the thickness is measured with a deviation about 10% (15 ± 2 µm). In this work, particular attention is paid to the evolution of the CCL microstructure, its thickness, and the Pt densification.

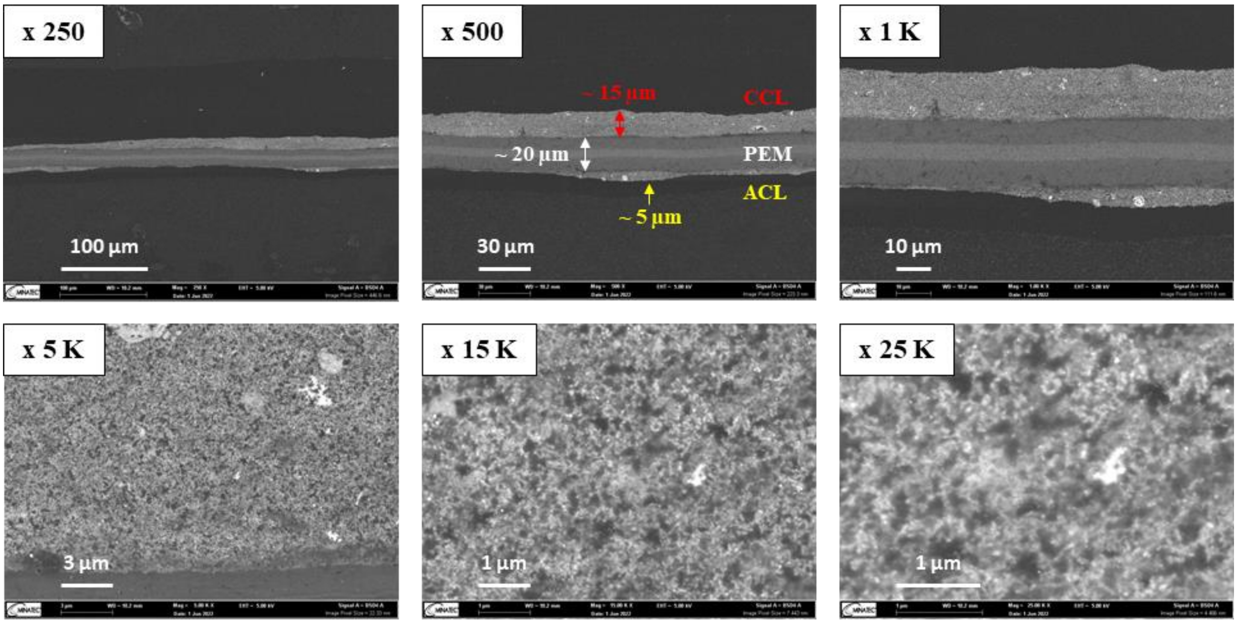

Figure III-21: SEM images of the fresh MEA cross-section at different magnifications

III.4.2.2. Water sorption measurements

The gravimetric sorption technique measures the amount of water adsorbed and then released by fresh and aged CCL. This technique will be useful to characterize the modifications of the CCL regarding water uptake (hydrophilicity/hydrophobicity of the carbon and in pores) after the different ageing protocols.

CCL powder is scraped from CCL and is deposited in the Dynamic Vapor Sorption (DVS) hardware (Surface Measurement Systems, UK) [136]. A preliminary step consists in drying the sample at 80 °C to initialize the mass. Then, DVS varies the vapor concentration at 25 °C and measures the change in mass during a water sorption and desorption cycle as illustrated in Figure III-22a for a fresh CCL. RH steps are long enough to ensure the equilibrium between the sample and the water uptake. Water sorption isotherm is then plotted in Figure III-22b. Fresh CCL takes up 10% of mass from dry (0% RH) to wet conditions (98% RH) following this procedure.

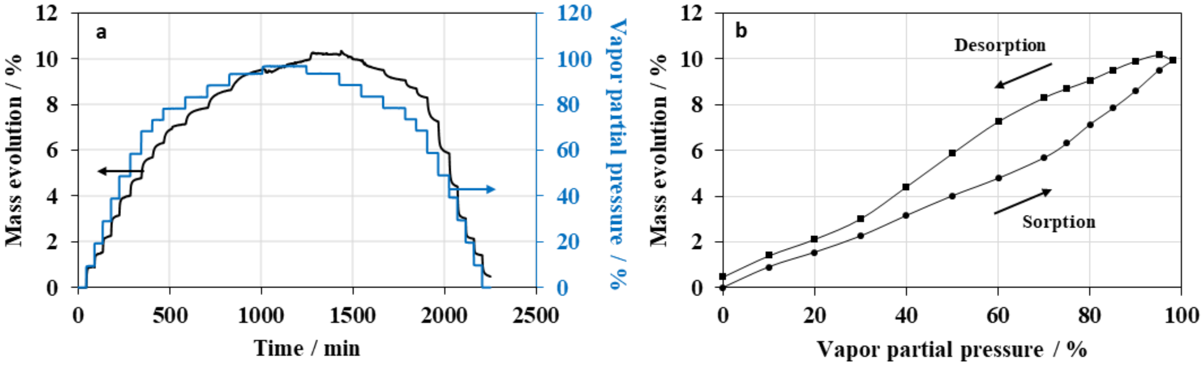

Figure III-22: (a) Water sorption kinetics for fresh CCL at 25 °C; (b) Water sorption isotherm for fresh CCL at 25 °C

III.4.2.3. Raman Spectroscopy

The Raman spectroscopy consists of irradiating a sample with monochromatic light with different wavelengths and to measure the scattered radiations. In this work, we used this technique to characterize the local MEA samples and especially the cathode layer to get further information about the evolution of carbon support structure during SU-AST ageing.

A plot of Raman scattered radiation depending on wave number is illustrated in Figure III-23 for two fresh MEA samples. For sake of comparison, the curves are normalized according to the intensity of the peak at 1,600 cm^{-1}. The nature of the carbon material can be identified from the peaks and bands associated to specific vibration modes (Table III-13) [137].

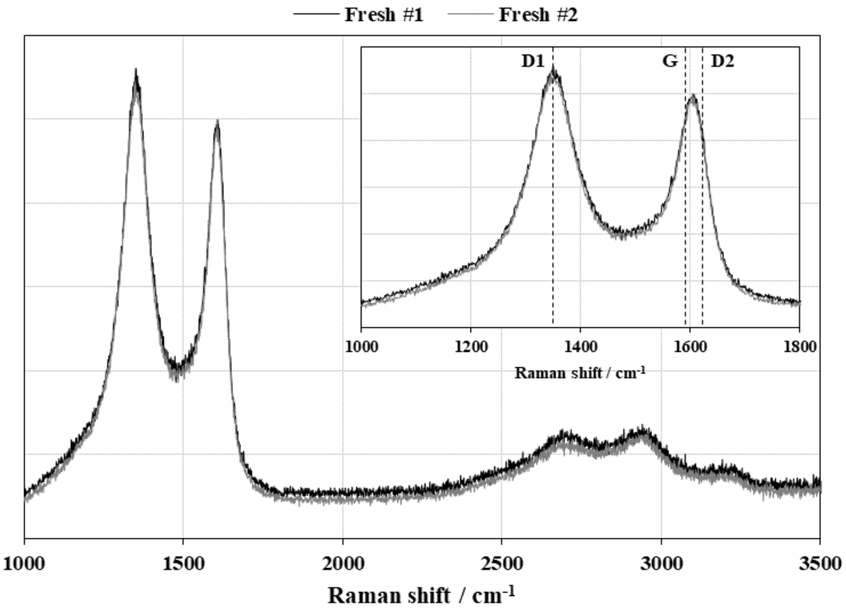

Figure III-23: Raman spectrum of the CCL of two fresh MEA

Table III-13: Vibration modes for carbon materials with Raman spectroscopy from [137]

Band	Raman shift	Vibration modes
G	1,585 cm^{-1}	Ordered graphitic lattice
D1	1,350 cm^{-1}	Disordered graphitic lattice – Graphene layer edge
D2	1,610 cm^{-1}	Disordered graphitic lattice – Surface graphene layer
C=O	1,760 cm^{-1}	Carbonyl surface functions

The Knight and White expression (III-3) is then classically used to evaluate the structural modification of the carbon support and the mean crystallite size of the carbon particles [138]. On our fresh sample MEA, the mean crystallite size L_a is estimated at 3.18 nm.

$$L_a = 4.4 * \left(\frac{I_{D1}}{I_G}\right) (nm) \tag{III-3}$$

III.5. CONCLUSION

In this chapter, experimental ageing protocols and *in-situ* / *post-mortem* characterization techniques performed in this work are reported.

The FC technology used here consists in real flow-field plates (X-design) developed by CEA with commercial MEA from IRD Fuel Cell (cf. section III.2.1). Single cell or short-stack configurations are assembled and are systematically subjected to a break-in phase (cf. section III.2.3.1) followed by an initial characterization by polarization curves and cyclic voltammetry (section III.2.3.2 and III.2.4). Then, two ageing tests developed in this thesis are cycled:

- The emulation of the SU phase (SU-AST) in single cell, as detailed in section III.3.1, with coupled the CO/CO_2 gas analysis, the polarization curve, and the cyclic voltammetry techniques during/after the ageing test;
- The realistic SU with H_2|Air front propagation along the anode channel and the SD phase (Stack-SU/SD AST) in short-stack, as detailed in III.3.2, with coupled the Current Density Distribution Mapping (S++® device) inserted in the center of the stack, the polarization curves and the cyclic voltammetry techniques, during/after the ageing test.

Both ageing tests are firstly tested and validated in reference case, *i.e.*, without protective strategy, in order to perform then sensitive studies according to “mitigating parameters” for the SU-AST protocol and “shunting device configurations” for the Stack-SU/SD AST protocol.

Finally, a *post-mortem* study on fresh and aged MEA samples after the SU-AST protocol in single cell characterizes the local electrochemical and physico-chemical properties modifications within the CCL, according to the “mitigating parameters”.

Chapter IV. SINGLE-CELL SENSITIVITY STUDY OF PERFORMANCE LOSSES BY EMULATING START-UP PHASES

IV.1. INTRODUCTION

In this chapter, the Start-Up Accelerated Stress Test (AST) "SU-AST" profile proposed in Chapter III (III.3.1) to mimic the potential variation at the cathode electrode during the H_2|Air front propagation is performed on 98 cm² single cell with state-of-art flow-field design for stack (III.2.1) [71]. This protocol is cycled 100 times as an ageing test. Periodic characterizations allow to assess the evolution of the electro-chemical and physico-chemical properties within CCL, and to measure the impact on cell performance.

The reference case in the following section IV.2 shows the overall evolution of the cell in terms of performance, electrochemical CV characterizations, and CO/CO_2 emissions. In fact, the results for the reference case are detailed in the section IV.2.1 while the sensitivity study of identified mitigating parameters is done in the section IV.2.2. A discussion part (section IV.2.3) is proposed in order to clarify the respective impact of the operating parameters.

To highlight the degradation mechanisms and the electro-chemical performance losses for each aged MEA, a complementary *post-mortem* study (section IV.3) is carried out in order to investigate the evolution of the physical-chemical (section IV.3.1) and electro-chemical (section IV.3.2) properties of the cathodic catalyst layer after our SU-AST protocol. By coupling all the techniques, a discussion on degradation mechanisms of the CCL in our ageing test is proposed in the section IV.3.3.

This experimental work made it possible to publish an article based on single cell results [139] and to file a patent.

IV.2. EVOLUTION OF PERFORMANCE DURING SU-AST

IV.2.1. Unprotected Start-Up phase (reference case)

IV.2.1.1. Cell performance evolution

Unprotected Start-Up phase has been emulated and carried out following the Accelerated Stress Test (AST) protocol described previously in section III.3.1 (1.6 V – 1.5 s – 80/80% RH – 60 °C). Drastic performance decay is obtained after 100 cycles (cf. Figure IV-1a). Average cell voltage losses per cycle at different current densities are: -0.48, -0.60 and - 0.86 $mV.cycle^{-1}$ @ 0.1, 0.5 and 1.2 $A.cm^{-2}$, respectively. Difference between cell voltage along SU-AST cycles (*i.e.,* every 20 cycles in Figure IV-1b) and initial performance shows an amplification of the degradations from low to high current density. However, an initial improvement of performance is noticed during the first 20 SU-AST cycles at 1.2 A.cm^{-2} and then followed by a steep decrease (cf. Figure IV-1b). This initial performance improvement at the highest current densities may reflect a favorable CCL structural modification at nano- and/or micro-scale affecting mass-transport properties in addition to the break-in phase. However, at low and medium current densities, the cell performance decreases continuously during the 100 cycles up to reach 10% drop of cell performance at 1.2 A.cm^{-2}.

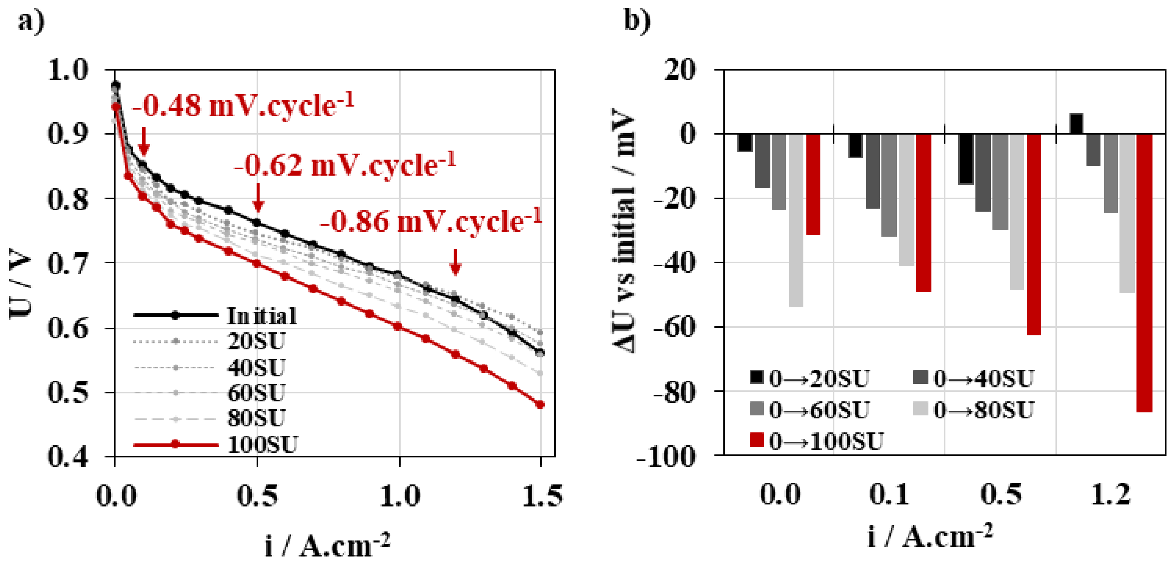

Figure IV-1: a) Periodic polarization curves measured initially and after 20, 40, 60, 80 and 100 SU-AST. b) Difference between initial cell voltage and after 20, 40, 60, 80 and 100 SU-AST cycles. Single cell operating conditions: H_2/Air – 80 °C – 50/50% RH – 1.5/1.5 bar$_{abs}$ (in) –St 1.5/2 (i_{min} = 0.2 A.cm^{-2})

IV.2.1.2. Voltammogram evolution

The evolution of CV profiles (1st and 3rd scan) from the 1st to 100th SU-AST cycles and every 20 cycles is shown in Figure IV-2a. The Pt-H$_{ads}$ desorption peak, used for ECSA calculation, is highlighted in Figure IV-2b. As shown on this figure, the overall area decreases as the number of cycle progresses with an emergence of more notable Pt-H$_{ads}$ desorption peaks related to (110) and (100) facets at about 0.15 and 0.25 V, respectively, suggesting a growth of Pt nanoparticles [140]. The evolution of the calculated ECSA appears in Figure IV-2c (grey points), normalized to its initial value (in other words, the first value is 100%). A quasi-linear ECSA loss is observed during cycles with a slope of -0.63%.cycle^{-1}.

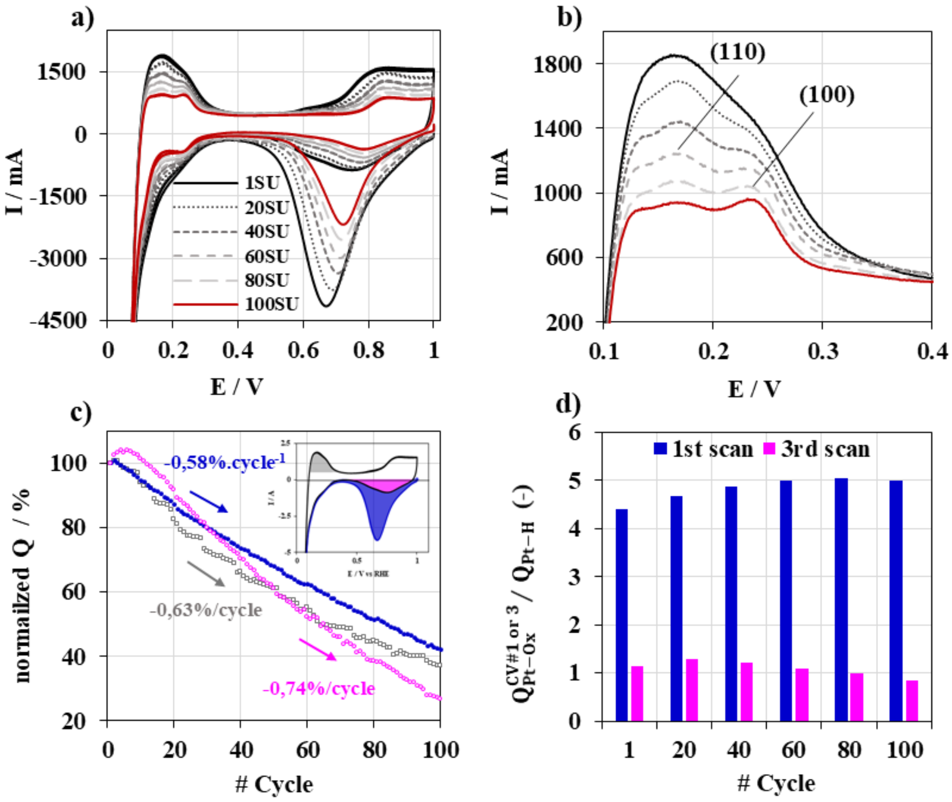

Figure IV-2: a) Voltammogram recorded during the first and third scan following "SU-phase"; b) zoom in Pt-H_{ads} desorption region from first to 100th SU-AST cycles; c) Normalized coulometry measurements relative to initial values and d) estimated oxide ratio at 1st, 20th, 40th, 60th, 80th and 100th cycles. Single cell operating conditions: H_2/N_2 – 60 °C – 80/80% RH – 1.0/1.0 bar_{abs} (out) –300/800 $nL.h^{-1}$

The evolution of the peak of the Pt-O_x reduction (in negative potential sweep) is shown in Figure IV-2a in the 0.45 – 1.0 V range. As expected, the intensity of the peak is higher for the first scan compared to the third one. Indeed, the first reduction peak includes the oxide species formed during the SU phase at 1.6 V during 1.5 s while the third scan reduces only the oxide species formed during the previous positive potential sweep up to 1.0 V_{RHE}. As illustrated on Figure IV-2c, a decrease of the coulometry normalized by its initial value is observed for the scan #1 (blue points) and #3 (pink points) with a linear negative slope at -0.74 and - 0.58%.$cycle^{-1}$, respectively). The shift of peak potential towards higher potential (Figure IV-2a) is also ascribed to the growth of the Pt nanoparticle size.

The ratio between the Pt-O_x oxide peak coulometry (blue/pink area) and the Pt-H_{ads} desorption coulometry (grey area) as a function of the number of SU is plotted on Figure IV-2d. It can be noted that for scan #1 and #3, these values evolve slightly during the SU-AST and are evaluated about 4.9 and 1.1 respectively. We can specify that an oxide ratio around 1.0 indicates the CV phase essentially formed –OH_{ad} (1e^-) according to reaction (I-11). A value between 1.0 and 2.0 indicates a formation of –O_{ad} (2e^-) according to reaction (I-12) [50]. A ratio much higher than 2.0 depicts more oxygenated species formation onto Pt surface such as $–O_{2,ad}$ (Pt^{+IV} state) and further sub-oxide formation due to Place-exchange mechanism above 1.1 V_{RHE} [51]. Thus, the SU phase condition (1.6 V – 1.5 s) induces an oxidation rate onto Pt about 5-fold higher than the conventional CV (from 0.065 to 1.0 V at 50 $mV.s^{-1}$). This significant Pt-O_x formation may accelerate the Pt dissolution and redeposition as formulated in the Chapter I (I.3.2.2.2) and participate to the overall ECSA loss. In addition, the Pt detachment and agglomeration can be also caused by the CSC mechanism as demonstrated hereafter.

IV.2.1.3. CSC evolution

Figure IV-3(a, b) details the CO_2 and CO emissions respectively during the 1st, the 20th and the 100th SU-AST cycle. The x-axis is corrected 180 s in comparison to the record illustrated in Figure III-9. During the 1st SU-AST cycle, sharp increasing of CO (up to 0.3 $µg.s^{-1}$) and CO_2 (up to ~15 $µg.s^{-1}$) gas emissions are measured in about 30 and 50 s as major peaks, respectively. Then, the emission rate quickly diminishes down to 0.0 $µg.s^{-1}$ for the CO, while the CO_2 shows three subsequent minor peaks in about 140 s. Along the ageing test, the major (CO and CO_2) and the minor peaks (CO_2) diminishes gradually. At the last cycles (100th), major peaks attain about 5 $µg.s^{-1}$ for the CO_2 and 0.08 $µg.s^{-1}$ for the CO gas. The CO_2 minor peaks are no longer detected.

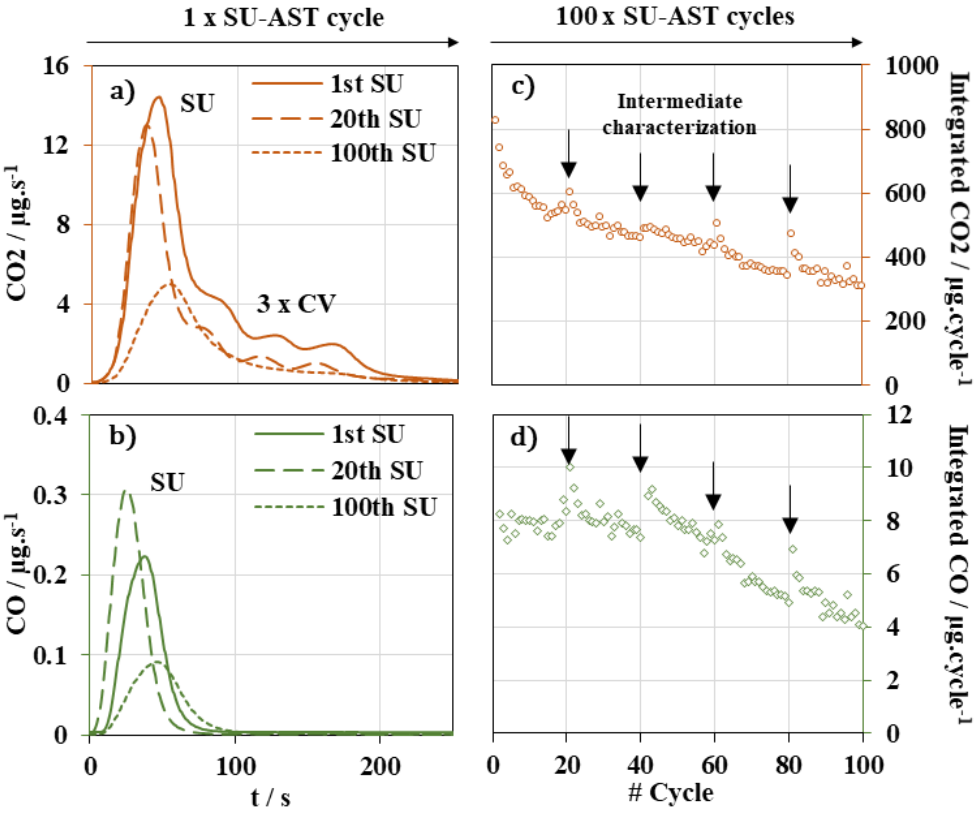

Figure IV-3: Detailed CO_2 (a) and CO (b) emission profiles during the 100 cycles in reference SU-AST; Integrated (c) CO_2 and (d) CO gas emission per cycle along reference SU-AST. Single cell operating conditions: H_2/N_2 – 60 °C – 80/80% RH – 1.0/1.0 bar_{abs} (out) –300/800 $nL.h^{-1}$

Major and minor peaks are in accordance the two carbon corrosion mechanisms due to the SU and CV phases. Firstly, SU-phase (potential > 1 V) induces mainly direct CSC mechanism over the whole surface of the carbon support, as explained previously in III.3.1.1, emitting the major CO and CO_2 peaks according to CSC reactions in section I.3.2.1.2 [24]–[28]. It can be noted that CO remains very low compared to CO_2 rate emission (100-fold lower). For a detection issue, the CO gas emission is not monitored for the next cases developed in the sensitivity study (section IV.2.2).

Secondly, the potential scans between 0.065 and 1.0 V during the 3-CV phase enhances catalyzed corrosion mechanism, leading to three CO_2 minor peak emissions (section I.3.2.1.2). In this case, Pt particles onto carbon support plays an important role to promote CSC reactions. Intermediate oxidized carbon species onto carbon support named CO_{surf} are formed during SU-phase can further move close to Pt active sites –(Pt-CO) and even get adsorbed onto Pt sites to finally react with oxygenated species (Pt-OH, H_2O), related to reactions mentioned in section I.3.2.1, during CV phase to finally generate CO_2 [20], [25], [29].

By repeating cycles, SU-induced CO and CO_2 peaks reduce gradually and may indicate a carbon support morphologic evolution. As studied by Castanheira *et al.* [141], amorphous and disordered zones in fresh CCL are easily corroded, producing a large amount of CO and CO_2 at the beginning of test. Then, the remaining ordered and graphitic zones are harder to corrode and can explain a lower amount of CO_2 production at the end of the test. Moreover, each CV also induces CO_2 peaks which shrink progressively and even disappear at the end of test after 100 cycles. This may be explained by a lower intermediate CO_{surf} formation during SU phase (not completely evolved in CO_2 gas) due to the evolution of carbon support and/or a lower catalytic effect due to the Pt nanoparticles evolution in terms of size and/or distribution over the carbon support.

Figure IV-3(c, d) illustrates CO and CO_2 emission rates integrated over each cycle duration. Both integrated CO and CO_2 emissions per cycle diminish progressively along SU-AST cycles (from 8 to 4 $\mu g_{CO}.cycle^{-1}$ and from 800 to 300 $\mu g_{CO2}.cycle^{-1}$) in accordance with the evolution of CO and CO_2 peaks, detailed above. To go further, the CSC of amorphous and disordered domains seem to occur preferentially during the first 20 cycles with a more important CO_2 rate. Nevertheless, the CSC of graphitic and ordered domains participates concomitantly to the CO_2 emission but with a lower rate during all cycles. Globally, cumulative CO and CO_2 emissions are respectively estimated: 6.4 μg_{CO} and 45.5 mg_{CO2} after 100 SU-AST reference cycles.

Let us also mention that an intensification of both CO and CO_2 gas emissions can be pointed out after each 20 cycles when SU-AST restarts after polarization curve. These performance characterizations may affect carbon support due to the presence of oxygen in the cathode side (Air feeding), the higher operating temperature (80 °C *vs*. 60 °C during SU-AST) and the water production within CCL during about 2 hours. Somehow, those operating conditions promote a higher CO_{surf} formation and/or local carbon support embrittlement that causes a higher production of CO_2 during the first cycles occurring after this periodic characterization under H_2/Air.

IV.2.2. Sensitive study of operating parameters in Start-Up phase

Once the SU-AST protocol tested and validated in the reference condition (1.6 V_{RHE} – 1.5 s – 60 °C – 80/80% RH), a parametric study has been achieved on four "mitigating" parameters identified in the section II.3 and described in the section III.3.1.2. The details of the SU-AST conditions for each parameter is given in the Table IV-1. Thus, eleven single cells with fresh MEA and the same flow-field plates are tested in this thesis work by exploring the influence of the E_{front} (from 1.6 to 1.0 V_{RHE}), the front duration t_{front} (from 1.5 to 0.5 s), the $RH_{a/c}$ of reactant gas (from 80/95 to 50/50% RH) and the cell temperature T_{cell} (from 60 to 30 °C).

Table IV-1: Summary of mitigation parameters used in the SU-AST sensitivity study

Case	Parameter	E_{front} (V)	t_{front} (s)	T_{cell} (°C)	$RH_{a/c}$ (%)
#1	**Reference**	**1.6**	**1.5**	**60**	**80/80**
#2		**1.4**	1.5	60	80/80
#3	E_{front}	**1.2**	1.5	60	80/80
#4		**1.0**	1.5	60	80/80
#5	t_{front}	1.6	**1.0**	60	80/80
#6		1.6	**0.5**	60	80/80
#7	T_{cell}	1.6	1.5	**45**	80/80
#8		1.6	1.5	**30**	80/80
#9		1.6	1.5	60	**80/95**
#10	$RH_{a/c}$	1.6	1.5	60	**80/50**
#11		1.6	1.5	60	**50/50**

IV.2.2.1. *Impact on the cell performance*

Performance evolutions measured by polarization curves between the fresh and the aged MEA (after 100 SU-AST cycles) are illustrated in Figure IV-4 depending on the mitigating parameters.

Regarding the effect of potential, for the ageing case at 1.6 V (reference: 1.6 V – 1.5 s – 80/80% RH – 60 °C) and 1.4 V, cell voltage trends during SU-AST are similar. In both cases, harsh losses of performance are observed: -0.86 and -0.73 $mV.cycle^{-1}$ at 1.2 $A.cm^{-2}$ for 1.6 and 1.4 V cases, respectively. On contrary, the 1.2 and 1.0 V cases reveal an improvement of performance at high current density: +0.17 and +0.24 $mV.cycle^{-1}$ at 1.2 $A.cm^{-2}$ after the 100 cycles, respectively. At 1.0 and 1.2 V, performances at low and medium current densities are rather not affected by the SU-AST protocol. No surprise, potential excursion during SU-phase seems to play a crucial role on performance evolutions.

Exposing cathodic electrode at 1.0 – 1.2 V (slightly beyond FC operation) may induce a catalytic depollution/evolution and/or a pore modification which is beneficial to fuel cell operation. That suggests a uncomplete breaking phase.

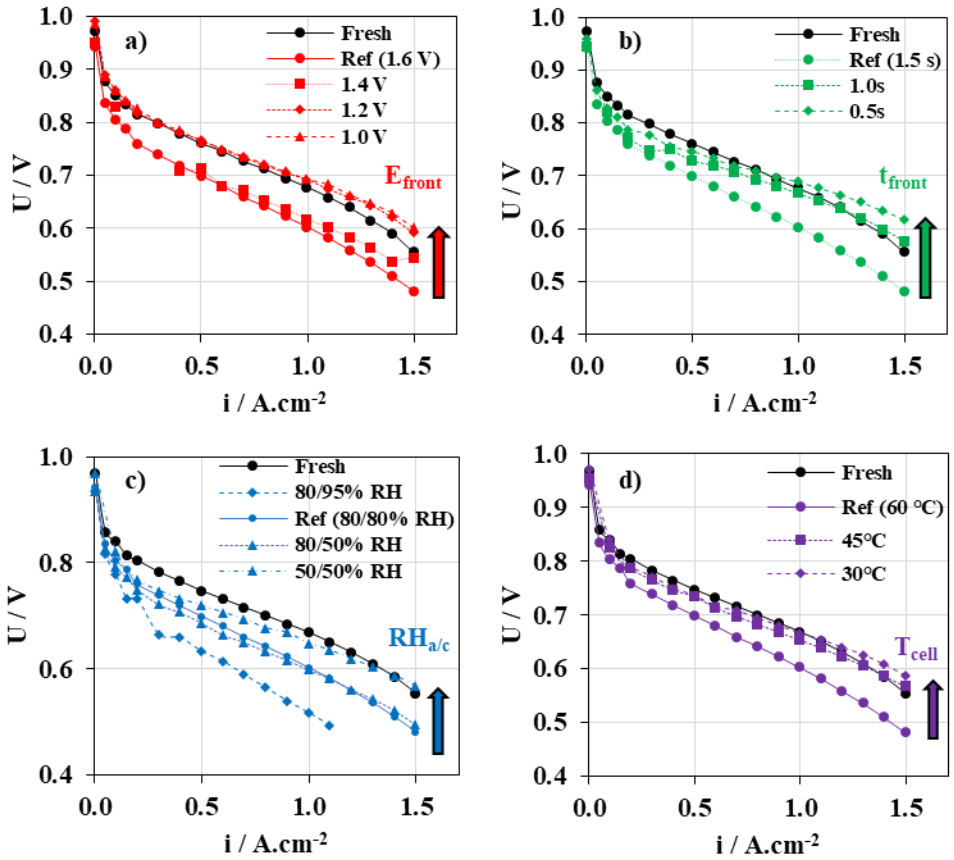

Figure IV-4: Fresh and aged (after 100 cycles) polarization curve according to a) the front potential E_{front}, b) the exposure time t_{front}, c) the relative humidity of the reactant gas $RH_{a/c}$ and d) the cell temperature T_{cell}. Single cell operating conditions: H_2/Air – 80 °C – 50/50% RH – 1.5/1.5 bar_{abs} (in) –ST 1.5/2 (i_{min} = 0.2 A.cm^{-2})

Regarding the effect of exposure time, lowering it from 1.5 s down to 1.0 and 0.5 s at 1.6 V varies the overall performance decay: from -0.86 to -0.02 and +0.23 mV.cycle^{-1} at 1.2 A.cm^{-2}, respectively. The ageing case at 0.5 s show a slight improvement of cell performance. Namely, the exposure time has only a significant impact on performance loss at high current density. Indeed, performance decay at low and medium current densities are similar below 1.0 s: -0.49, -0.45 and -0.41 mV.cycle^{-1} at 0.1 A.cm^{-2}, respectively.

The $RH_{a/c}$ parameter also shows an effect on the performance decay with a potential excursion at 1.6 V during 1.5 s. Lowering the cathode RH from 80 to 50% (keeping 80% at the anode side) slightly attenuates the cell performance decay: from -0.86 to -0.68 mV.cycle^{-1} at 1.2 A.cm^{-2}. On the contrary, a higher cathode RH at 95% significantly increases the losses of voltage in the whole range of current density: -1.60 mV.cycle^{-1} at 1.0 A.cm^{-2} (1.2 A.cm^{-2} could not be reached during final measurement). Lowering both anode and cathode RH at 50% is the most mitigating case with a minor decay at high current density: -0.08 mV.cycle^{-2} at 1.2 A.cm^{-2}. Lowering the cathode RH is not sufficient to mitigate the degradation mechanism. Indeed, the water supplied by the anode diffuses through the membrane to the cathode with the use of fine membrane (*ca*. 10 µm). It is necessary to reduce both anode and cathode RH conditions simultaneously.

Finally, lowering the cell temperature also reveals fruitful mitigation effect on the cell performance decay from -0.86 to -0.09 and +0.09 mV.cycle^{-1} at 1.2 A.cm^{-2} for 60 °C to 45 °C and 30 °C respectively. This latter case shows a gain of cell voltage at high current density after 100 cycles.

Even if a SU occurs with an H_2|Air front, it can be expected to minimize dramatically the effect of the high cathodic potential, by acting on the front time exposure (0.5 s), humidity (RH 50%) and cell temperature (30 °C).

IV.2.2.2. Impact on the electrochemical surface area

Effects of operating conditions on ECSA losses normalized to their initial values are investigated from the first scans on fresh MEAs and aged MEAs after 100 cycles, as illustrated in Figure IV-5. By comparison to the reference case (1.6 V – 1.5 s – 80/80% RH – 60 °C) for which the normalized ECSA loss is estimated at -63%$_{ECSA}$, the operating parameters affect differently the normalized ESCA as summarized in Figure IV-6.

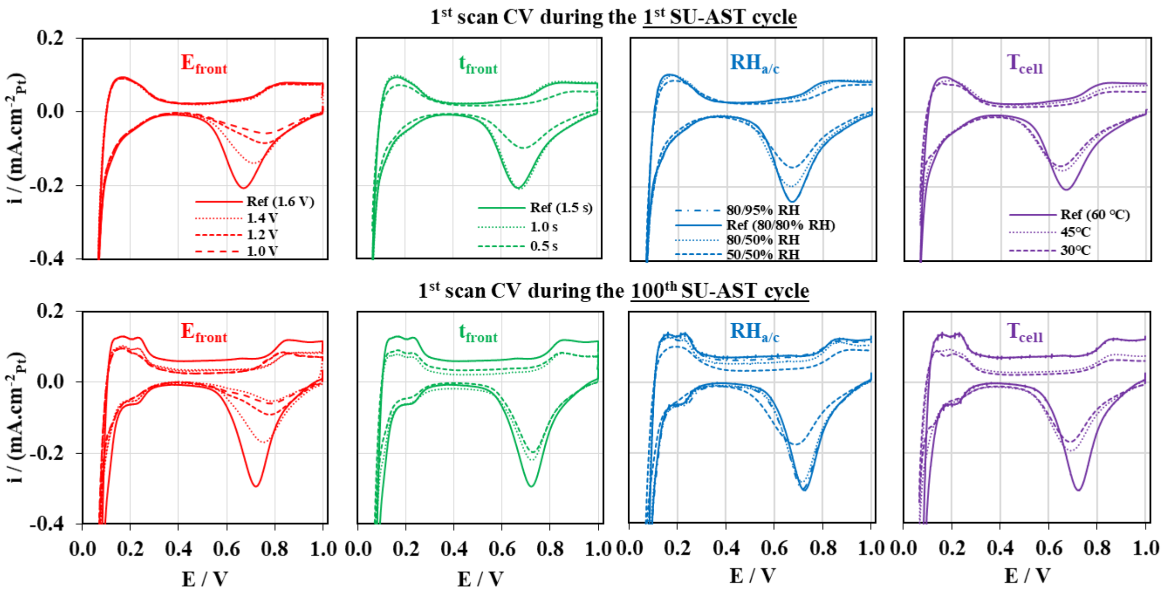

Figure IV-5: First scan of the voltammograms normalized by ECSA during the first and the last SU-AST cycle according to the mitigating parameters. Single cell operating conditions: H_2/N_2 – T_{cell} – $RH_{a/c}$ % – 1.0/1.0 bar$_{abs}$ (out) –300/800 nL.h^{-1}

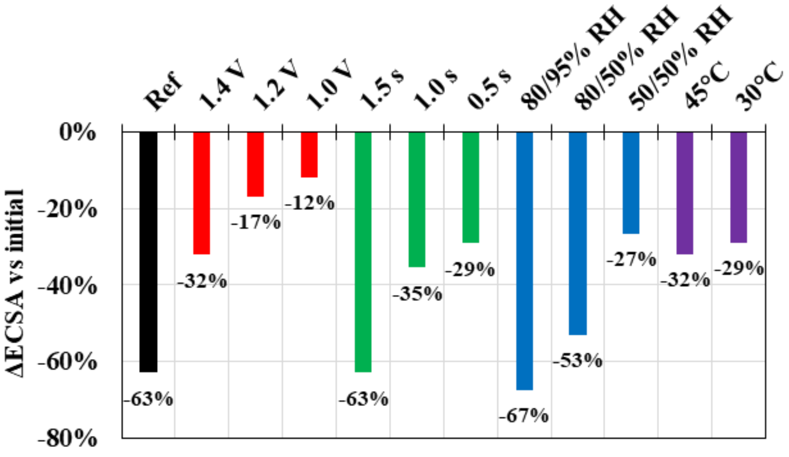

Figure IV-6: ECSA loss between the first and the last SU-AST cycles according to the mitigating parameters

Ratio calculations between Pt-O_x reductions ($Q_{PtOx\text{-}red}$) and Pt-H_{ads} desorptions ($Q_{Pt\text{-}Hdes}$) from the first scan are illustrated in Figure IV-7. They clearly depend on each operating conditions as explained below.

By exposing CCL to a higher potential in SU phase, the coulometry of Pt-O_x reduction is higher, and in addition, the peak is shifted at lower potential during the first negative scan: the peak position during the 1st scan is measured at 0.68 V and 0.78 V for the 1.6 and 1.4 V case. That suggests the nature of oxide species depend on the potential during SU phase. A higher potential excursion promotes a higher Pt oxidation degree as illustrated on Figure IV-7.

On the contrary, a lower duration at 1.6 V (less than 1.5 s) and a lower hygrometry of reactant gas (less than 80%) do not seem to affect the quantities and types of Pt oxide formed during SU phase. The peak potential values during the oxide reduction are identical for both mitigating parameters (about 0.675 V). However, the total charge of the Pt-O_x reduction is reduced, assuming lower kinetics of Pt oxidation reactions, excepted between the reference (1.5 s) and the 1.0 s cases during the 1st cycle. T_{cell} also modifies the profile related to the reduction of Pt-Ox. By decreasing the cell temperature, the position of the Pt-O_x peak decreases from 0.675 V to 0.65 V probably because of lower reduction kinetics and less Pt oxides formation during the positive scan (Pt oxidation kinetics also affected).

Finally, regarding the Pt oxidation degree, *i.e.*, the coulometry ratio between the Pt-O_x reduction and the Pt-H_{ad} desorption is evaluated according to the SU-AST conditions in the first CV scan, as summarized in Figure IV-7. The decrease of each parameter (E_{front}, t_{front}, $RH_{a/c}$, T_{cell}) hinders the Pt oxidation and likely the Pt dissolution / Place-exchange mechanism. Focusing on the third scan, this ratio value is the same in all SU-AST investigations (about 1.2). Repeated potential scan between 0.065 and 1.0 V establishes similar oxide degree due to its complete reduction/decontamination during the two first CV scans.

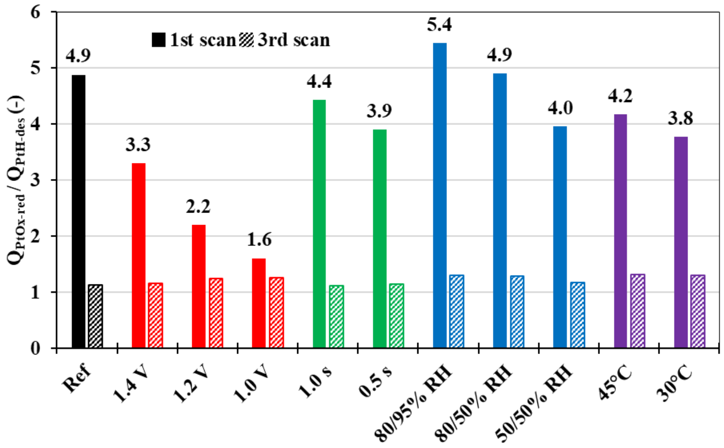

Figure IV-7: Oxide ratio related to the proton desorption charge estimated during the first and the third scan according to the mitigating parameters

IV.2.2.3. Impact on carbon support corrosion

The evolution of CO_2 emission rates per cycle along SU-AST protocol are presented in Figure IV-8, showing the impact of each operating parameters. For the $RH_{a/c}$ and T_{cell} parameters, no intermediate polarization has been performed. Thus, the intermediate intensifications of the CO_2 gas every 20 cycles are not observed.

Compared to the reference case (1.6 V), the cumulated CO_2 emission over the 100 cycles is reduced from 46 down to 15, 6 and 5 mg_{CO2} for the 1.4, 1.2 and 1.0 V cases, illustrating the impact of lowering the electrode potential. No significant difference is measured between 1.2 V and 1.0 V cases, in agreement with previous works showing a significantly lower CO_2 emission rate for potential below 1.2 V [24]–[28]. The CSC mechanism follows an exponential trend in terms of the potential above 1.2 V.

The evolution of CO_2 rates integrated per cycle along SU-AST protocol for 1.0 and 0.5 s cases makes possible the analysis of the impact of the exposure time. Compared to the reference case (1.5 s), cumulated CO_2 emissions are varied from 46 to 45 mg_{CO2} (1.0 s) and 15 mg_{CO2} (0.5 s). A strong similarity between 1.5 and 1.0 s case is observed whereas a three-fold factor between 1.5 s *vs.* 0.5 s is also observed on CO_2 emissions (46 *vs.* 15 mg_{CO2}, respectively).

As expected, lowering the $RH_{a/c}$ and/or T_{cell} plays important role on the CSC mechanism since these parameters can affect the water content in the electrode which promote the corrosion reactions. Indeed, total CO_2 gas emission detected varies from 45 mg_{CO2} in the reference case to 54, 40 and 19 mg_{CO2} (in 95/80%, 50/80% and 50/50% RH cases, respectively) and to 23 and 15 mg_{CO2} (in 45 °C and 30 °C cases, respectively).

In all cases, the evolution of the cumulated CO_2 emission per cycle seems to depict a morphologic modification with a preferential CSC of disordered domains during the first 20 cycles, as suggested by Castanheira *et al.* [141]. Let us stress that for all the most severe cases (1.6 V, 60 °C, RH ≥ 80%, $t_{front} \geq 1.0$ s), their CO_2 emission rates after 100 cycles are almost the same about 350 µg. The CSC is likely limited in those cases by the nature/structure of the remaining carbon particles.

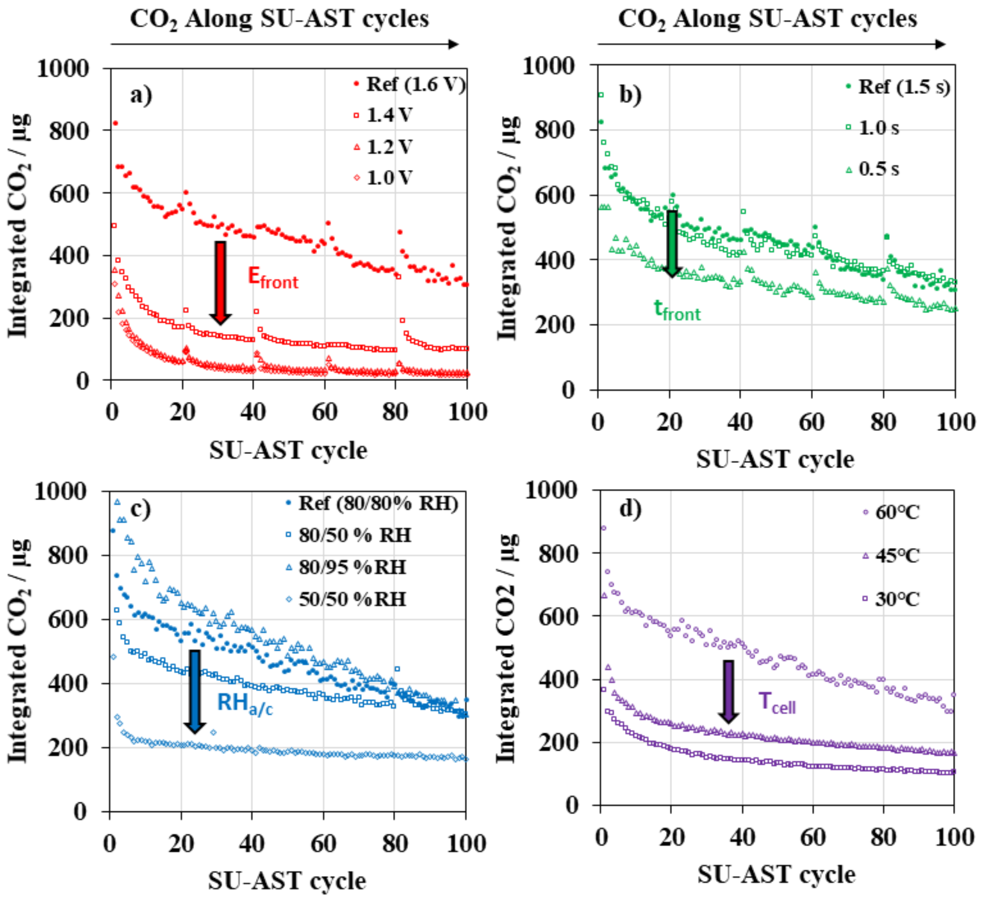

Figure IV-8: Integrated CO_2 gas emission per cycle along the SU-AST protocol according to the mitigating parameters. Single cell operating conditions: H_2/N_2 – T_{cell} – $RH_{a/c}$ % – 1.0/1.0 bar_{abs} (out) –300/800 $nL.h^{-1}$

IV.2.3. Discussion of *in-situ* SU-AST analysis

A deeper understanding on the degradation mechanisms of the CCL and their impact on cell performances is discussed in this section.

IV.2.3.1. Platinum and carbon support degradation mechanisms in SU-AST conditions

Figure IV-9 plots ECSA losses and cumulative CO_2 emissions along SU-AST cycles (every 20 cycles) for each operating parameter. Regarding Figure IV-9and the reference case, a proportionality appears between the ECSA losses and the cumulative CO_2 emissions along the SU-AST protocol, from the fresh (0 cycle) to the aged (100 cycles) conditions. This seems to suggest that ECSA losses could be mainly due to CSC mechanisms, through the detachment / agglomeration of Pt nanoparticles and the Place-exchange mechanism as discussed in section I.3.2.3.1. This strong relation is also observed through the investigation of the E_{front}, the $RH_{a/c}$ and the T_{cell} parameters, as illustrated in Figure IV-9(a, c, d). High potential excursion, high water content in the CCL (relative to $RH_{a/c}$) and high cell temperature accelerate the kinetics of the CSC mechanism, and thus, the Pt detachment / agglomeration.

However, ECSA losses and CO_2 emissions are less correlated on Figure IV-9b, where the impact of t_{front} is investigated. Cumulative CO_2 emission is constant when t_{front} decreases from 1.5 s to 1.0 s and is reduced by only 30 % at 0.5 s. This indicates that CO_2 is very likely emitted mainly at the beginning of the voltage plateau at 1.6 V, for a duration estimated below 1.0 s. In contrast, ECSA loss at 1.6 V is significantly lowered when t_{front} decreases from 1.5 s to 1.0 s, and only slightly reduced when switching from 1.0 s to 0.5 s. That highlights the Pt dissolution / redeposition (Place-Exchange) occurrence, simultaneously to the Pt detachment / agglomeration, due to the high potential excursions above 1.0 V. The t_{front} investigation seems to show that the kinetics of the Platinum oxidation is slower than the carbon oxidation.

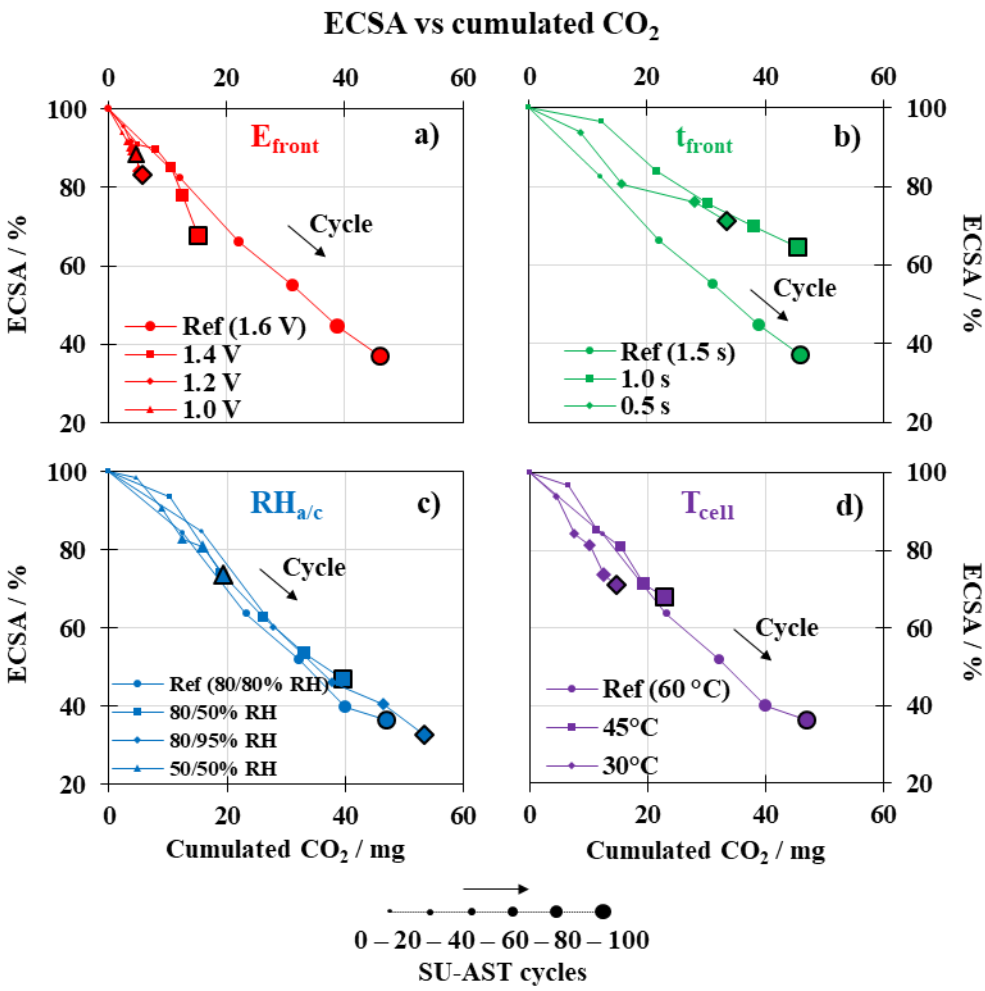

Figure IV-9: ECSA evolution vs. cumulated CO_2 emission every 20 cycles along the SU-AST according to the mitigating parameters

IV.2.3.2. Impact on the electro-chemical performance

The impact of the alteration of the cathode catalyst in terms of ECSA (combined effects between dissolution/redeposition + Place-exchange mechanism and detachment/agglomeration of Pt nanoparticles and carbon support corrosion) on cell performance is presented from Figure IV-10. In fact, cell voltage evolution are compared to initial performance at different current densities: at 0.1, 0.5 and 1.2 A cm^{-2}, as illustrated in Figure IV-10 (a, d, g), (b, e, h) and (c, f, i), respectively. They are plotted versus the ECSA losses along SU-AST cycles, with one point every 20 cycles for the E_{front} and t_{front} parameters and for the last cycle for the $RH_{a/c}$ and T_{cell} parameters.

The main observations of the cell voltage according to the current density are detailed as follows:

- At 0.1 A.cm^{-2}, the cell voltage is linear with the ECSA loss along the SU-AST protocol in most SU-AST cases. As expected, the activation limitation is predominant and is strongly linked to the Pt nanoparticles accessible to the reactant gas, protons and electrons. By lowering the four operating conditions (*vs.* the reference case), the ECSA loss is reduced, and the drop of the cell voltage is mitigated. Surprisingly, improvement of cell voltage is measured for the E_{front} below 1.2 V and the T_{cell} below to 45 °C (after 100 SU-AST cycles). For the SU-AST protocol at 1.0 V case, this improvement occurs during the first 40 cycles, followed by a progressive drop.
- At 0.5 A.cm^{-2}, the cell voltage evolutions are less linear with the ECSA losses as cycle progress. From 40 – 60 SU-AST cycles, the cell voltage decreases with probably the emergence of the mass-transport limitations related to the carbon support degradation. After 100 cycles, the voltage decays and the ECSA losses are mitigated by lowering the four operating parameters (*vs.* the reference case). Only the SU-AST protocol at 1.0 V demonstrates an improvement of the cell voltage during the 20 first cycles despites the ECSA loss, followed by a progressive drop of performance during the next 80 cycles.
- At 1.2 A.cm^{-2}, the cell evolutions are not linear with the ECSA loss along the SU-AST protocol. At this high current density, the mass-transport limitation is predominant, and this trend depicts an important impact of the CSC (linear with the ECSA loss) on the cell performance. Similar as 0.1 and 0.5 A.cm^{-2}, the four operating parameters strongly alter the cell voltage and ECSA losses (*vs.* the reference case). The lower the operating parameters, the softer the degradations within the CCL. On the contrary, the SU-AST protocol at 1.0 V still reveals an initial improvement of the cell voltage (similar as 0.1 and 0.5 A.cm^{-2}), followed by a slight drop during the last cycles.

Unexpected initial improvements during the first cycles are systematically observed on Figure IV-10 (d, f) at 1.2 A.cm^{-2}, suggesting that mass-transport at high current densities is improved. Beneficial CCL modifications have been proposed in section IV.2.1.1. Indeed, higher CO_2 rate in the first cycles (Figure IV-8a) confirms an easier CSC of amorphous/disordered domains leading to an improvement of cell performances, as already mentioned and suggested by Castanheira *et al.* [141]. This latter suggests that fresh CCL exhibits non-optimized carbon support properties (or micro/nano-structures within the CCL), which hinders ORR kinetics and/or gas transports abilities.

After these initial performance improvements, the additional cycles induce a harsh ECSA loss and voltage drop, except for the E_{front} case at 1.2 and 1.0 V. It should be noted that the non-linear evolutions of the cell voltage loss *vs.* ECSA loss in Figure IV-10 (c, f) can be explained by a progressive embrittlement leading to a collapse of carbon structure [58]. On the contrary, these initial improvements are conserved until the end-of-test for E_{front} below 1.2 V. In fact, at these potentials, further cycles weakly corrode the carbon microporous with a lower impact on ECSA and cell voltage losses. These observations highlight a beneficial effect to expose the cathodic potential above 1.0 V during break-in for conditioning carbon support. In fact, from this work, an ingenious experimental protocol has been validated and patented recently to optimize cell performances at high current density without deteriorating the performances at medium and low current densities.

Finally, by comparing the SU-AST protocols aged in case #2, #7 and #10 (1.4 V, 45 °C and 50/50% RH), total CO_2 emission and Pt ECSA losses are similar after the ageing test. However, it appears that the final cell voltage is not comparable. The performance decay is not fully in direct relationship with the amount of the carbon corroded and the Pt redeposited/agglomerated during our SU-AST protocol. The micro and nano-scale properties of the Pt/C are altered differently according to the operating conditions. Beyond the scope of this study, additional study to characterize the evolution of the nature/structure of the remaining Platinum and carbon particles would be needed.

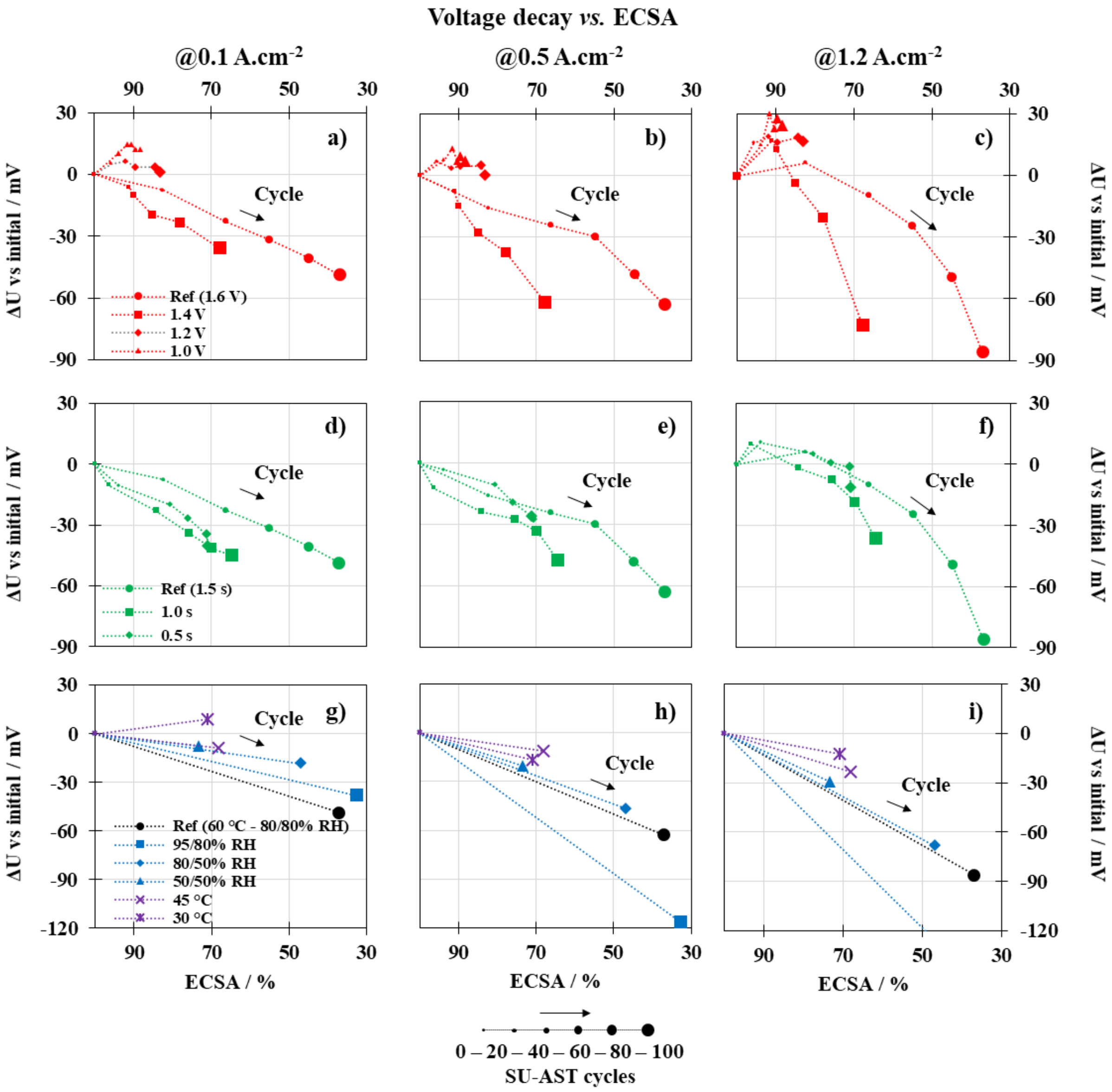

Figure IV-10: Cell voltage vs. ECSA evolution at 0.1 A.cm^{-2} (a, d, g), 0.5 A.cm^{-2} (b, e, h) and 1.2 A.cm^{-2} (c, f, i) every 20 cycles along SU-AST protocol for the E$_{front}$ and t$_{front}$ parameters and at the 100th cycle for the RH$_{a/c}$ and T$_{cell}$ parameters

IV.3. *POST-MORTEM* SU-AST ANALYSIS

After the experimental study in large single cell, the CCL morphological evolution coupled to local electro-chemical characterizations are performed here (presented in section III.4). These results shall be fruitful to distinguish, and quantity the different ageing mechanisms involved during SU phase according to the environmental conditions.

IV.3.1. Physico-Chemical properties evolution

IV.3.1.1. SEM observations

Cross-sectional observations by scanning electron microscopy of the fresh and aged MEAs make it possible to highlight the morphological evolution of the cathodic catalytic layer, including thinning related to the corrosion of the carbon support and the densification of the Pt nanoparticles related to dissolution/redeposition and detachment/agglomeration. This technique is explained in the Chapter III (section III.4.2.1).

IV.3.1.1.1. Spatial study of CCL thickness for the reference case

A first spatial study on the reference SU-AST case (1.6 V – 1.5 s – 80/80% RH – 60 °C) has been performed by probing locally the cross-section of the MEA along the cathode channel (inlet – middle – outlet) and under the rib / channel as illustrated in Figure IV-11. A variation about 10% of the CCL thickness under the channel is measured along the cathode channel: 9.2, 7.5 and 7.0 µm at the cathode inlet – middle – outlet, respectively. This deviation magnitude is similar with the one estimated for the fresh MEA in the reproducibility study (see section III.4.2.1).

A densification of the Pt nanoparticles is also observed compared to the fresh MEA (cf. Figure IV-11). The Pt band is present at the PEM|CCL interface (and not in the bulk membrane) because of the N_2 gas supply in the cathode during the SU-AST protocol. Moreover, compact areas under the rib are present within the CCL and their thicknesses are estimated to 5.8, 5.9 and 5.5 µm (respectively at the inlet - middle - outlet of the cathode). The compression level under the rib during the assembly phase may be responsible for this local higher collapse. For a sake of clarity, the next observations were made in areas supposed to face the channels, in the absence of the effect of mechanical deformation.

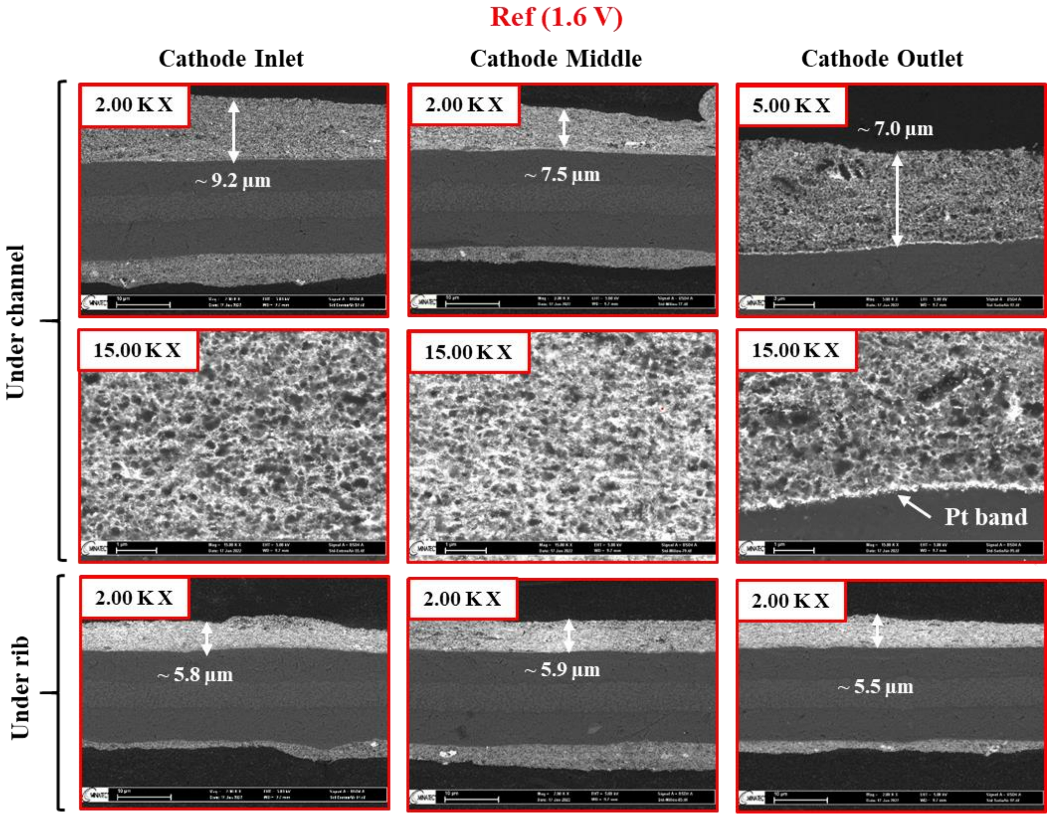

Figure IV-11: SEM cross-sectional images of fresh and aged MEA at 1.6 V located at the cathode inlet – middle – outlet areas under the channel and the rib

Figure IV-12 recapitulates the averaged thickness of the CCL for the fresh MEA and for each area on the aged MEA with the reference protocol at 1.6 V under the channel. Let us mention that the measurement on fresh MEA case does not require specific location since it has never been assembled in single cell and thus it is supposed homogeneous on the whole active area. The thinning of the CCL is about 50% compared to the fresh MEA after the SU-AST protocol at 1.6 V (case #1). The deviation is 10%, as estimated for the fresh MEA samples as mentioned in section III.4.2.1). Consequently, the homogeneous degradation of the CCL is validated on the active area as expected from the SU-AST protocol based on the polarization of the entire electrode (cf. Figure III-10). That is why, SEM will be performed only at the cathode middle under the channel for sake of simplicity on other samples. A Pt band related to the Platinum dissolution and precipitation (section I.3.2.2.2) is observed at the PEM|CCL interface due to inert gas atmosphere used during the SU-AST protocol (N_2).

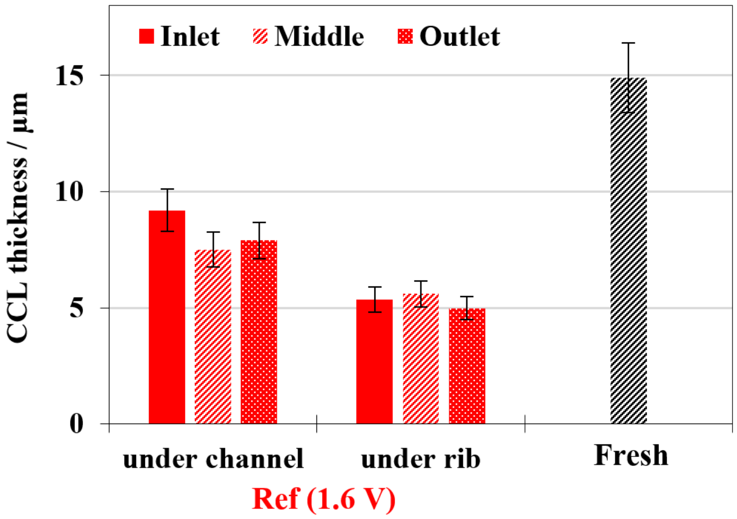

Figure IV-12: Estimated thickness of the CCL located under the rib/channel for the MEA aged at 1.6 V (ref) compared to the fresh MEA.

IV.3.1.1.2. Impact of operating parameters on CCL thickness

Figure IV-13a and Figure IV-13b emphasize the thinning of the CCL (magnification: 1.00 or 2.00 KX) and the Pt redistribution (magnification: 15 KX), respectively, probed at the MEA (middle area) according to the E_{front} potential values. After 100 SU-AST cycles, the CCL thickness decreases down from 14.9 µm to 7.5, 11.6, 13.5 and 14.7 µm, or about -50%, -22%, -6% and -1% (compared to the fresh sample) for aged MEA when E_{front} varies from 1.6, 1.4, 1.2 and 1.0 V, respectively. Moreover, the Pt densification is less pronounced below 1.4 V demonstrating a lower degradation of Pt particles, preferentially by Pt dissolution, likely less damaging than Pt detachment and agglomeration related to pronounced carbon support corrosion.

Finally, all the CCL thickness measurements are reported in Figure IV-14 according to the four operating parameters *vs.* fresh MEA. By comparison with the reference case, the lowering of:

- E_{front} down to 1.4, 1.2 and 1.0 V significantly diminishes the thinning of about 22%, 6% and 1%;
- t_{front} down to 1.0 and 0.5 s induces a thinning of about 49 and 38%, respectively;
- $RH_{a/c}$ down to 80/50 and 50/50% reduces the thinning at 39 and 10%, respectively. On the contrary, the 95/80% RH case increases the thinning up to 55%;
- T_{cell} down to 45 and 30 °C influence also the thinning by reducing it about 27 and 34%, respectively.

To better understand the influence of operating parameters, the measurements of the CCL thickness are compared with the total CO_2 emission during the SU-AST protocol. Figure IV-15 shows a quasi-linear relationship between the two parameters whatever the ageing case: the higher the CO_2 emission, the more damaged CCL. Thus, the porosity is progressively weakened as SU-AST cycles progress.

a) CCL thinning

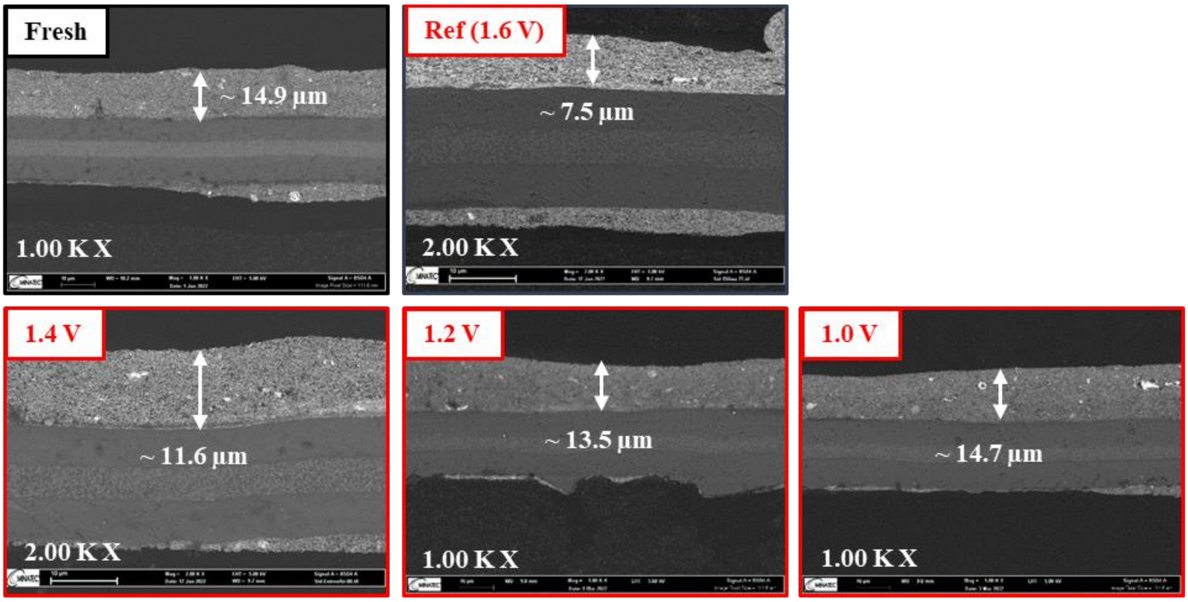

b) Pt redistribution

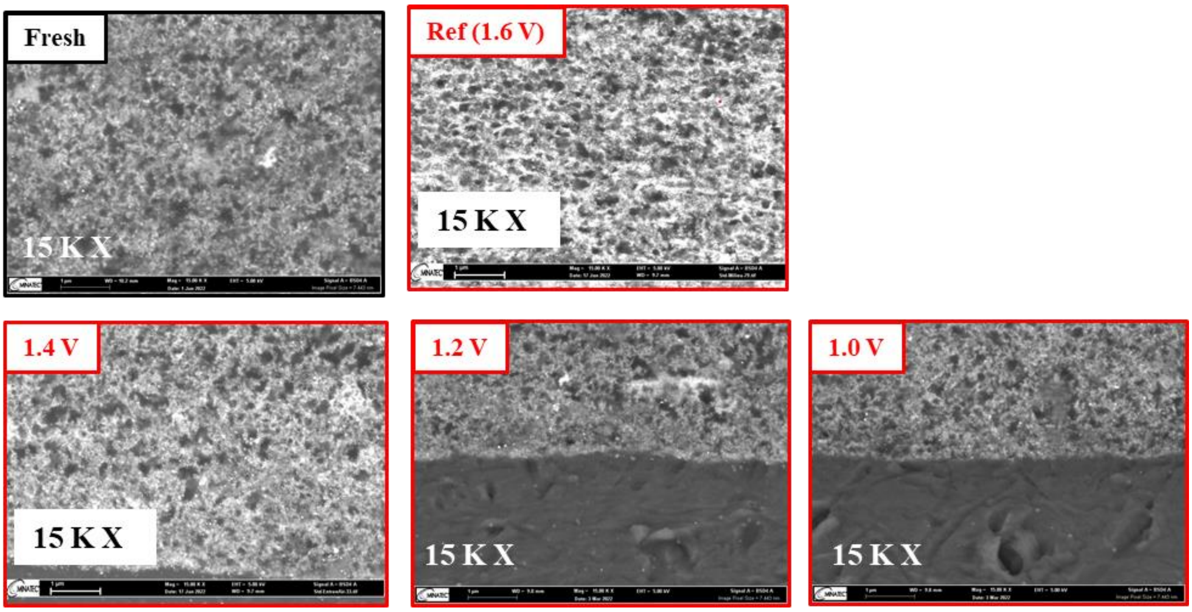

Figure IV-13: SEM cross-sectional images of aged MEA, after 100 SU-AST cycles, located at the cathode middle area under the channel, according to the E_{front} parameter at different magnification: a) 1.0 – 2.0 K X and b) 15 K X.

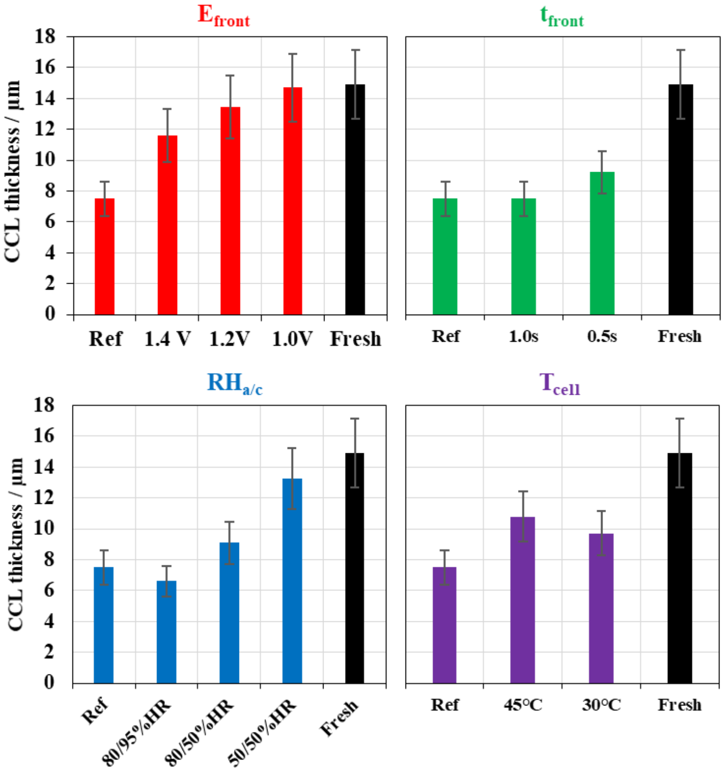

Figure IV-14: Estimated thickness of the CCL located at the cathode middle areas under the channel according to the four operating parameters after 100 SU-AST cycles

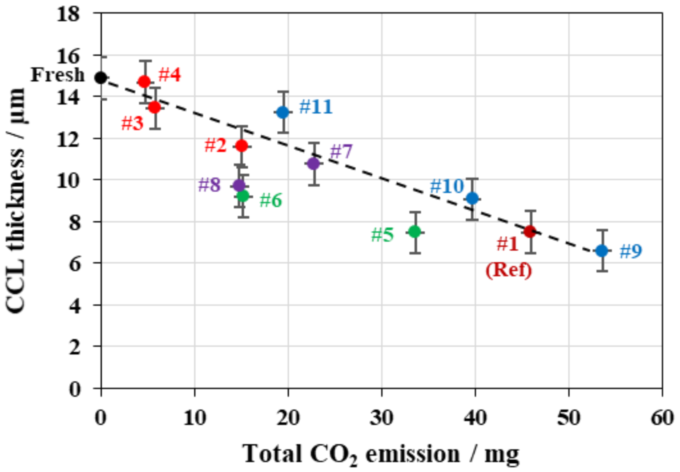

Figure IV-15: Thickness of the CCL vs. the cumulated CO_2 emission, after 100 SU-AST cycles, according to the E_{front} (red dot), t_{front} (green dot), $RH_{a/c}$ (blue dot) and T_{cell} (purple dot) cases as referred in Table IV-1.

IV.3.1.2. Water sorption

Previous SEM investigation depicts a strong influence of the CCL thinning with the CSC mechanism during the SU-AST protocol. Micro-structures of the CCL are modified which may hinder mass-transport properties to the active sites for gases and the water management within the CCL, limiting even more the sluggish ORR.

Gravimetric sorption technique is carried out in order to measure the water retention in the active layer once degraded according to the ageing conditions. This technique is explained in the Chapter III (section III.4.2.2) providing the measurements for the fresh MEA and validating its reproducibility. Please note that all the aged MEA have not been tested by this technique and it was used only for the most impactful parameters: E_{front} parameter (1.6, 1.5, 1.4, 1.2 and 1.0 V) in the section IV.3.1.2.1 and the 50/50% RH and 30 °C cases in the section IV.3.1.2.2.

IV.3.1.2.1. Front potential effect on water sorption of CCL

Focusing on the E_{front} effect, water sorption and desorption in the fresh and aged CCL samples from 0 to 98% RH is plotted in Figure IV-16a. In 0 – 30% RH range, the profiles are similar for all samples. The mass gain (*vs.* initial mass in dried conditions) during the sorption / desorption (positive / negative RH sweeps, respectively) are highlighted at 50, 80 and 98% RH in Figure IV-16b, c and d, respectively. The 50 and 80% RH levels show similar trends: the mass gain remains higher in the desorption than in the sorption phase. Indeed, the micro-porous carbon media adsorbs water molecules during the first sorption phase but the removal during the following desorption phase is incomplete due the strong affinity of the CCL powder with water. This hysteresis is more accentuated at 50% than at 80% RH for the fresh MEA (+49% and +27%, respectively). However, this trend is reversed for the reference aged MEA at 1.6 V (+17% and +29%, respectively). Consequently, the reference test at E_{front} 1.6 V affects strongly the water retention of the CCL. The higher E_{front} value during the SU-AST protocol, the lower water sorption into the CCL at 50, 80 and 98% RH. At 98% RH, the mass gain compared to the fresh case is reduced by -6%, -10%, -11%, -14% and -34% for the aged MEA at 1.0, 1.2, 1.4, 1.5 and 1.6 V, respectively. In other words, the damages in CCL due to CSC mechanism reduces its ability to adsorb water (Figure IV-17a and Figure IV-17b). The pore volumes may be also reduced during the CCL thinning / collapse and their filling capacity is therefore limited which can explain the decrease of the water retention in aged CCL.

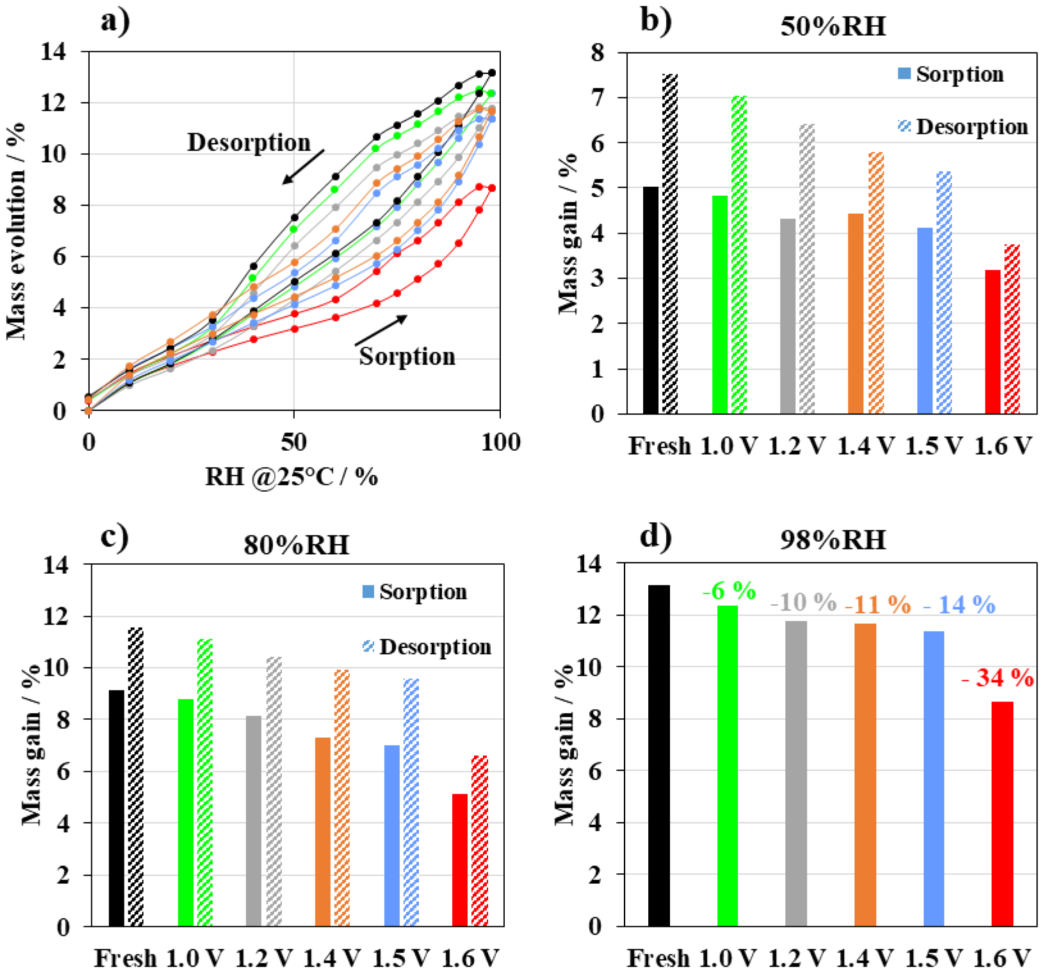

Figure IV-16: a) Water sorption isotherm for fresh and aged CCL at 25 °C according to the E_{front} parameter. Deduced mass gain compared to the initial mass in dried condition during the sorption / desorption phase at b) 50%, c) 80% and d) 98% RH

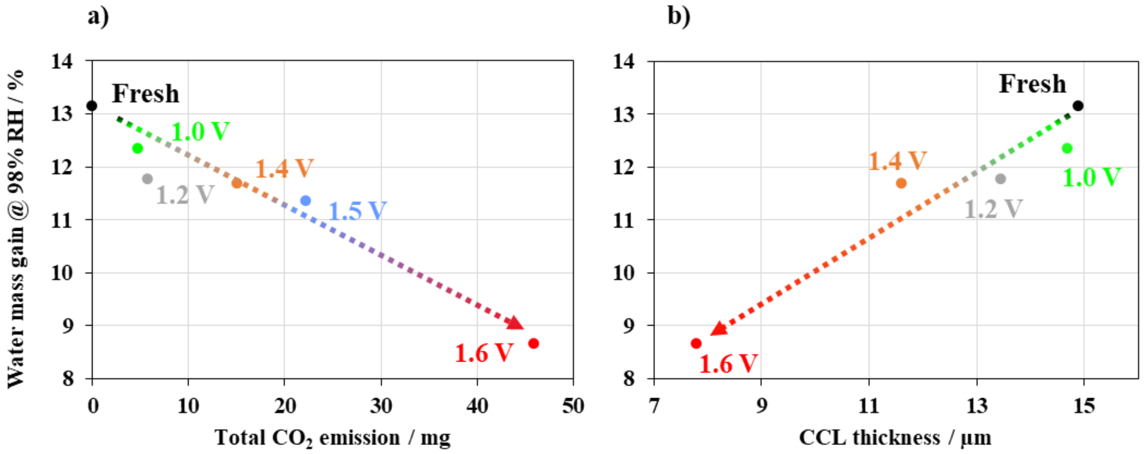

Figure IV-17: Water mass gain at 95% RH @ 25 °C vs. a) total CO_2 emission during SU-AST protocol and b) CCL thickness according to the E_{front} parameter

IV.3.1.2.2. Low temperature & RH effect on water sorption of CCL

Additionally, the less damaging operating cases (50/50% RH and 30 °C cases) have also been investigated by gravimetric sorption technique (see III.4.2.2). Figure IV-18 presents their respective water sorption isotherms and mass gains at 50, 80 and 95% RH. Despite the harsh potential exposition at 1.6 V during 1.5s, lowering both $RH_{a/c}$ and T_{cell} reveals an impact on water sorption: -6% and -3% *vs.* initial mass gain for aged MEA in 30 °C and 50/50% RH cases. The CSC kinetics is strongly slowed down under these operating conditions during the SU-AST protocol, reducing the CCL thinning, and thus, conserving the proper water management.

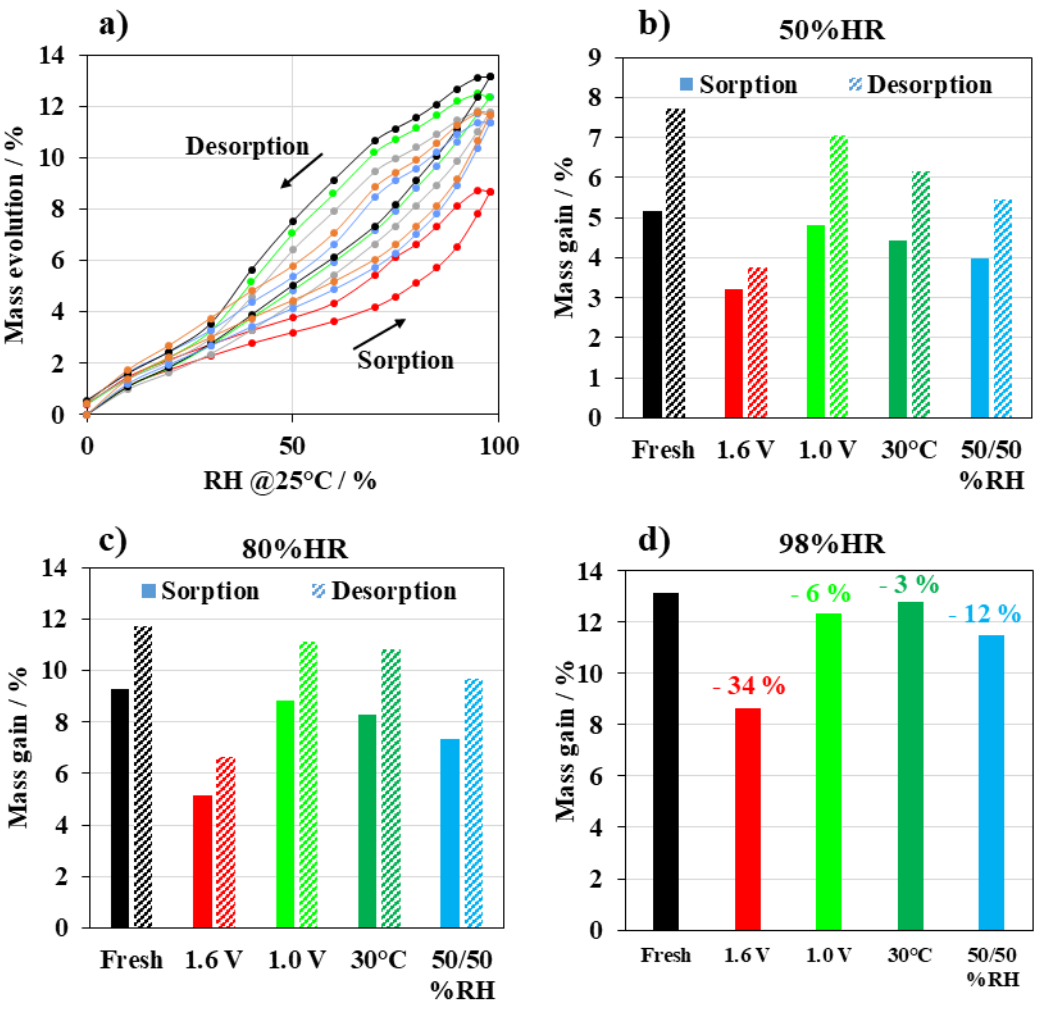

Figure IV-18: a) Water sorption isotherms for fresh and aged CCL at 25 °C according to the E_{front} parameter. Mass gain compared to the initial mass in dried conditions during the sorption / desorption phase at b) 50%, c) 80% and d) 98% RH

IV.3.1.3. Raman spectroscopy

Raman spectroscopy characterizations, explained in the Chapter III (sectionIII.4.2.3), have been carried out in collaboration with the LEPMI laboratory on three samples: fresh and aged MEA at 1.6 V and 1.0 V. The spectra are normalized to the "G band" peak at 1,585 cm^{-1} and the average crystallite size (*La*) of the carbon particles is also evaluated by the (III-3) formula (Figure IV-20).

The spectra of fresh and aged MEA at 1.0 V are hardly discriminable. Nevertheless, the slight increase of the D1 band (1,350 cm^{-1}) without modification of the G band might indicate the beginning of functionalization[4] of the carbon surface.

For the material aged at 1.6 V, the decrease of the D1 band attests the preferential corrosion of the amorphous/disordered domains which results into a higher graphitic / amorphous ratio of the carbon, as indicated by the significant increase in *La* size. A slight development of a C=O band around 1,750 cm^{-1} is also noticeable which probably reflects the formation of carbon surface carbonyls.

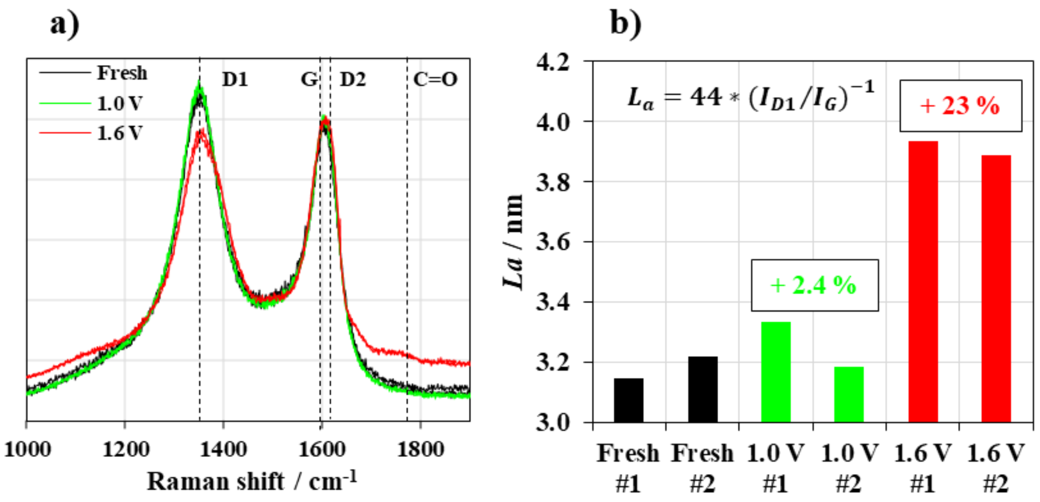

Figure IV-19: a) Normalized Raman spectra and b) deduced average crystallite size for fresh and aged MEA at 1.6 V and 1.0 V

---

[4] Creation of oxygenated groups onto carbon surface such as aldehyde, phenol, carboxylic acid, quinone/hydroquinone and lactone.

IV.3.2. Electro-Chemical properties evolution on aged CCL

In this section, local electro-chemical analyses are provided by differential single cell (1.8 cm²) with samples collected from fresh and aged MEA according to the different SU-AST protocols (cf. section IV.2). Experimental techniques are described in the Chapter III (III.4.1.1) with the validation of their reproducibility on fresh MEA.

IV.3.2.1. Evolution of performances on local aged MEA

IV.3.2.1.1. Spatial study along cathode channel

In order to validate the homogeneity of the degradation along the cathode as reported by the SEM analysis (section IV.3.1.1.1), polarization curves are carried out to ensure the reproducibility of the electrochemical response according to the sampling position (cf. Figure III-15). This verification was carried out with MEA samples aged under the reference case (1.6 V) and 1.4 V case. The polarization curves are plotted in Figure IV-20. The local performances are fairly close between the three positions. This confirms the ageing homogeneity in the cell in accordance with the potential profile applied on the overall active surface of the single cell in the SU-AST protocol (cf. Figure III-10). The homogeneity for these cases has also been validated by CV and PEIS characterizations but is not further detailed here for a sake of brevity. For the rest of this electrochemical *post-mortem* study, one sample per MEA is taken from the middle area of the cathode.

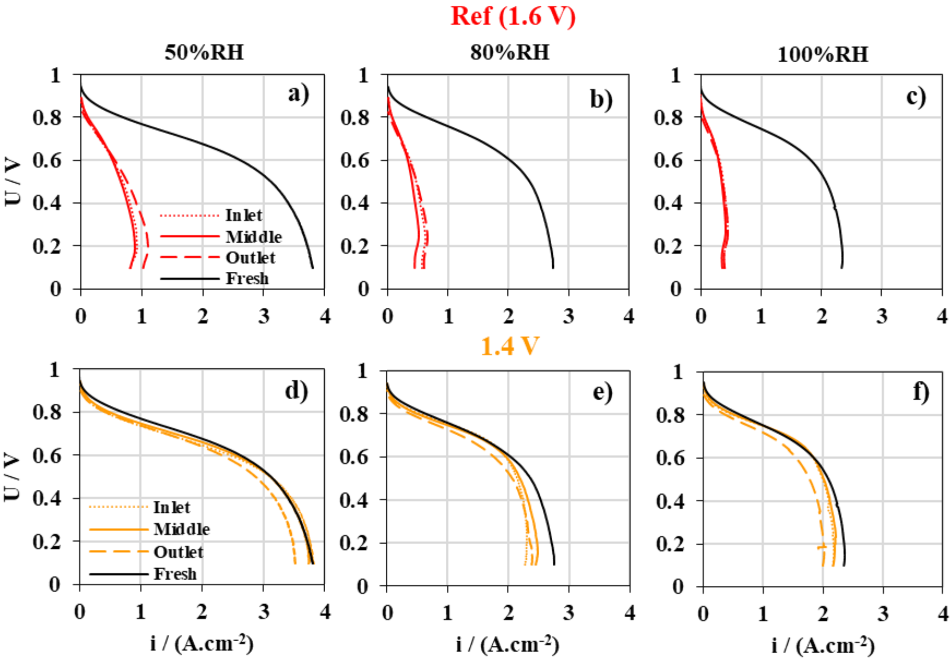

Figure IV-20: Polarization curves (10 mV.s^{-1}) in 1.8 cm² cell on fresh (black line) and aged MEA after 100 SU-AST cycles at 1.6 V (red line) and 1.4 V (orange line) taken from the cathode inlet – middle – outlet according to the relative humidity: (a, d) 50% RH, (b, e) 80% RH and (c, f) 100% RH. Operating conditions: H_2/Air – 80 °C – 1.5/1.5 bar$_{abs}$ (int) – 38/90 nL.h^{-1} (St 50/50 @ 1 A.cm^{-2})

IV.3.2.1.2. Impact of E_{front} parameter

The Figure IV-21 shows the polarization curves obtained on aged MEA according to different E_{front} at three relative humidity conditions: 50, 80 and 100%. Apart from the sample at 1.0 V, increasing the potential E_{front} induces a progressive performance degradation. The post-1.6 V curve (red line) shows very strong performance losses over the whole range of current studied, while for the other samples, the degradation is mainly observed from the medium up to the high current densities. Moreover, the loss is accentuated under high RH conditions, which reflects an inability of the cell to maintain good performance at high water content in accordance with sorption measurements and the loss of pore volume. Indeed, SEM technique reveals a CCL thinning and likely a loss of pores volume, which retains a smaller mass of water, based on gravimetric measurements. We can suppose that the CCL is then more easily saturated with water once collapsed.

Even in the low current density region, overvoltage gets higher as the humidity increases. The case of the 1.0 V reveals a slight improvement in performance as reported on large single cell investigation: the performance curve (green line) is above the fresh AME (black line) for all the three humidity conditions (above 1.5 A.cm^{-2}). Noted that a measurement concern (low performance level) for the 1.2 V case is very likely under 100% RH condition.

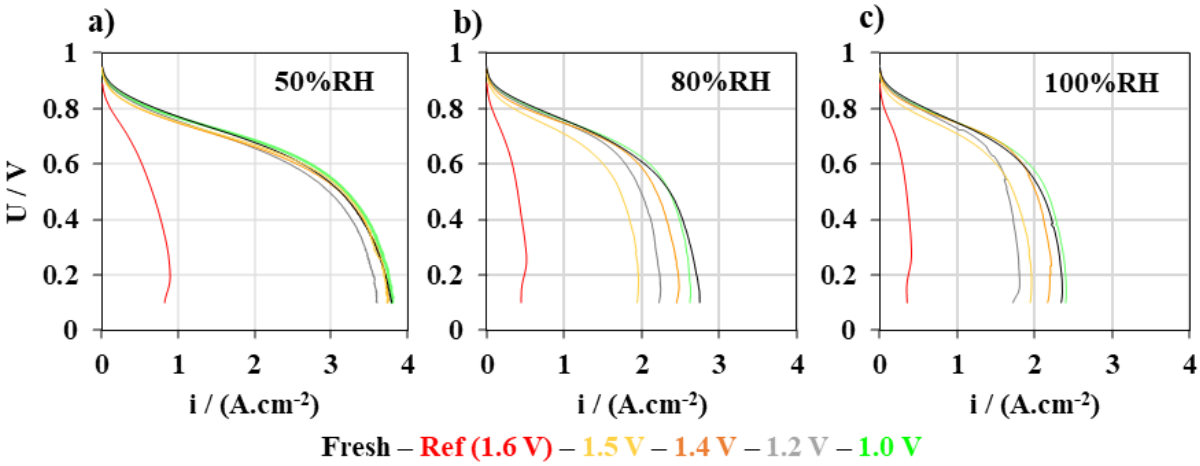

Figure IV-21: Polarization curves in 1.8 cm² cell for fresh and aged MEA after 100 SU-AST cycles according to the E_{front} parameter at different relative humidities: (a) 50/50% RH, (b) 80/80% RH and (c) 100/100% RH. Operating conditions: H_2/Air – 80 °C – 1.5/1.5 bar$_{abs}$ (in) – 38/90 nL.h^{-1} (St 50/50 @ 1 A.cm^{-2})

IV.3.2.1.3. Impact of exposure time t_{front}

The polarization curves (Figure IV-22) show a strong attenuated degradation as the front time at the maximal voltage (1.6 V) decreases. The performance measured at 0.5 s (purple line) is clearly above the others at 1.0 s and 1.5 s with the limiting current density decreasing from approximately 3.4 to 2.3 and 0.8 A.cm^{-2} respectively for the 50% RH condition. Moreover, it is rather close to the fresh case at low humidity (50/50%) while a drop in performance on activation appears when the humidity level increases similarly to previous cases with different E_{front} (see Figure IV-21).

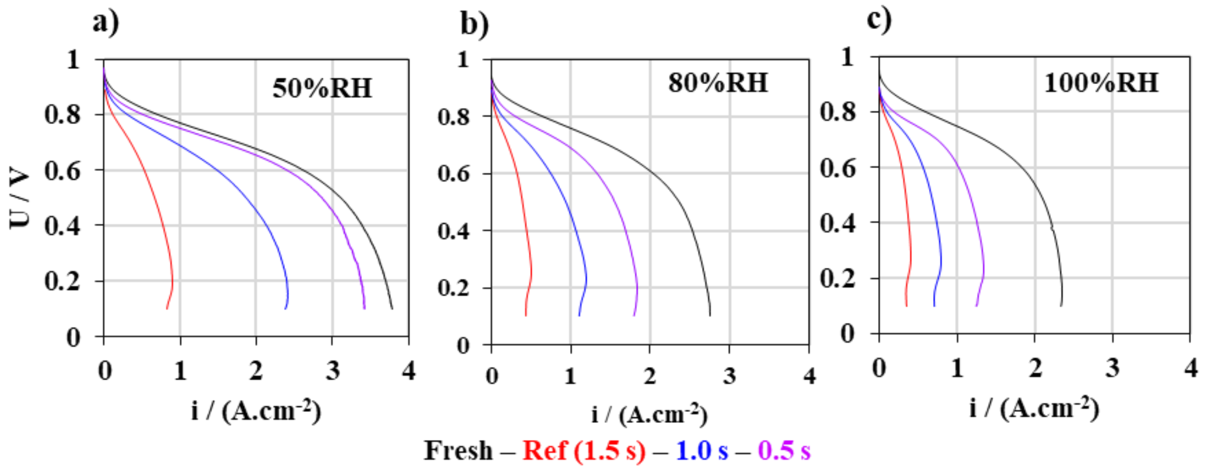

Figure IV-22: Polarization curve in 1.8 cm² cell for fresh and aged MEA after 100 SU-AST cycles according to the t_{front} parameter at different relative humidities: (a) 50/50% RH, (b) 80/80% RH and (c) 100/100% RH. Operating conditions: H_2/Air – 80 °C – 1.5/1.5 bar$_{abs}$ (in) – 38/90 nL.h^{-1} (St 50/50 @ 1 A.cm^{-2}).

IV.3.2.1.4. Impact of relative humidity of reactant gases $RH_{a/c}$

The third operating parameter studied is the relative humidity $RH_{a/c}$ for SU-AST. Figure IV-23 shows that decreasing the relative humidity during the ageing protocol results in a significant mitigation of the performance decay, compared to the reference case @ 1.6 V. Indeed, the polarization curve related to the 50/50% RH SU-AST case (blue line), for example, is very close to the fresh cell above 1.5 A.cm^{-2} at 50/50% RH polarization curve, with a slight loss of performance is visible at low current density. However, the 50/50%RH SU-AST case (blue line) shows a significant performance drop in wet conditions (80% and 100% RH).

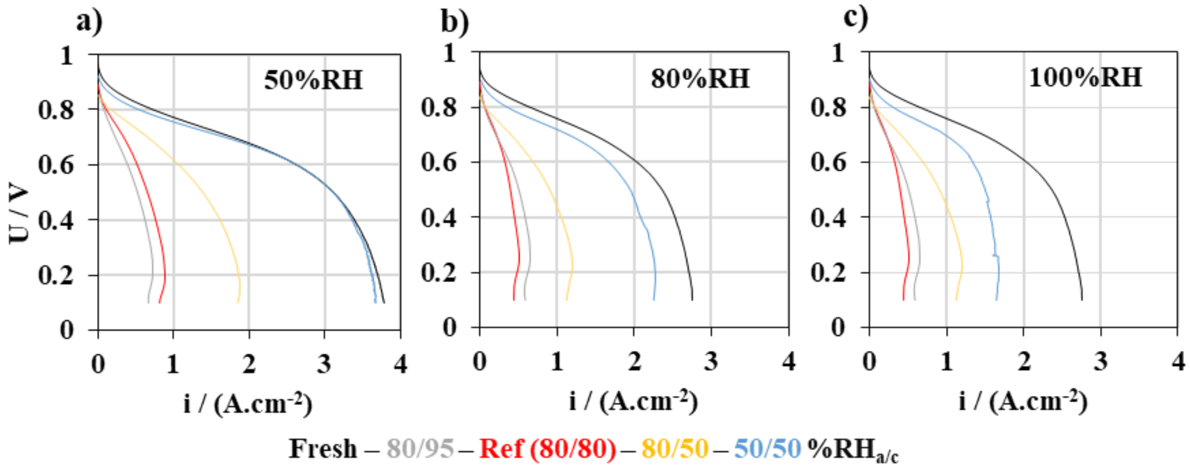

Figure IV-23: Polarization curves for fresh and local aged MEA after 100 SU-AT cycles according to the $RH_{a/c}$ parameter during SU-AST protocol at different relative humidities: (a) 50/50% RH, (b) 80/80% RH and (c) 100/100% RH. Operating conditions: H_2/Air – 80 °C – 1.5/1.5 bar_{abs} (in) – 38/90 $nL.h^{-1}$ (St 50/50 @ 1 $A.cm^{-2}$).

IV.3.2.1.5. Impact of cell temperature T_{cell}

The last parameter studied is the cell temperature during SU-AST. Three cells were subjected to a SU-AST at different temperatures: 30, 45 and 60 °C. Figure IV-24 shows the local polarization curves obtained in 1.8 cm² differential cell after the 100 SU-AST cycles. It appears that lowering the start-up temperature improves the final performance. At 50/50% RH, the polarization curves after ageing at 30 °C (green line) and 45 °C (pink line) are similar and even above the fresh cell (black line) indicating that the performance is not significantly altered under these SU-AST conditions. However, under high RH conditions (80 and 100%), the cell performance is actually lower than the fresh sample highlighting also in these cases an alteration of the water management within the CCL.

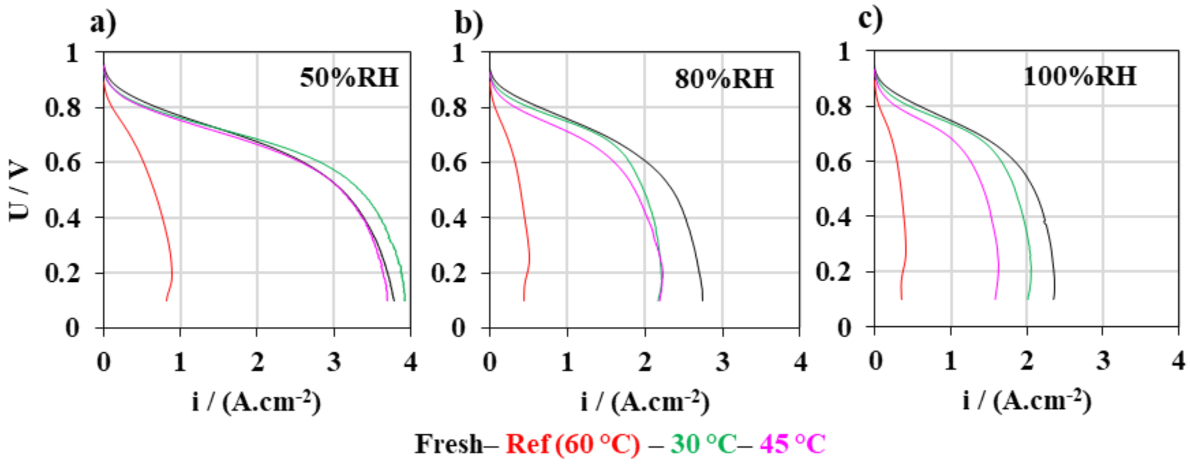

Figure IV-24: Polarization curves for fresh and local aged MEA after 100 SU-AST cycles according to the T_{cell} parameter at different relative humidities: (a) 50/50% RH, (b) 80/80% RH and (c) 100/100% RH. Operating conditions: H_2/Air – 80 °C – 1.5/1.5 bar_{abs} (in) – 38/90 $nL.h^{-1}$ (St 50/50 @ 1 $A.cm^{-2}$).

IV.3.2.2. Evolution of voltammograms under H_2/N_2 on local aged MEA

IV.3.2.2.1. Impact of the front potential E_{front}

The voltammograms carried out on aged MEA samples (middle area) according to the E_{front} parameter are plotted in Figure IV-25. The profiles depend slightly on the RH level of the reactant gas supply during the measurements. As a result, the estimation of the ECSA is also similar for the three RH conditions: 102, 118, 127 and 156 cm^2_{Pt}/cm^2_{geo}, for 1.6, 1.4, 1.2 and 1.0 V case, respectively. For comparison purposes, the ECSA at the 100th SU-AST cycle on large surface MEA (98 cm²) are estimated at: 76, 156, 170 and 176 cm^2_{Pt}/cm^2_{geo} for 1.6, 1.4, 1.2 and 1.0 V case, respectively.

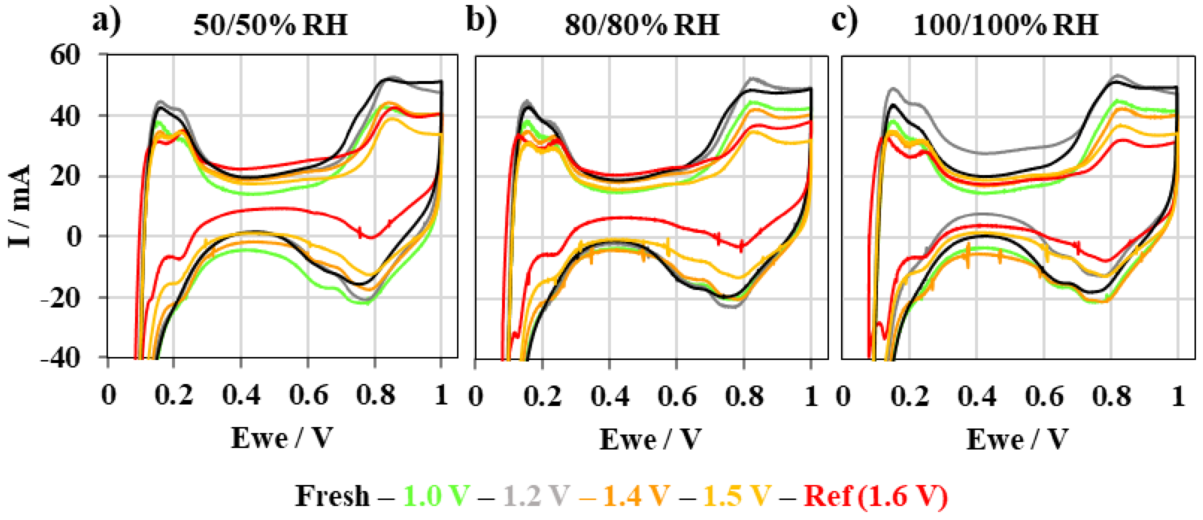

Figure IV-25: Voltammograms in 1.8 cm² cell (third scan, 50 mV.s^{-1}) at 50% (a), 80% (b) and 100% RH (c) on fresh and aged MEA after 100 SU-AST cycles according to the E_{front} parameter. Operating conditions: H_2/N_2 – 80 °C – 1.5/1.5 bar$_{abs}$ (in) – 38/90 nL.h^{-1} (St 50/50 @ 1 A.cm^{-2})

The respective ECSA variations compared to the fresh MEA cm^2_{Pt}/cm^2_{geo} on large and differential cell are:

- -62, -32, -17 and -12%$_{ECSA}$ in single cell configuration (98 cm²);
- -32, -23, -20 and +6%$_{ECSA}$ in single differential cell configuration (1.8 cm²).

The differences between ECSA measurements in large cell (98 cm²) and differential cell (1.8 cm²) remains unclear. They may come either from the definition of the lower potential limit in each case (and possibly some H_2 oxidation during the positive scan), from the capacitive and H_2 permeation correction (sometimes difficult on local MEA samples) and/or slightly different characterization conditions (see Table III-6 and Table III-10 for the large single cell and differential single cell configuration, respectively).

IV.3.2.2.2. Impact of overall operating parameters

ECSA losses in 50 – 80 – 100% RH according to each operating parameter (E_{front}, t_{front}, T_{cell} *and* $RH_{A/C}$) are plotted in Figure IV-26. Similarly to previous measurements on large single cell configuration, the ECSA loss is reduced by lowering t_{front} from 1.5 s down to 0.5 s (-32 *vs.* -19 %, respectively), $RH_{a/c}$ from 80/80 to 50/50 % RH (-9.5%) and T_{cell} from 60 to 30 °C (-26%), compared to the reference SU-AST case. This 1.0 V case is the only one which shows *ca.* 7% gain in ECSA after the SU-AST.

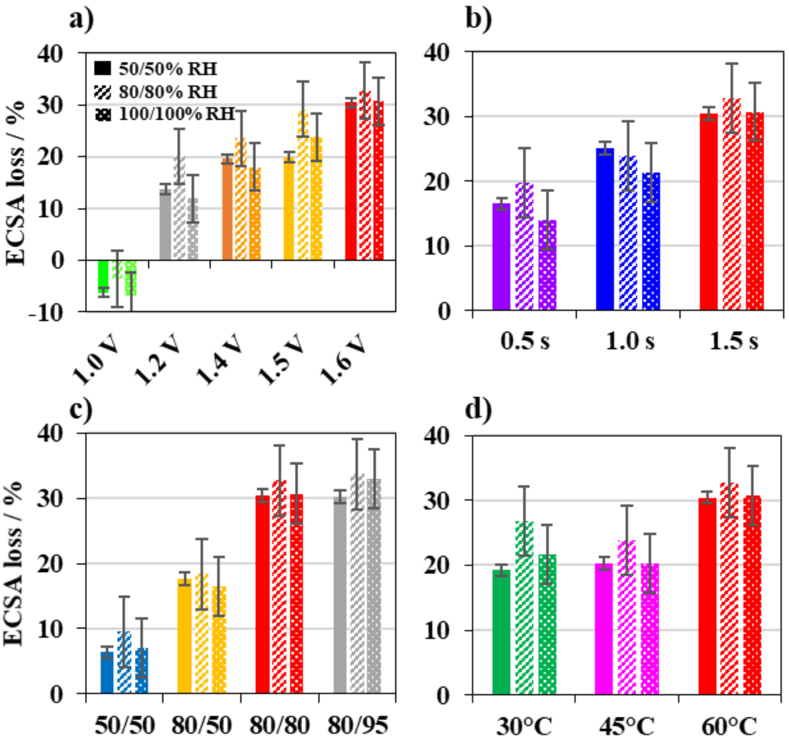

Figure IV-26: Estimation of the ECSA loss vs. initial value from voltammograms at 50, 80 and 100% RH on MEA samples (1.8 cm²) according to the four mitigating parameters

IV.3.2.3. Evolution of Electrochemical Impedance Spectroscopy on local aged MEA

Electrochemical impedance spectroscopies in potentiostatic mode at 0.85 / 0.675 / 0.5 V (under H_2/Air operation) and at 0.4 V (under H_2/N_2) has been performed under three RH conditions (50 – 80 – 100% RH). Equivalent electrical circuits, detailed in section III.4.1.3, were chosen to characterize (i) the proton resistance of the membrane, (ii) the charge transfer resistance and (iii) the proton resistance of the cathode catalyst layer, as already used in the literature [135].

IV.3.2.3.1. Impact of front potential *E_{front}*

The main characteristics deduced from the PEIS in FC operation (H_2/Air) are plotted in Figure IV-27 according to the E_{front} parameter. Here, we are interested in looking at the qualitative changes between the samples. From the equivalent model chosen in this study, three resistances are extracted:

- $\boldsymbol{R_{H+,MB}}$, the proton resistance in the ionomer of the membrane. The results do not show any significant modification after ageing test compared to the fresh sample. Indeed, it is expected that our AST does not specifically alter the protonic conductivity of the membrane. The slight variation observed between the three voltages are mainly due to the water production, changing the water content of the membrane, and thus, its protonic conductivity;
- $\boldsymbol{R_{ct}}$, the charge transfer resistance. It is inversely proportional to the current density and therefore dependent to the potential considering purely electro-kinetics aspects. Indeed, the decrease of charge transfer resistance is observed when potential drops from 0.85 down to 0.675 V. Nevertheless, the fitted charge transfer resistance at 0.5 V is higher than expected considering only kinetics limitations. This can be explained by mass-transport limitations phenomena (through-plane concentration gradient between the channels and the active layers) which become non-negligible despite the high stoichiometry applied (guaranteeing homogeneity along the cell between the inlet and the outlet). At this potential, it is reasonable to consider that the charge transfer resistance includes a through-plane mass-transport contribution. Thereafter, the analysis of PEIS in FC operation focuses on contributions at 0.85 and 0.675 V. The influence of the E_{front} potential on R_{ct} is not very significant from 1.0 up to 1.4 V. At 1.5 and 1.6 V, a strong increase of the R_{ct} value is observed. Moreover, high RH levels negatively affects R_{ct} especially for the most damaging cases.
- $\boldsymbol{R_{H+,CCL}}$, the proton resistance in the cathode. This equivalent resistance is deduced from a modified Warburg element and accounts for the proton mobility within the cathodic catalytic layer. For the fresh sample and for ageing samples with E_{front} below 1.5 V, no significant variation is observed. The lower resistance with increasing RH, the more accessible the platinum active sites to protons. For the aged at 1.6 V, a higher resistance is denoted at 50/50% RH, which continues to increase as the humidity increases suggesting a change in the mechanism for the operation of the cathode.

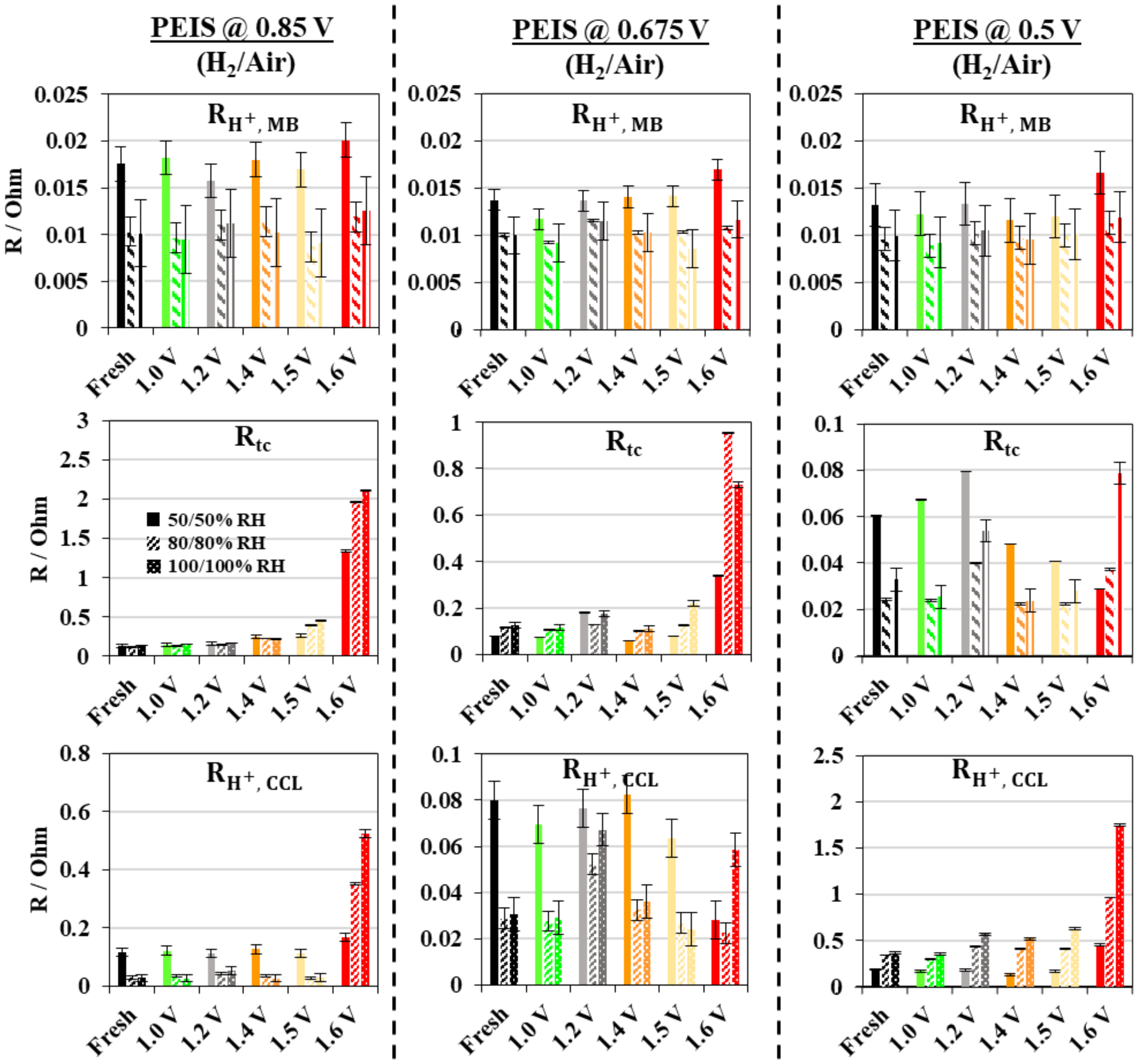

Figure IV-27: Resistances deduced from impedance spectra in 1.8 cm² cell at 0.85, 0.675 and 0.5 V under H_2/Air at different relative humidities during the PEIS characterizations and according to the E_{front} parameter. Operating conditions: H_2/Air – 80 °C – 1.5/1.5 bar_{abs} (in) – 38/90 $nL.h^{-1}$ (St 50/50 @ 1 $A.cm^{-2}$).

In the case where the cathodic compartment is supplied with nitrogen (to suppress the ORR), the only faradaic reaction occurring in the CCL at 0.4 V is the oxidation of H_2 that permeates through the membrane. At 0.4 V, the cell potential corresponds to the diffusion limited current region. The model used to fit impedance measurements yields the following resistances (see Figure IV-28):

- $\boldsymbol{R_{H+,MB}}$, the membrane resistance is equal to that obtained under H_2/Air and varies only with humidity;
- $\boldsymbol{R_{H+,CCL}}$, the resistance of the protons in the cathode deduced thanks to the modified Warburg elements. This resistance decreases as the value of the E_{front} parameter increases. The drop is drastic at 50/50% RH for the 1.6 V reference case. This therefore attests a major change in the active layer properties in this case. The thin/aged CCL retains less water since they are less porous but its easy water saturation with liquid water is likely responsible for the high protonic transport in the layer.

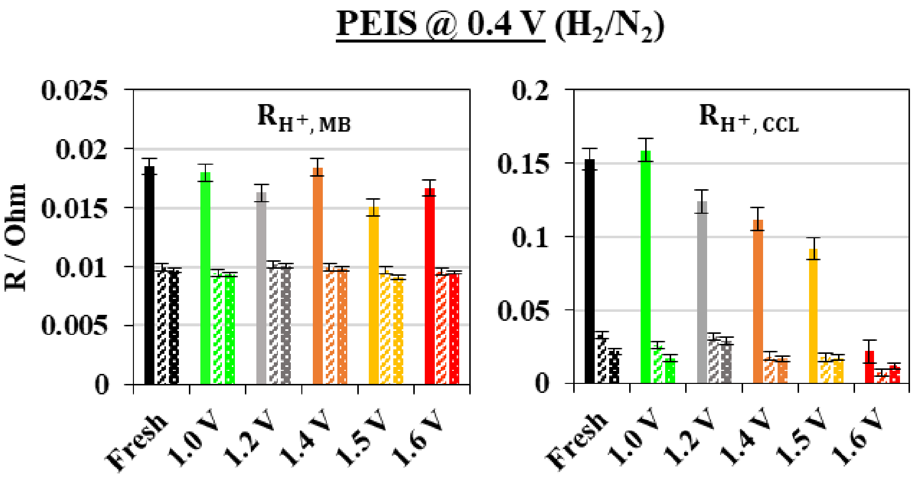

Figure IV-28: Resistances deduced from impedance spectra in 1.8 cm² cell at 0.4 V under H_2/N_2 at different relative humidity conditions according to the E_{front} parameter. Operating conditions: H_2/N_2 – 80 °C – 1.5/1.5 bar_{abs} (in) – 38/90 $nL.h^{-1}$ (St 50/50 @ 1 $A.cm^{-2}$).

IV.3.2.3.2. Impact of exposure time t_{front}

Regarding the t_{front} effect, the impedance spectroscopy is analyzed in FC operation (H_2/Air) at 0.85 and 0.675 V, and out of operation (H_2/N_2) at 0.4 V, as illustrated in in Figure IV-29. The main observations are:

- @ 0.85 V (H_2/Air): The increase of R_{ct} with t_{front} is probably related to the ECSA losses which are more and more important. Moreover, we see that contrary to the fresh sample, the RH condition has an influence on the R_{ct}: when RH increases R_{ct} increases. We also see that in the aged samples, especially in 1.0 and 1.5 s cases, $R_{H+,CCL}$ increases very strongly and also when RH increases.
- @ 0.675 V (H_2/Air): Globally the same observations as at 0.85 V can be denoted. The RH has a much greater impact for aged samples than for fresh sample. The proton resistance @ 50% RH is lower for the aged samples than for the fresh one. The impact of RH hardly follows a logic on aged samples.
- @ 0.4 V (H_2/N_2): The protonic resistance in aged CCL is always lower than the fresh sample.

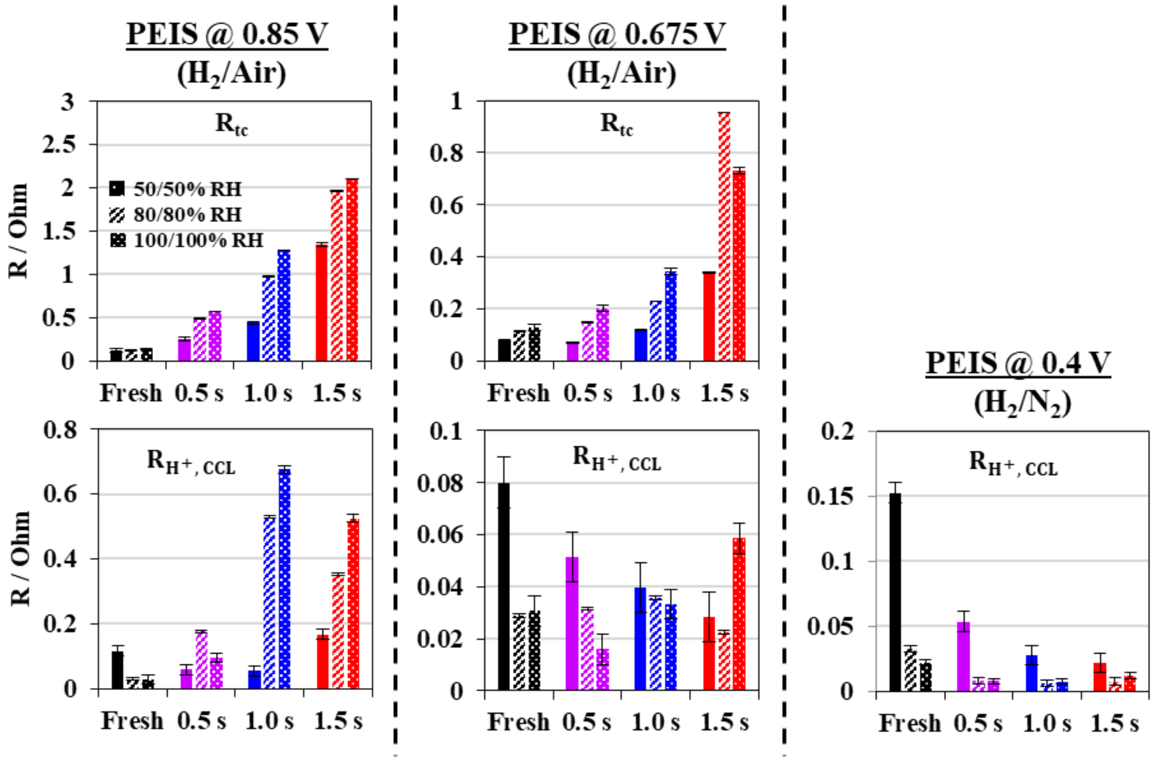

Figure IV-29: Resistances deduced from impedance spectra at 0.85 and 0.675 V under H_2/Air and at 0.4 V under H_2/N_2 at different relative humidities during the PEIS characterization according to the t_{front} parameter. Operating conditions: 80 °C – 1.5/1.5 bar_{abs} (in) – 38/90 nL.h^{-1} (St 50/50 @ 1 A.cm^{-2}).

IV.3.2.3.3. Impact of $RH_{a/c}$

Figure IV-30 shows the resistance variations of fresh and aged MEA after SU-AST according to the $RH_{a/c}$ parameters. Main qualitative observations are the following:

- @ 0.85 and 0.675 V (H_2/Air): We find globally the same tendency as with t_{front}. When RH increases, R_{ct} increases. In operation, $R_{H+,CCL}$ is larger on the aged samples and tends to increase when RH increases during PEIS. This behavior is opposite to the fresh sample;
- @ 0.4 V (H_2/N_2): $R_{H+,CCL}$ is much lower than for the fresh sample and all the lower as RH was high during AST.

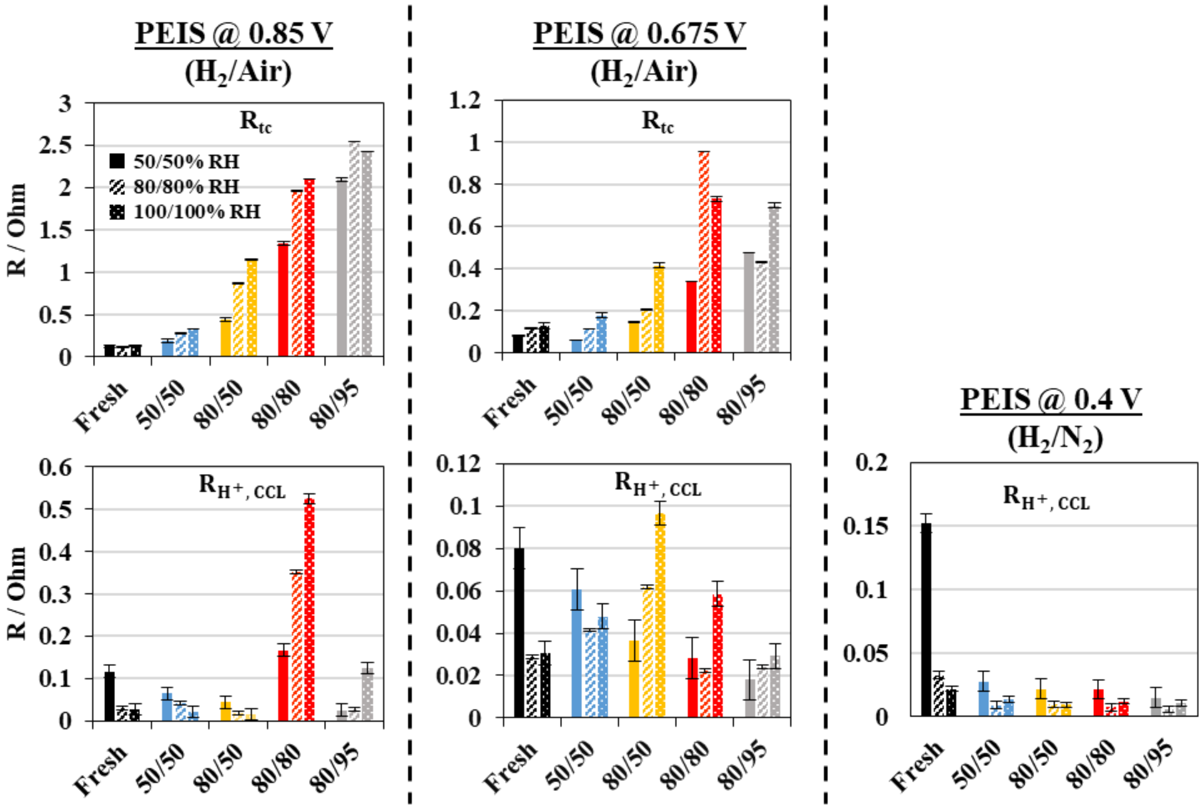

Figure IV-30: Resistances deduced from impedance spectra in 1.8 cm² at 0.85 and 0.675 V under H_2/Air and at 0.4 V under H_2/N_2 at different relative humidities during the PEIS characterization according to the $RH_{a/c}$ parameter. Operating conditions: 80 °C – 1.5/1.5 bar_{abs} (in) – 38/90 $nL.h^{-1}$ (St 50/50 @ 1 $A.cm^{-2}$).

IV.3.2.3.4. Impact of T_{cell}

Finally, the cell temperature also affects strongly both charge transfer and CCL protonic resistances as depicted from Figure IV-31 as follows:

- @ 0.85 and 0.675 V (H_2/Air): the 30 °C case is very close to fresh case while the 45 °C induces slight increase of R_{ct}. The protonic resistance slightly lower than new sample. Globally, the impact of temperature up to 45 °C *vs.* 60 °C in reference is limited;
- @ 0.4 V (H_2/N_2): At 30 and 45 °C, we note a decrease of the proton resistance *vs.* fresh (but less pronounced than at 60 °C).

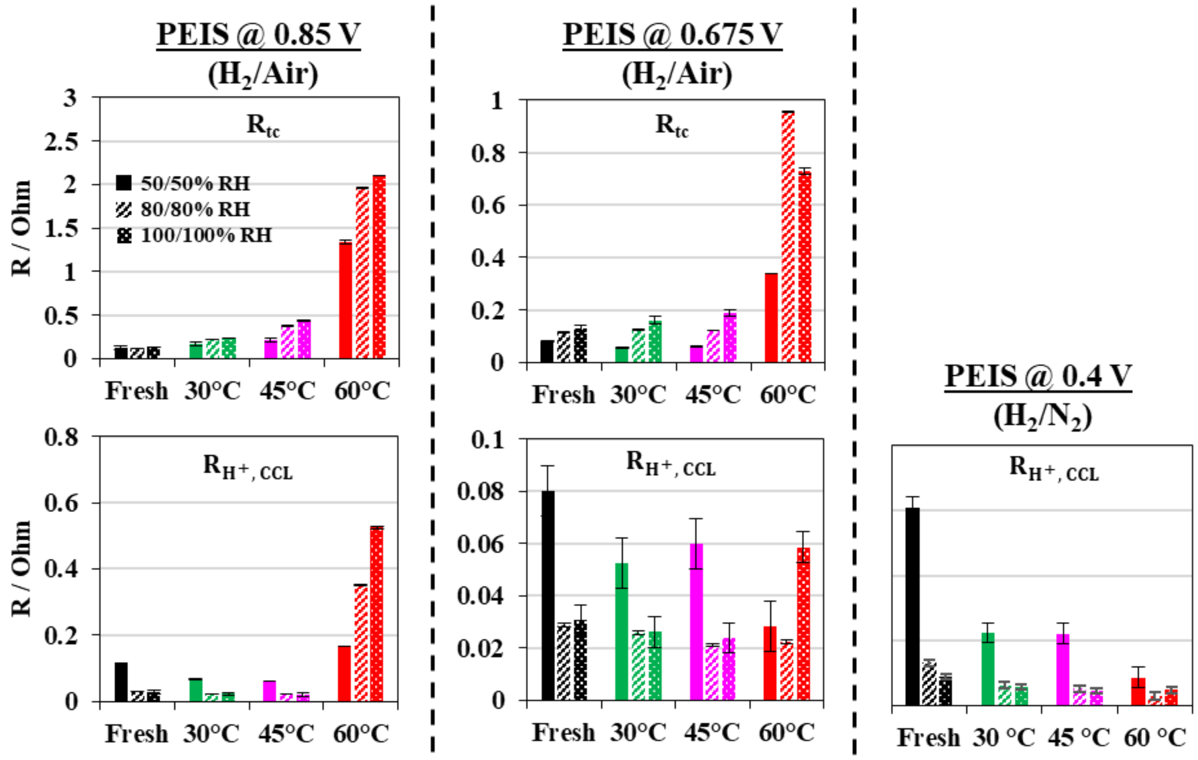

Figure IV-31: Resistances deduced from impedance spectra at 0.85 and 0.675 V under H_2/Air and at 0.4 V under H_2/N_2 at different relative humidities during the PEIS characterization according to the T_{cell} parameter. Operating conditions: 80 °C – 1.5/1.5 bar_{abs} (in) – 38/90 $nL.h^{-1}$ (St 50/50 @ 1 $A.cm^{-2}$).

To conclude, notable differences in impedance measurements and operating behaviors are observed. The SU-AST modifies the charge transfer and the apparent proton transport properties in the cathode layer probably in connection with the loss of ECSA and the modification of the micro-structure of the carbon support. Next section will discuss the major modifications of properties within the CCL.

IV.3.3. Discussion of *post-mortem* analysis

The different *post-mortem* analyses have given further evidence of the evolution of CCL electro-chemical and physico-chemical properties according to the SU-AST parameters. In this section, we will try to compare these different data and then to propose a degradation mechanism for the cathode in the most damaging case.

IV.3.3.1. Evolution of the electro-chemical vs. physico-chemical properties

To better understand the interactions between electro-chemical and physico-chemical properties evolution for each ageing SU-AST cases, Figure IV-32 presents the evolution of the charge transfer (a, b) and protonic resistance (c, d) in FC operation (H_2/Air @ 0.85 V) as well as the protonic resistance in H_2/N_2 operation (e, f) at 50/50% and 100/100% RH as a function of the respective CCL thickness for each aged MEA. Dotted lines have been placed to guide the reader's eyes to qualitatively illustrate the main trends / conclusions.

Regarding the R_{ct} in FC operation (H_2/Air) as plotted in Figure IV-32(a, b):

- @ 50% RH: A very little variation of R_{ct} is observed between samples weakly collapsed (thickness > 9µm). The 3 most degrading cases (Ref, 1.0 s and 80/95% RH case) with a strong CCL collapse (thickness < 9µm) show a clear increase.
- @100% RH: R_{ct} increase seems to initiate for higher thicknesses 11µm and R_{ct} values are also higher when RH increases.

For the $\boldsymbol{R_{H+,CCL}}$in FC operation (H_2/Air), referred in Figure IV-32(c, d):

- There seems to be two groups of points for strongly degraded samples: either $R_{H+,CCL}$ increases or decreases with the CCL thinning. It is difficult to exploit data even qualitatively (because the reference case is a bit apart);
- However, $R_{H+,CCL}$ does not fully fit our simple model (and not always easy to determine). We must be very careful about the interpretation. Especially if the post-degradation CCL operation becomes very heterogeneous.

Out of operation (under H_2/N_2), $R_{H+,CCL}$ measurements plotted in Figure IV-32(e, f) are easier to interpret here:

- Aged samples show lower H^+ resistances. Especially those exposed to 1.6 V (no matter the other parameter values), circled in orange, due to very likely modification of proton transport in the CCL after ageing at 1.6 V and whatever the thickness of the aged layer. This can be related to the more hydrophilic support carbon which promotes higher local water content;
- There seems to be also a link with the thickness. As the thickness of the CCL becomes thinner, the $R_{H+,CCL}$ appears to decrease (shorter protonic path and/or change in the structure of the ionomer or both);
- At 100% RH, all samples (except the 1.2 V) show a lower apparent proton resistance compared to the fresh samples.

To conclude, the coupling effect of the CCL microstructure modification, the decrease of ECSA and/or the change of proton mobility properties in the layer during SU-AST tests, strongly affect the electrochemical CCL operation and the cell performance as reported in this section. Regarding the most severe SU-AST conditions, CCL property evolutions make possible a proposal of mechanism degradation highlighted in following section (IV.3.3.2).

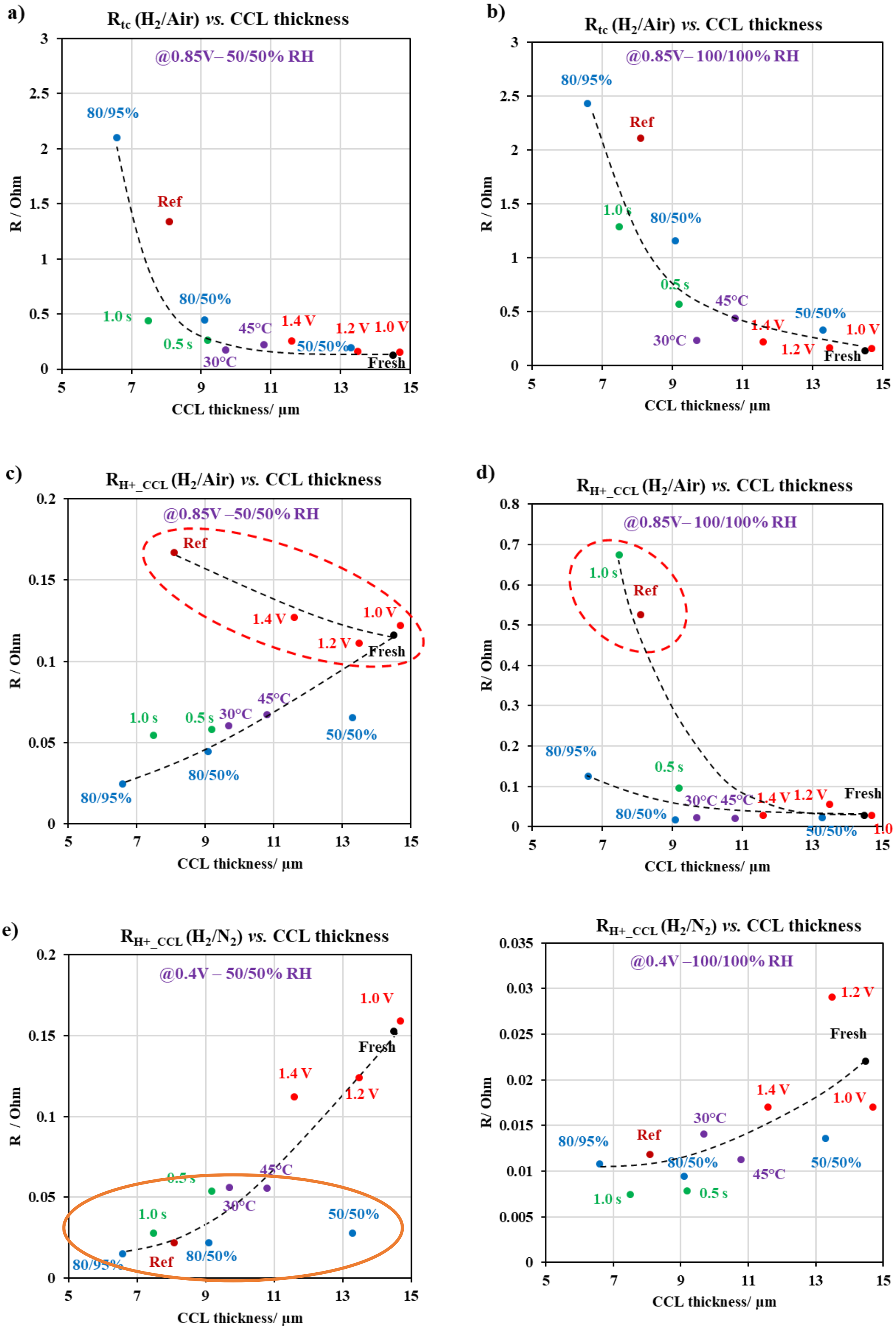

Figure IV-32: Resistances deduced at 0.85 V under H_2/Air and 0.4 V under H_2/N_2 vs. CCL thickness according to the four parameters. Operating conditions: 80 °C – 1.5/1.5 bar$_{abs}$ (in) – 38/90 nL.h^{-1} (St 50/50 @ 1 A.cm^{-2}).

IV.3.3.2. Proposal of CCL operation after degradation under most severe SU-AST conditions

Based on the SEM, the local electrochemical performances and the PEIS measurements for the most severe samples, with significant collapse of the cathodic microstructure, we can observe an opposite evolution of the proton resistance during FC operation and during H_2/N_2 characterizations, compared to the fresh sample. We propose here that the compaction of the aged CCL could lead to a delocalization of the electrochemical reactions at the edges instead of a distribution within the porous layer as schematized on Figure IV-33. For the fresh/non-aged samples (Figure IV-33a and b), the CCL operate probably as follows:

- In FC operation (H_2/Air) @50% RH: the HOR and ORR take place respectively in the anode and cathode catalyst layer, with the H^+ transport through the PEM. The ORR is supposed to be homogenous in the entire CCL. The oxidant gas diffuses through the thickness of the porous media from CCL|GDL to active sites, with a good transport of protons from PEM|CCL until active sites.
- In characterization mode (H_2/N_2) @ 50% RH: the HER and HOR takes place in the vicinity of the ACL|PEM and PEM|CCL interface, respectively at 0.4 V in the limit plateau. Hydrogen supplied at the anode side permeates to the cathode side though the PEM. At positive potential ($E_{cathode} > \mathrm{E}^0_{\mathrm{H^+/H_2}}$), the H_2 molecules are oxidized (HOR) close to Pt active sites, generating protons and electrons inside the cathode layer. In fresh state, Pt sites are insufficient at the PEM|CCL interface, forcing the H_2 molecule to diffuse in porous media. Then, protons migrate across the CCL (inducing protonic resistance within CCL) and the PEM until the anode side to evolve into H_2 gas by the HER, inversely to the HOR from reaction (I-1).

The CCL operation after the degradation under the most severe SU-AST conditions is illustrated in Figure IV-33(c, d) at 50% RH and Figure IV-33(e, f) at 100% RH. Following operating alterations are supported by the respective evolutions of R_{ct} and $R_{H+,CCL}$ observed in PEIS characterizations:

- In FC operation (H_2/Air): the oxygen flux is likely preferentially reduced at the CCL|MPL interface because the O_2 diffusion is also limited through the CCL by the low porosity. The higher apparent proton resistance compared to a porous cathode could then be related to the "forced" migration of the proton through the “entire” thickness of the cathode (large distance between the active sites for the ORR and the membrane). Between, 50 and 100% RH, the increase of $R_{H+,CCL}$ could be also explained by an even more restricted number of active sites available for ORR (concentration of the ORR on very few "triple point" sites) because of the "cathode flooding";

- Under H_2/N_2: the hydrogen permeation flow (from anode to cathode) is likely oxidized preferentially at the PEM|CCL interface due to the CCL collapse and the Pt redistribution increasing the Pt active sites to the HOR. Thus, the H_2 diffusion into the porous media is hindered, reducing the protons migration within the CCL. This leads to a very low apparent proton resistance in the cathode thickness (very small distance between the active sites for HOR and the membrane).

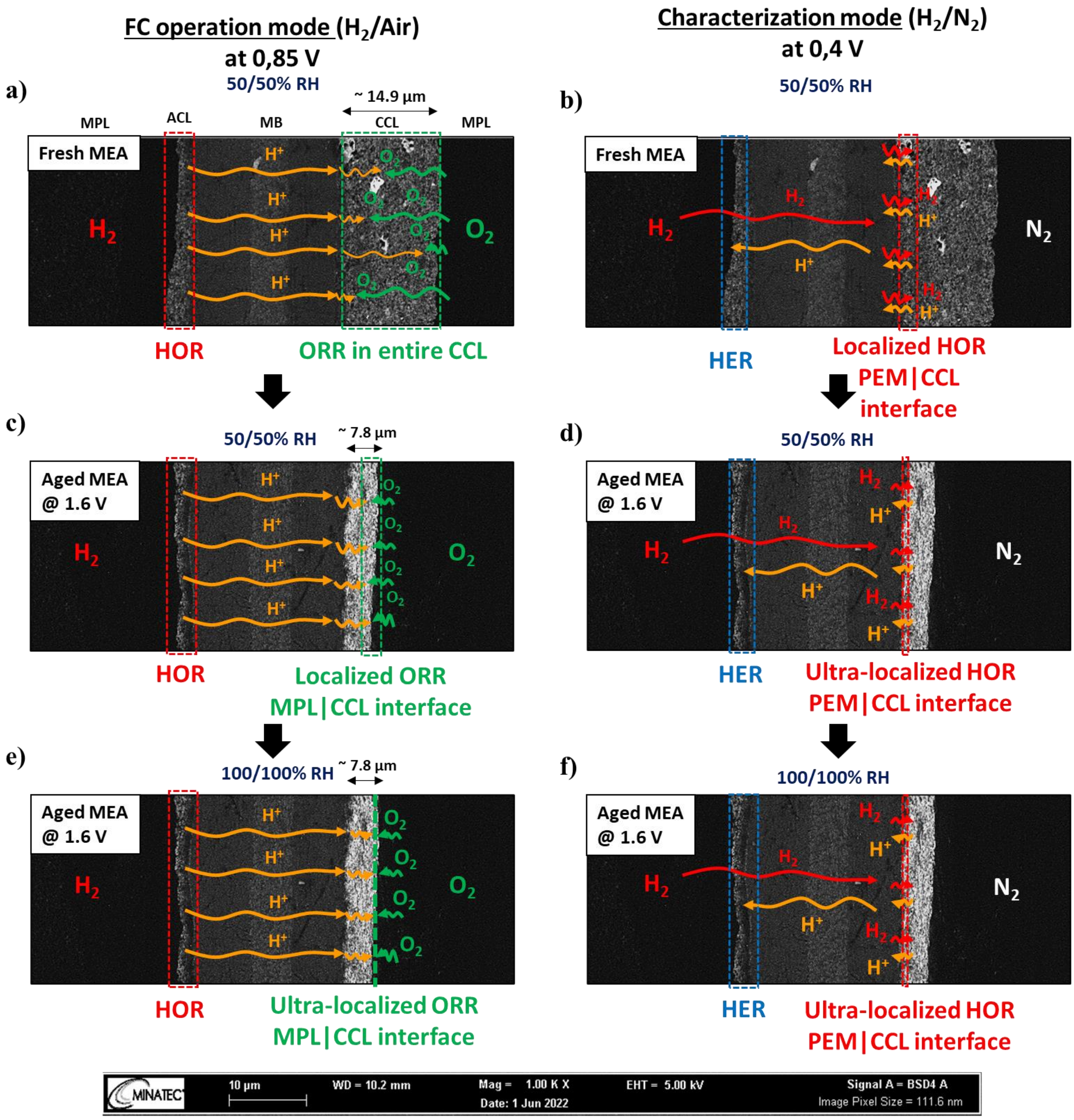

Figure IV-33: Proposal of local cathode operation for highly degraded CCL according to post-mortem results for the most severe SU-AST cases.

IV.4. CONCLUSIONS

Recognized as the most degrading mechanism during shut-down and start-up phases, the reverse current conditions and its mechanisms have been emulated via an innovative and original accelerated ageing test using a real and large PEMFC cell design. The validation of this protocol and the realization of a complete sensitivity study have been successfully carried out in this work.

From the analysis of the SU-AST protocol, cell voltage losses after the 100 cycles can be mitigated by optimizing each operating parameter with an unexpected improvement of the cell performances during the first cycles of the ageing tests related to beneficial physico-chemical changes of the CCL (higher porosity / better apparent proton conduction). After the 100 cycles, reducing the maximum potential from 1.6 to 1.4 V, therefore emulating a dummy load, reduces the performance decay about 15% @1.2 A.cm^{-2} and lowering exposure time to H_2|Air front from 1.5 to 1.0 s in the anode side mitigates cell voltage losses up to 58% @1.2 A.cm^{-2}. Additionally, the optimization of the initial conditions before the emulated start-up by lowering the $RH_{a/c}$ from 80/80% to 50/50% reduces the drop of the cell voltage of about 90% at 1.2 A.cm^{-2}. While no performance drop is noted after 100 cycles by lowering the cell temperature from 60 °C to 45 and 30 °C in this SU-AST protocol. This validates the initial choice to impose a high temperature in our AST in order to exacerbate degradation.

From *post-mortem* SU-AST analysis, it is possible to formulate hypothesis on the local degradation mechanisms of the cathodic catalytic layer. The high potential at the cathode (> 1.4 V over 100 cycles) progressively degrades the carbon support and modifies the microstructure and leads to the thinning and even collapse for the most severe cases (- 50% in terms of thickness) of the cathodic catalytic layer. In FC operation, this accentuates the limitation of the gas transport and alters the water management through the cathode layer and limits the performances particularly at high current densities. In parallel, the loss of active surface is induced by the detachment of the Pt nanoparticles with the support corrosion, and the dissolution / redeposition (including Place-Exchange) which also hinder the performances at low current density. Nevertheless, enhanced apparent transport of protons through the cathode is observed on aged samples. This evolution could be ascribed to either the modification/compaction of the ionomer phase in the cathode and/or the better retention of water due to the higher support hydrophilicity after SU-AST.

Finally, the decrease of the cathodic potential (E_{front}) proved to be the most promising mitigation approach. Limiting the maximum potential during the H_2|Air front strongly prevent the degradations of the catalyst and of the carbon support as well as of the loss of performance. Ideally, the cathodic potential should not exceed 1.2 V locally during the H_2|Air front. A technical means to achieve this is to divert the electric current by connecting leakage resistance during the shunt-down and start-up phases. This solution can be implemented according to several electrical architectures at the "complete stack" and/or "individual cell" levels. Their respective effectiveness to mitigate performance losses and to protect PEMFC during SU and SD events will be presented in the Chapter V.

Chapter V. EVALUATION IN SHORT-STACKS OF VARIOUS SHUNTING DEVICE CONFIGURATIONS DURING THE START-UP AND SHUT-DOWN PHASES

V.1. INTRODUCTION

From the emulation of SU phase conditions with a complete sensitive study at the "cell-scale" in previous chapter, keeping cathode potential as low as possible during the H_2|Air front has been highlighted as the most impactful strategy to attenuate the RCD impact on the cell performance decay. As reported in Chapter II, the most promising electrical strategy and architecture to adjust this cathode potential after long stop in Air/Air consists in the connection of a dummy load shunting the internal electrical current during the SU/SD events. Several patents have been registered on the use of resistance devices in both SU and SD phases as listed in Chapter II (cf. Table II-4). In "classical" literature, most of the experimental studies are performed either on single cell or short-stack with small active surface area (25 – 50 cm²) using laboratory "non-realistic" designs and the dummy load is often emulated by a current set point using an electronic load. Otherwise, passive, and resistive loads are successful alternatives and only few studies have shown that their actual use is without precise control of current diversion during shut-down periods.

In some patents, Reiser *et al.* [95] preconized to connect the dummy load across the stack as soon as the H_2 is introduced in the Air-filled anode during the SU phase while Goebel *et al.* [109] proposed to apply also this dummy load across the stack during the SD phase (gas consumption). The shunt connection can be achieved by two different dummy loads during the SD and SU phases, respectively [115]. These last 3 patents focus on the shunting device connected to the terminal plates of the FC stack. Bekkedahl *et al.* [116] have designed a "short circuit" system based on a device shunting each individual cell of stack in both SU/SD phases enabling its disconnection when the FC is in nominal operation [118]. Shimoi *et al.* [117] used individual resistances to derivate each cell separately. Despite these patents, no specific study has ever been conducted on the comparison of the effectiveness of the shunting architecture (stack *vs.* individual cell derivation) especially in the SU phase regarding the FC performance and durability.

This Chapter V highlights the transposition of these promising SU mitigation strategies using different shunting device configurations on a short-stack (6 cells) with real flow-field design and commercial MEA. A specific ageing test has been developed in order to cycle the SU phase with an H_2|Air front propagation along the anode channel as detailed in Chapter III (section III.3.2). For safety aspects, SD phase proceeds by H_2 consumption to reach an initial Air/Air fluidic configuration (avoiding Air injection in the test bench anode circuit) before the next SU phase. Precautions mentioned in the Chapter II (section II.4.1) have been applied to reduce the impact of SD phase on cell ageing by using a resistive load to accelerate the residual H_2 consumption and by closing valves at both stack anode inlet/outlet. On the whole, four different shunting configurations have been tested and compared according to the same Stack SU/SD-AST protocol (see Table III-9):

- 1 open-circuit configuration “OC” (unprotected as reference case);
- 1 individual cell resistance configuration “R_{cell}” (0.240 Ω);
- 2 stack resistance configurations “R_{stack}” (0.520 Ω “10 A” and 0.162 Ω “30 A”).

For the global stack configurations, the two resistances are estimated to derivate 10 and 30 A, respectively, in FC operation (H_2/Air) at the beginning of the test. We will refer to the terms R_{stack} (10 A) and R_{stack} (30 A) configurations instead of the resistance values for sake of simplicity.

Moreover, coupled global and local measurements by polarization curves and voltammogram techniques have been carried out to get valuable insights into the evolutions within the cells. Indeed, we have monitored and coupled the individual cell voltages with the local current density measurements thank to S++® device during the transient SU and SD events to deeply understand the origin of performances losses in each case and to be able to specify the best protective architecture.

V.2. PERFORMANCE EVOLUTIONS DURING STACK SU/SD-AST

This first section deals with the evolution of stack performance between the initial and after SU/SD ageing protocol according to the shunting device configurations. Firstly, the individual voltages and the local current density distribution along the cathode channel between the cells #3 and #4 are reported in the next section V.2.1. Secondly, the global and local evolution of voltammogram for ECSA monitoring along the cathode channel will be presented and discussed in section V.2.2.

V.2.1. Evolution of performances by polarization curve measurements

V.2.1.1. Fast polarization curves during Stack SU/SD-AST cycles

Open-Circuit and individual cell resistance configurations enable to perform "fast" polarization curves (@ 0.1 – 0.5 – 1.2 A.cm^{-2}) after each cycle along the Stack SU/SD-AST protocol (phase 1 from protocol detailed in Table III-9). Indeed, such measurements are not possible in global resistance configurations since the switch between the electronic load of the test bench and the passive resistive load is not automated. For both OC and R_{cell} cases, the Figure V-1 plots the evolution of the average cell voltage along the AST cycles.

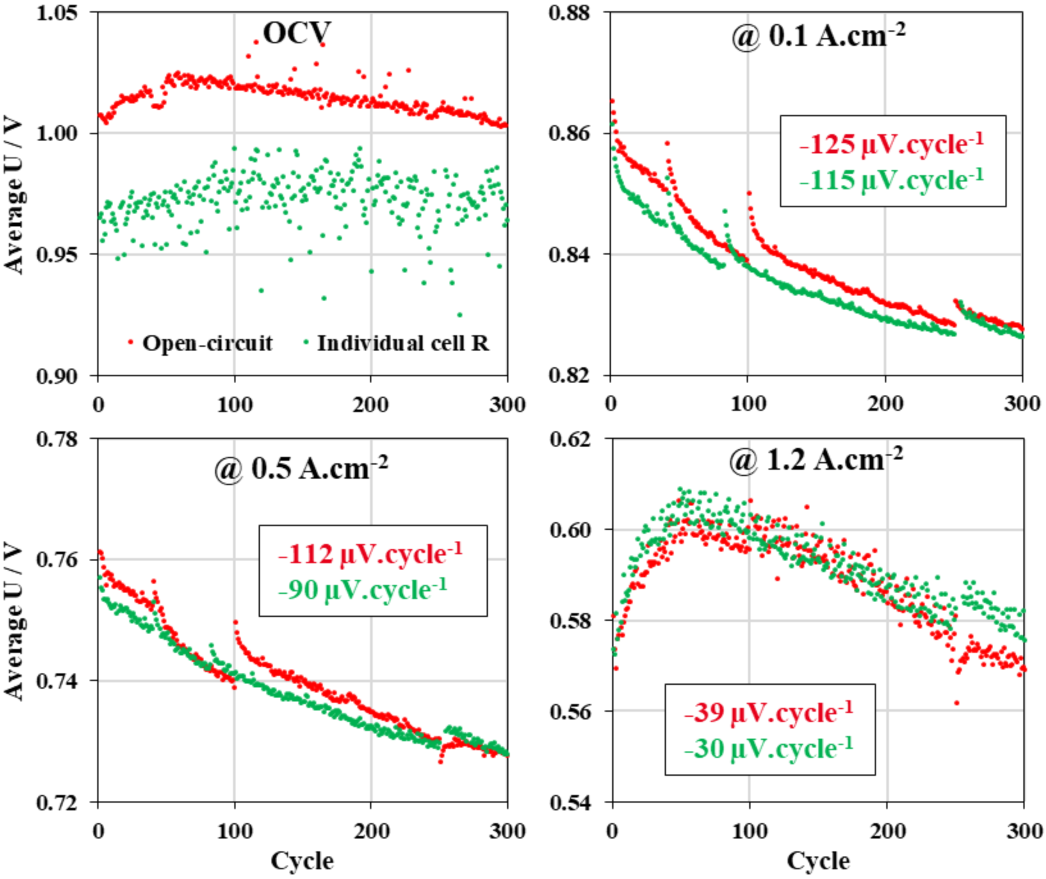

Figure V-1: Monitoring of the average stack voltage by fast polarization along stack SU/SD-AST cycles in open-circuit and R_{cell} configurations with average degradation rates. Stack operating conditions: H_2/Air – 60 °C – 80/80% RH – 1.0/1.0 bar_{abs} (out) – 586/1400 nL.h^{-1} (St 2/2 @1.2 A.cm^{-2})

In OC mode, low variation of the average voltage is visible meaning that as expected, membrane is not specially damaged during the Stack SU/SD AST. The small difference for OCV between both configurations is measured: about 1.01 and 0.97 V for the OC and R_{cell} configuration, respectively. The R_{cell} disconnection is probably not perfect inducing a leakage current via the R_{cell} device.

In operation, the average cell voltages recorded at 0.1 and 0.5 A.cm^{-2} diminish gradually for both configurations: -125 and -115 µV.cycle^{-1} at 0.1 A.cm^{-2}; -112 and -90 µV.cycle^{-1} at 0.5 A.cm^{-2}, in OC and R_{cell} configurations respectively. The mitigation of performance decay using R_{cell} configuration is estimated at 8% (0.1 A.cm^{-2}) and 19% (0.5 A.cm^{-2}) compared to the OC case. Intermittent improvements of the performance are measured at 0.1 and 0.5 A.cm^{-2} after about 40, 90 (or 100) and 250 cycles and can be ascribed to complete polarization curve and cyclic voltammetry measurements that can make the recovery of reversible losses possible.

At high current density (*i.e.* 1.2 A.cm^{-2}), both voltage profiles are similar with a progressive improvement of the performance during the first 50 cycles (from 0.57 V to 0.60 V), followed by a gradual decrease (down to 0.57 V) for the next 250 cycles until the end of test. Consequently, the global performance losses at 1.2 A.cm^{-2} between initial and post-300 cycles are non-linear and averaged at: -39 and -30 µV.cycle^{-1} in the OC and R_{cell} configurations, respectively. This initial improvement performance may reflect here again some beneficial modifications at the nano/micro-scales within the CCL after break-in already observed during emulated SU-phase in the Chapter IV.2.

V.2.1.2. Complete polarization curves measurements

V.2.1.2.1. Average stack voltage evolution

The global polarization curves at the beginning and at the end of the test are illustrated in the Figure V-2a for the four shunting device configurations: OC, R_{cell}, R_{stack} (30 A) and R_{stack} (10 A).

The OC and R_{cell} configurations depict almost similar loss of performance over the whole polarization curve at the end of the test (cf. Figure V-2b): -130 µV.cycle^{-1} (OC case) and -120 µV.cycle^{-1} (R_{cell} case) at 0.5 A.cm^{-2}, respectively. This observation is in fairly good agreement with the final performances measured by fast polarization steps in previous section. However, it is noteworthy to remind that both measurements are not carried out under the same operating conditions (see Table III-8 and Table III-10) which can account for the differences in terms of voltage decay values between “fast” and complete polarization curves.

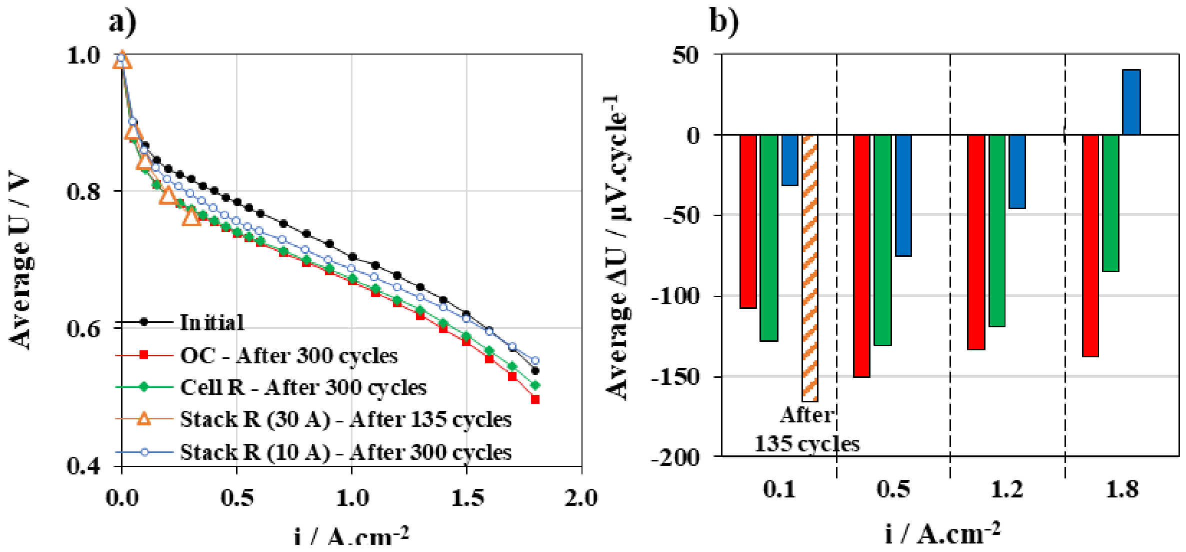

Figure V-2: a) Average stack polarization curves and b) average stack performance decays between Beginning and End of Stack SU/SD-AST tests according to the shunting device configuration. Stack operating conditions: H_2/Air – 80 °C – 50/50% RH – 1.8/1.8 bar$_{abs}$ (in) –St 2/2 (minimum flow-rates equivalent to 0.5 A.cm^{-2})

Interestingly, the R_{stack} (10 A) configuration mitigates strongly the performance decay in the entire polarization curve: -31 / -75 / -46 µV.cycle^{-1} at 0.1 / 0.5 / 1.2 A.cm^{-2}. A slight improvement is even measured at 1.8 A.cm^{-2} of about +40 µV.cycle^{-1} after 300 cycles. On the contrary, the R_{stack} (30 A) appears to be the most damaging configuration (even worse than the unprotected case) with a drastic performance decay of the cell #5 after 135 cycles (-939 µV.cycle^{-1} at 0.1 A.cm^{-2}) and this will be discussed in details hereafter. Consequently, the averaged polarization curve in Figure V-2a is calculated by excluding the performance of the cell #5. Despite this correction, the averaged voltage loss is still very high at 165 µV.cycle^{-1} at 0.1 A.cm^{-2}. Any performance measurements at higher current densities could be done for this configuration ($U_{cell\ \#5} < 0.1$ V).

V.2.1.2.2. Individual cell voltage evolution

The voltage decay of each cell is compared for the four configurations in Figure V-3. The open-circuit configuration shows an irregular distribution with a higher degradation rate for the cells close to the terminal plates (#1, #5 and #6). This heterogeneity is accentuated at high current density. For instance, the voltage loss is about 50 µV.cycle^{-1} for the cells in the center of the stack (#3 and #4) and is superior to 170 µV.cycle^{-1} for the cell #1, #5 and #6 @1.2 A.cm^{-2}. The gap between the average and the maximal voltage loss (cell #1) is estimated at 26%.

In the R_{cell} configuration, the voltage decay within the stack seems to be more homogeneous than in the open-circuit configuration whatever the current density. The voltage decay of the cell #5 and #6 are strongly reduced: from -176 to –87 µV.cycle^{-1} at 1.8 A.cm^{-2} for the cell #5; from -167 to 0 µV.cycle^{-1} at 1.8 A.cm^{-2} for the cell #6. Only cell #1 remains severely. While the impact of R_{cell} is minor on the performance decay for the cells in the center of the stack, this configuration tends to mitigate the side effects and make the individual loss voltages more uniform.

Interestingly, the R_{stack} (10 A) allows the reduction of the performance decay for all cells. From the cell #1 to #5, the individual cell evolutions are very similar, except the cell #6 which shows a higher performance decay. At 0.5 and 1.2 A.cm^{-2}, the voltage loss is measured at about-108 and -95 µV.cycle^{-1} for the cell #6, and, -70 and -41 µV.cycle^{-1} for others cells (#1 – 5), respectively. At 1.8 A.cm^{-2}, the final cell voltage at EoT is even improved by *ca*. 15 mV for the cells #1 – 5 (about +50 µV.cycle^{-1}), while a slight decay is observed for the cell #6 (-30 µV.cycle^{-1}). The difference between the maximal (cell #6) and the averaged performance decay at 1.2 A.cm^{-2} is significantly higher than in other configurations and estimated at 109%.

Finally, the R_{stack} (30 A) configuration induces the most severe degradation rates after only 135 cycles. Particularly, the cell #5 is highly affected with a voltage loss 6-fold higher than the other cells in the stack. Moreover, the respective degradation rates for cells #1 and #2 show a 2-fold higher value (-215 µV.cycle^{-1}) than in other configurations. On the whole, no mitigation and even an aggravation of degradation rates is observed in this R_{stack} (30 A) configuration compared to the unprotected reference case.

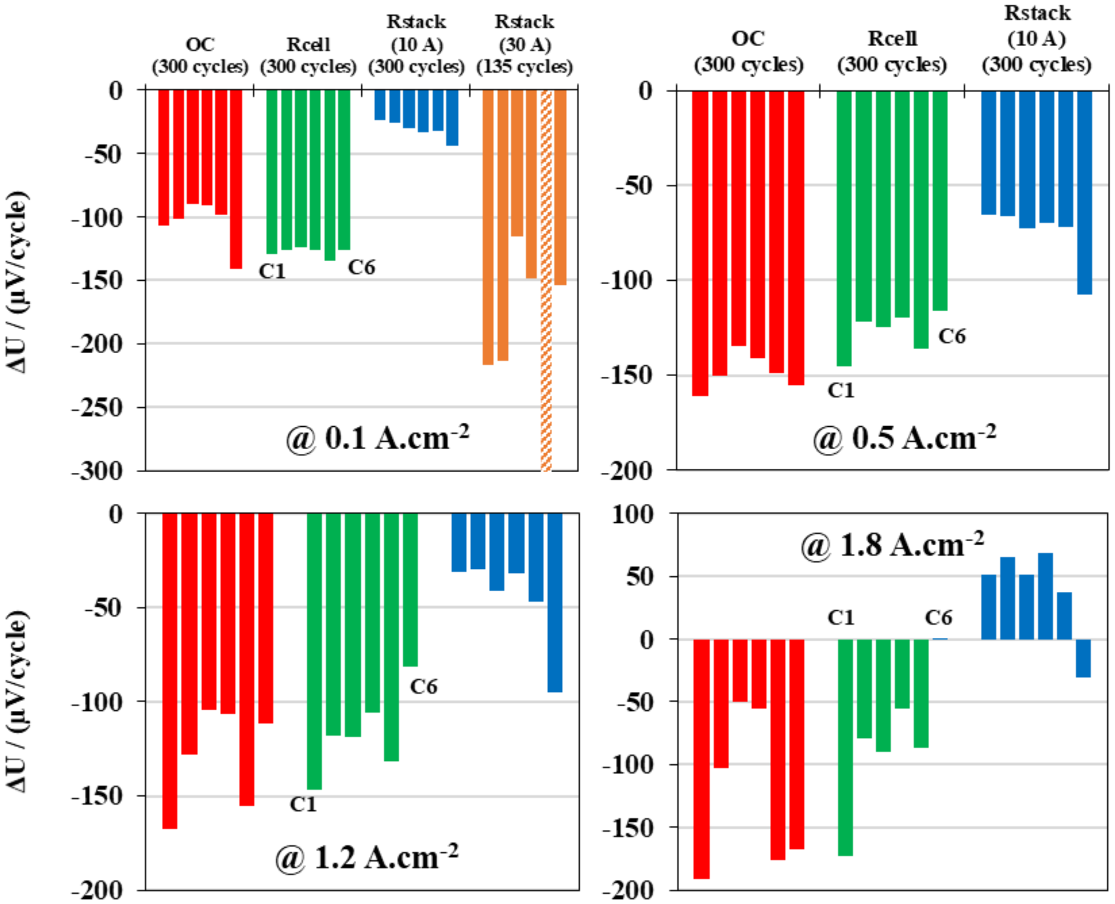

Figure V-3: Individual cell voltage degradation rates at 0.1 – 0.5 – 1.2 – 1.8 A.cm^{-2} according to the shunting device configuration. Stack operating conditions: H_2/Air – 80 °C – 50/50% RH – 1.8/1.8 bar$_{abs}$ (in) –St 2/2 (minimum flow-rates equivalent to 0.5 A.cm^{-2})

In summary, regarding the cell voltages losses compared to the unprotected case, the R_{cell} leads to a more uniform performance decay, but the protection level is rather low in comparison to the R_{stack} (10 A) case. Indeed, the latter significantly attenuates the global performance decay of the stack even if some side effect is probably present in the last cell of the stack according to fluid inlets/outlets position.

In comparaison, Bona *et al.* [100] tested both unprotected and stack resistance configurations on a 24-cell stack in SU/SD phase and measured average / maximal degradation rates at 72 (avg.) / 205 (max.) µV.cycle^{-1} and 45 (avg.) / 130 (max.) µV.cycle^{-1} respectively (@ 0.9 A.cm^{-2}). According to the authors, this 3-fold gap is ascribed to flooding during the SD phase within certain cells, blocking the H_2 access in the next SU phase and exacerbating the degradation rate. The presence of heterogeneities within our short-stack is comparable with the work of Bona *et al.* [100] and their existence justifies their deep study in short-stacks before the integration of the appropriate protective architecture on real full-size stack/system.

V.2.1.3. Local current density along cathode channel

Current Density Distribution Mapping (thanks to the S++® device) allows to probe the local performance between the cell #3 and #4. In this part, the CDDM results during the polarization curve at the beginning and the end of the test at 0.1 – 0.5 – 1.2 – 1.8 A.cm^{-2} are reported. This approach is carried out only on the OC, R_{cell} and R_{stack} (10 A) configurations. The local current density measurements are calculated for 6 zones along the cathode channel (cf. Figure III-7) and are plotted in Figure V-4 from the first zone #1 near the cathode inlet (facing the anode outlet) to the sixth zone #6 near the cathode outlet (facing the anode inlet). The solid and the dotted lines present the initial and the final distribution of the current density, respectively.

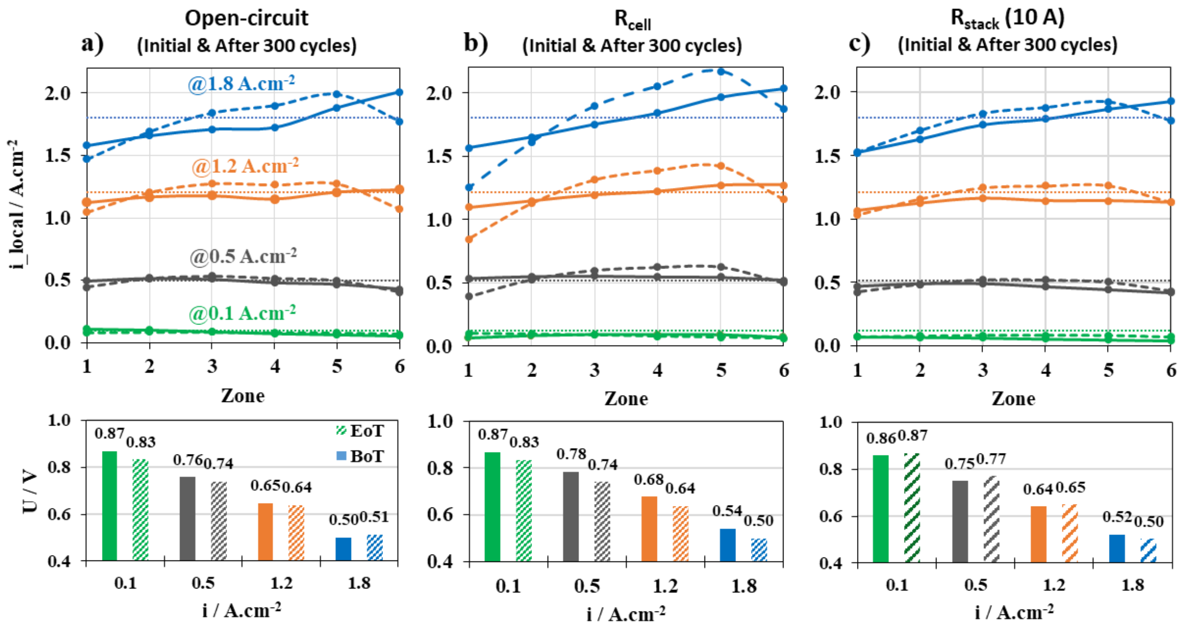

Figure V-4: Local current density distribution along the cathode channel from CDDM and the cell voltage #4 at the beginning and the end of Stack SU/SD AST conditions according to the shunting device configuration. Stack operating conditions: H_2/Air – 80 °C – 50/50% RH – 1.8/1.8 bar$_{abs}$ (in) –St 2/2 (minimum flow-rates equivalent to 0.5 A.cm^{-2})

First of all, the initial distribution for the three configurations at 0.1 and 0.5 A.cm^{-2} are homogeneous along the cathode channel while the local performances are more heterogeneous at 1.2 cm^{-2} and 1.8 A.cm^{-2}. Initially after break-in, the local current density progressively increases along the cathode circuit in our operating conditions. The most likely hypothesis is that the inlet cathode gas is too dry (St 2 at 80 °C @ 50% RH) and progressively gets humidified with the water produced in the cell.

At the end of the Stack SU/SD AST (300 cycles), the current density profiles do not vary at 0.1 A.cm^{-2} for each configuration. A slight reduction of the performance at the cathode inlet (facing anode outlet) is measured for the R_{cell} and the R_{stack} (10 A) configuration. At 1.2 and 1.8 A.cm^{-2}, both locations near the cathode inlet and outlet are affected for the three configurations. Consequently, higher local current densities are forced (and measured) at the center of the cell to ensure the total current conservation, leading to a curved distribution along the cathode channel. This trend is the most pronounced at 1.8 A.cm^{-2}.

Let us point out that the R_{cell} configuration induces a more heterogeneous current density profile than R_{stack} (10 A). Indeed, the local drops of the current density (compared to the OC configuration at EoT) are about:

- -20% (cathode inlet) and -7% (cathode outlet) respectively for R_{cell} configuration;
- 0% (cathode inlet) and -8% (cathode outlet) for R_{stack} configuration.

The most effective configuration to reduce local performance decay is the application of a global stack resistance. Further investigations are needed to understand local behavior during ageing test and especially the degradation rate near cathode outlet region.

V.2.2. Cyclic voltammetry measurements under H_2/N_2

V.2.2.1. Cathode ECSA assessment

In addition to the cell voltage monitoring during ageing test, voltammogram measurements are performed at the beginning and the end of the Stack SU/SD AST to assess the individual cathode ECSA loss for each cell according to the shunting configuration, as plotted in Figure V-5.

Stack SU/SD-AST strongly affects the Pt catalyst for the four configurations. After the ageing tests, the proton desorption coulometry in the 0.1 – 0.4 V region and thus the cathode ECSA is decreased during the ageing test. Both peaks related to the facets (110) and (100) are more pronounced implying nanoparticle growth caused by dissolution/redeposition and/or agglomeration. The relative ECSA losses compared to the initial value of each cell are summarized in Figure V-6 according to the shunting configuration.

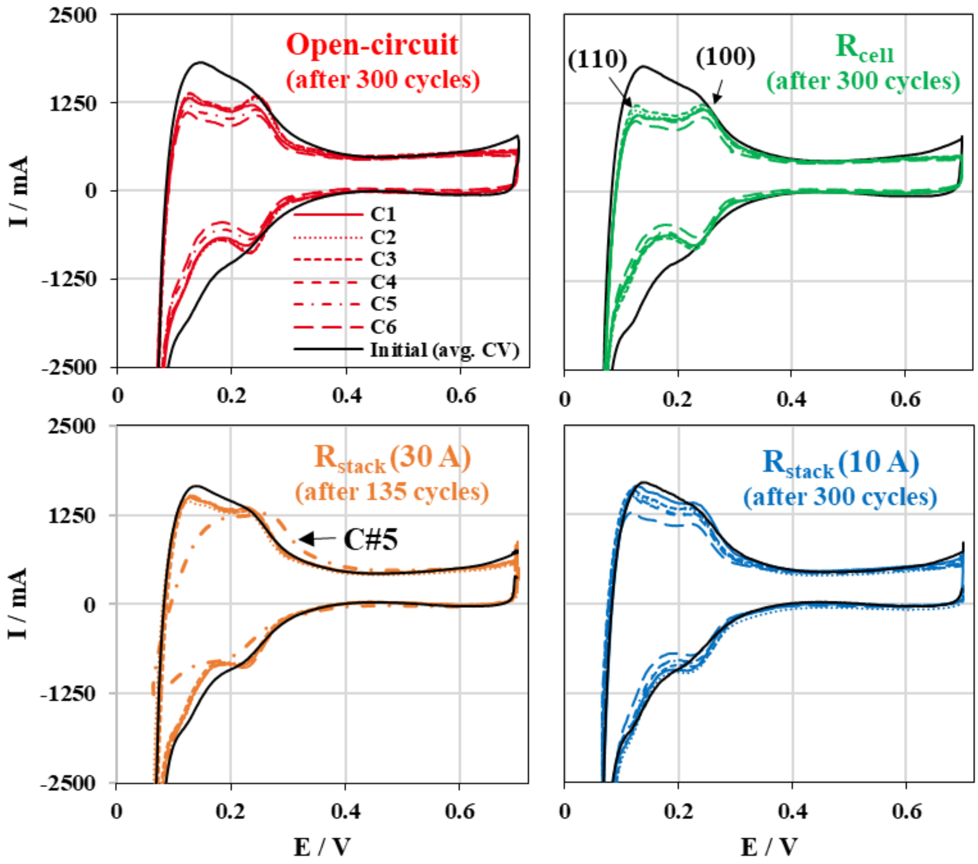

Figure V-5: CV profile at 50 mV.s^{-1} of the average stack at the BoT (black line) and of each cell at the EoT (colored lines) according to the shunting configuration. Stack operating conditions: H_2/N_2 – 60 °C – 80/80% RH – 1.0/1.0 bar$_{abs}$ (out) – 400/1200 nL.h^{-1}

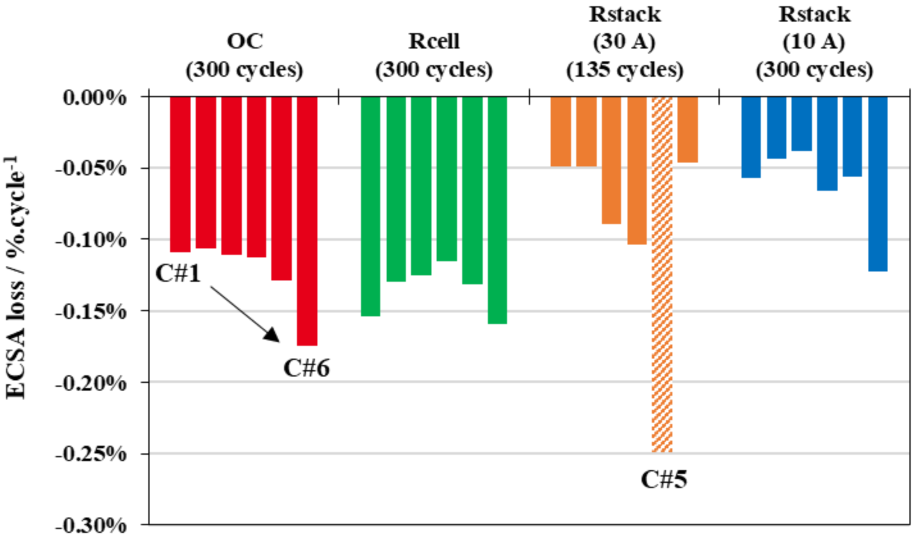

Figure V-6: Distribution of the ECSA losses for individual cells according to the shunting device configuration after 300 Stack SU/SD-AST cycles

In the OC configuration, the ECSA loss of individual cell gets higher and higher from the #1 to #6 (from -0.11 to -0.17$\%_{ECSA}$.cycle^{-1} respectively), in accordance with the distribution of the voltage losses at 0.1 A.cm^{-2} (Figure V-3). In the R_{cell} configuration, the individual ECSA losses are in the same range of values compared to the OC case (between -0.12 to -0.17$\%_{ECSA}$.cycle^{-1}). Nevertheless, cell #1 and cell #6 are the most affected by ECSA losses. Surprisingly, the R_{stack} (30 A) configuration demonstrating the most significant cell voltage losses at 0.1 A.cm^{-2} shows only low levels of ECSA loss for the cell #1, #2, #6 (about -0.05%.cycle^{-1}) but drastic loss for the cell #5 (-0.25%.cycle^{-1}) after 135 cycles. The low ECSA loss for the cells, except #5, is not correlated with the significant voltage decays of these cells deduced from the polarization curves (Figure V-3). This might signify that the cathode microstructure (due to harsh carbon support corrosion) is significantly altered in this case without impacting that much the nanostructure of individual Pt particles. Further *post-mortem* investigation would be required to confirm this hypothesis and/or identify other degradation sources. Finally, R_{stack} (10 A) configuration presents the lowest individual ECSA losses between -0.04 and -0.07%.cycle^{-1} for cells #1 to #5, while a two-fold higher loss is measured for the cell #6. This agrees with the degradation rates for cell #6 compared to other cells on the whole current density range (Figure V-3).

V.2.2.2. Local cathode ECSA assessment along cathode channel

In addition to local characterization under operation, CDDM is also used to reconstruct the local electrochemical response (between cell #3 and #4) for the six zones along the cathode channel during the measurements under H_2/N_2. This approach is carried out only on the OC, R_{cell} and R_{stack} (10 A) configurations. Figure V-7 plots the local CV profiles at the beginning and the end of the Stack SU/SD AST according to the shunting configuration. Figure V-8 summarizes the ECSA loss in each zone along the cathode channel for the R_{cell} and both R_{stack} (10 & 30 A) configurations. Please note that this local measurement technique has been developed during the experiments and thus it was not available yet for the first OC configuration.

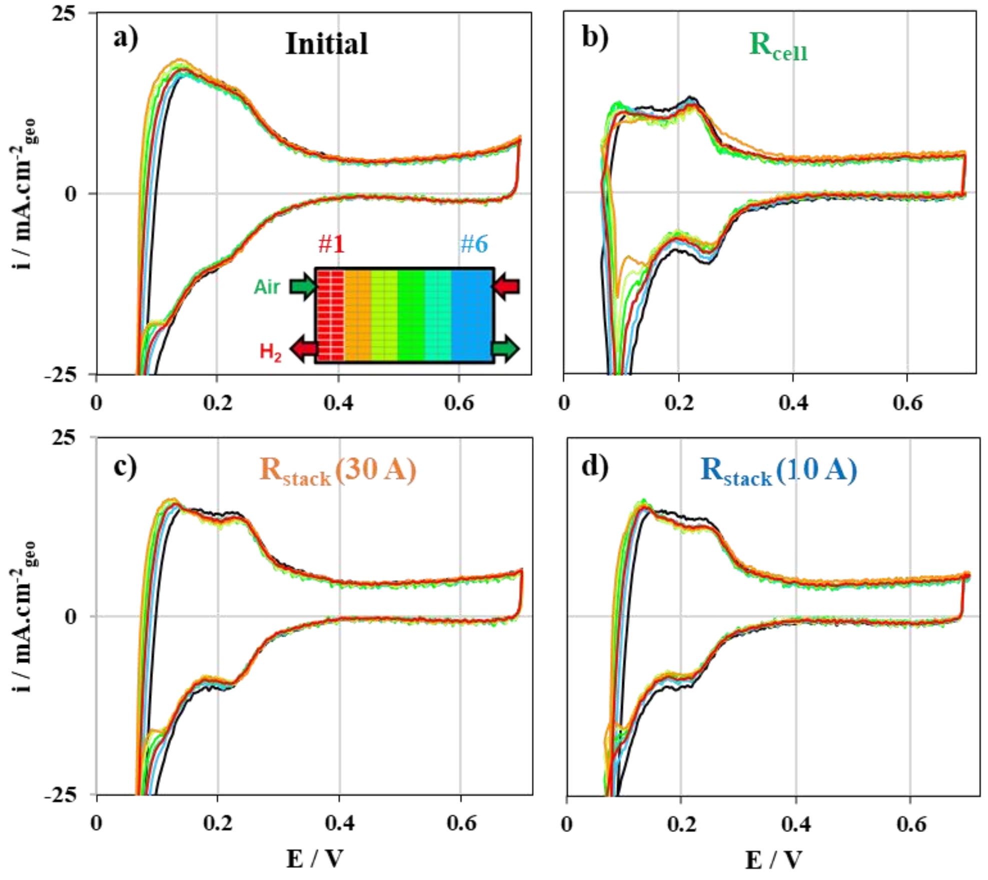

Figure V-7: Local CV profile at 50 mV.s^{-1} along the cell (colored lines) reconstructed from fast CDDM measurements at (a) the beginning and (b – d) the end of the test according to the shunting device configuration. Global cell response recorded by the potentiostat is represented in black. Stack operating conditions: H_2/N_2 – 60 °C – 80/80% RH – 1.0/1.0 bar$_{abs}$ (out) – 400/1200 nL.h^{-1} – CDDM acquisition frequency: 10 Hz

Even if differences are barely visible in the Figure V-7, the R_{cell} and R_{stack} (10 A) cases show an increasing Pt ECSA loss according to the H_2 anode flow circulation from -0.03 to -0.10%.cycle^{-1} in R_{stack} (10 A) configuration and from -0.08 to -0.16%.cycle^{-1} in R_{cell} configuration. This trend is slightly similar as the R_{stack} (30 A) configuration (from -0.04 to -0.11%.cycle^{-1}) with a high ECSA loss in the third zone, and no explanation for this peculiar behavior has been found. On the whole, the R_{stack} (10 A) configuration appears to be the most protective regarding the ECSA evolution during the Stack-SU/SD AST.

We can also notice that the cathode ECSA facing anode outlet is always more degraded than at the anode inlet which agree with the H_2|Air front propagation and the RCD mechanism caused by our protocol at each start-up. Nevertheless, these local ECSA losses are not fully in agreement with the local current distribution at medium/high "global" current densities where both inlet and outlet are strongly degraded after ageing. Thus, the loss of local current produced at the cathode outlet cannot be solely caused by the relatively low and local Pt ECSA degradation. Additional degradations in the CCL at the H_2 inlet/Air outlet region are therefore suspected and might be linked either with the stack operation and/or the SD phase.

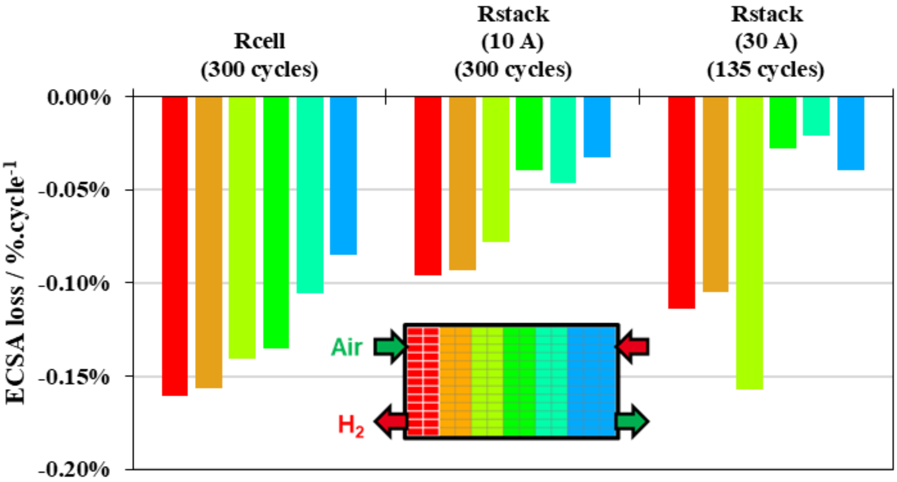

Figure V-8: Local ECSA loss along the cell based on fast CDDM measurements according to the shunting device configuration. See Figure V-7 for experimental details.

V.2.3. Summary of performance and ECSA losses in short-stack

In the four shunting configurations, the performance evolutions of the short-stack have been investigated. Both polarization curve and voltammetry analyses reveal heterogeneous distribution of the degradation rates along the stack between the cell and along the cathode channel according to the shunting device configurations as summarized in Table V-1.

Table V-1: Summary of the performance decay and the ECSA loss along the stack and the channel during the stack SU/SD –AST protocol according to the shunting device configurations

Cases	**Performance decay**	**ECSA loss**
Open-circuit	• Heterogeneous and harsh global loss (mostly for cell #1, #5 and #6) • Heterogeneous local loss (mostly near the inlet / outlet areas)	• Heterogeneous and increasing global ECSA loss from cell #1 to #6 • No local CV measurements available
R_{cell}	• Homogeneous and harsh global loss decay (mostly for cell #6) • Homogeneous and harsh local loss (higher degradation near the inlet than near the outlet area *vs.* the OC configuration)	• Lower global ECSA loss *vs.* OC configuration but heterogeneous distribution (cell #1 and #6 highly degraded) • Heterogeneous and increasing local ECSA loss from the outlet to the cathode inlet (*i.e.*, from the inlet to the anode outlet)
R_{stack} (30 A)	• Homogeneous and harsh global loss (drastic for cell #5) • Local performance investigation not possible *(polarization at EoT impossible)*	• Heterogeneous global ECSA loss from (drastic for cell #5) • Heterogeneous and increasing local ECSA loss from the outlet to the cathode inlet (*i.e.*, from the inlet to the anode outlet)
R_{stack} (10 A)	• Homogeneous and lower loss (except for cell #6) • No degradation near the inlet area, low degradation near the outlet area *vs.* the OC configuration	• Heterogeneous and much lower global ECSA loss from (except for cell #6) • Heterogeneous and increasing local ECSA loss from the outlet to the cathode inlet (*i.e.*, from the inlet to the anode outlet)

To conclude, applying our Stack-SU/SD AST on short-stacks with realistic flow-field design and commercial MEA has led to heterogeneous distribution of the degradations between the cells in the case of global resistances. Some side effects seem to affect the cells close to the terminal plates, rather than the cells in the center of the stack. This observation is probably due to a heterogeneous H_2 supply among the cells and a more limited access for the furthest cell (cell #6) from the stack H_2 inlet.

SD phase seems also to participate in the observed degradation despite the recommendations taken from the Chapter II (II.4.1). Vacuum/Pumping effect may be at stake and could be responsible for the preferential degradation of the cell #1 because of its proximity to the inlet and outlet pipe storing residual H_2 during stops. The anode outlet may be affected by the RCD mechanism in the SU phase whereas the anode inlet is likely degraded by the vacuum effect in the SD phase.

The R_{stack} (10 A) configuration appears to be the most protective architecture regarding the Stack-SU/SD AST protocol. The application of the individual resistances R_{cell} also protects the stack but at a lesser extent than R_{stack} (10 A). Nevertheless, the degradation rates tend to be more homogeneous among the cell and individual shunt appears interesting to mitigate side effects and specific individual degradation of a unique cell in the stack. Finally, the R_{stack} (30 A) is surprisingly more severe when one would expect more current bypass and thus better attenuation efficiency during SU. Degradations are amplified in this configuration during the SU and/or SD phases, as reported in following section.

V.3. DETAILED DESCRIPTION OF THE START-UP AND THE SHUT-DOWN PHASES

In order to clarify the causes of these non-uniform degradation rates between the cells and within the cell along the cathode channel, this section is dedicated to the detailed global and local description of the transient start-up and the shut-down phases according to the shunting configurations.

Indeed, the evolution of cell voltages and local current densities along the accelerated ageing test during the start-up phases (section V.3.1) and the shut-down phases (section V.3.2) are presented and discussed. Individual cell voltage monitoring gives information about the global operation of cells and describes the different phases from the Start-up (initially under Air/Air), then during FC operation (H_2/Air) as a function of the dummy load and finally until the complete shut-down state is reached (back to Air/Air). In addition, the S++® device gives access to the local current density distribution (between the cells #3 and #4) during the propagation of the H_2|Air front in the SU phase and also during the H_2 consumption process in the SD phase.

V.3.1. Start-Up phases

V.3.1.1. Analysis of local current density distribution during the SU phase: Reference Open-circuit configuration

Fast CDDM measurements with a 20 Hz frequency were successfully implemented to monitor the local density distribution as well as the propagation of the H_2|Air front from the anode inlet to the anode outlet. Figure V-9a presents the temporal evolution of CDDM images during the 1st SU phase (at beginning of test) with the unprotected reference configuration (open-circuit). The measured local current densities are either negative (-0.1 – 0.0 $A.cm^{-2}$ range) or positive (0.0 – 1.0 $A.cm^{-2}$ range) depending on the current direction, “reversely” or “conventionally”, according to FC nominal operation. The injection of the H_2 at 24 $nL.h^{-1}$ (equivalent to 0.1 $A.cm^{-2}$ at stoichiometry 1) in the Air-filled anode is started at 1.0 s. From 1.2 to 1.8 s, the propagation of H_2|Air front can be visualized by the opposite evolutions of FC and EC sub-parts within the cell. After 1.8 s (total front duration about 1.8 – 2.0 s), the anode is completely filled with H_2 and nominal FC voltage is observed.

The active surface can be discretized into 13 zones along the cathode channel (corresponding to the number of sensors along the cell length). The temporal evolution of these local current density profiles measured with the CDDM devices between the cell #3 and #4 during the H_2|Air front propagation along the anode channel is plotted in the Figure V-9b. Initially (t < 1.0 s), as the cell is under Air/Air conditions (with continuous and high Air flow at the cathode), all current densities are equal to 0 $A.cm^{-2}$. When H_2 is introduced at the anode inlet (t = 1.0 s), positive current density increases rapidly for the zones near the anode inlet which operates in FC mode (H_2/Air). Simultaneously, the zones near the anode outlet operate inversely in EC mode (Air/Air) with negative current densities. For t > 2.0 s, the anode is filled by H_2 and the whole cell operates in “open circuit” steady state. This global evolution describes very well the RCD mechanism caused by the front propagation.

Regarding the stack behavior, Figure V-9c plots the simultaneous profile of the individual cell voltages during the H_2 injection. Initially, all the cell voltages are measured at ~0.0 V (Air/Air). As soon as the H_2 is supplied, all the cell voltages increase and reach ~1.0 V within less than 1.0 – 1.5 s for the cell #1 - #5 and about 2 s for the cell #6. Such high cell voltage value at open-circuit is surely ascribed to the initial absence of H_2 at the cathode which mitigates the mixed potential effect.

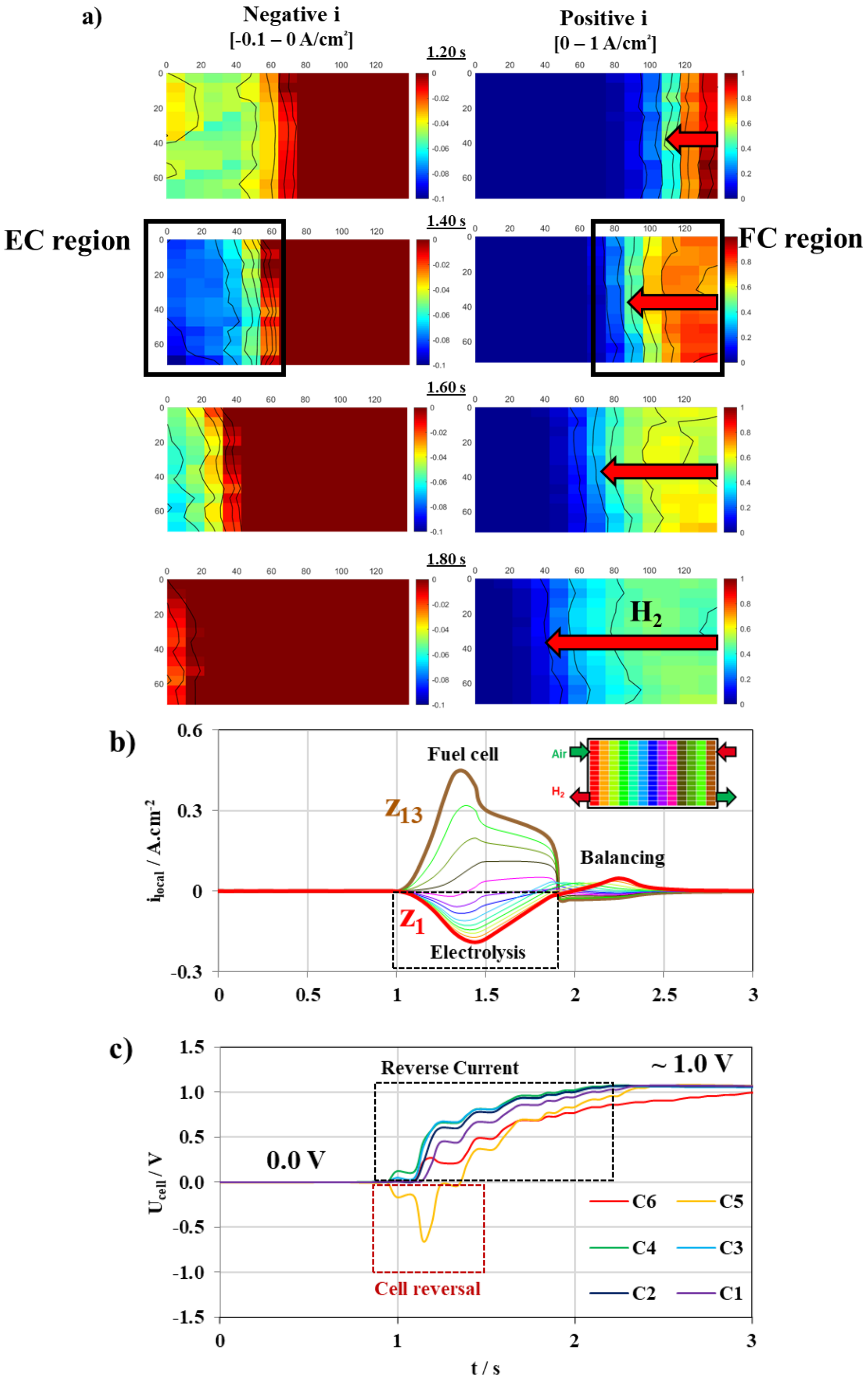

Figure V-9: a) CDDM in negative and positive range, b) the current density profile per zones along the cathode channel and c) the cell individual voltage profiles during start-up phase with the reference configuration (open-circuit) at the beginning of test

The cell #5 reacts differently from the rest of the cells and undergoes a reduction of its voltage down to -0.6 V during 0.2 s showing an inverted operation within the cell: the anode potential is higher than the cathode potential. Since the cathode is supplied by a non-limiting Air flow rate, we can assume that its potential is probably close to ~0.8 V_{RHE} due to the ORR reaction. Consequently, this implies that the anode side is close to ~1.2-1.3 V_{RHE} corresponding to the onset potential of water electrolysis reaction (OER). Such high potential is intended to promote severe corrosion of Pt and carbon support in the anode catalyst layer (see section I.3.2). In fact, a delayed H_2 supply in the cell #5 could yield to a macroscopic electrolysis operation since the neighboring cells in generator mode force the passage of the electrical current. Unlike the RCD mechanism, the cell potential reversal is the signature of an overall gas starvation [142]. Based on this assumption, the anodic potential can effectively reach high potential (> 1.0 V_{RHE}) to find possible oxidation reactions, preferentially OER in absence of H_2, while "nominal" ORR occurs at the cathode (presumed at 0.8 V_{RHE}). Moreover, the low Pt loading at the anode hinders the OER kinetics and it can accentuate the corrosion of the catalyst layer and thus the performance decay of the cell. After this reversal potential period, the Reverse Current Decay mechanism is then very likely to occur during the $H_2|Air$ front propagation. Defective flow-field plates are suggested as the main cause of the delayed H_2 supply.

Finally, cell #6 voltage reaches the OCV value ~ 1.0 V after *ca.* 2.0 s, which is 2 times longer than the "healthy" cells (#1 – #4) and can be caused by a slower H_2 supply.

As a conclusion, Figure V-10 schematizes the anode/cathode gas compositions as well as the individual cell behaviors within the short-stack during the SU phase. As expected, RCD mechanism is observed with the CDDM in all cells except cell #5. FC operation occurs at the anode inlet (facing the cathode outlet) and EC operation near the anode outlet (facing the cathode inlet). However, heterogeneous H_2 distribution has been evidenced between the cells. Indeed, cell #5 is hardly supplied with H_2 (at the benefice of the 5 other cells) in the SU phase and operate in electrolysis mode on its entire surface with a reversed potential. This potential inversion is intended to cause severe degradations in the anode catalyst layer.

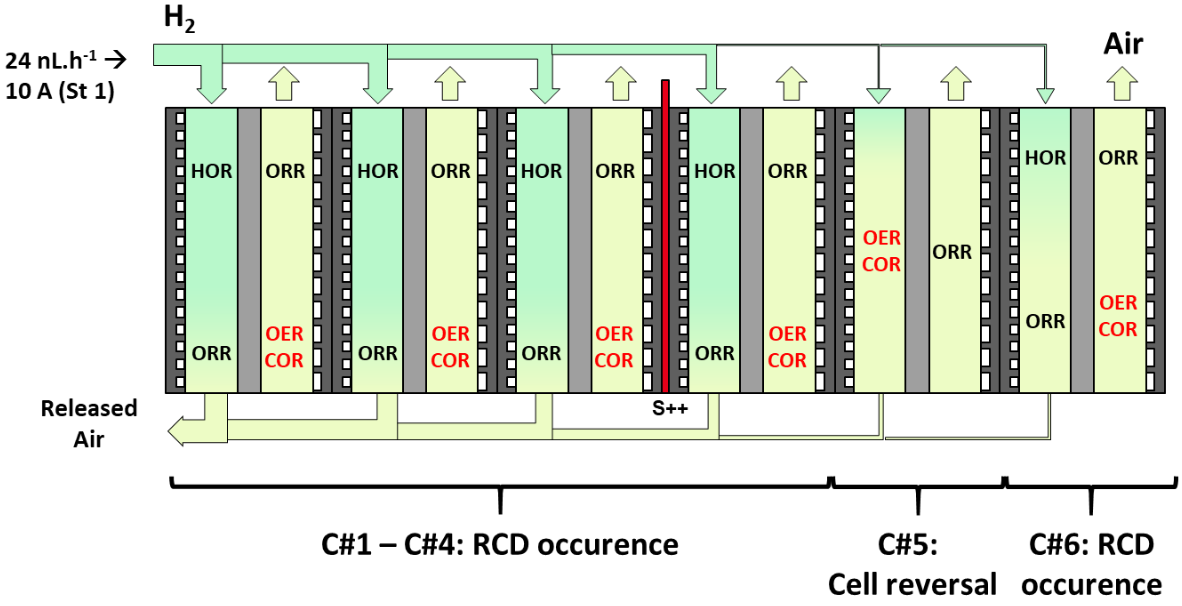

Figure V-10: Schematic representation of the short-stack in terms of individual gas supply and local possible reactions according to cell voltages and CDDM data during the SU phase (at t = 1.15 s) in open-circuit configuration

V.3.1.2. Comparison of the shunting configuration in the SU phase on the local cell operation

In this section, the SU phase is described and compared for each shunting device at the BoT and EoT of Stack SU/SD-AST cycles. All tested short-stacks were mounted using refurbished bipolar plates. The specific problem of cell #5 related to a defect on the bipolar plate has been observed during all the tests. The local current densities and the individual cell voltages have been monitored simultaneously as illustrated in Figure V-13 at the BoT and in Figure V-14 at the EoT.

V.3.1.2.1. Open-circuit configuration

At the beginning of the ageing test (for the 1st cycle), the start-up phase is described in the previous section V.3.1.1 with principal observations as follows:

- Rapid cell voltage elevation (0.0 V → 1.04 V) as soon as the H_2 is injected in the anode compartment for every cell (expect cell #5) with the RCD occurrence, as detected with the CDDM;
- Slower increase of the cell #6 voltage located at the furthest position *vs.* fluid inlets/outlets, probably due to a more limited (or retarded) H_2-supply;
- Unexpected decrease of the cell voltage for the cell #5 with the cell potential reversal, probably due to the defective flow-field plates.

At the end of the test (Figure V-14), the cell voltage and the current density profiles are like the ones at the BoT (Figure V-13). Nevertheless, the cell #5 decreases down to -1.28 V (*vs.* -0.6 V at BoT) as soon as the H_2 is injected because of Cell Reversal occurrence. Simultaneously, the voltage evolution of the cell #6 shows a peak emergence up to 1.34 V. This unexpected behavior might be caused by an internal operating balance between all cells and the transition from local electrolysis modes to global fuel cell mode inducing fast potential variation and possibly high capacitive current. Modeling approach would be needed here and could probably help to further understand this phenomenon.

V.3.1.2.2. Start-Up phase with the R_{cell}

At the beginning of the test, the use of R_{cell} greatly impacts the increase in potential of the cells at H_2 injection by notably limiting the maximum voltage, except for the cell #1 (at 0.77 V), during the low H_2 flow-rate period (24 $nL.h^{-1}$) in competition with the derivation of the internal current which attenuate the RCD mechanism. Figure V-11 schematizes the operation modes of cells right after the H_2 injection (at t ~ 5.0 s). Then, the cell voltages fluctuate during the next 10 seconds after H_2 supply (t = 1.0 s). Such improper FC operation may be caused by an unsuitable H_2 supply in the stack. A flow rate value equivalent to 10 A with a stoichiometry of 1 for 6 cells must be supplied in order to respect an $H_2|Air$ front propagation in *ca*. 0.5 s.

Indeed, the individual dummy load consumes partially the injected-H_2 and makes the total filling of the anode side more difficult and longer. This situation is well captured by the CDDM: in the zone #1 (anode outlet), the current density is almost zero, in opposition to the zone #13 which is active in FC mode near the anode inlet. Thus, all the injected-H_2 is progressively consumed at the anode inlet and barely reaches the anode outlet, which may lead to local fuel starvation and ultimately RCD mechanism. This hypothesis mostly concerns cells from #2 to #6 regarding the cell voltage close to 0.0 V. Only the cell #1 presents a suitable voltage about 0.77 V. Its location close to the stack fluid inlets may facilitate its supply by H_2.

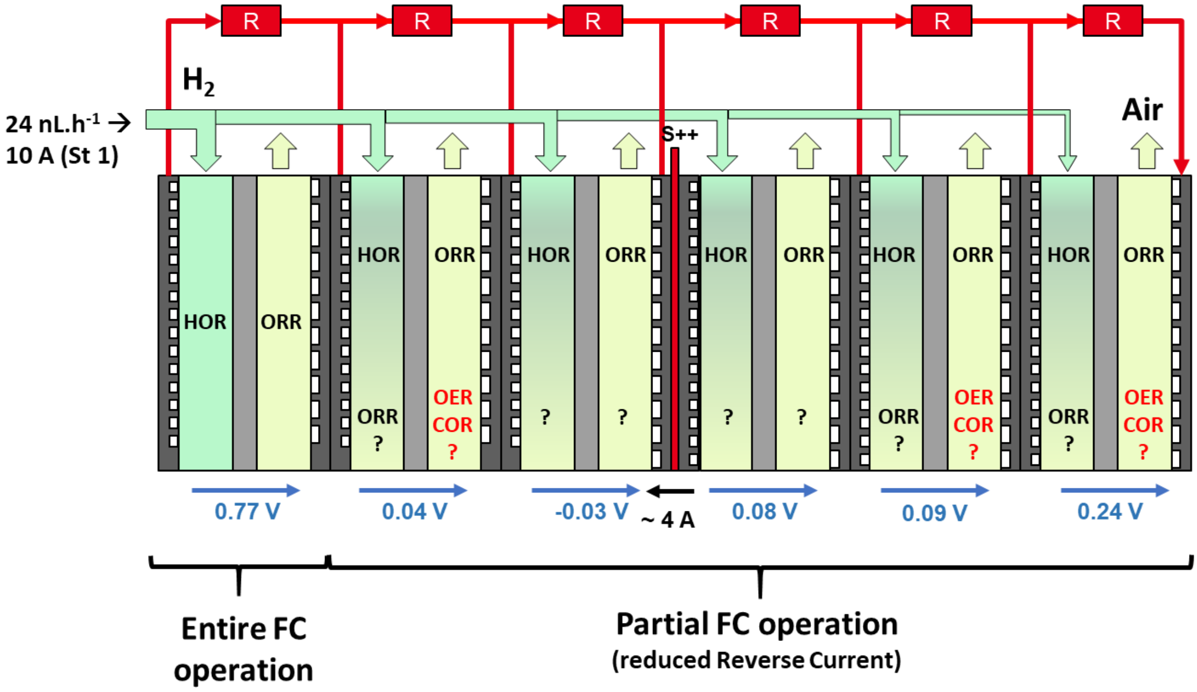

Figure V-11: Schematic representation of the short-stack in terms of individual gas supply and local possible reactions according to cell voltages and CDDM data during the SU phase in R_{cell} configuration (at t = 5.0 s).

The high H_2 flow rate (589 nL.h^{-1} equivalent to 1.2 A.cm^{-2} @ St 2) and the R_{cell} disconnection (t > 10 s) provoke a second minor H_2|Air front propagation leading ultimately a stable cell voltage at open-circuit up to 1.06 V. Cell #5 behavior can be explained by its defective H_2 supply causing cell potential reversal (see Figure V-12)

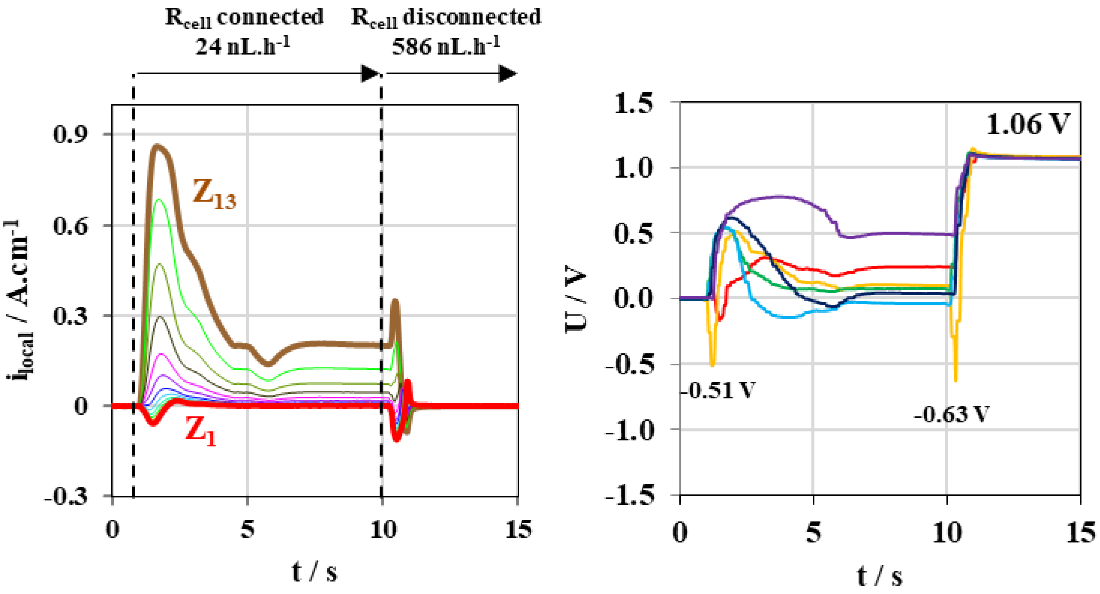

Figure V-12: Local current density profiles along the cathode channel and individual cell voltage profiles during the start-up phase and the following 15 s at the BoT of the test with R_{cell} configuration

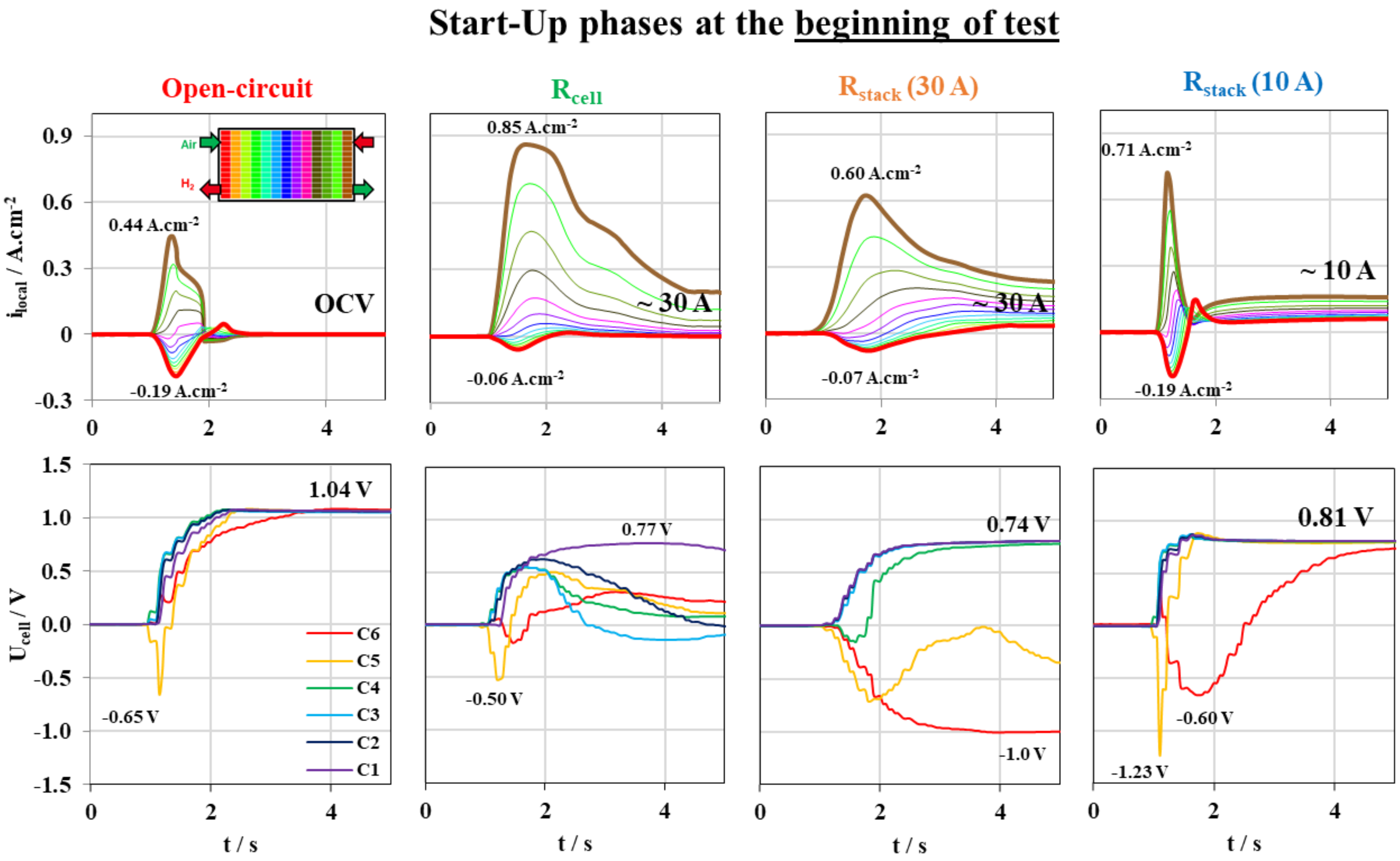

Figure V-13: Local current density profiles along the cathode channel and individual cell voltage profiles during the start-up phase at the beginning of the test according to the shunting device configuration

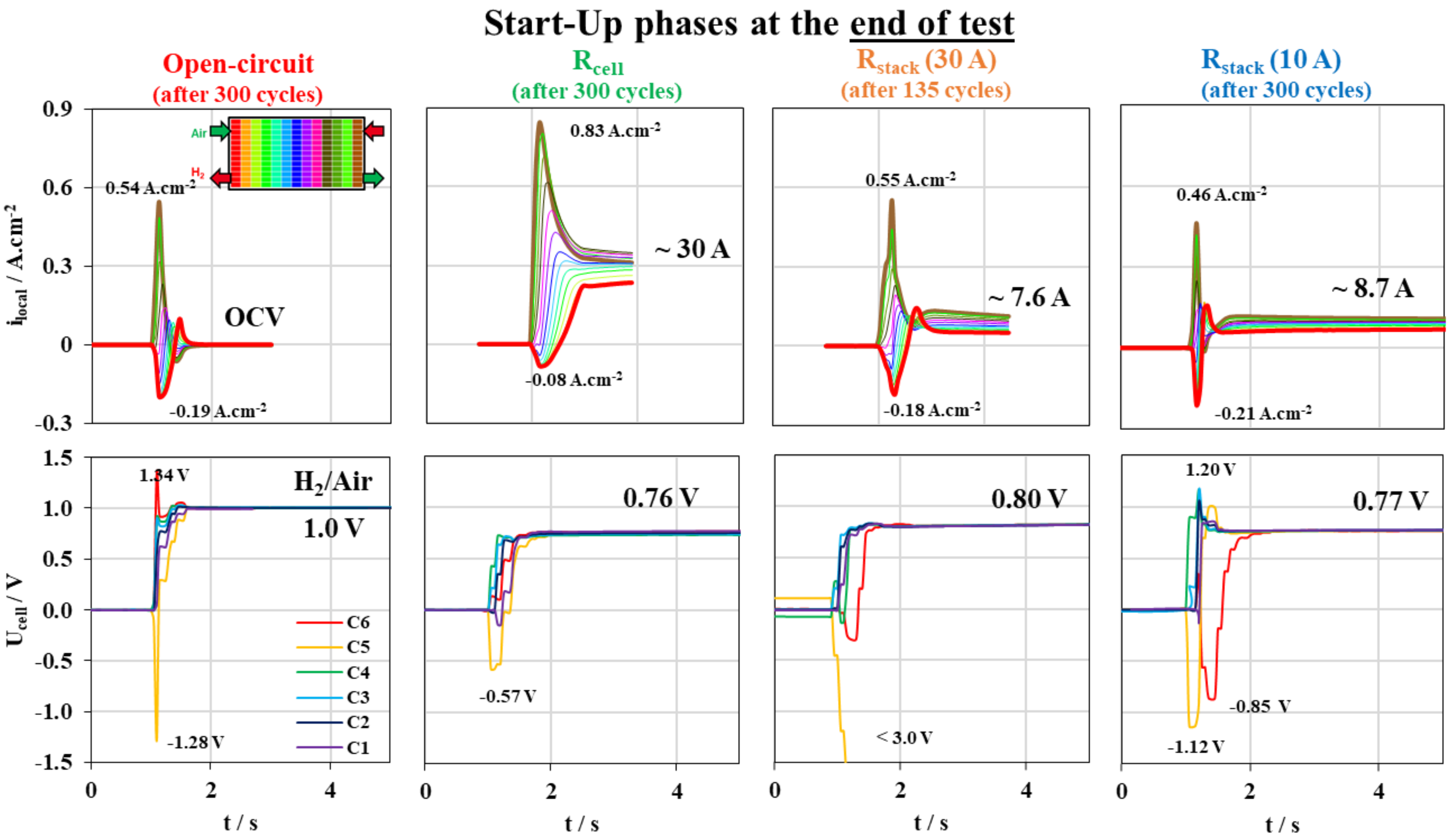

Figure V-14: Local current density profiles along the cathode channel and individual cell voltage profiles during the start-up phase at the end of the test according to the shunting device configuration

On the one hand, the individual resistances tend to limit the EC operation during the front propagation by shunting the current produced in the FC region. However, on the other hand and under our low H_2 flow rate conditions, they also slow down the anode filling since all H_2 is progressively consumed near the anode inlet.

At EoT (Figure V-14), strong evolution is observed between the beginning and the end of the tests. Cell voltages elevate immediately and similarly up to 0.76 V. Cell #5 operates always in EC mode by lowering down to -0.57 V as soon as the H_2 is injected. Then, every cell operates in FC operation in the entire surface right after the SU-phase, in opposition to the beginning of the test. The ageing test may facilitate the homogenous H_2 filling by repeating stack SU/SD-AST cycles. Nevertheless, this behavior cannot be really explained so far.

V.3.1.2.3. Start-Up phase with the R_{stack} (30 A)

At the beginning of test, the application of the stack resistance (30 A) in the SU-phase for the cells #1 to #4 is characterized by an elevation from 0.0 V (under Air/Air) up to 0.74 V (under H_2/Air) resulting quickly in proper FC operation for those cells. Meanwhile, both cells #5 and #6 switch under long EC operation with the most negative voltage values among all configurations. Figure V-15 summarizes the distribution of cell operation modes in the short-stack after 5.0 s. During this period, the global current delivered by the stack is measured at 10 A restricted by the low H_2 flow-rate after the SU phase (*vs.* 30 A as expected under nominal FC operation with a higher H_2 flow-rate at t > 10 s). Favored by the low global resistance, the current generated by the cells #1 – #4 (in FC operation) is easily injected through cells #5 and #6 in EC operation exacerbating (*vs*. R_{stack} 10 A case) the cell reversal as these cells are improperly supplied by H_2.

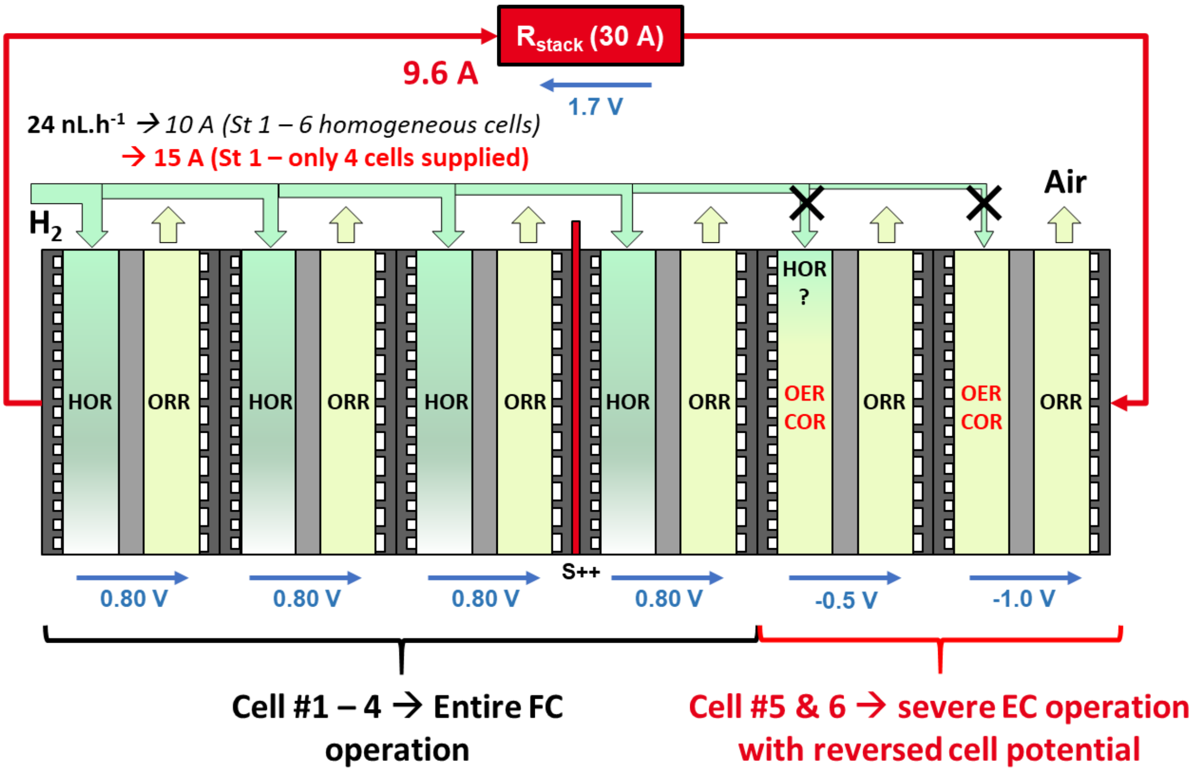

Figure V-15: Schematic representation of the short-stack in terms of individual gas supply and local possible reactions according to cell voltages and CDDM data at t = 5.0 s following H_2 injection with R_{stack} (30 A) configuration

Regarding the CDDM analysis at the BoT (Figure V-16), current density profiles show an elevation (up to 0.60 A.cm^{-2}) in the zone #1 and a reduction (down to -0.07 A.cm^{-2}) in the zone #13, related to the FC and EC operation respectively. After the complete H_2 filling (for cell #1 – #4), gradual distribution of the local current density is measured. The low current density near the anode outlet reflects a possible local fuel starvation event since injected-H_2 is consumed preferentially at the anode inlet (see Figure V-15).

After 10 s, the supply of nominal H_2 flow-rate at 589 nL.h^{-1} (equivalent to 2 A.cm^{-2} A @ St 2) keeping the global dummy load connected disrupts cell voltages as already detected in the R_{cell} configuration as illustrated in Figure V-16. The cells #5 and #6 switch suddenly in FC mode according to the high voltage elevation from -1.0 V up to 0.75 V. During this transition, the voltages of cells #1 – #4 decrease abruptly to 0.1 V approximately. The internal balance of the cell potentials and the inherent balance of current distribution within the stack as observed from CDDM (between cell #3 and #4) are the most probable hypotheses to explain these voltage disturbances. After this transient phase, every cell operates properly at about 0.75 V at 0.3 A/cm².

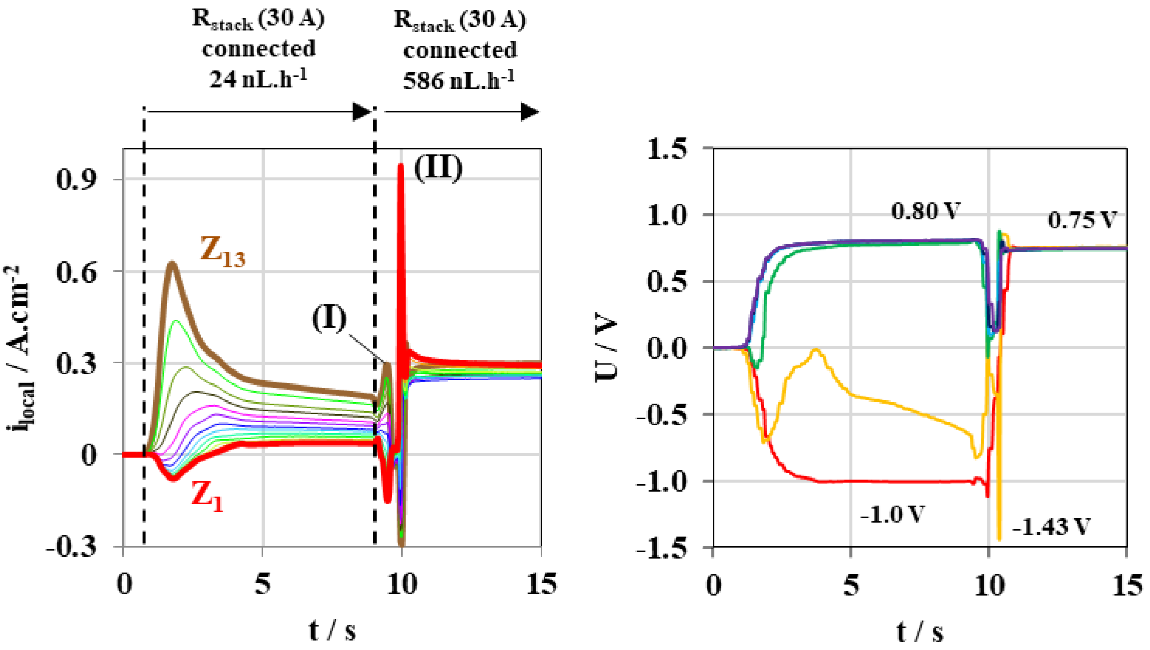

Figure V-16: Local current density profiles along the cathode channel and individual cell voltage profiles during the start-up phase and the following 15 s at the BoT with R_{stack} (30 A) configuration

Regarding the CDDM analysis, two peaks are observed as soon as the nominal H_2 supply is ordered (t = 9.0 s):

- The first peak (I) is similar to the R_{cell} configuration with the RCD occurrence when the neighboring cells #5 and #6 are filled with H_2: the current density in the zone #1 decreases (in EC operation) and increases in the zone #13 (in FC operation);
- Oppositely, a drop of the current density in the zone #13 (in EC operation) and a severe increase in the zone #1 (in FC operation) up to 0.92 A.cm^{-2} characterize the second peak (II). The inversion of operation in both zones is not clear. The most likely explanation is the balance of the internal current in the stack when the cell #5 and #6 increases from -1.0 V to 0.76 V, inducing significant capacitive currents. The latter may also explain the short and simultaneous voltage drop for the cells #1 – #4.

At the end of the test (Figure V-14), cell voltage profile changes significantly due to the degradation and performance decay of the cell #5 as revealed previously in section V.2. Its continuous negative voltage depicts an impossibility to operate in FC mode. Cell #6 demonstrates a delay on the voltage elevation related to its unsuitable fuel supply. Finally, the CDDM demonstrates a slight modification of the current density profile for each zone with an elevation up to 0.55 A.cm^{-2} and a reduction down to -0.18 A.cm^{-2} for the zone #1 and #13, respectively. Degradations in cell #5 seem to be self-sustained and to worsen during ageing.

V.3.1.2.4. Start-Up phase with the R_{stack} (10 A)

At BoT, by reducing the external electrical current delivered by the stack during the SU phase with a higher resistance load (0.540 instead of 0.162 Ω), the cell voltages tend rapidly to steady state at 0.81 V @ 10 A, with lower duration in EC operation for the cell #5 and #6. Indeed, the H_2 filling in the anode is here facilitated when the shunting current is lowered. In this case, only cell #6 is prone to encounter difficulties to be supplied properly by H_2 and suffers from less severe cell reversal (minimum at -0.65 V during only *ca.* 5 s) than in the R_{stack} (30 A) (down to -1.0 V for 10 s). Figure V-17 schematizes the operation mode of cells as soon as the cell from #1 to #5 are properly supplied by H_2.

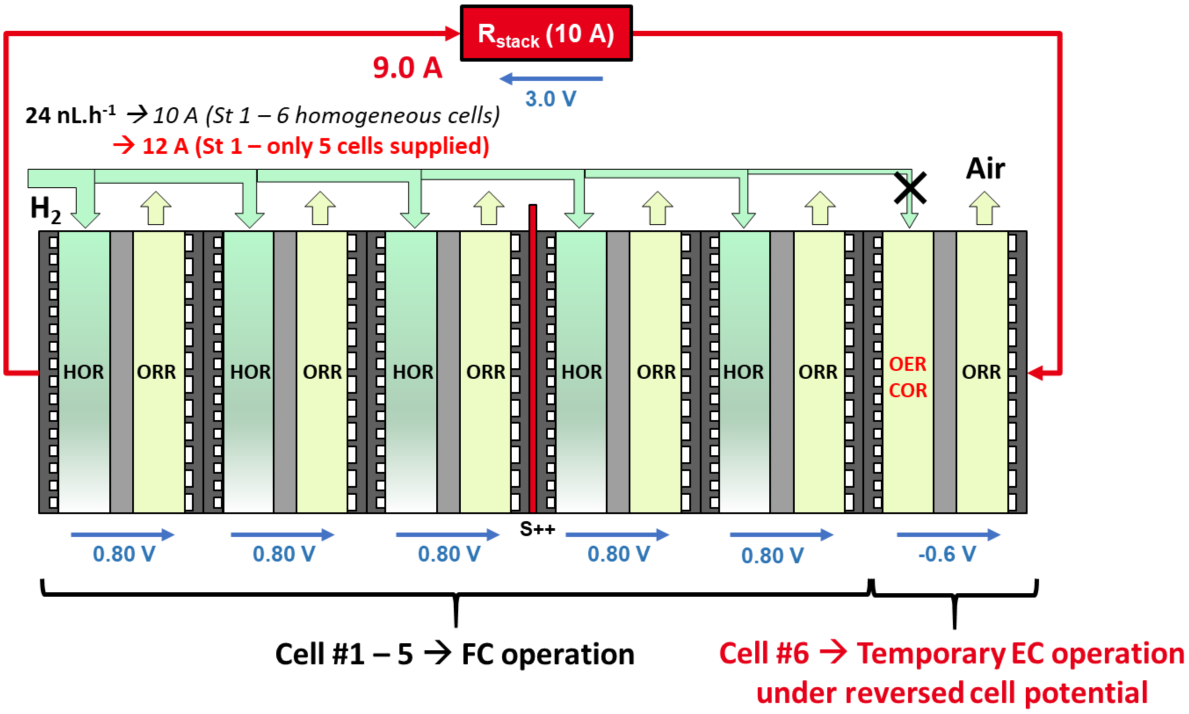

Figure V-17: Schematic representation of the short-stack in terms of individual gas supply and local possible reactions according to cell voltages and CDDM data at t = 5.0 s following H_2 injection with R_{stack} (10 A) configuration

At EoT (Figure V-14), profiles are only slightly modified due to the low degradations during the ageing test (section V.2). FC operates at 0.77 V @ 8.7 A once the anode is entirely filled by H_2. In the transient phase, cells #5 and #6 still suffer from electrolysis operation for few seconds with a minor rate for the cell #5. However, cells #1 - #4 are prone to voltage elevation up to 1.20 V during the transient phase (at t = 1.2 – 1.5 s), especially when voltage of cells #5 and #6 decrease down -1.12 and -0.85 V, respectively. In this case, the internal current balance affects all the cells and is probably responsible for the voltage elevation. At EoT, the proper functioning of the cell #5 is conserved which demonstrates a protective effect in this configuration even for this defective cell.

V.3.2. Shut-down phases

V.3.2.1. Analysis of local current density distribution during the SD phase: reference open-circuit configuration

Figure V-18a reveals the symmetrical distribution of the current density (in 0.0 – 0.6 A.cm^{-2} range) from the middle of the cell towards each extremity during the shut-down phase with the open-circuit Stack-SU/SD AST (with R_{cell} connection during the SD phase, according to the protocol detailed in Table III-9). H_2 supply is shut off at t = 0.0 s and the H_2 consumption lasts about 4.0 s. The center of the cell is easily and quickly depleted (fast decrease of local current) whereas the cell extremities concentrate most of the local current distribution. This symmetric heterogeneity is related to the diffusion (vacuum and pumping effects) of residual H_2 in the volumes of the manifolds, the terminal plates, and the pipes before the valves. For sake of clarity, Figure V-18b plots the current density profiles for the 13 zones (from the anode outlet Z#1 to the anode inlet Z#13). Initial current is averaged at 30 A between the cell #3 and #4. As H_2 is locally depleted, the current densities in the center of the MEA surface (Z#4 – Z#10) are steadily reduced to 0.0 A.cm^{-2}. In the meantime, the current densities in anode outlet and inlet zones (Z#1 – #3 and Z#11 – #13, respectively) reach a maximal current density estimated at about 0.5-0.6 A.cm^{-2} followed by a reduction down to 0.0 A.cm^{-2}, reflecting the complete depletion of H_2 in the cell.

Regarding the voltage evolution within the short-stack, every cell voltage is initially at 0.76 V with the R_{cell} application. As soon as the SD process is started (H_2 supply stopped and valves closed at stack inlet/outlet), cell voltages progressively tend to 0.0 V (leading ultimately to Air/Air). During this transient phase, cells #3 and #4, in the middle of the stack, are depleted faster from residual H_2 and attain negative cell voltage, indicating the cell reversal mode. Indeed, once hydrogen is fully consumed, the electrical current can be imposed by neighboring cells which requires oxidation reactions at the anode side. In parallel, cells #2 and #5 with residual H_2 tend gently to 0.0 A.cm^{-2} with minor cell reversal occurrence.

Finally at longer time, both cells #1 and #6 encounter difficulty to discharge once other cells are out of FC operation and their cell voltage diminishes very slowly. This long discharge process can promote the internal reverse currents with the coexistence of H_2-containing areas with O_2-containing areas generated by the permeation of Air from cathode side.

V.3.2.1. Comparison of the shunting configurations in the SD phase on the local cell operation

In this section, the SD phase is described for the R_{cell} and both R_{stack} shunting device configurations during the first and the last cycle of the Stack SU/SD-AST cycles. The CDDM measurements during the

1st and last SD phases on stack aged with the OC configuration has not been performed. The local current density and the cell voltages have been simultaneously monitored as illustrated in Figure V-19 (BoT) and Figure V-20 (EoT).

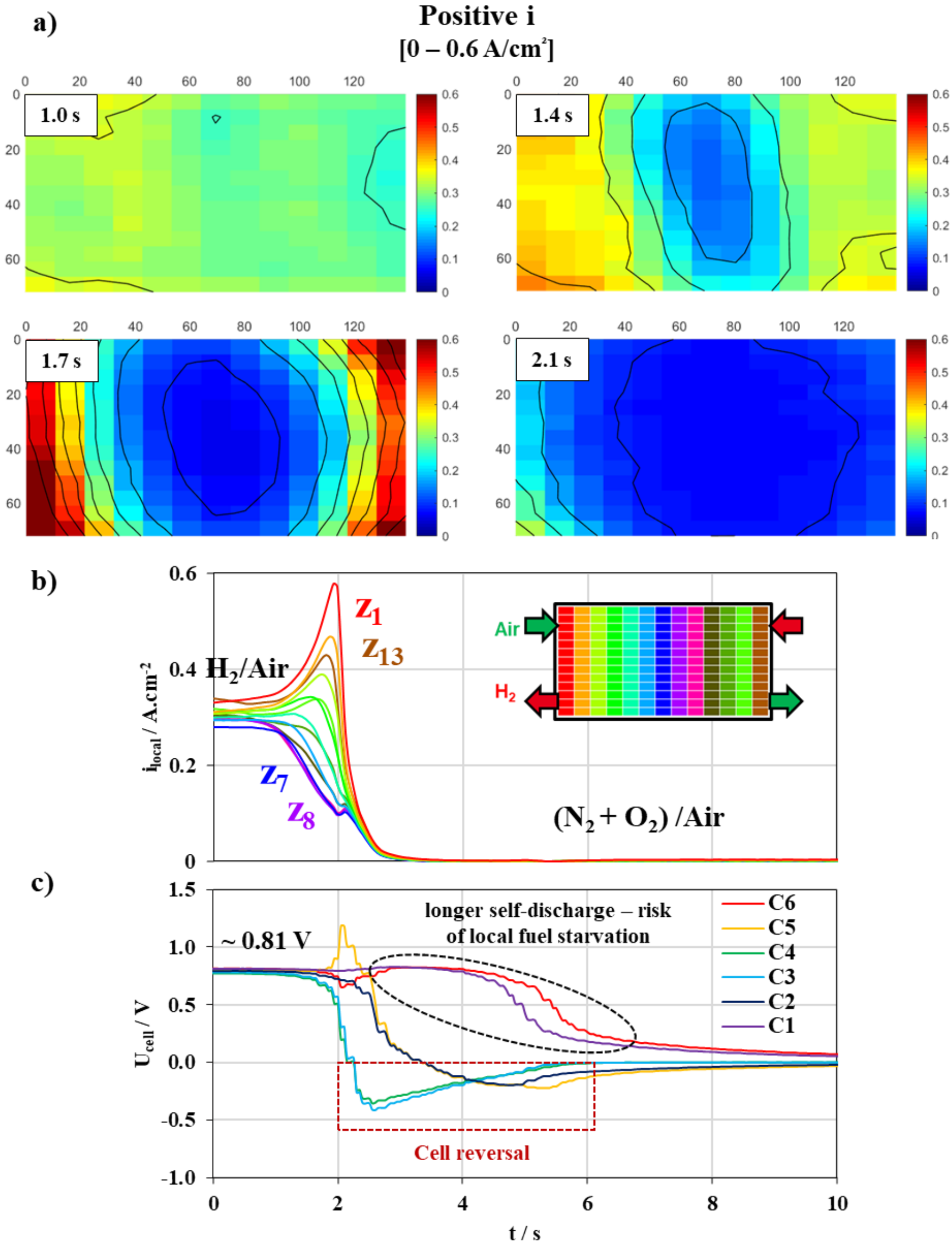

Figure V-18: a) Temporal evolution of CDDM during the shut-down phase by H_2 consumption with the R_{cell} configuration; b) evolution of the local current density profiles per zones along the cell and c) evolution of the individual cell voltages. H_2 supply is stopped at t = 0.0 s.

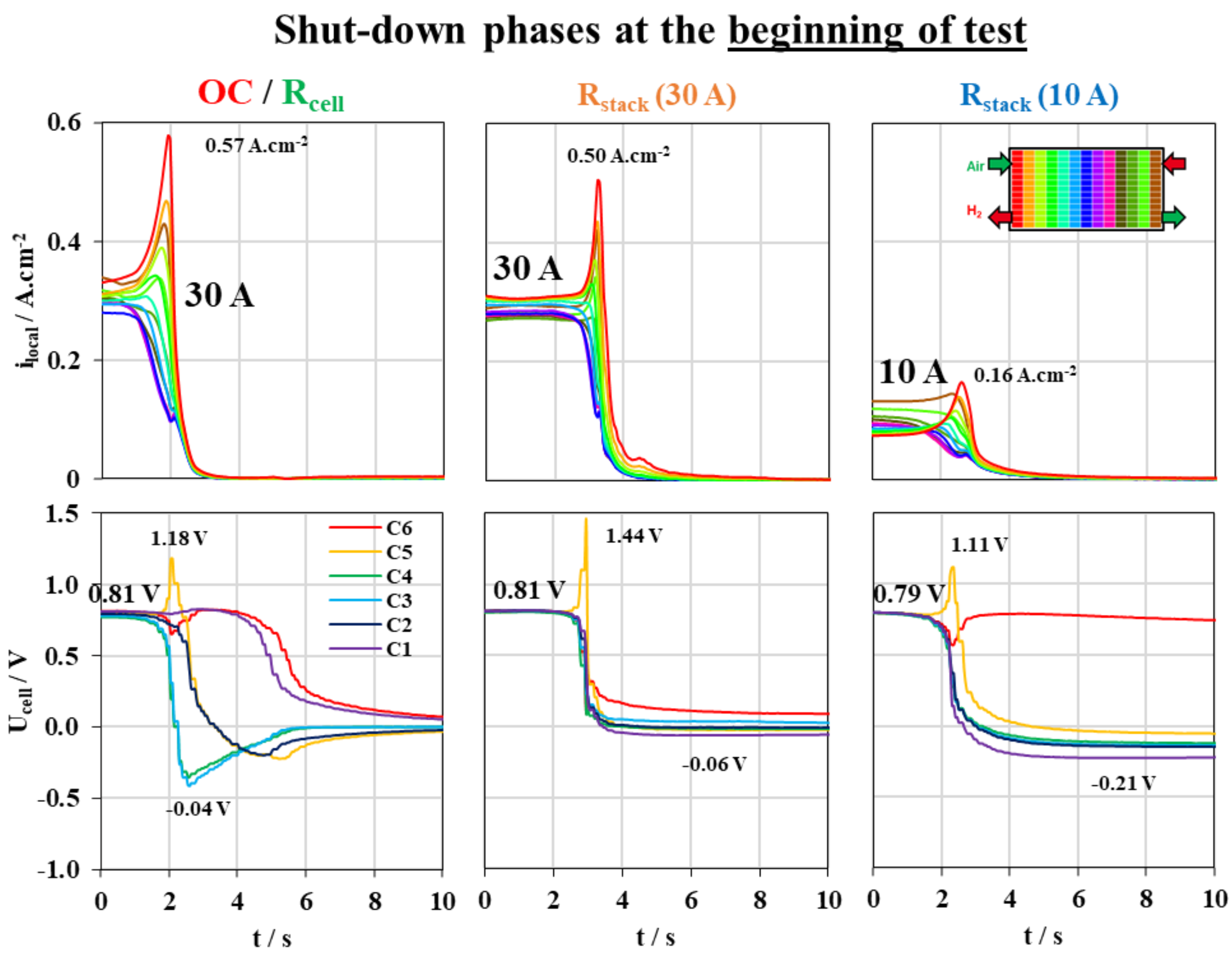

Figure V-19: Local current density profiles per zone along the cell and individual cell voltage profile along the stack during the first shut-down phase at the beginning of the Stack-SU/SD AST according to the shunting device configuration

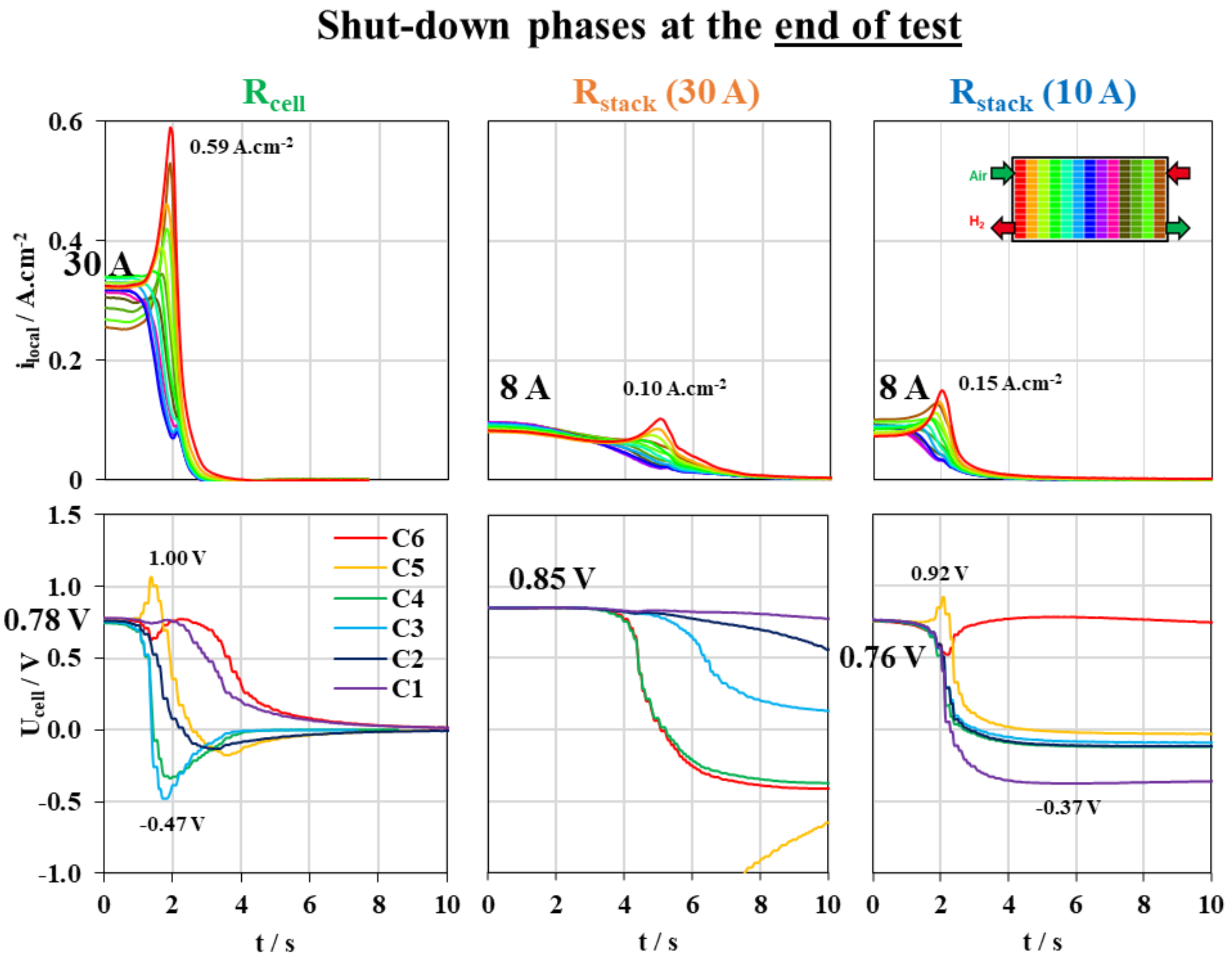

Shut-down phases at the end of test

Figure V-20: Local current density profiles per zone along the cell and individual cell voltage profile along the stack during the first shut-down phase at the end of the Stack-SU/SD AST according to the shunting device configuration

V.3.2.1.1. Shut-down phases with R_{cell} configuration

At the beginning of the test, distinctive transient evolution is detected according to the cell location as explained in previous section V.3.2.1:

- Cells in the center #3 and #4 consumes more rapidly the residual H_2 and results in electrolysis operation (with cell reversal occurrence) while other cells pursue the depletion process;
- Cells #2 and #5 evolve similarly until the complete depletion with a minor rate than cells #3 and #4. An abnormal elevation of the cell voltage #5 at 1.18 V is measured and is not understood currently;
- The longest process is identified in the cells #1 and #6, likely due to extra H_2 supply from stack internal volume and/or lower discharge currents.

To further understand this symmetrical evolution of the cell voltages within the stack, equivalent electrical circuit of the stack have been modelled considering the individual resistances and individual electrical generators using PSIM® software. Initially before the SD phase, all cells are in FC operation at about 0.76 V. Simulation provides a symmetrical current distribution in the stack as illustrated in Figure V-21. Total internal current about 30 A is simulated between the cells #3 and #4, as measured with the CDDM device in nominal FC operation at BoT. Then, the simulation also shows different internal current values: 25 A between the cell #2 and #5, and 15 A between the cell #1 and #6 in agreement with individual cell voltage (U_1 & $U_6 > U_2$ & $U_5 > U_3$ & U_4). This specific distribution is related to the coupling between the individual Rcell elements (2.5 mΩ) and the contactor resistance (119 mΩ). Thus, during the SD process, the cells in the center are submitted to higher current in addition to limited H_2 supply from manifold. This combination can explain their fast H_2 consumption and concomitant cell voltage drop in the SD phase. Inversely, the current circulating in the extremity cells is two-fold lower inducing to a slow H_2 consumption.

At the end of the test, no significant variation is noted during the ageing test according to the performance decay reported in section V.2. Overall, the R_{cell} configuration used in this work generates a heterogeneous current distribution within the stack which leads to different H_2 consumption rates and different cell voltage profile during the SD. This effect is also exacerbated by the local H_2 supply along the stack which depends strongly on internal volumes and cell position.

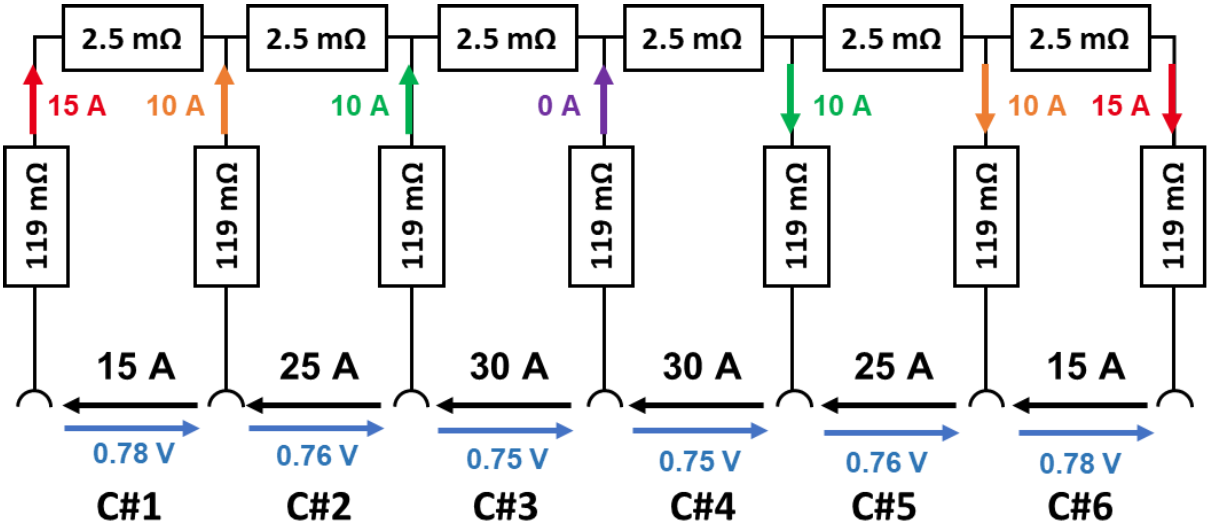

Figure V-21: Prediction of the internal current distribution between the cells using the individual R_{cell} derivation in nominal FC operation (H_2/Air) Cell voltages measured experimentally are also mentioned.

V.3.2.1.2. Shut-down phases with R_{stack} (30 A) & 10 (A) configuration

At BoT, initial cell voltages are measured at 0.81 and 0.79 V by connecting the R_{stack} absorbing 10 and 30 A, respectively. At 1.0 s, the SD processes are initiated, and cell voltages decrease down to ~0.0 V in about 4.0 s for the both cases. The consumption H_2 is homogenous for the cell #1 - #5 for both R_{stack} case. Cell #5 is briefly subject to a high voltage elevation up to 1.44 V and 1.11 V for the R_{stack} (30 A) and R_{stack} (10 A) cases respectively, as observed with the R_{cell} configuration, while cell #6 voltage decreases slowly for the R_{stack} (10 A). Since H_2 consumption is simultaneously faster for the first five cells, cell #6 can then no longer be actively discharged. Thus, the cell #6 voltage drop is then mainly driven by the internal H_2 combustion with O_2 permeating across the membrane and this high potential holding (during ~ 200 s) could affect the membrane durability for long-term consideration as described in the Chapter I (I.3.2.2).

During SD, the CDDM measurements showed the high elevation of the current density near the outlet / inlet areas, and the rapid decrease in the center of the cell. The maximal current density is detected in the zone #1 (cathode inlet / anode outlet) at 0.50 A.cm^2 (+44%) and 0.16 A.cm^2 (+40%) in comparison with the external current density expected at 0.3 and 0.1 A.cm^{-2} for the R_{stack} (30 A) and R_{stack} (10 A) configurations, respectively.

At the end of the test, cell voltage profiles strongly vary in the R_{stack} (30 A) and the average cell voltage and current density under nominal FC operation are strongly altered: 0.3 → 0.08 $A.cm^{-2}$ and 0.81 → 0.85 V (from BoT to EoT after only 135 cycles) due to the overall performance decay, especially for the cell #5 (Figure V-3);

For the R_{stack} (30 A), the voltage of the cell #5 during SD can be strongly reversed down to -3.0 V. Moreover, cell #5 is not able anymore to operate in FC mode (not represented in Figure V-20). Regarding other cells, only cells #4 and #6 discharge in less than 4 s, oppositely to the cells #1, #2 and #3. Since the latter cells are close to the anodic stack inlet / outlet volumes, they may have to consume higher quantities of $H_{2.}$ For the R_{stack} (10 A) after 300 cycles, local current profiles are only slightly affected by the ageing test. Cell voltages still decrease quickly for the cell #1 – #5 while cell #6 is maintained at high potential.

V.3.3. Summary of degradations of the SU and SD phases in stack-scale

In the four shunting configurations, the transient SU and SD phases have been investigated. All the main observations regarding the global and local transient mechanisms during SU/SD phases are summarized in Table V-2. Briefly, both cell voltages and local current density distributions analyses reveal Reverse Current Decay mechanism when H_2|Air front propagates along the anode side in the SU phase. Additionally, faulty H_2 supply in the short-stack, especially in cell #5 and #6, contributes to the potential reversal mechanism detected by the negative cell voltage excursion. Heterogeneous H_2 consumption in the stack and along the channel during the SD phases is also detected. High abnormal cell voltage elevation is measured for the cell #5.

Table V-2: Summary of the degradations observed in the short-stack during both SU and SD phases according to the shunting device configurations

Cases	Start-Up phase	Shut-Down phase
Open-circuit	• Homogeneous H_2 filling for each cell • Homogenous cell voltage elevation	• Inter-cell effect: Symmetrical and heterogeneous H_2 consumption along the stack (faster in the middle cells) • Intra-cell effect: Symmetrical and heterogeneous H_2 consumption in each cell (faster in the middle area than at the inlet/outlet areas) • Abnormal voltage elevation for the cell #5 (> 1.0 V)
R_{cell}	• H_2 filling preferentially for cell #1 – 4 • Delayed H_2 injection for cell #5 and #6 • Incomplete FC operation after SU phase for every cell (local fuel starvation at the anode outlet)	• Similar to open-circuit case
R_{stack} (30 A)	• H_2 filling preferentially for cell #1 – 4 • Delayed H_2 injection for cell #5 and #6 • Normal FC operation after SU phase for cells #1 – 4 • Negative cell voltage down to -1.0 V for cells #5 – 6 (overall fuel starvation)	• Inter-cell effect: Homogeneous H_2 consumption along the stack • Intra-cell effect: Abnormal voltage elevation for the cell #5 (> 1.0 V)
R_{stack} (10 A)	• H_2 filling preferentially for cell #1 – 5 • Delayed H_2 injection for cell #6 • Normal FC operation after SU phase for cell #1 – 5 • Negative cell voltage down to -1.0 V for cell #6 (overall fuel starvation)	• Inter-cell effect: Homogeneous H_2 consumption along the stack (except for cell #6) • Intra-cell effect: Low H_2 consumption for cell #6 remaining in idling / OCV mode for ~ 200 s • Intra-cell effect: Abnormal voltage elevation for the cell #5 (> 1.0 V)

V.4. CONCLUSIONS

This last chapter was dedicated to study several shunting architectures to reduce the cathode potential in the start-up phase. Commonly in literature and patents, the main load is disconnected and switched by a resistive dummy load which partially shunts the internal current exchanged between the FC and the EC regions during the H_2|Air front propagation. Dummy load can be either connected to the terminal plates, shunting the entire stack, or connected to the individual flow-field plates, shunting cell by cell independently. However, a comparative study between these configurations has never been investigated on the same stack.

In this work, a Stack-SU/SD AST protocol has been designed in order to cycle SU phase in presence of the H_2|Air front at the anode side with the application of different shunting devices. Four shunting configurations are tested: open-circuit as reference (without resistive load), individual cell resistance (R_{cell}: 0.240 Ω) and stack resistance (R_{stack}: 0.520 and 0.162 Ω absorbing up to 10 and 30 A, respectively, in nominal FC operation). The SD proceeds by the consumption of residual H_2 in the anode side to result in Air/Air fluidic configuration before the next SU phase. The recommendations mentioned in Chapter II were taken into account to prevent degradations as much as possible related to the H_2 consumption process. For that, similar resistive load as during the SU phase was used and solenoid valves at the anode inlet / outlet were closed. This specific AST has been carried out and cycled with coupled monitoring characterizations by polarization curve and voltammetry techniques to assess global performance decay for each cell, and locally along the cell with CDDM device (S++®).

By using our 6-cell stack, the average degradation rate in our SU/SD AST protocol is reduced by applying shunting device compared to the reference / unprotected configuration: -10% and -65% at 1.2 $A.cm^{-2}$ with the R_{cell} and the R_{stack} (10 A) configurations, respectively.

On the one hand, the R_{stack} (10 A) resistance leads to the lowest performance degradation over the entire stack but significant heterogeneity in degradation between cells is observed (107% between average and maximal performance decay). This configuration is not suitable to mitigate uniformly the impact of the SU/SD phase within the stack. On the other hand, the individual cell resistance strategy gives rise to a higher average degradation but evenly distributed along the stack (only 24 % between average and maximal performance decay). The latter seems to be beneficial by shunting a part of the electrical current from each cell. However, its global mitigation effect is insufficient due to technical limitations since this shunting device was designed to derivate only up to 5 A per cell.

To the best of our knowledge, this work has been showing for the first time the reverse current propagation within a stack using CDDM device (S++® card). As soon as the H_2 is injected, positive current density corresponding to the FC operation is detected near the anode inlet. On the contrary, negative current density is observed near the anode outlet which characterizes the electrolysis mode. For this purpose, the most damaged area in FC operation is identified at the cathode inlet (facing the anode outlet) due to the degradation reactions (CSC + Pt ECSA loss). By applying the R_{cell}, the localized degradation seems exacerbated, compared to the R_{stack} (10 A) configuration which strongly mitigate the performance decay. That indicates a more beneficial effect of the stack resistance than the individual resistance during the SU phase. In addition, a highly degraded area near the anode inlet is also identified that cannot be entirely related to the SU phase. The most likely explanation emphasizes the vacuum effect with residual H_2 in the inlet volumes during the H_2 consumption phase. In our SU/SD AST protocol, reverse current between residual H_2 and O_2 permeating from the cathode cannot be ruled out and can also lead to the non-negligible degradation also during the shut-down process despite the experimental precautions.

In perspective, this study shows that coupling simultaneously both R_{stack} and R_{cell} during SU phase and/or the R_{cell} during the SD phase, could be interesting. Indeed, the R_{cell} manage to deplete uniformly the residual H_2 in the stack during the SD phase by promoting the self-discharge of each cell. On the contrary, the R_{stack} deviates a more significant current during the SU phase, strongly mitigating the performance decay. However, in this study, the low H_2 injection rate equivalent to 0.1 $A.cm^{-2}$ (at stoichiometry 1) is actually not representative but made it possible to monitor the local conditions with the CDDM device. Indeed, our Stack SU/SD AST conditions yields to faulty H_2 supply when the current absorbed by the dummy load is too high. The non-supplied cells (remaining under Air/Air fluidic conditions) operate then in electrolysis mode due to the current generated by neighboring cells (under H_2/Air fluidic conditions). In this irregular configuration, the cells in Air/Air suffer from global fuel starvation favoring cell reversal operation and leading to harsh performance losses. Contrary to the most common reverse current decay mechanism, the oxidation reactions at high potential can take place within the entire anode catalyst layer, degrading the carbon support and the Pt nanoparticles. Preventive solution would consist in increasing significantly the H_2 injection rate in order to, firstly, reduce the residence time of the H_2|Air front, and secondly, limit the cell reversal occurrence with a more uniform H_2 filling in all cells.

Finally, the measurements of the respective impact of the SU or SD phases on the performance decay requires to employ N_2 purge to avoid undesired degradations within the stack. For instance, to study the SU phase, this work should be repeated by replacing the H_2 consumption in the SD phase by N_2 injection via a secondary circuit to remove residual H_2 in the fuel cell while keeping the primary circuit under H_2 for the next start-up. When cell voltages are low enough, anode inlet / outlet can be closed, and Air can diffuse from the cathode side. Regarding the detailed investigation of SD protocol, proper and safe SU phases would be here required by using for instance N_2 purge at both anode and cathode sides prior to H_2 injection and followed then by Air supply.

GENERAL CONCLUSION & PERSPECTIVES

In this thesis work, the alteration of the PEMFC performance during the start-up (SU) and shut-down (SD) phases are investigated through two novel Accelerating Stress Tests: SU-AST protocol at single cell level and SU/SD-AST at short-stack level, with real flow-field design and commercial MEA. The experimental approach is designed to identify the most impactful parameters during these transient events and the most promising system architecture to prevent the degradations and to support PEMFC system designers.

Firstly, the SU-AST protocol at single cell level has been developed to emulate the high potential elevation at the cathode side as realistically as possible during the H_2|Air front propagation along the anode side. This emulated potential profile is cycled with *in-situ* coupled monitoring techniques to characterize the degradations of the platinum nanoparticles and the carbon support components in the cathode catalyst layer. Hence, their impact on the cell performance losses along the SU-AST protocol is evaluated. After the validation under a reference SU-AST case (emulating an unprotected SU phase), a sensitive study of the main operating parameters has been performed as follows:

- E_{front}, the maximal potential profile, emulating the lowering of the cathode potential by applying dummy load (from 1.6 to 1.0 V_{RHE});
- t_{front}, the exposure time at the maximal potential, relative to the velocity of the H_2 injected in Air-filled anode in SU phase (from 1.5 to 0.5 s);
- $RH_{a/c}$, the relative humidity of both anode and cathode gas supplies (from 95/80% to 50/50%);
- T_{cell}, the cell temperature (from 60 down to 30 °C).

Their respective effects on the degradation mechanisms and the performance decay are thus quantified. Decreasing the value of each parameter in our SU-AST protocol has a favorable effect on the performance loss mitigation. Degradation could even be quite totally mitigated by acting at the same on the time duration of the H_2|Air front (t_{front} <0.5 s), and the cell temperature (T_{cell} < 30 °C) and humidity ($RH_{a/c}$ < 50%). However, the most impactful parameter is the maximal cathode potential (E_{front}) reached during the front. Ideally, this potential should not exceed 1.2 V. Indeed, below this threshold value, the corrosion of the carbon support of the graphitized domains is low, and consequently, the detachment / agglomeration of the platinum nanoparticles is also hindered. ECSA losses are mainly governed by the Pt dissolution/redeposition and the Place-exchange mechanism as soon as the potential exceeds 1.0 V. Ultimately, the performance drop is strongly alleviated by reducing the cathode potential from 1.6 to 1.2 V during SU-AST. Surprisingly, the SU-AST at 1.0 V even yields to a slight improvement of the final performance. This unexpected evolution may be related to a beneficial structural modification of the CCL at nano/micro-scale.

Additional *post-mortem* analyses have provided key-data on the CCL properties modifications in our SU-AST protocol to better understand the degradation mechanisms within the cathode catalyst layer. Physico-chemical and electro-chemical measurements on small samples, taken from aged MEA, highlight respectively the evolution for each SU-AST case. The CCL thicknesses thinning are closely related to the carbon support corrosion. Thus, the SU-AST case at 1.6 V shows a thinning of about 50% while the 1.0 V case barely modifies the cathode thickness. Because of CCL thickness reduction, the loss of porous volume can alter the water management properties as observed by a lowered water sorption capacity on aged samples compared to the fresh CCL. Moreover, the hydrophilicity of the carbon support is also very probably increased by the surface functionalization during ageing. The electrochemical performance drop at high current density and high RH observed on small aged MEA samples confirms the reduced water management capability for the most severely degraded CCL which is likely responsible for mass-transport limitation of oxygen within the aged cathode layer. Based on this *post-mortem* analysis, a degradation mechanism of the CCL during our most severe SU-AST cases at 1.6 V is proposed as follows. In the fresh MEA, the ORR supposedly takes place in the entire CCL: oxygen and proton can be transported through the whole layer. Once aged and thinned, the oxygen diffusion into the decreased porous network is harder and is also hindered by easier saturation with liquid water. Thus, ORR is likely delocalized near the cathode catalyst | GDL interface. Protons are forced to cross the whole thickness of CCL until the active sites, justifying the elevation of the effective proton resistance in FC operation. Alleviating these drastic CCL properties modifications, and the concomitant drop of the electrochemical performance, is possible with the implementation of optimized mitigation strategy and appropriate architecture in PEMFC system.

However, the degradation rate of the carbon support and the Pt nanoparticles at E_{front} = 1.4 V is similar to that at t_{front} = 0.5 s, $RH_{a/c}$ = 50% and T_{cell} = 30 °C, while the performance decay are much higher at 1.4 V. The performance loss is not implicitly related to the amount of Pt/C corroded. Likewise, it is impossible to experimentally distinguish in our SU-AST profile, the contribution of the potential cycling (3*0.065 ↔ 1.0 V) and the high potential holding (up to 1.6 V) on the final degradations of the Pt nanoparticles and the carbon support. Beyond the scope of this study, additional *post-mortem* study based on nano-scale observations would provide key-data on the distinctive modifications of the Pt/C materials and structures according to the operating conditions used in our SU-AST protocol.

The way to reduce the most impactful E_{front} parameter in the SU phase under initial Air/Air configuration in both anode and cathode compartments before SU is to derivate partially the internal currents exchanged between the respective Fuel cell and electrolysis regions when the H_2|Air front is propagated along the anode side. From literature and patents, a dummy load can effectively be connected either on the terminal plates (shunting the entire stack) or bipolar plates (shunting each cell separately). In order to compare the impact of both shunting architectures on the performance decay and the stack durability, a second accelerated stress test has been designed to cycle SU phase with the H_2|Air front propagation while the SD phase proceeds by H_2 consumption using recommended procedures to prevent as much as possible additional degradations and in order to have Air at the anode. Four shunting configurations are tested: open-circuit as reference case (without resistive load), individual cell resistance (0.240 Ω) and stack resistance (0.520 Ω and 0.162 Ω). Global measurements (per cell) and local measurements (along the cathode channel) have been performed to characterize the performance evolution. Local operation inside the stack is probed with a Current Density Distribution Mapping device (CDDM).

Both R_{cell} and R_{stack} (10 A) devices mitigate the global performance decay of the stack along our Stack-SU/SD AST protocol, with a higher protection level for the R_{stack} (10 A). However, the latter does not reduce uniformly the individual cell degradation rates. The difference between the maximal loss and the average loss of the cell voltages is about 109%, while the R_{cell} case is about 24%. Indeed, the R_{cell} case is able to the shunt independently each cell and to avoid singular degrading operation. By analyzing the CDDM measurements in nominal FC operation at the beginning and at the end of test, the most degraded zone is the cathode inlet (facing the anode outlet) strongly exposed to the reverse current phenomena and the high cathode potential excursion during the SU phase. The cathode outlet (facing the anode inlet) is probably damaged due to the SD phase and the vacuum/pumping effect with residual H_2 in the inlet volumes during the H_2 consumption phase. Thus, degradations related to SD phase are non-negligible despite the application of experimental recommendations and these aspects should be taken into considerations for future work.

To better understand these heterogeneous degradation rates, an innovative approach has been employed in this work by visualizing the H_2|Air front propagation and the inherent internal currents during the SU phase and the H_2 consumption process during the SD phase with fast acquisition (around 20 Hz) of CDDM data.

Transient local currents and cell voltage measurements have highlighted two degradation mechanisms in the SU phase: (1) the Reverse Current Decay mechanism when Air-filled anode compartments are partially purged with H_2, and surprisingly, (2) the cell reversal mechanism when the H_2 injection is delayed in certain cells. The latter cells operate therefore in electrolysis under anodic and cathodic Air/Air fluidic configuration while neighbouring cells in FC operation under H_2/Air delivers some current. Such abnormal and transient phase is observed in our study by using more realistic stack design than the ones usually published in the literature, commonly short-stack with small surface area and/or laboratory flow-field design limiting the heterogeneous gas supply. Moreover, the cell reversal occurrence is promoted when the derivative current density circulating in the entire stack and the in the stack resistance is too important (with low-resistive dummy load, *i.e.*, 0.162 Ω in our work) compared to the H_2 injection rate, namely when the H_2 stoichiometry is close to one. In this case, injected H_2 is mostly consumed at the first well-fed cells at the intake (close to H_2 stack port entrance) and make the anode filling of last cells impossible, less well-supplied. In conclusion, the injection of H_2 into a real PEMFC system should be as fast as possible to reduce the exposure time of the H_2|Air front and the occurrence of cell voltage reversal.

In SD phase, the H_2 consumption can also be heterogeneous between the cells and along the cathode channel. Within the cell, faster fuel depletion occurs rather in the center of the MEA surface than at the inlet / outlet areas which are still supplied by residual H_2 stored in the inlet / outlet pipes. At the stack scale, the depletion can be uniform when a low current density is imposed for each cell (*i.e.*, with R_{stack} "10 A" in our work). On the contrary, the individual R_{cell} case consumes H_2 preferentially at the center of the stack causing then certain cells to remains in idling / OCV mode.

Consequently, the R_{cell} configuration seems to be more suitable for the SD phase and the R_{stack} for the SU phase and this dual architecture should be optimized in additional investigations. It would also be recommended to investigate independently each phase by using N_2 purges to ensure soft conditions for the other phase. Finally, this optimized combination (R_{stack} + R_{cell}) should lead to the most efficient protection when the anodic compartment is filled with Air during the long stop, before the next SU phase. However, the effect of fluidic heterogeneities intra-cell and inter-in full-size stack with a significant number of cells would require as well additional investigations.

Moreover, to get an overview of alternative SU/SD process regarding the Chapter II, our Stack-SU/SD AST protocol could also be modified to perform the SD process by O_2 consumption resulting in H_2/H_2 fluidic configuration, followed by the SU phase with an H_2|Air front propagation along the cathode channel. This SD process by the oxygen depletion at the cathode is considered to be the most suitable, keeping the anode compartment under H_2. In this case, the SU phase after a short stop under H_2/H_2 is then supposed to be harmless. Nevertheless, no study has ever been published in the literature to characterize the possible effect of Air|H_2 front on the cathode side during the SU phase (high current density at low potential), despite the numerous patents filed. Furthermore, oxygen depletion can entail pressure variation between anode and cathode sides, which could lead to mechanical degradation. In addition, the usage of vacuum procedure could provoke an uncontrolled drying effect known to be harmful for cells. Moreover, further study on the leakage aspects during complete shut-down (H_2/H_2) and the possible impact of the slow infiltration of oxygen within the stack (mainly expected on the membrane due to peroxide formation) would be needed to define the "long" and the "short" stop duration according to the stack designs and system architectures. Indeed, RCD mechanism may occur during the next SU phase depending on the stop duration. On the whole, the complete assessment of each SU and SD scenario, independently, with a real stack design should provide both optimized architectures and operating strategies to increase the PEMFC durability.

REFERENCES

[1] S. Mekhilef, R. Saidur, and A. Safari, "Comparative study of different fuel cell technologies," *Renewable and Sustainable Energy Reviews*, vol. 16, no. 1, pp. 981–989, Jan. 2012, doi: 10.1016/j.rser.2011.09.020.

[2] "Un pacte vert pour l'Europe," *Commission européenne - European Commission*. https://ec.europa.eu/info/strategy/priorities-2019-2024/european-green-deal_fr (accessed May 23, 2022).

[3] "Schmidt Automotive Research," *schmidtmatthias.de*. https://www.schmidtmatthias.de (accessed May 23, 2022).

[4] "Faurecia remporte un contrat majeur de systèmes de stockage à hydrogène pour les poids lourds Hyundai," *Faurecia*. http://www.faurecia.com/newsroom/faurecia-remporte-un-contrat-majeur-de-systemes-de-stockage-hydrogene-pour-les-poids-lourds-hyundai (accessed May 23, 2022).

[5] J.-P. Poirot-Crouvezier, "Modélisation dynamique des phénomènes hydrauliques, thermiques et électriques dans un groupe électrogène à pile à combustible destiné à l'application automobile," Theses, Institut National Polytechnique de Grenoble, 2000. Accessed: Sep. 15, 2020. [Online]. Available: https://hal.archives-ouvertes.fr/tel-02907129

[6] J. Matthey, "The Role of Platinum in Proton Exchange Membrane Fuel Cells," *Johnson Matthey Technology Review*. https://www.technology.matthey.com/article/57/4/259-271/ (accessed Oct. 26, 2021).

[7] E. H. Majlan, D. Rohendi, W. R. W. Daud, T. Husaini, and M. A. Haque, "Electrode for proton exchange membrane fuel cells: A review," *Renewable and Sustainable Energy Reviews*, vol. 89, pp. 117–134, 2018, doi: 10.1016/j.rser.2018.03.007.

[8] Y. Yang, X. Zhou, B. Li, and C. Zhang, "Recent progress of the gas diffusion layer in proton exchange membrane fuel cells: Material and structure designs of microporous layer," *International Journal of Hydrogen Energy*, vol. 46, no. 5, pp. 4259–4282, 2021, doi: 10.1016/j.ijhydene.2020.10.185.

[9] S. Park, J.-W. Lee, and B. N. Popov, "A review of gas diffusion layer in PEM fuel cells: Materials and designs," *International Journal of Hydrogen Energy*, vol. 37, no. 7, pp. 5850–5865, Apr. 2012, doi: 10.1016/j.ijhydene.2011.12.148.

[10] S. Rodosik, "Etude de l'impact d'architectures fluidiques innovantes sur la gestion, la performance et la durabilité de systèmes de pile à combustible PEMFC pour les transports," phdthesis, Université Grenoble Alpes, 2019. Accessed: Jun. 29, 2022. [Online]. Available: https://tel.archives-ouvertes.fr/tel-02493175

[11] "Hydrogen Roadmap Europe: A sustainable pathway for the European Energy Transition | www.fch.europa.eu." https://www.fch.europa.eu/news/hydrogen-roadmap-europe-sustainable-pathway-european-energy-transition (accessed Apr. 20, 2022).

[12] "Behind the scenes: The 2020 Automotive Fuel Cell Roadmap - Advanced Propulsion Centre," Feb. 12, 2021. https://www.apcuk.co.uk/behind-the-scenes-the-2020-automotive-fuel-cell-roadmap/ (accessed Apr. 20, 2022).

[13] "US DRIVE Fuel Cell Technical Team Roadmap," *Energy.gov*. https://www.energy.gov/eere/vehicles/downloads/us-drive-fuel-cell-technical-team-roadmap (accessed Apr. 20, 2022).

[14] "Strategy for Developing Hydrogen and Fuel-Cell Technologies Formulated." https://www.meti.go.jp/english/press/2019/0918_001.html (accessed Apr. 20, 2022).

[15] X. Ren, Y. Wang, A. Liu, Z. Zhang, Q. Lv, and B. Liu, "Current progress and performance improvement of Pt/C catalysts for fuel cells," *Journal of Materials Chemistry A*, vol. 8, no. 46, pp. 24284–24306, 2020, doi: 10.1039/d0ta08312g.

[16] S. T. Thompson *et al.*, “Direct hydrogen fuel cell electric vehicle cost analysis: System and high-volume manufacturing description, validation, and outlook,” *Journal of Power Sources*, vol. 399, pp. 304–313, Sep. 2018, doi: 10.1016/j.jpowsour.2018.07.100.

[17] “DOE Technical Targets for Polymer Electrolyte Membrane Fuel Cell Components,” *Energy.gov*. https://www.energy.gov/eere/fuelcells/doe-technical-targets-polymer-electrolyte-membrane-fuel-cell-components (accessed Oct. 26, 2021).

[18] P. Pei, Q. Chang, and T. Tang, “A quick evaluating method for automotive fuel cell lifetime,” *International Journal of Hydrogen Energy*, vol. 33, no. 14, pp. 3829–3836, 2008, doi: 10.1016/j.ijhydene.2008.04.048.

[19] P. Ren, P. Pei, Y. Li, Z. Wu, D. Chen, and S. Huang, “Degradation mechanisms of proton exchange membrane fuel cell under typical automotive operating conditions,” *Progress in Energy and Combustion Science*, vol. 80, p. 100859, Sep. 2020, doi: 10.1016/j.pecs.2020.100859.

[20] K. Kinoshita and J. A. S. Bett, “Determination of carbon surface oxides on platinum-catalyzed carbon,” *Carbon*, vol. 12, no. 5, pp. 525–533, Oct. 1974, doi: 10.1016/0008-6223(74)90054-2.

[21] M. Zago *et al.*, “Experimental analysis of recoverable performance loss induced by platinum oxide formation at the polymer electrolyte membrane fuel cell cathode,” *Journal of Power Sources*, vol. 455, p. 227990, Apr. 2020, doi: 10.1016/j.jpowsour.2020.227990.

[22] T. Jahnke, G. A. Futter, A. Baricci, C. Rabissi, and A. Casalegno, “Physical Modeling of Catalyst Degradation in Low Temperature Fuel Cells: Platinum Oxidation, Dissolution, Particle Growth and Platinum Band Formation,” *J. Electrochem. Soc.*, vol. 167, no. 1, p. 013523, Nov. 2019, doi: 10.1149/2.0232001JES.

[23] P. Gazdzick, J. Mitzel, D. Garcia Sanchez, M. Schulze, and K. A. Friedrich, “Evaluation of reversible and irreversible degradation rates of polymer electrolyte membrane fuel cells tested in automotive conditions,” *Journal of Power Sources*, vol. 327, pp. 86–95, Sep. 2016, doi: 10.1016/j.jpowsour.2016.07.049.

[24] L. M. Roen, C. H. Paik, and T. D. Jarvi, “Electrocatalytic Corrosion of Carbon Support in PEMFC Cathodes,” *Electrochemical and Solid-State Letters*, vol. 7, no. 1, pp. A19–A22, 2004, doi: 10.1149/1.1630412.

[25] S. Maass, F. Finsterwalder, G. Frank, R. Hartmann, and C. Merten, “Carbon support oxidation in PEM fuel cell cathodes,” *Journal of Power Sources*, vol. 176, no. 2, pp. 444–451, Feb. 2008, doi: 10.1016/j.jpowsour.2007.08.053.

[26] N. Macauley *et al.*, “Carbon Corrosion in PEM Fuel Cells and the Development of Accelerated Stress Tests,” *J. Electrochem. Soc.*, vol. 165, no. 6, p. F3148, Mar. 2018, doi: 10.1149/2.0061806jes.

[27] N. Linse, L. Gubler, G. G. Scherer, and A. Wokaun, “The effect of platinum on carbon corrosion behavior in polymer electrolyte fuel cells,” *Electrochimica Acta*, vol. 56, no. 22, pp. 7541–7549, 2011, doi: 10.1016/j.electacta.2011.06.093.

[28] W. Li and A. M. Lane, “Investigation of Pt catalytic effects on carbon support corrosion of the cathode catalyst in PEM fuel cells using DEMS spectra,” *Electrochemistry Communications*, vol. 11, no. 6, pp. 1187–1190, 2009, doi: 10.1016/j.elecom.2009.04.001.

[29] F. Maillard, A. Bonnefont, and F. Micoud, “An EC-FTIR study on the catalytic role of Pt in carbon corrosion,” *Electrochemistry Communications*, vol. 13, no. 10, pp. 1109–1111, 2011, doi: 10.1016/j.elecom.2011.07.011.

[30] L. Castanheira, W. O. Silva, F. H. B. Lima, A. Crisci, L. Dubau, and F. Maillard, “Carbon Corrosion in Proton-Exchange Membrane Fuel Cells: Effect of the Carbon Structure, the Degradation Protocol, and the Gas Atmosphere,” *ACS Catal.*, vol. 5, no. 4, pp. 2184–2194, Apr. 2015, doi: 10.1021/cs501973j.

[31] D. Garcia-Sanchez, T. Morawietz, P. G. da Rocha, R. Hiesgen, P. Gazdzicki, and K. A. Friedrich, “Local impact of load cycling on degradation in polymer electrolyte fuel cells,” *Applied Energy*, vol. 259, p. 114210, Feb. 2020, doi: 10.1016/j.apenergy.2019.114210.

[32] S. Kundu, M. Fowler, L. C. Simon, and R. Abouatallah, “Reversible and irreversible degradation in fuel cells during Open Circuit Voltage durability testing,” *Journal of Power Sources*, vol. 182, no. 1, pp. 254–258, Jul. 2008, doi: 10.1016/j.jpowsour.2008.04.009.

[33] N. Zhao, Y. Chu, Z. Xie, K. Eggen, F. Girard, and Z. Shi, “Effects of Fuel Cell Operating Conditions on Proton Exchange Membrane Durability at Open-Circuit Voltage,” *Fuel Cells*, vol. 20, no. 2, pp. 176–184, 2020, doi: 10.1002/fuce.201900173.

[34] Z. Zhao, L. Castanheira, L. Dubau, G. Berthomé, A. Crisci, and F. Maillard, “Carbon corrosion and platinum nanoparticles ripening under open circuit potential conditions,” *Journal of Power Sources*, vol. 230, pp. 236–243, May 2013, doi: 10.1016/j.jpowsour.2012.12.053.

[35] C. G. Chung, L. Kim, Y. W. Sung, J. Lee, and J. S. Chung, “Degradation mechanism of electrocatalyst during long-term operation of PEMFC,” *International Journal of Hydrogen Energy*, vol. 34, no. 21, pp. 8974–8981, Nov. 2009, doi: 10.1016/j.ijhydene.2009.08.094.

[36] E. Guilminot, A. Corcella, F. Charlot, F. Maillard, and M. Chatenet, “Detection of Pt z + Ions and Pt Nanoparticles Inside the Membrane of a Used PEMFC,” *J. Electrochem. Soc.*, vol. 154, no. 1, p. B96, Dec. 2006, doi: 10.1149/1.2388863.

[37] R. M. Darling and J. P. Meyers, “Kinetic Model of Platinum Dissolution in PEMFCs,” *J. Electrochem. Soc.*, vol. 150, no. 11, pp. A1523–A1527, Jan. 2003, doi: 10.1149/1.1613669.

[38] W. J. Plieth, “Electrochemical properties of small clusters of metal atoms and their role in surface enhanced Raman scattering,” *Journal of Physical Chemistry*, vol. 86, no. 16, pp. 3166–3170, 1982, doi: 10.1021/j100213a020.

[39] P. J. Ferreira *et al.*, “Instability of Pt ∕ C Electrocatalysts in Proton Exchange Membrane Fuel Cells: A Mechanistic Investigation,” *J. Electrochem. Soc.*, vol. 152, no. 11, p. A2256, Oct. 2005, doi: 10.1149/1.2050347.

[40] S. Cherevko *et al.*, “Dissolution of Platinum in the Operational Range of Fuel Cells,” *ChemElectroChem*, vol. 2, no. 10, pp. 1471–1478, Oct. 2015, doi: 10.1002/celc.201500098.

[41] D. J. Myers, X. Wang, M. C. Smith, and K. L. More, “Potentiostatic and Potential Cycling Dissolution of Polycrystalline Platinum and Platinum Nano-Particle Fuel Cell Catalysts,” *J. Electrochem. Soc.*, vol. 165, no. 6, p. F3178, Mar. 2018, doi: 10.1149/2.0211806jes.

[42] L. Gubler, S. M. Dockheer, and W. H. Koppenol, “Radical (HO•, H• and HOO•) Formation and Ionomer Degradation in Polymer Electrolyte Fuel Cells,” *J. Electrochem. Soc.*, vol. 158, no. 7, p. B755, Apr. 2011, doi: 10.1149/1.3581040.

[43] G. A. Futter, A. Latz, and T. Jahnke, “Physical modeling of chemical membrane degradation in polymer electrolyte membrane fuel cells: Influence of pressure, relative humidity and cell voltage,” *Journal of Power Sources*, vol. 410–411, pp. 78–90, Jan. 2019, doi: 10.1016/j.jpowsour.2018.10.085.

[44] V. O. Mittal, H. R. Kunz, and J. M. Fenton, “Is H2O2 Involved in the Membrane Degradation Mechanism in PEMFC?,” *Electrochem. Solid-State Lett.*, vol. 9, no. 6, p. A299, Apr. 2006, doi: 10.1149/1.2192696.

[45] V. O. Mittal, H. R. Kunz, and J. M. Fenton, “Membrane Degradation Mechanisms in PEMFCs,” *J. Electrochem. Soc.*, vol. 154, no. 7, p. B652, May 2007, doi: 10.1149/1.2734869.

[46] C. A. Reiser *et al.*, “A reverse-current decay mechanism for fuel cells,” *Electrochemical and Solid-State Letters*, vol. 8, no. 6, pp. A273–A276, 2005, doi: 10.1149/1.1896466.

[47] J. P. Meyers and R. M. Darling, “Model of carbon corrosion in PEM fuel cells,” *Journal of the Electrochemical Society*, vol. 153, no. 8, pp. A1432–A1442, 2006, doi: 10.1149/1.2203811.

[48] Q. Shen *et al.*, “Study on the processes of start-up and shutdown in proton exchange membrane fuel cells,” *Journal of Power Sources*, vol. 189, no. 2, pp. 1114–1119, Apr. 2009, doi: 10.1016/j.jpowsour.2008.12.075.

[49] J. Kim, J. Lee, and Y. Tak, “Relationship between carbon corrosion and positive electrode potential in a proton-exchange membrane fuel cell during start/stop operation,” *Journal of Power Sources*, vol. 192, no. 2, pp. 674–678, Jul. 2009, doi: 10.1016/j.jpowsour.2009.03.039.

[50] G. Maranzana, A. Lamibrac, J. Dillet, S. Abbou, S. Didierjean, and O. Lottin, “Startup (and Shutdown) Model for Polymer Electrolyte Membrane Fuel Cells,” *J. Electrochem. Soc.*, vol. 162, no. 7, p. F694, Apr. 2015, doi: 10.1149/2.0451507jes.

[51] A. A. Topalov, S. Cherevko, A. R. Zeradjanin, J. C. Meier, I. Katsounaros, and K. J. J. Mayrhofer, “Towards a comprehensive understanding of platinum dissolution in acidic media,” *Chemical Science*, vol. 5, no. 2, pp. 631–638, 2014, doi: 10.1039/C3SC52411F.

[52] A. Kneer, N. Wagner, C. Sadeler, A.-C. Scherzer, and D. Gerteisen, “Effect of Dwell Time and Scan Rate during Voltage Cycling on Catalyst Degradation in PEM Fuel Cells,” *J. Electrochem. Soc.*, vol. 165, no. 10, p. F805, Jul. 2018, doi: 10.1149/2.0651810jes.

[53] D. J. S. Sandbeck *et al.*, “Particle Size Effect on Platinum Dissolution: Practical Considerations for Fuel Cells,” *ACS Appl. Mater. Interfaces*, vol. 12, no. 23, pp. 25718–25727, Jun. 2020, doi: 10.1021/acsami.0c02801.

[54] A. A. Topalov *et al.*, “Dissolution of Platinum: Limits for the Deployment of Electrochemical Energy Conversion?,” *Angewandte Chemie International Edition*, vol. 51, no. 50, pp. 12613–12615, 2012, doi: 10.1002/anie.201207256.

[55] J.-H. Park *et al.*, “Understanding the mechanism of membrane electrode assembly degradation by carbon corrosion by analyzing the microstructural changes in the cathode catalyst layers and polarization losses in proton exchange membrane fuel cell,” *Electrochimica Acta*, vol. 83, pp. 294–304, Nov. 2012, doi: 10.1016/j.electacta.2012.07.117.

[56] R. Sharma and S. M. Andersen, “An opinion on catalyst degradation mechanisms during catalyst support focused accelerated stress test (AST) for proton exchange membrane fuel cells (PEMFCs),” *Applied Catalysis B: Environmental*, vol. 239, pp. 636–643, Dec. 2018, doi: 10.1016/j.apcatb.2018.08.045.

[57] S. Takao *et al.*, “Observation of Degradation of Pt and Carbon Support in Polymer Electrolyte Fuel Cell Using Combined Nano-X-ray Absorption Fine Structure and Transmission Electron Microscopy Techniques,” *ACS Appl. Mater. Interfaces*, vol. 10, no. 33, pp. 27734–27744, Aug. 2018, doi: 10.1021/acsami.8b04407.

[58] Z. Hu *et al.*, “Carbon corrosion induced fuel cell accelerated degradation warning: From mechanism to diagnosis,” *Electrochimica Acta*, vol. 389, 2021, doi: 10.1016/j.electacta.2021.138627.

[59] Z. Hu *et al.*, “Mechanistic insight into the accelerated decay of fuel cells from catalyst-layer structural failure,” *Energy Conversion and Management*, vol. 227, p. 113568, Jan. 2021, doi: 10.1016/j.enconman.2020.113568.

[60] H. Schulenburg *et al.*, “3D Imaging of Catalyst Support Corrosion in Polymer Electrolyte Fuel Cells,” *J. Phys. Chem. C*, vol. 115, no. 29, pp. 14236–14243, Jul. 2011, doi: 10.1021/jp203016u.

[61] B. Avasarala, R. Moore, and P. Haldar, “Surface oxidation of carbon supports due to potential cycling under PEM fuel cell conditions,” *Electrochimica Acta*, vol. 55, no. 16, pp. 4765–4771, Jun. 2010, doi: 10.1016/j.electacta.2010.03.056.

[62] J. Jung *et al.*, “Electrochemical impedance analysis with transmission line model for accelerated carbon corrosion in polymer electrolyte membrane fuel cells,” *International Journal of Hydrogen Energy*, vol. 43, no. 32, pp. 15457–15465, Aug. 2018, doi: 10.1016/j.ijhydene.2018.06.093.

[63] Y. Yu, H. Li, H. Wang, X.-Z. Yuan, G. Wang, and M. Pan, “A review on performance degradation of proton exchange membrane fuel cells during startup and shutdown processes: Causes, consequences, and mitigation strategies,” *Journal of Power Sources*, vol. 205, pp. 10–23, 2012, doi: 10.1016/j.jpowsour.2012.01.059.

[64] T. Zhang, P. Wang, H. Chen, and P. Pei, “A review of automotive proton exchange membrane fuel cell degradation under start-stop operating condition,” *Applied Energy*, vol. 223, pp. 249–262, 2018, doi: 10.1016/j.apenergy.2018.04.049.

[65] Y. Yamashita *et al.*, “Durability of Pt catalysts supported on graphitized carbon-black M during gas-exchange start-up operation similar to that used for fuel cell vehicles,” *Journal of the Electrochemical Society*, vol. 163, no. 7, pp. F644–F650, 2016, doi: 10.1149/2.0771607jes.

[66] J. L. Bott-Neto *et al.*, “Utilization of graphitized and fluorinated carbon as platinum nanoparticles supports for application in proton exchange membrane fuel cell cathodes,” *Journal of Power Sources*, vol. 404, pp. 28–38, Nov. 2018, doi: 10.1016/j.jpowsour.2018.10.004.

[67] E. You, M. Min, S.-A. Jin, T. Kim, and C. Pak, “Highly durable, cost-effective, and multifunctional carbon-supported irRu-based catalyst for automotive polymer electrolyte fuel cell anodes,” *Journal of the Electrochemical Society*, vol. 165, no. 6, pp. F3094–F3099, 2018, doi: 10.1149/2.0121806jes.

[68] T. Binninger *et al.*, “Stabilization of Pt Nanoparticles Due to Electrochemical Transistor Switching of Oxide Support Conductivity,” *Chemistry of Materials*, vol. 29, no. 7, pp. 2831–2843, 2017, doi: 10.1021/acs.chemmater.6b04851.

[69] J. Luo *et al.*, “Highly Selective TiN-Supported Highly Dispersed Pt Catalyst: Ultra Active toward Hydrogen Oxidation and Inactive toward Oxygen Reduction,” *ACS Applied Materials and Interfaces*, vol. 10, no. 4, pp. 3530–3537, 2018, doi: 10.1021/acsami.7b15159.

[70] H. Shintani, Y. Kojima, K. Kakinuma, M. Watanabe, and M. Uchida, “Novel strategy to mitigate cathode catalyst degradation during air/air startup cycling via the atmospheric resistive switching mechanism of a hydrogen anode with a platinum catalyst supported on tantalum-doped titanium dioxide,” *Journal of Power Sources*, vol. 294, pp. 292–298, Oct. 2015, doi: 10.1016/j.jpowsour.2015.06.072.

[71] B. Randrianarizafy, P. Schott, M. Gerard, and Y. Bultel, “Modelling Carbon Corrosion during a PEMFC Startup: Simulation of Mitigation Strategies,” *Energies*, vol. 13, no. 9, Art. no. 9, Jan. 2020, doi: 10.3390/en13092338.

[72] A. Lamibrac, “Étude des dégradations dans les piles à combustible PEMFC pendant les phases de démarrage/arrêt,” These de doctorat, Université de Lorraine, 2013. Accessed: Sep. 15, 2020. [Online]. Available: https://www.theses.fr/2013LORR0117

[73] B. Randrianarizafy, “Multi-physics modeling of startup and shutdown of a PEM fuel cell and study of the carbon support degradation : mitigation strategies and design optimization,” phdthesis, Université Grenoble Alpes, 2018. Accessed: Sep. 17, 2020. [Online]. Available: https://tel.archives-ouvertes.fr/tel-02140284

[74] J. Dillet *et al.*, “Impact of flow rates and electrode specifications on degradations during repeated startups and shutdowns in polymer-electrolyte membrane fuel cells,” *Journal of Power Sources*, vol. 250, pp. 68–79, 2014, doi: 10.1016/j.jpowsour.2013.10.141.

[75] J. Dillet *et al.*, “Internal currents, CO2 emissions and decrease of the Pt electrochemical surface area during fuel cell start-up and shut-down,” presented at the ECS Transactions, ECS Transactions, 2012, pp. 701–710. doi: 10.1149/05002.0701ecst.

[76] S. Komini Babu *et al.*, “Spatially resolved degradation during startup and shutdown in polymer electrolyte membrane fuel cell operation,” *Applied Energy*, vol. 254, p. 113659, Nov. 2019, doi: 10.1016/j.apenergy.2019.113659.

[77] A. Lamibrac *et al.*, “Experimental characterization of internal currents during the start-up of a proton exchange membrane fuel cell,” *Journal of Power Sources*, vol. 196, no. 22, pp. 9451–9458, Nov. 2011, doi: 10.1016/j.jpowsour.2011.07.013.

[78] W. Gu, R. N. Carter, P. T. Yu, and H. A. Gasteiger, “Start/Stop and Local H2 Starvation Mechanisms of Carbon Corrosion: Model vs. Experiment,” *ECS Trans.*, vol. 11, no. 1, pp. 963–973, Sep. 2007, doi: 10.1149/1.2781008.

[79] S. Kreitmeier, A. Wokaun, and F. N. Büchi, “Local catalyst support degradation during polymer electrolyte fuel cell start-up and shutdown,” *Journal of the Electrochemical Society*, vol. 159, no. 11, pp. F787–F793, 2012, doi: 10.1149/2.019212jes.

[80] Y. Ishigami *et al.*, “Corrosion of carbon supports at cathode during hydrogen/air replacement at anode studied by visualization of oxygen partial pressures in a PEFC—Start-up/shut-down simulation,” *Journal of Power Sources*, vol. 196, no. 6, pp. 3003–3008, Mar. 2011, doi: 10.1016/j.jpowsour.2010.11.092.

[81] S. Ghosh, H. Ohashi, H. Tabata, Y. Hashimasa, and T. Yamaguchi, “In-plane and through-plane non-uniform carbon corrosion of polymer electrolyte fuel cell cathode catalyst layer during

extended potential cycles," *Journal of Power Sources*, vol. 362, pp. 291–298, Sep. 2017, doi: 10.1016/j.jpowsour.2017.07.017.

[82] J. Durst *et al.*, "Degradation heterogeneities induced by repetitive start/stop events in proton exchange membrane fuel cell: Inlet vs. outlet and channel vs. land," *Applied Catalysis B: Environmental*, vol. 138–139, pp. 416–426, Jul. 2013, doi: 10.1016/j.apcatb.2013.03.021.

[83] I. A. Schneider and S. von Dahlen, "Start-Stop Phenomena in Channel and Land Areas of a Polymer Electrolyte Fuel Cell," *Electrochem. Solid-State Lett.*, vol. 14, no. 2, p. B30, Dec. 2010, doi: 10.1149/1.3518520.

[84] N. Linse, G. G. Scherer, A. Wokaun, and L. Gubler, "Quantitative analysis of carbon corrosion during fuel cell start-up and shut-down by anode purging," *Journal of Power Sources*, vol. 219, pp. 240–248, 2012, doi: 10.1016/j.jpowsour.2012.07.037.

[85] K. Eom *et al.*, "Effects of residual oxygen partial pressure on the degradation of polymer electrolyte membrane fuel cells under reverse current conditions," *Journal of Power Sources*, vol. 198, pp. 42–50, 2012, doi: 10.1016/j.jpowsour.2011.09.085.

[86] T. Mittermeier, A. Weiß, F. Hasché, G. Hübner, and H. A. Gasteiger, "PEM fuel cell start-up/shut-down losses vs temperature for non-graphitized and graphitized cathode carbon supports," *Journal of the Electrochemical Society*, vol. 164, no. 2, pp. F127–F137, 2017, doi: 10.1149/2.1061702jes.

[87] Y. Y. Jo *et al.*, "Degradation of polymer electrolyte membrane fuel cells repetitively exposed to reverse current condition under different temperature," *Journal of Power Sources*, vol. 196, no. 23, pp. 9906–9915, 2011, doi: 10.1016/j.jpowsour.2011.08.035.

[88] E. Brightman and G. Hinds, "In situ mapping of potential transients during start-up and shut-down of a polymer electrolyte membrane fuel cell," *Journal of Power Sources*, vol. 267, pp. 160–170, Dec. 2014, doi: 10.1016/j.jpowsour.2014.05.040.

[89] T. Mittermeier, A. Weiß, F. Hasché, and H. A. Gasteiger, "PEM fuel cell start-up/shut-down losses vs relative humidity: The impact of water in the electrode layer on carbon corrosion," *Journal of the Electrochemical Society*, vol. 165, no. 16, pp. F1349–F1357, 2018, doi: 10.1149/2.0931816jes.

[90] J. H. Kim *et al.*, "Effects of cathode inlet relative humidity on PEMFC durability during startup-shutdown cycling: I. Electrochemical study," *Journal of the Electrochemical Society*, vol. 157, no. 1, pp. B104–B112, 2010, doi: 10.1149/1.3254170.

[91] J. H. Kim *et al.*, "Effects of cathode inlet relative humidity on PEMFC durability during startup-shutdown cycling: II. Diagnostic study," *Journal of the Electrochemical Society*, vol. 157, no. 5, pp. B633–B642, 2010, doi: 10.1149/1.3327888.

[92] P. T. Yu, W. Gu, R. Makharia, F. T. Wagner, and H. A. Gasteiger, "The impact of carbon stability on PEM fuel cell startup and shutdown voltage degradation," *ECS Trans.*, vol. 3, no. 1, pp. 797–809, Oct. 2006, doi: 10.1149/1.2356199.

[93] C. Reiser, D. Yang, and R. Sawyer, "Procedure for starting up a fuel cell system using a fuel purge," US20020076582A1, Jun. 20, 2002 Accessed: Sep. 15, 2020. [Online]. Available: https://patents.google.com/patent/US20020076582A1/en?oq=US+2002%2f0076582+A1

[94] C. A. Reiser, D. Yang, and R. D. Sawyer, "Procedure for starting up a fuel cell system using a fuel purge," US6887599B2, May 03, 2005 Accessed: Sep. 15, 2020. [Online]. Available: https://patents.google.com/patent/US6887599B2/en?oq=US+6%2c887%2c599+B2

[95] C. A. Reiser, D. Yang, and R. D. Sawyer, "Procedure for starting up a fuel cell system using a fuel purge," US7410712B2, Aug. 12, 2008 Accessed: Sep. 15, 2020. [Online]. Available: https://patents.google.com/patent/US7410712B2/en?oq=US+7%2c410%2c712+B2

[96] J. H. Kim *et al.*, "Development of a Durable PEMFC Start-Up Process by Applying a Dummy Load: II. Diagnostic Study," *J. Electrochem. Soc.*, vol. 157, no. 1, p. B118, Nov. 2009, doi: 10.1149/1.3246003.

[97] J. H. Kim *et al.*, "Development of a Durable PEMFC Startup Process by Applying a Dummy Load: I. Electrochemical Study," *J. Electrochem. Soc.*, vol. 156, no. 8, p. B955, Jun. 2009, doi: 10.1149/1.3148222.

[98] Y. Yang, W. Li, R. Lin, S. Xia, and Z. Jiang, “Impact of dummy load shut-down strategy on performance and durability of proton exchange membrane fuel cell stack,” *Journal of Power Sources*, vol. 404, pp. 126–134, Nov. 2018, doi: 10.1016/j.jpowsour.2018.10.003.

[99] R. Lin, D. Liu, S. Xia, T. Ma, and B. Dutruel, “Stack shut-down strategy optimisation of proton exchange membrane fuel cell with the segment stack technology,” *International Journal of Hydrogen Energy*, vol. 45, no. 1, pp. 1030–1044, Jan. 2020, doi: 10.1016/j.ijhydene.2019.10.218.

[100] D. Bona, D. E. Curtin, F. Pedrazzo, and E. M. Tresso, “Using a Stack Shunt to Mitigate Catalyst Support Carbon Corrosion in Polymer Electrolyte Membrane Fuel Cell Stacks During Start-Stop Cycling,” *J. Fuel Cell Sci. Technol*, vol. 11, no. 1, Feb. 2014, doi: 10.1115/1.4025535.

[101] Y. Yu *et al.*, “Current mapping of a proton exchange membrane fuel cell with a segmented current collector during the gas starvation and shutdown processes,” *International Journal of Hydrogen Energy*, vol. 37, no. 20, pp. 15288–15300, Oct. 2012, doi: 10.1016/j.ijhydene.2012.07.023.

[102] Q. Zhang, R. Lin, X. Cui, S. X. Xia, Z. Yang, and Y. T. Chang, “Study of the two-phase dummy load shut-down strategy for proton exchange membrane fuel cells,” *Journal of Power Sources*, vol. 341, pp. 230–239, Feb. 2017, doi: 10.1016/j.jpowsour.2016.11.098.

[103] R. Lin, S. Xia, Q. Zhang, and B. Dutruel, “Comparison Between the Constant Dummy Load and Step Load Shut-Down Strategy for PEMFCs,” *Fuel Cells*, vol. 18, no. 3, pp. 306–314, 2018, doi: 10.1002/fuce.201700095.

[104] Y. Yu, Z. Tu, H. Zhang, Z. Zhan, and M. Pan, “Comparison of degradation behaviors for open-ended and closed proton exchange membrane fuel cells during startup and shutdown cycles,” *Journal of Power Sources*, vol. 196, no. 11, pp. 5077–5083, Jun. 2011, doi: 10.1016/j.jpowsour.2011.01.075.

[105] A. Oyarce *et al.*, “Comparing shut-down strategies for proton exchange membrane fuel cells,” *Journal of Power Sources*, vol. 254, pp. 232–240, May 2014, doi: 10.1016/j.jpowsour.2013.12.058.

[106] H.-J. Kim *et al.*, “Development of shut-down process for a proton exchange membrane fuel cell,” *Journal of Power Sources*, vol. 180, no. 2, pp. 814–820, Jun. 2008, doi: 10.1016/j.jpowsour.2007.12.112.

[107] Y. Yu, G. Wang, Z. Tu, Z. Zhan, and M. Pan, “Effect of gas shutoff sequences on the degradation of proton exchange membrane fuel cells with dummy load during startup and shutdown cycles,” *Electrochimica Acta*, vol. 71, pp. 181–193, Jun. 2012, doi: 10.1016/j.electacta.2012.03.141.

[108] Y. Y. Jo *et al.*, “Effects of a hydrogen and air supply procedure on the performance degradation of PEMFCs,” *International Journal of Hydrogen Energy*, vol. 35, no. 23, pp. 13118–13124, Dec. 2010, doi: 10.1016/j.ijhydene.2010.04.072.

[109] S. Goebel, “Fuel cell shutdown and startup using a cathode recycle loop,” US20050058859A1, Mar. 17, 2005 Accessed: Sep. 15, 2020. [Online]. Available: https://patents.google.com/patent/US20050058859A1/en?oq=US+2005%2f0058859

[110] P. Yu and F. Wagner, “Method of using H2 purge for stack startup/shutdown to improve stack durability,” US20060046106A1, Mar. 02, 2006 Accessed: Sep. 15, 2020. [Online]. Available: https://patents.google.com/patent/US20060046106A1/en?oq=US+2006%2f0046106+A1

[111] C. Paik, J. A. Adams, G. S. Saloka, and M. S. Sulek, “Oxygen removal systems during fuel cell shutdown,” US20090023040A1, Jan. 22, 2009 Accessed: Sep. 15, 2020. [Online]. Available: https://patents.google.com/patent/US20090023040A1/en?oq=US+2009%2f0023040+A1

[112] S. G. Goebel, “Operational method for a simplified fuel cell system,” US9537160B2, Jan. 03, 2017 Accessed: Sep. 15, 2020. [Online]. Available: https://patents.google.com/patent/US9537160B2/en?oq=US+9%2c537%2c160+B2

[113] C. G. Hochgraf, P. T. Yu, F. T. Wagner, and R. S. Foley, “Life extension of PEM fuel cell using startup method,” US8828616B2, Sep. 09, 2014 Accessed: Sep. 15, 2020. [Online]. Available: https://patents.google.com/patent/US8828616B2/en?oq=US+8%2c828%2c616+B2

[114] J. Usborne, K. Kratschmar, D. Leboe, and N. Fagan, “Preventing corrosion during start up and shut down of a fuel cell,” US20080032163A1, Feb. 07, 2008 Accessed: Sep. 15, 2020. [Online].

Available: https://patents.google.com/patent/US20080032163A1/en?oq=US+2008%2f0032163+A1

[115] J. Y. Yang, F.-B. Weng, C.-K. Cheng, and T.-W. Kuo, "Fuel cell system and startup and shutdown method therefor," US20180166715A1, Jun. 14, 2018 Accessed: Sep. 15, 2020. [Online]. Available: https://patents.google.com/patent/US20180166715A1/en?oq=US+2018%2f0166715+Al

[116] T. A. Bekkedahl *et al.*, "Reducing fuel cell cathode potential during startup and shutdown," US6913845B2, Jul. 05, 2005 Accessed: Sep. 15, 2020. [Online]. Available: https://patents.google.com/patent/US6913845B2/en?patents=false&oq=US+6%2c913%2c845+B2

[117] R. Shimoi and Y. Ono, "(54) FUEL CELL SYSTEM," US 2007/0224482 A1

[118] D. P. Miller, J. A. Rock, and C. M. Marsiglio, "Individual cell shorting during startup and shutdown using an integrated switch," US7927752B2, Apr. 19, 2011 Accessed: Sep. 15, 2020. [Online]. Available: https://patents.google.com/patent/US7927752B2/en?oq=US+7%2c927%2c752+B2

[119] G. Paganelli, "Pile a combustible et procedure d'arrêt d'une pile a combustible," EP2494642B1, Dec. 13, 2017 Accessed: Sep. 15, 2020. [Online]. Available: https://patents.google.com/patent/EP2494642B1/fr?inventor=PAGANELLI+GINO&oq=PAGANELLI+GINO

[120] R. J. Balliet and C. A. Reiser, "System and method for shutting down a fuel cell power plant," US6835479B2, Dec. 28, 2004 Accessed: Sep. 15, 2020. [Online]. Available: https://patents.google.com/patent/US6835479B2/en?oq=US+6%2c835%2c479+B2

[121] J. McElroy, D. Davis, and M. Gasda, "Starting up and shutting down a fuel cell stack," US20070154752A1, Jul. 05, 2007 Accessed: Sep. 15, 2020. [Online]. Available: https://patents.google.com/patent/US20070154752A1/en?oq=US+2007%2f0154752

[122] P. T. Yu, F. T. Wagner, G. W. Skala, B. Lakshmanan, and J. P. Salvador, "Method of mitigating fuel cell degradation due to startup and shutdown via hydrogen/nitrogen storage," US20080145716A1, Jun. 19, 2008 Accessed: Sep. 15, 2020. [Online]. Available: https://patents.google.com/patent/US20080145716A1/en?oq=US+2008%2f0145716

[123] K. Ojima and K. Taruya, "Fuel cell system and method of shutting down the same," US20170346117A1, Nov. 30, 2017 Accessed: Sep. 15, 2020. [Online]. Available: https://patents.google.com/patent/US20170346117A1/en?oq=US+2017%2f0346117+Al

[124] D. A. Condit and R. D. Breault, "Shut-down procedure for hydrogen-air fuel cell system," US6635370B2, Oct. 21, 2003 Accessed: Sep. 15, 2020. [Online]. Available: https://patents.google.com/patent/US6635370B2/en?oq=US+6%2c635%2c370+B2

[125] D. A. Arthur *et al.*, "Fuel cell operational methods for hydrogen addition after shutdown," US8232014B2, Jul. 31, 2012 Accessed: Sep. 15, 2020. [Online]. Available: https://patents.google.com/patent/US8232014/en?oq=US+8%2c232%2c014+B2

[126] P. Margiott, F. Preli, G. Kulp, M. Perry, C. Reiser, and R. Balliet, "Fuel cell operational methods for hydrogen addition after shutdown," US 8,232,014B2, Dec. 11, 2009 Accessed: Sep. 15, 2020. [Online]. Available: https://patents.google.com/patent/US8232014B2/en

[127] "IRD Fuel Cells." https://irdfuelcells.com/ (accessed Jun. 28, 2022).

[128] "SIGRACET® Fuel Cell Components," *SGL Carbon*. https://www.sglcarbon.com/en/markets-solutions/material/sigracet-fuel-cell-components/ (accessed Jun. 28, 2022).

[129] "Development of PEM Fuel Cell Stack Reference Test Procedures for Industry | StackTest Project | Fact Sheet | FP7 | CORDIS | European Commission." https://cordis.europa.eu/project/id/303445 (accessed Nov. 13, 2022).

[130] S. Trasatti and O. A. Petrii, "Real surface area measurements in electrochemistry," *Pure and Applied Chemistry*, vol. 63, no. 5, pp. 711–734, Jan. 1991, doi: 10.1351/pac199163050711.

[131] "S++ Simulation Services." http://www.splusplus.com/ (accessed Nov. 14, 2022).

[132] "Fuel Cell Tech Team Accelerated Stress Test and Polarization Curve Protocols for PEM Fuel Cells," *Energy.gov*. https://www.energy.gov/eere/fuelcells/downloads/fuel-cell-tech-team-accelerated-stress-test-and-polarization-curve (accessed Apr. 08, 2021).

[133] W. Gu, R. N. Carter, P. T. Yu, and H. A. Gasteiger, “Start/Stop and Local H2 Starvation Mechanisms of Carbon Corrosion: Model vs. Experiment,” *ECS Trans.*, vol. 11, no. 1, p. 963, Sep. 2007, doi: 10.1149/1.2781008.

[134] “CVM Modules - SMART TESTSOLUTIONS GmbH.” https://www.smart-testsolutions.de/en/products/cvm/cvm-modules.html (accessed Nov. 16, 2022).

[135] M. Fontana, “Tapis de nanotubes de carbone structurés comme nouveau microporeux pour couche de diffusion de gaz des piles à combustible,” PhD thesis, Université Grenoble Alpes, 2021. Accessed: Jan. 04, 2023. [Online]. Available: https://theses.hal.science/tel-03256127

[136] J. Dowd, “DVS Resolution,” *Surface Measurement Systems*. https://www.surfacemeasurementsystems.com/products/dynamic-vapor-sorption-instruments/vapor-sorption-analyzer/dvs-resolution/ (accessed Jul. 06, 2022).

[137] L. F. R. Castanheira, “Corrosion of high surface area carbon supports used in proton-exchange membrane fuel cell electrodes,” PhD thesis, Université Grenoble Alpes, 2014. Accessed: Nov. 18, 2019. [Online]. Available: https://tel.archives-ouvertes.fr/tel-01303814

[138] D. S. Knight and W. B. White, “Characterization of diamond films by Raman spectroscopy,” *Journal of Materials Research*, vol. 4, no. 2, pp. 385–393, Apr. 1989, doi: 10.1557/JMR.1989.0385.

[139] T. Drugeot *et al.*, “Experimental assessment of proton exchange membrane fuel cell performance degradations during emulated start-up/shut-down phases,” *International Journal of Hydrogen Energy*, Dec. 2022, doi: 10.1016/j.ijhydene.2022.11.020.

[140] F. Maillard, S. Schreier, M. Hanzlik, E. R. Savinova, S. Weinkauf, and U. Stimming, “Influence of particle agglomeration on the catalytic activity of carbon-supported Pt nanoparticles in CO monolayer oxidation,” *Physical Chemistry Chemical Physics*, vol. 7, no. 2, pp. 385–393, 2005, doi: 10.1039/B411377B.

[141] L. Castanheira *et al.*, “Carbon Corrosion in Proton-Exchange Membrane Fuel Cells: From Model Experiments to Real-Life Operation in Membrane Electrode Assemblies,” *ACS Catal.*, vol. 4, no. 7, pp. 2258–2267, Jul. 2014, doi: 10.1021/cs500449q.

[142] H. Chen, X. Zhao, T. Zhang, and P. Pei, “The reactant starvation of the proton exchange membrane fuel cells for vehicular applications: A review,” *Energy Conversion and Management*, vol. 182, pp. 282–298, 2019, doi: 10.1016/j.enconman.2018.12.049.